Enhancing the stability of railroad ballast with geogrid reinforcement: an experimental and discrete element modeling study

By

Romaric Léo Esteban Desbrousses

Department of Civil Engineering

McGill University

Montreal, QC

June 2024

A thesis submitted to

McGill University

In partial fulfillment of the degree of

Doctor of Philosophy

© 2024 Romaric Léo Esteban Desbrousses

Abstract

Canada possesses an extensive rail network that is mainly supported by ballasted substructures in which a ballast layer lies immediately beneath the rail-tie assembly. The ballast layer performs multiple key functions in a track structure that include supporting the tracks, maintaining their alignment, and transferring train loads to the underlying soil layers. Due to its unbound nature, ballast undergoes substantial deformations when exposed to train loading that disturb the track alignment and compromise the track riding safety. Geogrids have recently emerged as a viable means to stabilize ballast and mitigate its deformations. A geogrid's ability to reinforce ballast hinges on its interaction with ballast particles, which is a function of parameters such as the geogrid aperture size and location in the ballast layer as well as the subgrade strength that must be investigated. Additionally, geogrids tend to exhibit temperature-dependent mechanical properties. Considering that Canadian railroads tend to be exposed to significant seasonal temperature fluctuations, it is important to determine whether such changes impact the performance of geogrid-reinforced ballast.

This thesis begins with an overview of the behavior of ballasted railroad tracks. The use of geogrids to stabilize ballast is then addressed and the various factors influencing the performance of geogrids in ballast are discussed. Chapter 3 then introduces an experimental campaign designed to assess the effect of temperature on the mechanical behavior of a large-aperture biaxial geogrid and a geogrid composite. Single-rib tensile tests are performed in a temperature-controlled environment on specimens of both materials at temperatures ranging from -30ºC to 40ºC. The tests reveal that both materials are sensitive to temperature and exhibit increasingly brittle responses as the temperature decreases below 20ºC and ductile behaviors at elevated temperatures.

In Chapter 4, a series of large-scale ballast box tests is conducted to investigate the effect of the geogrid placement depth and subgrade strength on the cyclic loading response of geogrid-reinforced ballast. In these experiments, 300mm-thick ballast layers are constructed over artificial subgrades with California Bearing Ratios of 25, 13, and 5 and are reinforced with a single geogrid layer located at depths of 150mm, 200mm, and 250mm beneath the tie. The results indicate that the geogrid placement depth wields a negligible impact on the response of geogrid-reinforced ballast supported by a strong subgrade. However, for softer subgrades, shallow placement depths

enhance a geogrid's ability to reinforce ballast, leading to smaller tie settlement and greater tie support stiffness.

Finally, building on the observations drawn in Chapter 4, three-dimensional distinct element simulations of the ballast box tests are performed to delve into the micromechanical features of the ballast-geogrid interaction mechanism. The geogrid placement depth is first varied from 50mm to 250mm below the tie and the simulations reveal that geogrids located within the ballast layer's upper 150mm are more effective at stabilizing ballast by virtue of being located within the volume of aggregate that displaces the most in response to cyclic loading. The geogrid aperture size ratio (A/D) is then varied from 1.09 to 2.91 while the geogrid stiffness is assigned values ranging from 9.54 to 18kN/m corresponding to the geogrid's tensile strength at 2% strain at temperatures ranging from 40^{o}C to -30^{o}C as discussed in Chapter 3. An $A/D \geq 1.45$ is required for a stable geogrid-ballast interlock to form, as lower ratios imply the geogrid aperture size is too small to allow ballast interlocking, leading to the formation of a preferential slippage plane along the geogrid's interface. On the other hand, the range of stiffnesses considered in the simulations appears to wield a marginal effect on the behavior of geogrid-reinforced ballast.

Résumé

Le réseau ferroviaire canadien est largement soutenu par des fondations ballastées où une couche de ballast se trouvant sous les traverses joue un rôle clef dans la stabilisation et l'ancrage des voies et la transmission des charges dues au trafic ferroviaire. La granularité du ballast entraîne son tassement sous l'effet des passages répétés de trains, causant des déformations qui altèrent l'alignement de la voie. Afin de contrer cette dégradation, les géogrilles sont employées pour renforcer le ballast grâce à un mécanisme de verrouillage offert par leur structure ouverte qui permet aux grains de ballast de s'imbriquer avec ces dernières. L'efficacité des géogrilles est influencée par la taille de leurs ouvertures, leur profondeur d'installation, et la raideur de la plateforme sous-jacente.

Cette recherche explore initialement la structure des voies ballastées, suivie d'une analyse de l'application des géogrilles pour la stabilisation du ballast. Une série d'essais de traction sur des géogrilles à des températures allant de -30ºC à 40ºC révèle les effets des changements thermiques sur leurs propriétés. Les géogrilles testées à basse température se comportent de façon fragile tandis que ces dernières deviennent ductiles quand la température de l'essai augmente.

Dans le Chapitre 4, des expériences à échelle réelle sur des échantillons de ballast, renforcés par des géogrilles placées à différentes profondeurs (150, 200, et 250mm sous la traverse), montrent que la raideur de la plateforme influence considérablement la profondeur optimale d'installation de la géogrille pour une stabilisation efficace. Sur des plateformes plus souples, une insertion moins profonde de la géogrille favorise un renforcement plus efficace du ballast, résultant en une diminution notable du tassement.

Dans le Chapitre 5, un modèle en trois dimensions est conçu pour simuler les expériences effectuées dans la Chapitre 4 en utilisant la méthode des éléments discrets dans le but d'étudier les aspects microscopiques de l'interaction entre une géogrille et les grains de ballast. Dans ces simulations, la profondeur d'ancrage d'une géogrille est variée entre 50mm et 250mm sous une traverse. Les résultats dévoilent l'existence de deux régimes de déplacement des grains de ballast dans une couche de 300mm. Les premiers 150mm de ballast en dessous de la traverse sont ceux qui subissent les déplacements les plus importants en réponse aux charges auxquels ils sont soumis. Par conséquent, l'insertion d'une géogrille à une profondeur plus petite ou égale à 150mm génère

les plus grandes réductions de tassement. Le ratio *A/D* de la taille d'ouverture de la géogrille est ensuite varié dans un intervalle allant de 1.09 à 2.91 tandis que la raideur de la géogrille est changée dans un intervalle de 9.54 à 18kN/m qui correspond à résistance à la traction de la géogrille à 2% de déformation à des température allant de 40°C à -30°C. Un ratio $A/D \geq 1.45$ est nécessaire afin d'assurer un verrouillage robuste alors que des ratios plus petits insinuent que les ouvertures des géogrilles sont trop petites pour permettre aux grains de les pénétrer. Cependant, les résistances à la traction de la géogrille considérées dans cette étude paramétrique n'ont pas d'effet particulier sur la capacité de la géogrille à stabiliser la couche de ballast.

Acknowledgments

This research project was conducted in the Department of Civil Engineering at McGill University under the supervision of Prof. Mohamed Meguid. I would like to thank Prof. Meguid for his invaluable advice, guidance, and unwavering support throughout my Ph.D. I also wish to express my gratitude to Mr. Sam Bhat of Titan Environmental Containment for supporting me during my doctoral studies, providing the geosynthetics used in my experiments, and giving technical advice. Additionally, I would like to extend my genuine appreciation for the Vadasz family foundation for their generous financial support.

I am very fortunate to have pursued my doctoral studies within Prof. Meguid's Geo-Group as I got to interact with truly brilliant individuals during my stay at McGill University. I would like to extend my gratitude to the current and past Geo-Group members: Mohamed Shokr, Dr. Ahmed Ibrahim, Jian Huo, Ali Pezeshki, Moustafa Ibrahim, Jana Jarjour, Dr. Mohammad Alobaidi, Abdelrahman Elrawy, Dr. Zainab Almheiri, Alix Kabre, Jiahao Xu, and Shaira Cruz for their amazing support and kindness.

I also go on with a debt of gratitude to the fantastic team of technicians at the McGill Jamieson Structures Laboratory who were instrumental in helping me design and build my experimental setup. A special thanks goes to Dr. William Cook, Mr. John Bartczak, and Mr. Mike Stephens.

And last but not least, I would like to thank my loved ones for their unwavering support throughout my journey as a Ph.D. student.

List of Publications

The following publications have resulted from the research work completed towards the doctoral degree:

Refereed Journal Papers

[J1] Desbrousses, R.L.E., Meguid, M.A., and Bhat, S. (2022). Effect of Temperature on the Mechanical Properties of Two Polymeric Geogrid Materials. *Geosynthetics International.* 29(3). 326-336.

[J2] Desbrousses, R.L.E., Meguid, M.A., and Bhat, S. (2023). Experimental Investigation of the Effects of Subgrade Strength and Geogrid Location on the Cyclic Response of Geogrid-Reinforced Ballast. *International Journal of Geosynthetics and Ground Engineering*. 9(67).

[J3] Desbrousses, R.L.E., Meguid, M.A., and Bhat, S. (2024). Discrete Element Study on the Effects of Geogrid Characteristics on the Mechanical Response of Reinforced Ballast under Cyclic Loading. *Transportation Infrastructure Geotechnology.*

[J4] Ibrahim, A., Desbrousses, R.L.E., Xu, J., and Meguid, M.A. (2024). Investigation of the Mechanical Response of Recovered Geogrids under Repeated Loading. *Geosynthetics International.*

Conference Proceeding Papers

[C1] Desbrousses, R.L.E. and Meguid, M.A. (2021). On the Analysis and Design of Reinforced Railway Embankments in Cold Climates: A Review. In: Walbridge, S., *et al. Proceedings of the Canadian Society of Civil Engineering Annual Conference 2021*. CSCE 2021. Lecture Notes in Civil Engineering, vol 240. Springer, Singapore.

[C2] Desbrousses, R.L.E. and Meguid, M.A. (2022). Effect of Subgrade Compressibility on the Reinforcing Performance of Railroad Geogrids: Insights from Finite Element Analysis. In: *GeoCalgary 2022*. Canadian Geotechnical Society, Calgary, AB.

[C3] Desbrousses, R.L.E. and Meguid, M.A. (2023). Geogrids in Cold Climates: Insights from In-Isolation Tensile Tests at Low Temperatures. In *Geosynthetics: Leading the Way to a Resilient Planet* (pp. 467-473). ICG Rome 2023, Rome, Italy. CRC Press.

[C4] Desbrousses, R.L.E. and Meguid, M.A. (2023). On the Design of a Pneumatic Cyclic Loading Setup for Geotechnical Testing. In: *GeoSaskatoon 2023*. Canadian Geotechnical Society, Saskatoon, SK.

[C5] Desbrousses, R.L.E., Meguid, M.A., and Bhat, S. (2024). On the Effect of Subgrade Strength on the Performance of Geogrid-Reinforced Railway Ballast. In: *GeoAmericas 2024.* International Geosynthetics Society, Toronto, ON.

Table of Contents

Abstract i
Résumé iii
Acknowledgments v
List of Publications vi
Table of Contents viii
List of Tables xi
List of Figures xii
Chapter 1 : Introduction 1
1.1. Background and Research Motivation 1
1.2. Objectives and Scope 3
1.3. Original Contributions 4
1.4. Contribution of Authors 5
1.5. Thesis Organization 5
Chapter 2 : Literature Review 8
2.1. Introduction 8
2.2. Components of Ballasted Railway Tracks 8
2.2.1. Superstructure 9
2.2.2. Substructure 9
2.3. Track Forces on Railroad Ballast 11
2.4. Behavior of Railroad Ballast Subjected to Cyclic Loading 13
2.4.1. Resilient Behavior 16
2.4.2. Permanent Deformation 19
2.5. Geotechnical Issues in Ballasted Substructures 23
2.5.1. Ballast Deformation 23
2.5.2. Ballast Fouling 23
2.5.3. Subgrade 25
2.6. Designing Ballasted Railroad Track Foundations 28
2.6.1. AREMA Method 29
2.6.2. British Design Method (Heath et al., 1972) 30
2.6.3. Raymond (1978) Modified AREMA Method 31
2.6.4. Li and Selig (1998a) Method 32

2.6.5. UIC Design Method ... 33
2.6.6. Sayeed and Shahin (2018a) Method ... 34
2.7. Geogrid Reinforcement of Railroad Ballast ... 34
2.7.1. Geogrid-Ballast Interaction Mechanism ... 35
2.7.2. Behavior of Geogrid-Reinforced Ballast ... 37
2.7.3. Factors Affecting the Performance of Geogrid-Reinforced Ballast ... 42
2.8. Summary ... 45
Chapter 3 : Effect of Temperature on the Mechanical Properties of Two Polymeric Geogrid Materials ... 48
3.1. Introduction ... 49
3.2. Experimental Program ... 53
3.2.1. Tested Materials ... 54
3.2.2. Testing Equipment ... 54
3.3. Test Results and Discussion ... 57
3.3.1. Biaxial Geogrid ... 57
3.3.2. Biaxial PP Geogrid Composite ... 64
3.4. Conclusions ... 69
Chapter 4 : Experimental Investigation of the Effects of Subgrade Strength and Geogrid Location on the Cyclic Response of Geogrid-Reinforced Ballast ... 73
4.1. Introduction ... 74
4.2. Methodology ... 77
4.2.1. Materials ... 77
4.2.2. Experimental Setup ... 79
4.3. Results ... 82
4.3.1. Permanent Settlement ... 82
4.3.2. Resilient Settlement ... 86
4.3.3. Tie Support Stiffness ... 89
4.3.4. Damping Ratio ... 91
4.3.5. Limitations ... 94
4.4. Conclusions ... 95
Chapter 5 : The Effects of Geogrid Characteristics on the Mechanical Response of Reinforced Ballast under Cyclic Loading: A Discrete Element Study ... 98
5.1. Introduction ... 99
5.2. Overview of the Experimental Campaign ... 101
5.3. Discrete Element Modeling of Geogrid-Reinforced Railroad Ballast ... 103

5.3.1. Railroad Ballast 104
5.3.2. Geogrid 108
5.3.3. Ballast Box and Geogrid-Ballast Assemblies 113
5.3.4. Simulation Summary 115
5.4. Results and Analysis 118
5.4.1. Macroscopic Behavior 118
5.4.2. Microscale Response 121
5.4.3. Geogrid Response 130
5.5. Parametric Study 133
5.5.1. Effect of Geogrid Aperture Size Ratio 134
5.5.2. Effect of Geogrid Stiffness 136
5.6. Discussion 137
5.7. Conclusions 141
Chapter 6 : Critical Discussion 143
6.1. Introduction 143
6.2. Exploring the Impact of Temperature on the Tensile Strength of Geogrids 144
6.3. Understanding the Interplay Between Geogrid Placement Depth, Subgrade Strength, and the Behavior of Geogrid-Reinforced Ballast 147
6.4. Influence of Geogrid Aperture Size, Stiffness, and Placement Depth: A Discrete Element Study 150
6.5. Conclusions 154
Chapter 7 : Conclusions 155
7.1. General Conclusions 155
7.2. Recommendations for Future Work 156
References 158
Appendix 183
A.1. Introduction 183
A.2. Soil Container 183
A.3. Pneumatic Cyclic Loading Apparatus 184
A.3.1. Load Measurement and Application 185
A.3.2. Pneumatic Circuit and Process Control 187
A.3.3. Displacement Measurement and Data Acquisition 189

List of Tables

Table 2.1: Summary of Available Track Foundation Design Methods. 28

Table 2.2: Recommended Geogrid Aperture Size Ratios. 43

Table 2.3: Recommended Geogrid Placement Depth for Optimum Reinforcement of Railroad Ballast. 45

Table 3.1: Summary of Previous Research on the Effect of Temperature on the Mechanical Properties of Geosynthetics. 52

Table 3.2: Minimum Average Roll Value Properties for the Biaxial Geogrid and Biaxial Geogrid Composite (Titan Environmental Containment, 2020, 2021). 54

Table 3.3: Temperature-Induced Changes in Rupture Strength (T_{ult}) 59

Table 3.4: Rupture Strength (T_{ult}) at Temperatures Ranging from -30°C to 20°C. 66

Table 4.1: Properties of the Crushed Granite Aggregate. 78

Table 4.2: Physical and Mechanical Properties of the Biaxial Geogrid (Desbrousses et al., 2021; Titan Environmental Containment, 2020). 79

Table 4.3: Rubber Mat Properties. 79

Table 4.4: Test Summary. 80

Table 5.1: Mechanical Properties of the Large Aperture Biaxial Polypropylene Geogrid. 103

Table 5.2: Contact Model Parameters Used for the Ballast Particles and the Box's Walls. 109

Table 5.3: Contact Model Parameters Used for the Biaxial Geogrid. 112

Table 5.4: Simulation Summary. 117

Table 5.5: Effect of Geogrid Stiffness on the Tie Settlement, Energy Dissipated by Frictional Sliding, and Parallel Bond Strain Energy after Twenty Load Cycles. 137

Table 5.6: Summary of Studies Investigating the Effect of Geogrid Placement Depth and Aperture Size. 140

List of Figures

Figure 2.1: Typical Ballasted Railway Track Structure.. 9
Figure 2.2: Track Forces Exerted by Passing Trains and their Effect on Substructure Stresses (redrawn and adapted from Selig and Waters (1994)).. 13
Figure 2.3: Residual and Resilient Strains during a Given Loading Cycle and the Corresponding Resilient Modulus. 14
Figure 2.4: Evolution of the Tie Settlement Obtained in Ballast Box Tests Showing the Fast Settlement Accumulation at the Onset of Cyclic Loading Followed by More Gradual Settlement Increases (adapted from Desbrousses et al. (2023)). 15
Figure 2.5: Various Sources of Ballast Fouling Material (Selig and Waters, 1994). 24
Figure 2.6: (a) Typical Ballasted Substructure and (b) Progressive Shear Failure....................... 26
Figure 2.7: (a) Ballasted Substructure and its (b) Excessive Plastic Deformation. 27
Figure 2.8: Granular Layer Used in Most Design Methods... 29
Figure 2.9: Design Chart Developed by Heath et al. (1972). 31
Figure 2.10: Design Charts Used to Prevent (a) Progressive Shear Failure and (b) Excessive Plastic Deformation (Li and Selig, 1998a). 33
Figure 2.11: Design Charts Used to Select the Granular Layer Thickness Required to Prevent (a) Progressive Shear Failure and (b) Excessive Plastic Deformation in the Subgrade (adapted from Sayeed and Shahin (2018a)). 35
Figure 2.12: Open Structure of a Typical Biaxial Geogrid... 36
Figure 2.13: Geogrid Placed at the Ballast/Subballast Interface Limiting the Development of Tensile Stresses in the Ballast Layer. 37
Figure 3.1: Example of a Typical Installation of Different Reinforcement Layers Within a Railway Embankment. 53
Figure 3.2: Large Aperture Biaxial PP Geogrid. 55
Figure 3.3: Biaxial Geogrid Composite. 55
Figure 3.4: Diagram of the Test Set Up Used to Perform Tensile Tests in a Temperature-Controlled Environment.. 56
Figure 3.5: Average Load-Strain Relationship for the Geogrid at Temperatures Ranging from -30ºC to 40ºC.. 58

Figure 3.6: Effect of Temperature on the Normalized Rupture Strength of the Geogrid ($T_{ult}/T_{ult@20}$). 59
Figure 3.7: (a) Normalized Rupture Strength of the Geogrid vs. Temperature, (b) A^f from -10°C to 40°C, (c) A^f from -30°C to -10°C, (d) A^f over the Range of Investigated Temperatures............. 60
Figure 3.8: Effect of Temperature on the Normalized Tensile Strength of the Geogrid at 2% Strain ($T_{2\%}/T_{2\%@20}$). 61
Figure 3.9: Variations in Normalized Ultimate Strain with Temperature for the Geogrid Material. 62
Figure 3.10: Failure Modes of the Geogrid at (a) -30°C, (b) -10°C, (c) 0°C, (d) 20°C, (e) 30°C, and (f) 40°C. 64
Figure 3.11: Average Load-Strain Relationships for the Geogrid Composite at Different Temperatures........ 65
Figure 3.12: Normalized Rupture Strength of the Geogrid Composites at Each Tested Temperature. 66
Figure 3.13: Normalized Tensile Strength of the Geogrid Composite at 2% Strain at Each Tested Temperature. 67
Figure 3.14: Normalized Ultimate Strain of the Geogrid Composite at Temperatures Ranging from -30°C to 20°C........ 68
Figure 3.15: Failure Modes for the Geogrid Composite at (a) -30°C, (b) -20°C, (c) -10°C, (d) 0°C, (e) 10°C, and (f) 20°C........ 71
Figure 4.1: Particle Size Distribution of the Granite Aggregate Used in the Ballast Box Tests. . 78
Figure 4.2: (a) Pneumatic Cyclic Loading Apparatus and its Ballast Box, (b) Plan View of the Ballast Box, (c) Laboratory Set Up........ 81
Figure 4.3: Tie Settlement Curves Recorded in (a) Unreinforced Ballast Samples and Geogrid-Reinforced Ballast Layers Supported by the (b) Competent, (c) Fair, and (d) Soft Subgrades.... 83
Figure 4.4: Final Tie Settlement Reduction Factors in Geogrid-Reinforced Ballast Layers........ 85
Figure 4.5: Evolution of the Reduction Factor Generated by a Geogrid as a Function of its Placement Depth and the Subgrade Strength after (a) 10,000, (b) 20,000, (c) 30,000, and (d) 40,000 Load Cycles. 87

Figure 4.6: Variations in the Tie's Resilient Deformation Recorded in (a) Unreinforced Ballast Samples and Geogrid-Reinforced Ballast Layers Supported by the (b) Competent, (c) Fair, and (d) Soft Subgrades. 88
Figure 4.7: Variations in Tie Support Stiffness Recorded in (a) Unreinforced Ballast Samples and Geogrid-Reinforced Ballast Layers Supported by the (b) Competent, (c) Fair, and (d) Soft Subgrades. 90
Figure 4.8: Hysteresis Loops Recorded during the Ballast Box Test Performed on the Unreinforced Tie-Ballast Assembly Supported by the Soft Subgrade and the Areas Used to Evaluate its Damping Ratio. 93
Figure 4.9: Evolution of the Ballast-Subgrade Assembly's Damping Recorded in (a) Unreinforced Ballast Samples and Geogrid-Reinforced Ballast Layers Supported by the (b) Competent, (c) Fair, and (d) Soft Subgrades. 94
Figure 5.1: (a) Schematic diagram of the ballast box test and (b) laboratory setup used by Desbrousses et al. (2023) [Adapted from Desbrousses et al. (2023) with permission]. 103
Figure 5.2: Modeling Ballast Particles using the Clump Logic: (a) Ballast Particle, (b) PFC 3D Clump, and (c) Linear Contact Model and its Rheological Components. 106
Figure 5.3: (a) Simulating the triaxial tests performed by Suiker et al. (2005) and comparing the experimental data with the discrete element simulations at confining pressures of (b) 10.3kPa, (c) 41.3kPa, and (d) 68.9kPa. 108
Figure 5.4: Discrete Element Model of the Biaxial Geogrid Showing the Boundary Conditions Used in the Multi-Rib Tensile Test and the Rheological Components of the Linear Parallel Bond Contact Model. 111
Figure 5.5: Comparing Experimental Data Obtained by Desbrousses et al. (2021) with the Discrete Element Simulations of the (a) Single-Rib and (b) Multi-Rib Tensile Tests. 113
Figure 5.6: (a) Boundary Conditions Used in the Aperture Stability Modulus Test and (b) Displacement of the Geogrid Ribs Following the Application of the Twisting Moment. 115
Figure 5.7: Sample Generation Procedure Using the Improve Multi-Layer Compaction Method (IMCM) Showing the (a) Generation of the First 50mm-Thick Lift, (b) Creation of the Second Lift, (c) Compaction of the Third Lift, (d) Incorporation of a Geogrid 150mm Above the Box, and (e) Compacted 300mm-Thick Ballast Layer. 116

Figure 5.8: Calibrating the Box's Bottom Wall's Spring Stiffness to Simulate the Presence of Subgrades with CBRs of 25 and 5 Below the Ballast Layer. 117
Figure 5.9: Accumulation of Tie Settlement in Unreinforced and Geogrid-Reinforced Ballast Layers Supported by a Subgrade with a CBR of (a) 25 and (b) 5. 118
Figure 5.10: Variations in the Incremental Tie Settlement with Cyclic Loading in Unreinforced and Geogrid-Reinforced Ballast Layers Supported by a Subgrade with a CBR of (a) 25 and (b) 5. 120
Figure 5.11: Total Displacement Vectors Plotted at the Same Scale during the Twentieth Load Cycle in the (a) Unreinforced Ballast Layer and Geogrid-Reinforced Ballast Layers with Geogrids Located at Depths of (b) 250mm, (c) 200mm, (d) 150mm, (e) 100mm, and (f) 50mm. 121
Figure 5.12: (a) Variation of the Average Particle Velocity with Depth as a Function of the Geogrid Placement Depth and (b) Effect of the Geogrid Location on the Variation of Average Particle Angular Velocity with Depth. 124
Figure 5.13: Contact Force Chains During the Twentieth Load Cycle in (a) Unreinforced and Reinforced Ballast Layers with a Geogrid Located at a Depth of (b) 250mm, (c) 200mm, (d) 150mm, (e) 100mm, and (f) 50mm. 126
Figure 5.14: Effect of Geogrid Placement Depth on the Variations in Average Contact Force among Type III Contacts in Unreinforced and Geogrid-Reinforced Ballast Assemblies. 127
Figure 5.15: Evolution of the Coordination Number during Cyclic Loading in Unreinforced and Geogrid-Reinforced Ballast Layers. 128
Figure 5.16: Energy Dissipated by Frictional Sliding in the Unreinforced and Reinforced Ballast Layers with Geogrids Located at Depths of 150mm, 100mm, and 50mm. 130
Figure 5.17: Total Displacement Vectors (in meters) of the Parallel-Bonded Balls Drawn at the Same Scale for the Geogrids Placed at Depths of (a) 50mm, (b) 100mm, (c) 150mm, (d) 200mm, and (e) 250mm. 131
Figure 5.18: Accumulation of Strain Energy Stored in the Geogrid's Parallel Bond Springs during Cyclic Loading. 133
Figure 5.19: Effect of the Geogrid Aperture Size Ratio (*A/D*) on the Evolution of the Tie Settlement in Ballast Layers Reinforced with a Geogrid Located 150mm Beneath the Tie. 134
Figure 5.20: Effect of the Geogrid Aperture Size Ratio (*A/D*) on the (a) Average Particle Velocity and (b) Average Particle Angular Velocity. 135

Figure 5.21: Optimum Size of the Geogrid's Apertures Based on Total Tie Settlement Considerations....... 136
Figure A.1: (a) Overview of the Soil Container, (b) Inner Movable Walls, (c) Tensioning System and Steel Spacers. 184
Figure A.2: Soil Container with a Width of (a) 305mm, (b) 610mm, (c) 915mm, and (d) 1,220mm. 185
Figure A.3: Pneumatic Cyclic Loading Setup with the Soil Container (1: 400,000lb-Capacity Load Frame, 2: Pneumatic Actuator, 3: Load Cell, 4: Linear Bearing, 5: Ball Joint). 186
Figure A.4: Load Cell, Linear Bearing, and Ball Joint. 187
Figure A.5: Simplified Schematic of the Pneumatic Circuit. 188

Chapter 1: Introduction

1.1. Background and Research Motivation

With over 49,000km of tracks operated, Canada possesses the world's fifth-largest rail network (Transport Canada, 2023). Railroads play a pivotal role in the transportation of people and goods across the country, with an estimated 88 million passengers and 341 million tons of freight being transported by rail in 2018 (Railway Association of Canada, 2018). Since 2010, demand for train transportation has spiked in Canada, with the number of passengers and tons of freight transported by rail surging by 46.8% and 17.5% respectively (Railway Association of Canada, 2020). Soaring demand for rail transport exerts additional strain on Canadian rail infrastructure by increasing train traffic and loads on railroad tracks, which may contribute to their degradation (Bourgonje & Diercks, 2011).

Track deterioration, often characterized by a loss of track alignment and geometry, creates dangerous track riding conditions which may lead to train derailment, economic losses, and potentially involve the loss of human life. As such, maintaining acceptable track stability is crucial to providing safe operating conditions. The majority of railroad tracks in Canada are supported by ballasted substructures (Scanlan, 2018), which are multi-layer soil systems consisting of a ballast layer overlying a subballast stratum resting on a subgrade soil. The ballast layer is the uppermost component of the substructure. It is typically made of coarse angular narrowly graded crushed stones and fulfills key functions in a ballasted track structure, including supporting the overlying tracks and maintaining their stability (D. Li et al., 2015; Selig & Waters, 1994). Due to its unbound and discrete nature, railroad ballast deforms substantially under cyclic train loading due to the densification and lateral spread of its particles coupled with the progressive degradation caused by sustained exposure to train loading (Bruzek et al., 2016; Indraratna et al., 2005; Sussmann et al., 2012). The accumulation of deformations in the ballast layer may then trigger the development of differential tie settlement and variations in track alignment. Overall, approximately 40% of all track deflections stem from deformations occurring in the ballast layer, particularly in cases where the underlying subgrade is stable (Bourgonje & Diercks, 2011; Kashani & Hyslip, 2018; Selig & Waters, 1994). Excessive ballast deformation is typically addressed by either imposing speed limits on affected track sections, thereby having a detrimental economic impact on the tracks' profitability or by performing costly ballast maintenance operations, such as tamping or stone-blowing, to restore the track geometry to an acceptable level (Anderson & Key, 2000; Chrismer & Davis, 2000; Touqan et al., 2020). Large sums of money are spent each year on maintaining railroad ballast, with Canadian railroads allocating approximately 40% of their budget to procuring, distributing, and rehabilitating ballast (Chrismer & Davis, 2000; Raymond et al., 1983). As such, there exists a strong incentive to identify means to reinforce ballast, minimize its deformation, and in turn curtail its operating costs.

It is in this context that geosynthetics are used to reinforce ballasted substructures to improve their stability (Göbel et al., 1994). Geosynthetics typically used in railroad substructures include geogrids, geotextiles, geogrid composites, and geocells. Depending on their type, geosynthetics may perform one or several functions such as reinforcement, filtration, drainage, and separation (Koerner, 2005). Railroad ballast is commonly reinforced with geogrids, which are polymeric geosynthetics with an open structure characterized by large openings, called apertures, bordered by orthogonal ribs (AREMA, 2010; Kwan, 2006; Selig & Waters, 1994). A geogrid reinforces ballast by leveraging its open structure to allow the surrounding ballast particles to strike through its plane and become wedged in its apertures, resulting in the formation of a tight interlock between the grid and the surrounding particulate medium (Jewell et al., 1984). This then allows the geogrid to confine the ballast aggregate, prevent its lateral spread, and resist the tensile stresses the ballast is unable to withstand. The inclusion of geogrids in railroad ballast has been shown to reduce the tie settlement (Bathurst & Raymond, 1987; Brown, Kwan, et al., 2007; Indraratna et al., 2013; Luo, Zhao, Cai, et al., 2023a; McDowell & Stickley, 2006; Sadeghi et al., 2023), minimize ballast particle breakage and lateral spreading (Hussaini et al., 2015, 2015, 2015; Indraratna et al., 2013; Luo, Zhao, Cai, et al., 2023a; T. Ngo et al., 2021), increase the track substructure's bearing capacity (Das, 2016), and increase the time interval between ballast maintenance operations (Bathurst & Raymond, 1987; Brown, Kwan, et al., 2007).

Geogrids are generally made out of polymeric materials called thermoplastics that exhibit temperature-dependent mechanical properties. When used to reinforce railroad ballast, geogrids tend to be placed within 300mm of a soil surface exposed to the air, which raises the question of determining how fluctuations in ambient air temperature impact a geogrid's behavior. This is particularly relevant in the context of Canadian railroads which are typically exposed to significant seasonal temperature fluctuations that may be felt up to a depth of 10m in soil (Roustaei & Hendry, 2023; Segrestin & Jailloux, 1988; Zarnani et al., 2011). Additionally, the performance of a geogrid embedded in railroad ballast is contingent on the geogrid's aperture size and placement depth in a ballast layer, and the compressibility of the underlying subgrade. As such, the research presented in this thesis is motivated by characterizing the effect of temperature on the mechanical properties of geogrids and understanding the intricate relationship between geogrid attributes and the geosynthetic's ability to reinforce railroad ballast. This is achieved by performing an experimental campaign in which geogrids are tested in a temperature-controlled environment and the behavior of geogrids embedded at different depths in railroad ballast layers supported by subgrades of varying compressibility are evaluated. The distinct element method is then employed to explore the micromechanical features of the ballast/geogrid interaction and delve into the effects of the geogrid placement depth, aperture size, and stiffness.

1.2. Objectives and Scope

The first objective of this study is to characterize the effect of temperature on the mechanical properties of two geogrid materials used to reinforce ballasted substructures. The first geosynthetic is a large-aperture biaxial polypropylene geogrid while the second is a geogrid composite consisting of a geogrid heat-bonded to a geotextile. This objective is achieved by taking the following steps:

i. Perform single-rib tensile tests on specimens of each geogrid material at temperatures ranging from -30ºC to 40ºC and -30ºC to 20ºC for the geogrid and geogrid composite respectively
ii. Analyze the tensile load and elongation data of the tested specimens at each temperature
iii. Observe failure patterns for each material and tie them back to temperature changes

The second objective of this research involves investigating the effect of geogrid placement depth and subgrade strength on the response of geogrid-reinforced ballast subjected to cyclic loading. To do so, the following sub-objectives are considered:

i. Conduct ballast box tests on unreinforced and geogrid-reinforced 300mm-thick layers of railroad ballast subjected to 40,000 load cycles
ii. Consider geogrid placement depths of 150mm, 200mm, and 250mm below the tie
iii. Use subgrades with California Bearing Ratios (CBR) of 25, 13, and 5

iv. Monitor the evolution of the tie's permanent and resilient settlement and support stiffness and the ballast layer's damping ratio

v. Analyze the experimental data and draw conclusions on the effect of subgrade strength and geogrid placement depth on the behavior of geogrid-reinforced ballast

The third objective of this thesis involves exploring the micromechanical features of the geogrid/ballast interaction mechanism and assessing its sensitivity to the geogrid's placement depth, aperture size, and stiffness. A three-dimensional distinct element model of the ballast box test is developed and a parametric study is conducted in which the geogrid placement depth, aperture size, and stiffness are changed. This objective is achieved by considering the following sub-objectives:

i. Develop and validate a distinct element model of the ballast box test

ii. Carry out a parametric study where:
    a. The geogrid placement depth is varied from 50mm to 250mm beneath the tie
    b. The geogrid aperture size is varied over an interval corresponding to geogrid aperture size (A) to mean ballast diameter (D_{50}) ratios of 1.09 to 2.07
    c. The geogrid stiffness is assigned values ranging from 9.54 to 18.00kN/m which correspond to the geogrid's tensile strengths at 2% strain obtained at temperatures ranging from 40ºC to -30ºC as discussed in Objective 1

iii. Analyze the ballast particles' displacement vectors, contact force chains, and total energy dissipation and identify the effects produced by each parameter considered in the parametric study

1.3. Original Contributions

This thesis contributes to the existing state of practice and literature on three fronts. First, an experimental investigation is devised to investigate the effect of temperature on the properties of two geogrid materials. Second, the relationship between the geogrid placement depth and subgrade strength and its influence on the ability of a geogrid to reinforce ballast is experimentally examined. Finally, a distinct element model is developed to explore the micromechanical behavior of geogrid-reinforced ballast. The following are the salient features of the original contributions arising from the work discussed in this thesis:

i. Characterize the behavior of two geogrid materials at temperatures ranging from -30ºC to 40ºC
ii. Carry out an experimental parametric study to investigate the interplay between geogrid placement depth and subgrade strength
iii. Discuss the implications of variations in subgrade strength and geogrid location on the behavior of geogrid-reinforced ballast exposed to cyclic loading
iv. Develop a distinct element model of the ballast box tests considering unreinforced and geogrid-reinforced ballast layers
v. Perform a parametric study to explore the micromechanical behavior of geogrid-reinforced ballast and assess the effect of the geogrid placement depth, stiffness, and aperture size

1.4. Contribution of Authors

The chapters of this thesis are the candidate's original work. The literature review presented in Chapter 2 was written by the candidate and reviewed by Prof. Meguid. The experiments discussed in Chapter 3 were performed by the candidate following a methodology devised by the candidate with technical guidance from Prof. Meguid. The resulting manuscript was drafted by the candidate while rounds of revisions and edits were done by Prof. Meguid and Mr. Sam Bhat. The ballast box tests described in Chapter 4 were carried out using an experimental setup developed and built by the candidate with technical assistance provided by the McGill University Jamieson Structures Laboratory's coordinator Dr. William Cook and technicians John Bartczak and Mike Stephens. Resources needed to build the setup were acquired by Prof. Meguid. The manuscript outlining the findings of the experimental work was drafted by the candidate and edited by Prof. Meguid and Mr. Sam Bhat. Formulation of the distinct element model presented in Chapter 5 and the required programming in *FISH* language was performed by the candidate under the supervision of Prof. Meguid. The resulting micromechanical analysis was achieved using codes written in *MATLAB* by the candidate. The corresponding manuscript was drafted by the candidate and reviewed and edited by Prof. Meguid and Mr. Sam Bhat.

1.5. Thesis Organization

This thesis is manuscript-based. Three out of the seven chapters included herein are manuscripts prepared for potential publication in peer-reviewed journals that are either published or currently under review. Excluding the present introductory chapter, the thesis is structured as follows.

A comprehensive survey of the literature dealing with the behavior of unreinforced and geogrid-reinforced railroad ballast is presented in Chapter 2. The chapter starts by describing the various geotechnical components of conventional ballasted track substructures. The review then delves into the behavior of railroad ballast subjected to cyclic loading and outlines the parameters affecting the ballast's resilient and permanent deformation behavior. This provides a segue into discussing the most common geotechnical issues ballasted substructures must contend with. Outlining common geotechnical issues encountered in railroad tracks sets the background for a review of the various methods used to design unreinforced ballast layers. Geogrids are then introduced as a means to reinforce ballasted substructures and a review of their working mechanism is provided. A section discussing the parameters wielding an appreciable influence over the performance of geogrids embedded in railroad ballast is also included.

In Chapter 3, the single-rib tensile tests conducted in a temperature-controlled environment on a biaxial geogrid and a geogrid composite are discussed. Upon explaining the rationale behind the experiments, the experimental methodology is reviewed. The effect of changing temperature on the mechanical properties and failure patterns of the two materials is discussed later in the chapter.

An experimental campaign investigating the effects of subgrade strength and geogrid location on the cyclic response of geogrid-reinforced ballast is reviewed in Chapter 4. An overview of the experimental methodology is first provided. During the ballast box tests, the tie's permanent and resilient deformation, tie support stiffness, and ballast damping ratio are monitored. The response of unreinforced and geogrid-reinforced ballast layers supported by subgrades with California Bearing Ratios of 25, 13, and 5 are then compared. Conclusions on the influence of the subgrade strength and geogrid placement depth are drawn from the experimental data and their implications are discussed.

Chapter 5 introduces the discrete element model developed to simulate ballast box tests and explore the micromechanical features of the geogrid/ballast interaction mechanism. The chapter covers the methodology used to develop and calibrate the model. A parametric study is conducted to assess the particulate scale implications of reinforcing ballast with geogrids. The performance of an unreinforced ballast layer is compared to that of geogrid-reinforced ballast layers in which the geogrid placement depth, aperture size, and stiffness are varied. Analyzing the simulation data offers insights into particle motion, load transmission through interparticle contacts, and energy dissipation in the unreinforced and geogrid-reinforced granular layers. By comparing the behavior of unreinforced and geogrid-reinforced ballast, the simulations discussed in Chapter 5 complement the experimental results reported in Chapter 4.

Chapter 6 synthesizes the findings presented in Chapters 3, 4, and 5. It explores the broader implications of each research endeavor and their respective conclusions. It also acknowledges the limitations of the research and proposes potential avenues for future research.

Chapter 7 provides the closing statements of this thesis by presenting overarching conclusions and recommendations for future research directions.

Chapter 2: Literature Review

2.1. Introduction

Railroads constitute a key component of the Canadian transportation infrastructure, allowing the efficient movement of passengers and goods across the country. The structural integrity and reliability of the rail infrastructure are crucial for the rail network's economic viability and safety. A critical aspect of railway engineering is the design and maintenance of track structures in which railroad ballast acts as one of the primary load-bearing elements. Ballast, typically consisting of crushed rocks, supports the track superstructure while facilitating drainage and distributing train loads to the underlying subgrade. However, the mechanical behavior of ballast along with its ability to perform its functions satisfactorily face challenges caused by the repeated traffic loads and the degradation of its aggregates which lead to track settlement, deformation, and loss of geometry.

In response to these issues, reinforcing railroad ballast with polymeric geogrids emerges as a promising solution. A geogrid is a geosynthetic with an open structure designed to enhance the mechanical properties of railroad ballast through the formation of an interlock between the geogrid and the surrounding aggregates. This leads the geogrid to confine ballast particles, resulting in an improvement in the granular material's load-spreading ability and minimizing its deformation.

This literature review seeks to synthesize the current knowledge on geogrid-reinforced railroad ballast. The behavior of unreinforced railroad ballast subjected to cyclic loading is discussed first. The mechanical behavior of reinforced ballast under cyclic loading is then explored by highlighting the key features of geogrids that contribute to their effective performance and interaction with the surrounding ballast particles.

2.2. Components of Ballasted Railway Tracks

The primary function of ballasted railroad tracks is the provision of a safe and stable platform that conforms to strict vertical and horizontal alignment requirements to support train traffic. A ballasted track structure generally comprises a superstructure and a substructure as depicted in Figure 2.1. The superstructure consists of a rail-fastener-tie assembly that supports passing trains while transferring their loads to the underlying substructure. The substructure is a multi-strata soil system located beneath the superstructure that consists of the ballast, subballast, and subgrade layers.

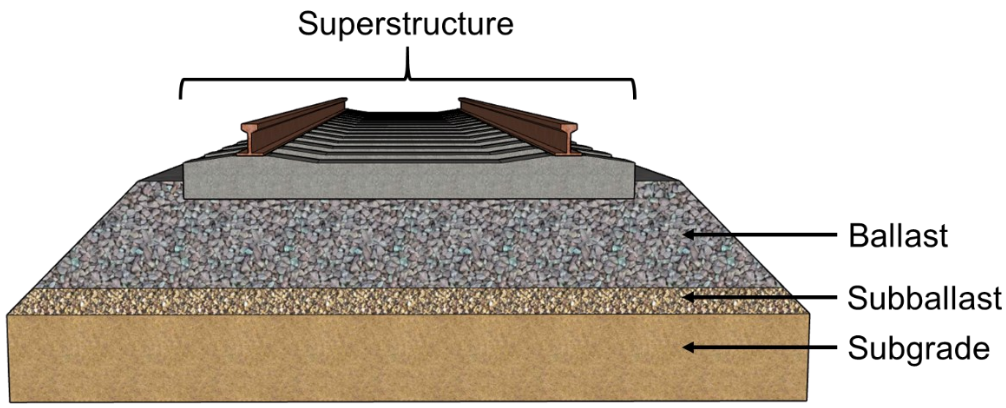

Figure 2.1: Typical Ballasted Railway Track Structure.

2.2.1. Superstructure

Rails are longitudinal steel members that are in direct contact with passing train wheels. They are supported by evenly-spaced ties and must be sufficiently stiff to transfer the train wheel loads to their supports without experiencing excessive deflection between the ties. The track riding quality is affected by the rail and wheel surface profiles. Irregularities and defects in the rails and wheels may generate large dynamic loads that cause large stresses to be transferred to the substructure. The increase in the loads supported by the substructure may then trigger an increase in permanent settlement and cause differential track settlement.

The rails are connected to the ties by fasteners. The fastening system restrains the rails and keeps them in contact with the ties while resisting their vertical, lateral, longitudinal, and overturning movements. The ties are the bottommost component of the substructure. They are generally made of either wood or concrete. Ties directly support the rails and transfer the train loads to the underlying ballast layer at an acceptable stress level. Combined with the fasteners, the ties resist the lateral, longitudinal, and vertical rail movements.

2.2.2. Substructure

2.2.2.1. Ballast

The ballast layer is an assembly of hard, durable, angular, non-cementing, and free-draining crushed rocks used to support the track superstructure. It generally consists of coarse, uniformly graded aggregate derived from either fine-grained igneous rocks or coarse-grained and well-cemented sedimentary rocks (Guo, Xie, et al., 2022; Raymond & Diyaljee, 1979). As it is located beneath the superstructure, the ballast layer plays an important role in the stability of the overall track structure. Its main functions include anchoring the rail-tie assembly, safely distributing and transferring the train loads to the underlying soil layers, providing damping and resilience, providing ample void space to allow for quick drainage and accommodate the storage of fouling material, and shielding the subgrade from climatic forces (e.g., temperature changes) (AREMA, 2010; Desbrousses & Meguid, 2021, 2022; Guo, Marikine, et al., 2022; Guo, Xie, et al., 2022; D. Li et al., 2015; Selig & Waters, 1994).

Although no universal specifications on the selection of ballast aggregate exist, countries and railway organizations worldwide have developed their own guidelines (AREMA, 2010; Canadian National Railway, 2015; UIC, 2008). Ballast property requirements generally consider features known to affect the material's mechanical behavior such as the ballast's parent rock type, the size, shape, angularity, and roughness of its particles, their abrasion resistance, their particle size distribution, etc. Common ballast parent rocks include granite, traprock, quartzite, and carbonate rocks (e.g., limestone and dolomite) (AREMA, 2010). The type of parent rock from which the ballast aggregate is sourced has a bearing on the resulting ballast particles' size, shape, and angularity, which all contribute to the material's shear strength (Indraratna & Salim, 2005; D. Li et al., 2015).

The morphology of ballast particles influences the ballast's shear strength and deformation behavior by affecting the particles' ability to interlock (Indraratna et al., 1998; Y. Sun et al., 2014). For optimal performance, it is recommended ballast particles be well-proportioned and cubical with sharp edges and a rough surface texture (Indraratna et al., 1998; Jia et al., 2019; Pan et al., 2006; Tutumluer & Pan, 2008). As the particle size distribution of ballast aggregate influences the ballast's shear strength, deformation behavior, and drainage properties (Bian et al., 2016; Fardin Rosa et al., 2021; Indraratna et al., 2009; Raymond & Diyaljee, 1979; Y. Sun et al., 2017), ballast particles are generally screened to conform to a uniform gradation to provide a combination of adequate shear strength with ample void space.

2.2.2.2. Subballast

The subballast separates the ballast from the subgrade and is generally made of well-graded crushed rock or broadly graded sandy-gravel mixtures (Indraratna & Salim, 2005; D. Li et al., 2015; Selig & Waters, 1994). It is used to provide drainage out of the track structure, reduce the magnitude of traffic stresses and safely transfer them to the subgrade, separate the ballast and subgrade materials, prevent ballast fouling by the upward migration of subgrade fines, preclude subgrade attrition, and provide frost protection to the subgrade (de Paiva et al., 2018; Indraratna & Salim, 2005; D. Li et al., 2015; Selig & Waters, 1994). Particular attention must be paid to the subballast's grain size distribution given its influence on the layer's conflicting functions of drainage and separation. The subballast must be well-draining with a permeability smaller than that of the ballast but sufficiently high to allow the infiltrating water coming from the ballast to drain away from the track structure into the side ditches while preventing poor drainage conditions in the subgrade (Lackenby, 2006). However, the subballast's gradation must also be such that it precludes the intermixing of ballast and subgrade materials along with the upward migration of subgrade fines into the ballast. In cold regions, the subballast may be composed of two layers of non-frost susceptible material with one layer fulfilling the traditional functions of a subballast and the second acting as an insulator (Desbrousses & Meguid, 2021; Nurmikolu, 2012).

2.2.2.3. Subgrade

The subgrade lies at the bottom of the substructure. It usually consists of either naturally occurring soil or fill and provides a bearing platform for the entire track structure. The subgrade has a tremendous influence on the stability of a railroad track structure and is often the root cause of track failure or excessive maintenance needs (Indraratna, Salim, et al., 2011; D. Li & Selig, 1995; Selig & Waters, 1994). The subgrade soil should be able to resist traffic-induced stresses without deforming excessively, stable under its own weight and that of the track structure to avoid consolidation settlement and massive shear failure, and non-frost susceptible or prone to volumetric changes due to variations in its moisture content (D. Li & Selig, 1995; Selig & Sluz, 1978; Selig & Waters, 1994).

2.3. Track Forces on Railroad Ballast

During its service life, railroad ballast is subjected to a combination of vertical, lateral, and longitudinal forces arising from the passage of trains, maintenance operations, track characteristics, and climatic forces (Kwan, 2006; D. Li et al., 2015; Lim, 2004; Selig & Waters, 1994; Wu et al., 2023). The vertical forces acting on a ballasted track substructure include the vertical train wheel loads and the squeezing force applied to the ballast layer by tamping tines during ballast maintenance operations. The vertical train wheel load consists of a static dead load superimposed by a dynamic component. The static wheel load is equal to the train's weight divided by the number of wheels. The vertical wheel load's dynamic increment is a function of the operating conditions and track and train characteristics such as the train's velocity, tie spacing, rail irregularities, wheel defects, etc. (Selig & Waters, 1994). When a train wheel applies a downward force on the rail, a number of ties are involved in transferring the load to the underlying ballast, with the number of ties partaking in the load distribution being dictated by the tie spacing and rail moment of inertia (AREMA, 2010; Selig & Waters, 1994). The vertical wheel load causes the uplift of the rail and ties some distance away from the wheel-rail contact point as shown in Figure 2.2 (Kwan, 2006; Lim, 2004). The magnitude of the uplift depends on the wheel load and the self-weight of the superstructure. As the passing train moves forward, the advancing wheel pushes the uplifted rail and ties downward, imparting an impact load on the underlying ballast that increases with increasing train speed and track irregularities (Choi et al., 2020; Selig & Waters, 1994). This impact load may lead to additional ballast settlement and breakdown of the ballast aggregate.

Ballast tamping operations apply another significant vertical force on railroad ballast (Lim, 2004; Selig & Waters, 1994). Tamping is a maintenance technique commonly used to restore the geometry of ballasted tracks. It involves lifting the ties, inserting tamping tines into the underlying ballast, and squeezing and vibrating the ballast aggregate between the tines to fill the gap beneath the tie (Abadi et al., 2018; Anderson & Key, 2000; Chrismer & Davis, 2000; Guo et al., 2021; Selig & Waters, 1994; S. Shi et al., 2022). The insertion of tamping tines into ballast and the subsequent application of a squeezing force are recognized as major sources of ballast particle breakage.

Lateral forces applied to the ballast layer arise from the buckling of the rails caused by the high longitudinal rail compressive stresses and the lateral wheel force (Esmaeili, Nouri, et al., 2017; D. Li et al., 2015; Lim, 2004; Ngamkhanong et al., 2021; Selig & Waters, 1994). The lateral wheel force is generated by the train's reaction to geometric rail irregularities and centrifugal forces in curved track sections. Railroad ballast must also resist longitudinal forces acting parallel to the rails. These forces are caused by the thermal contraction and expansion of the rails, rail wave action, and the locomotive traction forces that accompany the train's acceleration and braking motion (Selig & Waters, 1994).

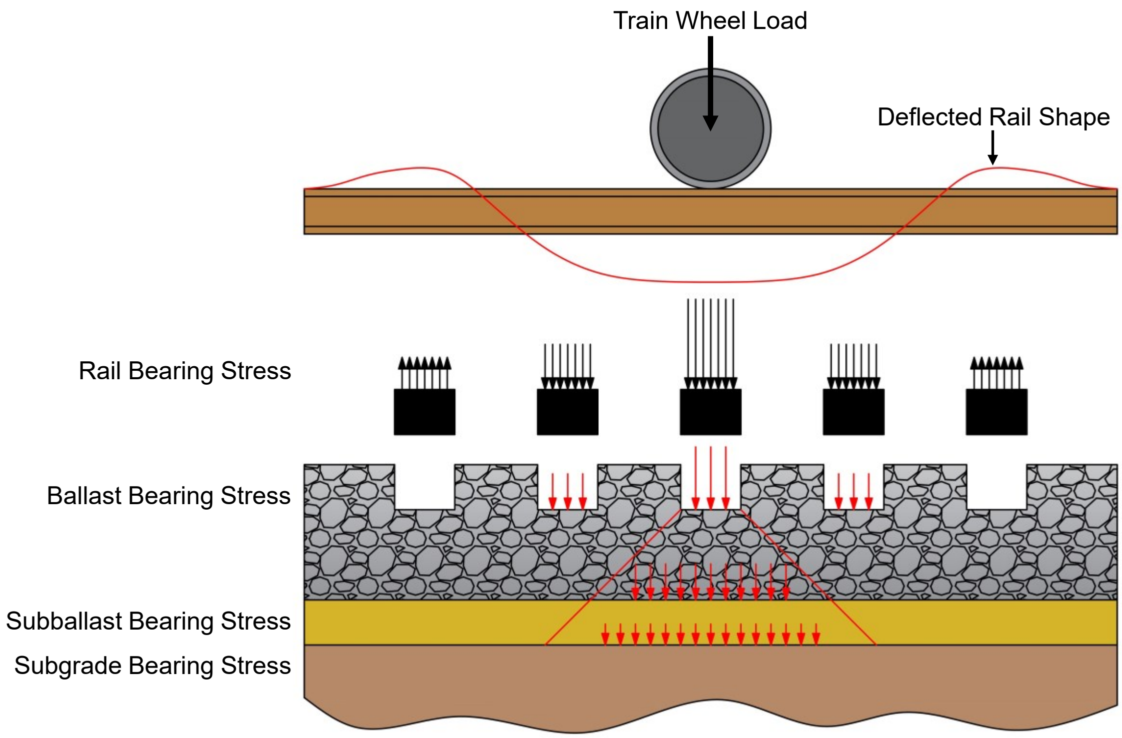

Figure 2.2: Track Forces Exerted by Passing Trains and their Effect on Substructure Stresses (redrawn and adapted from Selig and Waters (1994)).

2.4. Behavior of Railroad Ballast Subjected to Cyclic Loading

Railroad ballast is an unbound granular material consisting of coarse angular particles. In a ballasted substructure, it is typically placed above weaker soil layers such as the subgrade and the subballast. Additionally, current ballast placement techniques are such that it is practically self-supporting, i.e., subjected to low confining pressures, and free to spread laterally in response to cyclic train loading (Indraratna et al., 2005; Lackenby et al., 2007). The application of repeated train loads triggers the development of resilient and residual deformations, also called recoverable and permanent deformations, in the granular layer, making it one of the largest contributors to tie settlement in ballasted railroad tracks. The deformations that take place in a ballast layer are affected by factors such as the loading frequency, the number of load cycles, the cyclic deviator stress, and the ballast's confining pressure, density, moisture content, and type of aggregate (Indraratna et al., 2005; Kashani et al., 2018; Lackenby et al., 2007; Shenton, 1978; Q. Sun et al., 2014, 2019; Q. D. Sun et al., 2016; Thakur et al., 2013).

A freshly built or recently tamped ballast layer is in a relatively loose state, characterized by a large void ratio and interparticle contacts occurring at discrete points over small areas (Kumar et al., 2019; Sussmann et al., 2012). The application of the first load cycles is the source of significant permanent deformations in the ballast assembly as it forces ballast particles to rearrange into a denser packing, causing a reduction in the ballast's void ratio and ballast particle breakage. At the onset of cyclic load, permanent deformations accumulate at a fast rate, with the first load cycles generating large residual strains followed by progressively smaller plastic strain increments with subsequent load cycles. The densification of the ballast layer is accompanied by the development of tight interlocking forces between contacting ballast particles, resulting in an increase in the ballast's layer stiffness and a corresponding reduction in the rate at which permanent deformations develop. During cyclic loading, the stiffness of railroad ballast is commonly described by the resilient modulus (M_r) which is defined as the ratio of the cyclic deviator stress ($\Delta\sigma_d$) to the resilient strain (ϵ_r) for a given load cycle (Elliott & Thornton, 1986). Figure 2.3 represents the resilient modulus and the resilient strain obtained during a given load cycle.

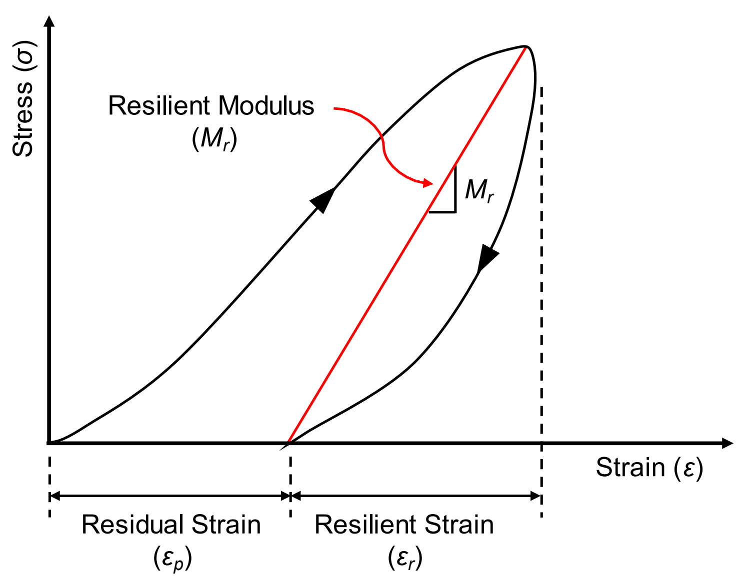

Figure 2.3: Residual and Resilient Strains during a Given Loading Cycle and the Corresponding Resilient Modulus.

Following the application of a sufficiently large number of cycles, the ballast particles rearrange into a dense stable state characterized by a lower void ratio and high interlocking forces between contacting particles (Dahlberg, 2001; Kumar et al., 2019; D. Li et al., 2015; Selig & Waters, 1994). At this stage, the rate at which residual deformation builds up decreases considerably, particle breakage is minimized, and the ballast layer behaves increasingly elastically under individual load cycles, with its resilient modulus displaying only minor variations with further cyclic loading. Figure 2.4 depicts the difference between the rapid settlement accumulation at the onset of cyclic loading and the slower increases in subsidence that follow.

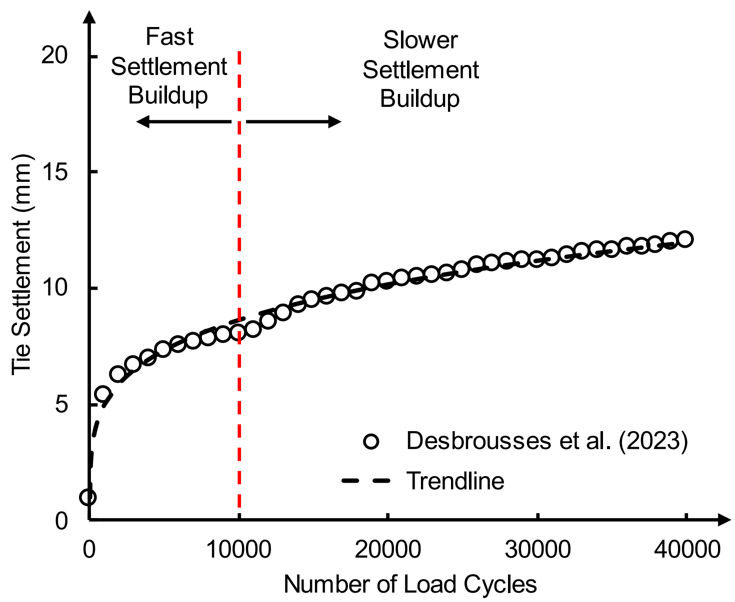

Figure 2.4: Evolution of the Tie Settlement Obtained in Ballast Box Tests Showing the Fast Settlement Accumulation at the Onset of Cyclic Loading Followed by More Gradual Settlement Increases (adapted from Desbrousses et al. (2023)).

Over time, permanent deformations begin to once again accumulate at an increasing rate in the ballast layer due to the wear and tear of ballast particles caused by sustained exposure to traffic loading. The breakdown of the ballast aggregate, together with the possible upward migration into the ballast layer of fine particles from the subgrade or the downward infiltration of fines dropped onto the tracks, contributes to the progressive filling of the voids between ballast particles in a process known as fouling. Fouled ballast typically possesses a lower shear strength and poorer drainage properties than fresh ballast (Huang et al., 2009; Sussmann et al., 2012). As such, it is prone to causing drainage problems in the substructure and being the source of additional deformations, thereby exacerbating existing track differential settlement and potentially warranting the scheduling of tamping operations to restore the track geometry.

2.4.1. Resilient Behavior

The passage of trains imposes complex loading conditions on railroad ballast characterized by the application of stress pulses on the ballast layer and the rotation of principal stresses. Under cyclic loading, the deformation response of ballast consists of a resilient (elastic) and residual (permanent) component. The application of the first load cycles is usually accompanied by substantial plastic strains whose magnitude decreases with increasing load repetitions. Following a sufficiently large number of train passes, the ballast layer behaves almost elastically and only marginal plastic deformations occur. As such, the long-term response of ballast exposed to cyclic loading is commonly described by its resilient modulus (M_r) which is defined as the ratio of the cyclic deviator stress to the resilient axial strain and provides a direct measure of the ballast's stiffness (Brown, 1996; Elliott & Thornton, 1986). The resilient behavior and in turn the resilient modulus of railroad ballast are affected by a score of factors which include the ballast's stress level, gradation, particle size and shape, moisture content, density, number of load cycles, and loading frequency.

2.4.1.1. Effect of Ballast Type and Morphology

The morphological features (particle size and shape) of unbound aggregate materials such as railroad ballast influence their resilient modulus (Hicks, 1970; Lekarp et al., 2000a; Thom & Brown, 1989), with particles possessing sharp edges and rough surfaces generally yielding high resilient moduli. Hicks and Monismith (1971) performed repeated load triaxial tests on angular crushed rocks and well-graded subangular gravel and found that the resilient modulus of granular material increases with increasing particle angularity. Similarly, Barksdale and Itani (1989) investigated the effect of particle shape, surface roughness, and angularity on the resilient modulus of unbound aggregate materials using cyclic loading triaxial tests. They reported that the resilient modulus of angular aggregates could be up to 50% greater than that of rounded granular materials. Additionally, Pan et al. (2006) carried out repeated loading triaxial tests on different granular soils and indicated that an increase in particle angularity and surface roughness results in an increase in the resilient modulus, with particle angularity being the most important factor due to its role in promoting a better particle interlock.

2.4.1.2.Effect of the Number of Load Cycles

Railroad ballast being an unbound discrete material, its resilient modulus is, to a certain extent, affected by the number of load cycles it is subjected to (Alva-Hurtado & Selig, 1981; Indraratna et al., 2009; Lekarp et al., 2000a). Experimental data obtained from cyclic loading triaxial tests suggests that the resilient modulus increases at the onset of cyclic loading due to the particle rearrangement that accompanies that material's densification. After a certain number of load cycles, however, the resilient modulus reaches a stable value, although no clear consensus has been reached regarding how many cycles are needed for the resilient modulus to stabilize. Hicks (1970) found that the resilient modulus of granular soils reaches an almost constant value following about 100 load cycles at the same stress amplitude. Brown (1974) performed repeated loading triaxial tests on crushed granite aggregate and reported it took approximately 1,000 load cycles for the resilient modulus to reach a stable value. Similarly, Thakur et al. (2013) observed that, for a given confining pressure, the resilient modulus of railroad ballast first increases during the first few load cycles due to particle rearrangement and breakage before attaining an almost constant value after about 10,000 load repetitions. On the other hand, upon performing ballast box tests, Navaratnarajah and Indraratna (2017) reported substantial increases in the ballast's resilient modulus until at least 200,000 load cycles.

2.4.1.3. Effect of Loading Frequency

Conflicting information exists on the effect of frequency on the resilient modulus of railroad ballast. Hicks (1970) determined that frequency has a negligible impact on the resilient modulus of granular soils. Similarly, Shenton (1978) conducted cyclic triaxial tests on ballast samples and found that the loading frequency wields only a minor impact on the resilient modulus of ballast past 10,000 load cycles. However, cyclic loading triaxial tests performed by Thakur et al. (2013) at loading frequencies of 10, 20, and 40Hz and by Sun et al. (2019) at gradually increasing frequencies of 6, 12, 18, 24, and 30Hz on railroad ballast revealed that an increase in frequency causes a decrease in resilient modulus owing to the increasing particle rearrangement that accompanies elevated loading frequencies. This contrasts with the findings reported by Navaratnarajah and Indraratna (2017) who performed ballast box tests at frequencies of 15, 20, and 25Hz and by Sun et al. (2016) who carried out triaxial tests at frequencies of 5, 10, 20, and 40Hz and concluded that an increase in loading frequency is met by an increase in the ballast's resilient modulus.

2.4.1.4. Effect of Stress Level

The stress level is widely recognized as being one of the most important factors affecting the resilient modulus of railroad ballast (Brown, 1996; Knutson & Thompson, 1977, 1978; Lekarp et al., 2000a; Raymond & Williams, 1978). The stress level is commonly described using either the confining pressure (σ_3'), cyclic deviator stress ($\Delta\sigma_d'$), and bulk stress ($\theta = \sigma_1' + \sigma_2' + \sigma_3'$), with the resilient modulus of railroad ballast having been shown to increase in response to a rise in the confining pressure, deviator stress, or bulk stress (Alva-Hurtado & Selig, 1981; Indraratna et al., 2009; Navaratnarajah & Indraratna, 2017; Thakur et al., 2013). Lackenby et al. (2007) investigated the effect of confining pressure and deviator stress on the resilient modulus of railroad ballast by conducting triaxial tests at confining pressures of 10, 30, and 60kPa and deviator stresses of 230, 500, and 750kPa. They observed consistent increases in resilient modulus with an increase in either confining pressure or cyclic deviator stress. Similarly, cyclic loading triaxial tests performed by Sun et al. (2019) at confining pressures of 10, 30, and 60kPa and deviator stresses up to 230kPa revealed that the resilient modulus of railroad ballast increases with increasing bulk stress.

2.4.1.5. Effect of Moisture Content

The resilient modulus of railroad ballast is strongly tied to its moisture content. After conducting cyclic loading triaxial tests on five different types of aggregate for a total of 70,000 cycles, Barksdale and Itani (1989) reported that soaking unbound granular materials can result in reductions in resilient modulus between 20 to 50% depending on the aggregate type. Heydinger et al. (1996) further stated that moist granular soils generally possess a lower resilient modulus, particularly at low confining pressures. Raad et al. (1992) compared the resilient modulus of moist and saturated granular bases subjected to strain-controlled repeated triaxial loading. They found that the resilient modulus of the saturated samples decreases due to an increase in pore water pressure and a corresponding decrease in effective stress. Tian et al. (1998) examined the changes in resilient modulus in two coarse-grained soils caused by three moisture contents of 2% below optimum, the optimum moisture content, and 2% above optimum. They concluded that increasing the moisture above the optimum moisture content leads to the greatest decrease in resilient modulus.

2.4.1.6. Effect of Density and Gradation

The resilient modulus of railroad ballast is sensitive to its particle size distribution and density. Increasing the ballast density generally translates into an increase in its resilient modulus while broadly-graded ballast tends to exhibit a higher resilient modulus than when it is narrowly-graded (Heydinger et al., 1996). Triaxial tests conducted by Knutson and Thompson (1977) and Raymond and Diyaljee (1979) showed that the resilient modulus of broadly graded ballast is greater than that of uniformly graded ballast. Barksdale and Itani (1989) further demonstrated that using too fine a gradation for railroad ballast could decrease its resilient modulus by as much as 60%. Janardhanam and Desai (1983) and Pan et al. (2006) indicated that the resilient modulus increases with the size of the aggregate, with the resilient modulus exhibiting an almost linear increase with an increase in the mean particle diameter at low confining pressures.

Increasing the density of railroad ballast results in a better packing arrangement. This increases the average number of contacts per particle, leading to a reduction in the average interparticle contact stress and overall deformation which translates into an increase in the ballast's resilient modulus (Lekarp et al., 2000a). Barksdale and Itani (1989) suggested that the resilient modulus grows significantly following an increase in density at low stress levels, while the influence of density becomes minor at higher stress levels. Similarly, Shenton (1978) conducted triaxial tests on railroad ballast and observed that a 5% change in bulk density could double the strain in ballast.

2.4.2. Permanent Deformation

The accumulation of non-recoverable deformation in the ballast layer is a gradual process driven by the breakage and rearrangement of ballast particles into a denser packing in response to the application of repeated train loads. Deformations in the ballast layer lead to track settlement which typically takes place in two stages. First, track settlement grows rapidly in freshly laid or recently tamped tracks due to the substantial densification of the ballast layer during the first load cycles. Subsequently, following a large number of load cycles, track settlement continues to grow due to the combined densification of the ballast layer, interpenetration of the ballast aggregate into the subballast and subgrade, breakage of the ballast particles, and lateral spreading of the ballast particles (Dahlberg, 2001). The permanent deformation of railroad ballast is influenced by several key factors that include the stress level, loading frequency, ballast density and gradation, number of load cycles, and moisture content.

2.4.2.1. Effect of the Stress Level

The stress level railroad ballast is subjected to is one of the factors that wields the greatest influence over its permanent deformation response. Shenton (1978) conducted repeated loading triaxial tests on railroad ballast to investigate the effect of cycling the deviator stress between 98 and 392kPa on the permanent strain response of ballast. It was observed that only the larger deviator stresses dominate the deformation response, with deviator stresses smaller than 50% of the largest one producing only marginal deformations. Raymond and Williams (1978) examined the effect of confining pressure on the deformation behavior of ballast under triaxial conditions and stated that increasing the confining pressure translates into a higher ballast strength, lower permanent deformation, and reduced particle breakage. These findings were echoed by the works of Indraratna et al. (2005) and Lackenby et al. (2007) who performed a series of cyclic loading triaxial tests on ballast samples using confining pressures ranging from 1 to 240kPa and deviatoric stresses of 230, 500, and 750kPa to study the effect of confining pressure and deviator stress on the deformation behavior of railroad ballast. They defined the existence of three regimens of ballast deformation based on the confining pressure. At low confining pressures (<30kPa), ballast samples tend to experience considerable axial and expansive radial strains caused by dilation which gives rise to pronounced particle breakage due to poor particle packing. At confining pressures ranging from 30 to 75kPa, dilation decreases as an optimum particle packing is reached where particles are tightly held together which increases the interparticle contact areas and improves the contact stress distribution. The axial strain is considerably reduced at these confining pressures and the overall volumetric response of ballast is compressive. However, higher confining pressures (>75kPa) lead to increased particle breakage due to excessive stress levels at the particle contacts while the axial strain remains low owing to the increased confinement. These findings were echoed by Thakur et al. (2013) who gradually decreased the confining pressure from 120kPa to 30kPa during triaxial tests and reported that the axial strain increases following each reduction in confining pressure and takes about 1,000 load repetitions to stabilize following a change in confining pressure.

2.4.2.2. Effect of Loading Frequency

For a given deviator stress and confining pressure, the loading frequency influences the magnitude and rate at which ballast deformation takes place. Sun et al. (2014, 2019) performed triaxial tests on ballast samples at frequencies ranging from 5Hz to 6Hz for 500,000 load cycles and defined three ranges of ballast behavior based on the loading frequency. At frequencies smaller than 20Hz, ballast specimens undergo a rapid increase in axial strain during the first 1,000 load cycles that amount to 75 to 90% of the final axial strain. The axial strain then reaches a relatively steady value that no longer increases significantly with further cyclic loading. At loading frequencies between 30 and 50Hz, ballast samples are initially unstable and reach a steady axial strain value within 2,000 load cycles. However, after 20,000 to 100,000 load cycles, ballast particles begin to wear out and deformation picks up. Finally, at loading frequencies exceeding 60Hz, plastic collapse of the ballast specimens occurs within 1,000 load cycles. Indraratna et al. (2010) conducted triaxial tests on railroad ballast at loading frequencies of 10, 20, 30, and 40Hz and reported that increasing the loading frequency results in an increase in the axial strain. They further stated that at low frequencies (10-30Hz), the ballast's volumetric strain increases and reaches a stable value after 5,000 load cycles while 10,000 load repetitions are needed to stabilize the axial strain at a loading frequency of 40Hz.

2.4.2.3. Effect of the Number of Load Cycles

The permanent deformation behavior of railroad ballast is a function of the number of load repetitions, with load cycles generally triggering a rapid increase in permanent deformation due to the breakage and rearrangement of ballast particles followed by a gradually decreasing rise in permanent deformation with further cyclic loading (Lekarp et al., 2000b). After a large number of load cycles, the ballast layer reaches a state where it behaves almost elastically (Alva-Hurtado & Selig, 1981; Dahlberg, 2001; Desbrousses et al., 2023; Janardhanam & Desai, 1983). Cyclic triaxial tests performed on railroad ballast by Shenton (1978), Raymond and Williams (1978), and Knutson and Thompson (1978) revealed that the first load applications cause a large increase in permanent axial strain. The incremental permanent axial strain generated by subsequent load cycles progressively decreases until about 1,000 to 10,000 load repetitions, at which point the incremental axial strain becomes very small. Raymond and Williams (1978) and Indraratna et al.

(2010) attributed the rapid rise in non-recoverable deformation in ballast at the onset of cyclic loading to particle rearrangement and the breakage of individual ballast particles.

2.4.2.4. Effect of Moisture

The presence of excess moisture in railroad ballast may decrease its shear strength and increase its propensity to undergo large deformations. Kashani et al. (2017) performed large-scale ballast box tests on dry and wet clean and fouled ballast samples. They reported that an increase in the moisture content of clean ballast from dry to field conditions does not cause a substantial increase in permanent deformation but that reaching moisture contents close to saturation sparks a rise in ballast settlement under cyclic loading. Moderately and heavily fouled ballast, on the other hand, is more sensitive to an increase in water content, with ballast deformations becoming more pronounced with an increase in moisture content. Similarly, Kashani et al. (2018) investigated the effects of different moisture content on the deformation behavior of clean, moderately, and highly fouled ballast under triaxial conditions. They found that a 1% increase in water content results in 25%, 6%, and 4% reductions in the shear strength of clean, moderately, and highly fouled ballast respectively along with a 12% decrease in the friction angle of clean ballast and a 2% decrease of the friction angle of fouled ballast. Similarly, Qian et al. (2016, 2022) conducted triaxial tests on dry and wet samples of clean and fouled ballast. Their work showed that excess moisture triggers a substantial increase in permanent strains along with a loss of shear strength in the tested ballast samples.

2.4.2.5. Effect of Density and Gradation

The density of a ballast layer is crucial for its long-term performance, with better compacted and denser ballast aggregate being more resistant to undergoing large axial strains than poorly compacted ballast (Alva-Hurtado & Selig, 1981; Knutson & Thompson, 1978; Lekarp et al., 2000b; Pan et al., 2006). Shenton (1978) indicated that a 5% change in the density of railroad ballast can double the strain accumulated at the end of cyclic loading triaxial tests. Other researchers emphasized the importance of the ballast's particle size distribution to limit the accumulation of permanent strain. Raymond and Diyaljee (1979) found that broadly graded ballast experiences smaller plastic deformations than uniformly graded ballast under triaxial conditions. Indraratna et al. (2016) and Sun et al. (2017) observed that increasing the maximum particle size of ballast leads to reduced axial and radial strains while increasing the density improves the ballast's shearing resistance and decreases its permanent deformation. Indraratna et al. (2016) further revealed that the optimum packing arrangement in a ballast layer is reached when the coefficient of uniformity is between 1.2 and 2.5 and showed that narrowly graded ballast tends to require a larger number of load cycles to reach a stable deformation state.

2.5. Geotechnical Issues in Ballasted Substructures

The repeated dynamic loads exerted by trains, in conjunction with various substructure-specific factors, can lead to suboptimal substructure performance. This often manifests as excessive and uneven track settlement, posing safety risks for train operations. Substructure problems may arise in the granular layers, i.e., ballast and subballast, through their respective deformation and the degradation of their constituent materials, or in the subgrade soil.

2.5.1. Ballast Deformation

The unbound nature and limited lateral confinement of the ballast layer lead to significant vertical and lateral deformations in the granular layer under cyclic train loads. Vertical deformations occur due to aggregate densification driven by cyclic loading and the lateral displacement of ballast particles. This lateral spread not only increases track settlement but also undermines the rail buckling resistance which relies on the ties and ballast for stability and alignment (Jing & Aela, 2020; D. Li et al., 2015; Ngamkhanong et al., 2021; Selig & Waters, 1994). Additionally, track settlement may vary along its length due to differing subgrade conditions, resulting in greater ballast deformations along certain track sections (Hussaini, 2013; D. Li et al., 2015).

2.5.2. Ballast Fouling

Ballast fouling is the process by which the large voids between ballast particles become filled with finer materials (Bruzek et al., 2016; Ionescu, 2004; Sussmann et al., 2012). According to a study led by Selig and Waters (1994), fouling materials are primarily derived from the breakdown of ballast particles, accounting for 76% of all fines found in a typical ballast layer as shown in Figure 2.5. Other less common sources of fouling materials include the upward migration of fine particles from the underlying soil strata beneath the ballast layer and the downward infiltration of fines deposited on the tracks into the ballast layer such as windblown sand in a desert environment (Esmaeili, Aela, et al., 2017; Esmaeili et al., 2019; Sadeghi et al., 2020, 2023) or coal dust in tracks used to transport coal (J. Chen, Vinod, et al., 2022; N. T. Ngo et al., 2014; L. Wang et al., 2021).

The generation of fine particles stemming from the degradation of the ballast aggregate takes place in two stages (D. Li et al., 2015). The first stage involves the production of relatively coarse fouling material at the onset of cyclic loading due to the splitting of particles and the breakage of their angular corners and asperities as the ballast particles rearrange into a denser packing. This type of fouling material generally passes the No. 4 sieve and is retained on the No. 200 sieve. As indicated by Li et al. (2015), the presence of coarse fouling material does not necessarily have a detrimental impact on the mechanical properties of railroad ballast. Indeed, the presence of coarse fouling material between the existing ballast particles restrains their motion and supplements the development of interlocking forces between ballast grains, thereby contributing to the stiffening of the ballast layer commonly observed during cyclic loading.

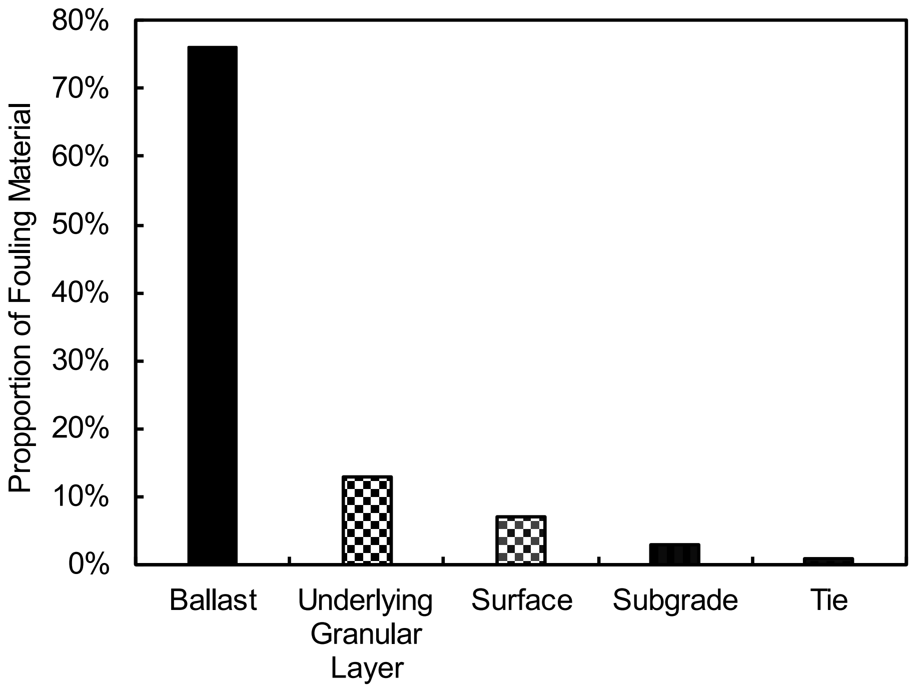

Figure 2.5: Various Sources of Ballast Fouling Material (Selig and Waters, 1994).

The second stage of fouling is characterized by the production of fine fouling material due to the wear and tear of ballast particles under sustained exposure to cyclic loading. These fine particles pass the No. 200 sieve and pose a significant challenge to the functions normally fulfilled by railroad ballast. The increasing presence of fine particles in the ballast's voids reduces the layer's initially high void ratio and surrounds the ballast particles up to the point where ballast grains can only interact by mobilizing the weaker fouling fines (Huang et al., 2009; Huang & Tutumluer, 2011). This in turn leads ballast particles to flow laterally under traffic loading, resulting in additional permanent deformation of the track structure. Additionally, the high amount of fines in fouled ballast reduces the layer's drainage capacity which tends to trap water. As such, pore water pressure may then be generated in the ballast's voids under cyclic train loading, which reduces the layer's shear strength. A lower ballast shear strength and a correspondingly decreased stiffness would create conditions where greater stresses are transferred to the underlying soil layers, potentially paving the way for bearing capacity failure and excessive permanent track settlement (Kashani et al., 2017).

2.5.3. Subgrade

The subgrade provides a bearing platform on which the entire track structure rests and as such plays a critical role in maintaining satisfactory track alignment. While most track deformations can be tied to the ballast layers, geotechnical problems occurring in the subgrade may nevertheless disturb the geometry of the track structure (Brough et al., 2003; D. Li, 2018). Li and Selig (1995) identified three factors as being the root causes of most subgrade problems. The first factor is loading, which can be divided into static loads coming from the self-weight of the track structure and the trains and the train-induced cyclic dynamic loads. The second factor relates to the subgrade soil type, with most problematic subgrades being highly plastic fine-grained soils. The third factor pertains to the environmental conditions the subgrade is exposed to, i.e., its moisture content and temperature. Combinations of these three factors contribute to the occurrence of the two most common types of subgrade failures: progressive shear failure and excessive plastic deformation, as well as other failures such as massive shear failure, subgrade attrition, liquefaction, and shrinking and swelling.

Progressive shear failure primarily develops in fine-grained soils with a high clay content and is characterized by the overstressing of the subgrade at its interface with the subballast layer (Brough et al., 2003; D. Li & Selig, 1995, 1998a; Selig & Waters, 1994). Under cyclic loading, portions of the subgrade soil located at shallow depths below the subballast interface are gradually squeezed upwards and sideways towards the ballast shoulder (Selig & Waters, 1994). This creates a side heave matched by a corresponding depression of the subgrade surface and a depression beneath the tracks which disturbs the track geometry as shown in Figure 2.6. This depression below the tracks is usually corrected by adding ballast material under the ties, thereby increasing the ballast thickness. Although this decreases the stress at the ballast surface, adding ballast tends to create ballast pockets that trap water near the subgrade, potentially offsetting any improvement brought about by the additional ballast thickness (D. Li & Wilk, 2021; Usman et al., 2015).

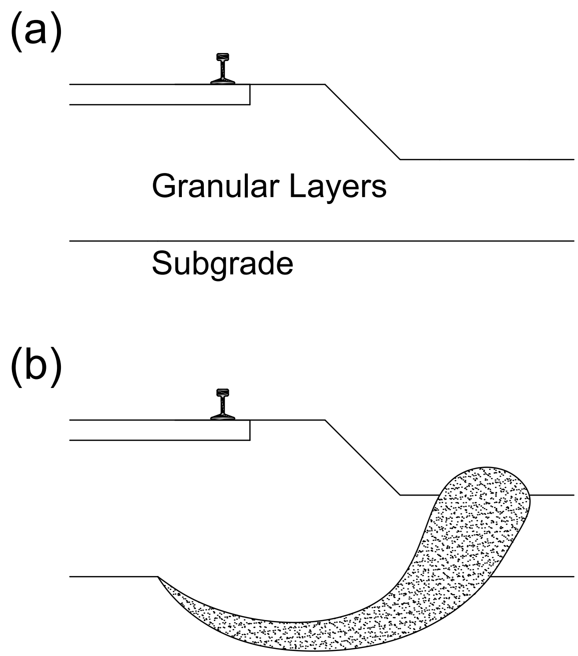

Figure 2.6: (a) Typical Ballasted Substructure and (b) Progressive Shear Failure.

Soft subgrade soils extending to a considerable depth may develop excessive plastic deformations under cyclic train loading that include the vertical deformation component of progressive shear failure coupled with that of soil consolidation as depicted in Figure 2.7 (D. Li & Selig, 1998a; Sayeed & Shahin, 2018a). This type of failure is common in newly constructed subgrades and cohesive soils with access to water (D. Li & Selig, 1995). Under repeated train loads, a depression forms in the subgrade soil and traps water which softens the surrounding soil. Additional train passes squeeze the subgrade soil to the sides of the depression while the soil below softens, creating an even deeper depression that becomes a water-filled ballast pocket. This in turn leads to track settlement which is usually mitigated by adding more ballast (D. Li & Selig, 1995; D. Li & Wilk, 2021). The addition of ballast usually exacerbates existing problems by creating an even larger ballast pocket in the subgrade that traps more water, further softens the subgrade, contributes to the migration of fine particles into the ballast, and impedes satisfactory ballast performance.

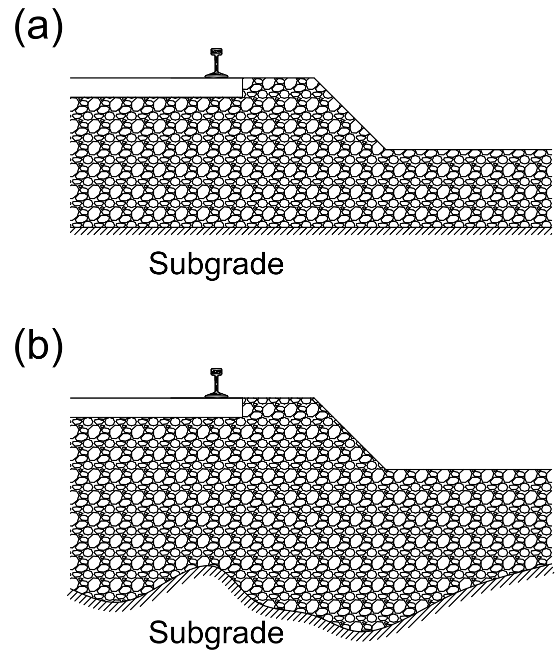

Figure 2.7: (a) Ballasted Substructure and its (b) Excessive Plastic Deformation.

Another type of subgrade failure is the massive shear failure defined by the sudden loss of track geometry following construction or heavy rainfall or flooding events (D. Li et al., 2015; Selig & Waters, 1994). It usually occurs in poorly drained fine-grained subgrade soils subjected to a significant stress increase following the construction of a new track structure or an increase in water content and correspondingly pore water pressure. The performance of a railroad subgrade may also be compromised by its attrition if it is in direct contact with ballast particles (D. Li et al., 2015; D. Li & Selig, 1995; Selig & Waters, 1994). Under cyclic loading, ballast aggregates gradually grind the subgrade surface, producing a powder of fine materials and a corresponding depression in the subgrade. If water is present, the ground subgrade fines may turn into a slurry that can be pumped into the ballast layer under cyclic loading, thereby contributing to its fouling and resulting in a reduction in the ballast shear strength and an increase in track settlement.

Subgrade soils consisting of saturated loose silt or fine sand subjected to dynamic loads may fail due to liquefaction (Selig & Waters, 1994; Usman et al., 2015). Cyclic dynamic loads and the vibrations they generate may increase the pore water pressure in these soils until it exceeds the total stress in the soil mass, leading to a loss of shear strength and the corresponding swift accumulation of track settlement and loss of track geometry. On the other hand, subgrade soils with a high clay content may be prone to shrinking when dry and swelling when wet, triggering volumetric changes in the soil that induce differential subgrade deformations and subsequently disturb the track alignment (Selig & Waters, 1994; Usman et al., 2015).

2.6. Designing Ballasted Railroad Track Foundations

A conventional ballasted substructure is composed of a ballast layer overlying a subballast layer supported by the subgrade. The ballast and subballast layers, often referred to as the granular layer, are typically proportioned to adequately transfer the train-induced loads to the underlying subgrade while reducing their magnitudes such that they may be safely borne by the subgrade soil. If an insufficiently thick granular layer is provided, high train-induced repeated stresses will be transferred to the subgrade, putting it at risk of undergoing excessive deformations. On the other hand, providing an excessively thick granular layer will generate unnecessary costs and may not have a positive effect on track stability. A variety of design methods have been developed to determine the minimum required thickness of the granular layer to preclude subgrade overstressing and excessive deformations. Figure 2.8 shows the granular layer considered by most design methods and Table 2.1 provides an overview of the existing design methods.

Table 2.1: Summary of Available Track Foundation Design Methods.

Method	Design Criteria	Traffic Parameters	Soil Parameters
AREMA	σ_{all} = 138kPa	Single wheel	None
Heath et al.	Threshold stress	Single wheel	Subgrade type
Raymond	σ_{all}	Single wheel	Subgrade type
Li and Selig	Progressive shear failure & excessive plastic deformation	Multiple wheels, repeated load cycles	Ballast (E_b), subgrade (σ, E_s, type)
Sayeed and Shahin	Progressive shear failure & excessive plastic deformation	Multiple wheels, repeated load cycles	Ballast: Mohr-Coulomb Subgrade: linear elastic
UIC	Bearing capacity	Single wheel	Subgrade quality and bearing capacity

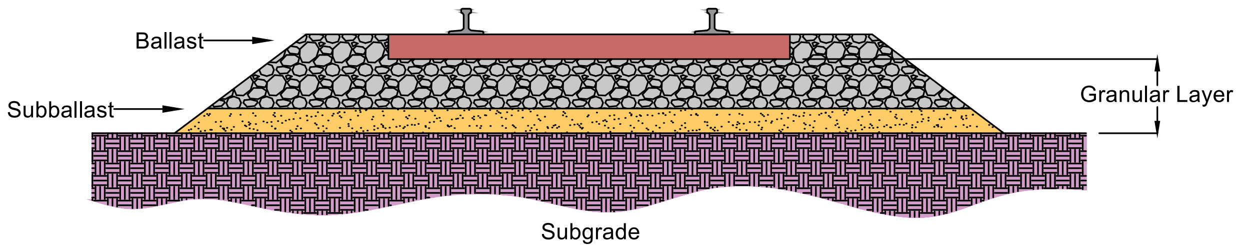

Figure 2.8: Granular Layer Used in Most Design Methods.

2.6.1. AREMA Method

AREMA's Manual for Railway Engineering (AREMA, 2010) provides a method to determine the required granular thickness (h) that needs to be provided over a subgrade soil to prevent its exposure to large vertical stresses. The method relies on an equation developed by Talbot in the 1920s that estimates the vertical pressure (p_c) on the subgrade induced by a bearing pressure (p_a) at the tie-ballast interface supported by a granular layer of thickness h as follows:

$$p_c = 16.8 \times \frac{p_a}{h^{1.25}} \tag{2.1}$$

To prevent subgrade overstressing, AREMA recommends using an allowable subgrade stress of 138kPa, regardless of the subgrade soil type, giving a granular layer thickness of:

$$h = \left(16.8 \times \frac{p_a}{p_c}\right)^{\frac{4}{5}} \tag{2.2}$$

The bearing pressure at the tie-ballast interface (p_a) is determined from the following equation:

$$p_a = \frac{2P\left(1 + \frac{IF}{100}\right)\left(\frac{DF}{100}\right)}{A} \tag{2.3}$$

Where $IF = \frac{33V}{100D}$ is the impact factor that considers the train's velocity (V) and the train's wheel diameter (D) and DF is a distribution factor that is a function of the type of tie and tie spacing that gives a measure of the proportion of the axle load carried by a given tie.

The use of the AREMA method represents an oversimplification of actual field conditions encountered in railroad tracks, particularly in the case of heavy axle loads and high train speeds (D. Li & Selig, 1998a; Sayeed & Shahin, 2018a). The Talbot equation does not consider subgrade soil conditions, the effects of dynamic loading, and the stiffness of the overlying granular layers. Additionally, the use of a universal allowable bearing pressure of 138kPa fails to capture variations in subgrade strength caused by different soil types and may lead to insufficient granular thickness for soft subgrades and excessively thick granular layers for competent subgrade soils.

2.6.2. British Design Method (Heath et al., 1972)

Heath et al. (1972) developed a design method to estimate the thickness of a granular layer required to limit the magnitude of the train-induced deviator stress that develops in the subgrade below a threshold stress to protect the subgrade against failure due to excessive plastic deformation. This design method stems from observations made by Heath et al. (1972) upon performing repeated loading triaxial tests on clay soils, during which they observed that the soils' deformation response could be divided into two groups based on the stress level. For soils subjected to a deviator stress smaller than the threshold stress, plastic strains accumulate at a low rate and stabilize after a large number of load cycles. However, soils exposed to a stress level greater than the threshold stress experience a rapid increase in plastic strain with cyclic loading, resulting in fast failure of the specimens. As such, Heath et al. (1972) proceeded to create a design method that precludes the development of deviator stresses exceeding a subgrade's threshold stress by providing a sufficiently thick granular layer. To do so, the authors assumed the entire substructure to be an isotropically elastic homogeneous infinite half-space to calculate the deviator stress induced in the subgrade by a maximum axle load. By comparing the variations in deviator stress with depth below the tie with the variations in threshold stress with depth in the substructure, Heath et al. (1972) created a design chart (Figure 2.9) that helps select the required granular thickness for a given axle load to generate a stress in the subgrade soil equal to its threshold stress.

Although this method is widely recognized as being technically sound (Burrow et al., 2007; D. Li & Selig, 1998a; Raymond & Williams, 1978; Sayeed & Shahin, 2018a), its main drawbacks include the extensive amount of laboratory testing required to determine a soil's threshold stress and its applicability which is mainly confined to clays and highly compressible silts. Li and Selig (1998a) further highlighted that this method fails to consider the stiffness difference between the subgrade and the overlying granular layer and that it does not account for the cumulative tonnage the subgrade is subjected to.

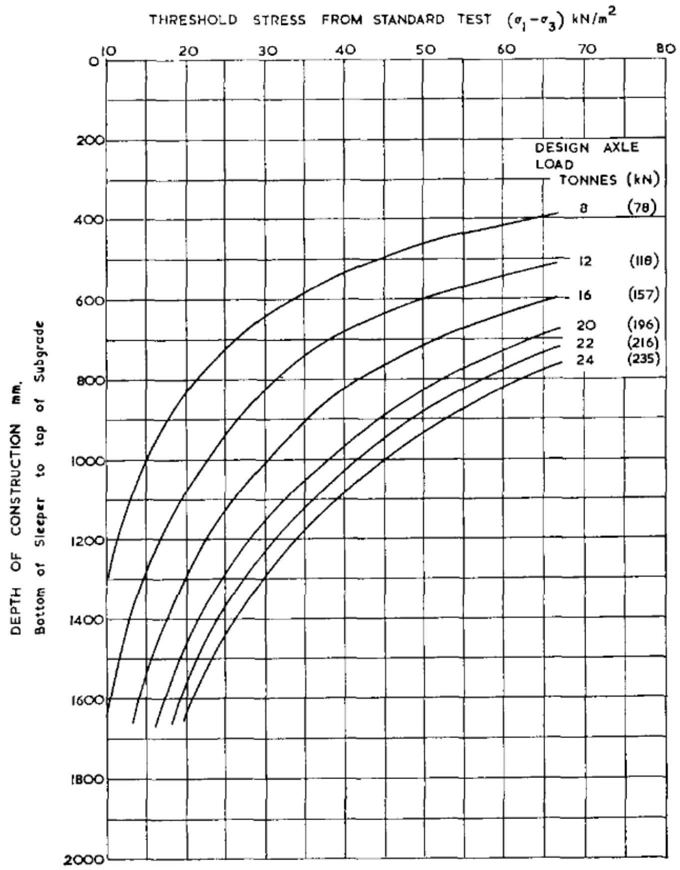

Figure 2.9: Design Chart Developed by Heath et al. (1972).

2.6.3. Raymond (1978) Modified AREMA Method

Raymond (1978) modified AREMA's design procedure by replacing the universal allowable subgrade stress of 138kPa with safe bearing pressures determined based on the type of subgrade soil given in Casagrande's soil classification system. To determine the stress generated on the subgrade by passing trains, Raymond (1978) used Boussinesq's equation for vertically loaded surface areas, assumed the contact pressure is uniformly distributed at the tie/ballast interface, and considered the case where a given axle load is supported by three ties, with the center tie carrying 50% of the load and the adjoining ties each carrying 25% of the load. To account for the dynamic nature of train loads, static wheel loads are multiplied by a dynamic amplification factor of 2. Design charts were then developed to estimate the minimum ballast thickness required to prevent subgrade overstressing based on the axle load and the minimum strength of different subgrade soil types. Despite improving AREMA's method by accounting for the soil type to determine a subgrade's allowable bearing pressure, this method fails to consider the effects of cyclic loading on the performance of the substructure and treats the substructure as a homogeneous half-space to compute the vertical stress in the subgrade.

2.6.4. Li and Selig (1998a) Method

Li and Selig (1998a, 1998b) proposed a method to determine the minimum granular layer thickness required to prevent two common types of cyclic loading-induced subgrade failures: progressive shear failure and excessive plastic deformation. Progressive shear failure occurs when the surface of a subgrade soil gets progressively sheared and remolded during cyclic loading, causing it to squeeze laterally and upward. This results in the formation of a surface heave at the trackside and a corresponding depression below the tracks. To prevent progressive shear failure, Li and Selig (1998a) indicated that the cumulative plastic strain (ϵ_p) in the subgrade should remain below an allowable cumulative plastic strain (ϵ_{pa}):

$$\epsilon_p \leq \epsilon_{pa} \tag{2.4}$$

Excessive plastic deformation in the subgrade, on the other hand, typically takes place in soft subgrade soils that extend to a considerable depth. In that type of failure, ballast pockets develop in the subgrade following the combined progressive shear deformation and compaction of the subgrade under repeated loading. Li and Selig stated that excessive plastic deformation may be avoided by limiting the total cumulative deformation of the subgrade (ρ) below an allowable cumulative plastic deformation (ρ_a):

$$\rho \leq \rho_a \tag{2.5}$$

Two sets of charts were then produced to select the required granular layer thickness to prevent progressive shear failure and excessive plastic deformation respectively. A sample of these charts is provided in Figure 2.10. The charts designed to avoid progressive shear failure consider the granular layer thickness a function of the ballast and subgrade resilient moduli, the subgrade soil type, the number of load repetitions, and the dynamic wheel load. In the charts describing excessive plastic deformation, the subgrade depth is added as an extra variable.

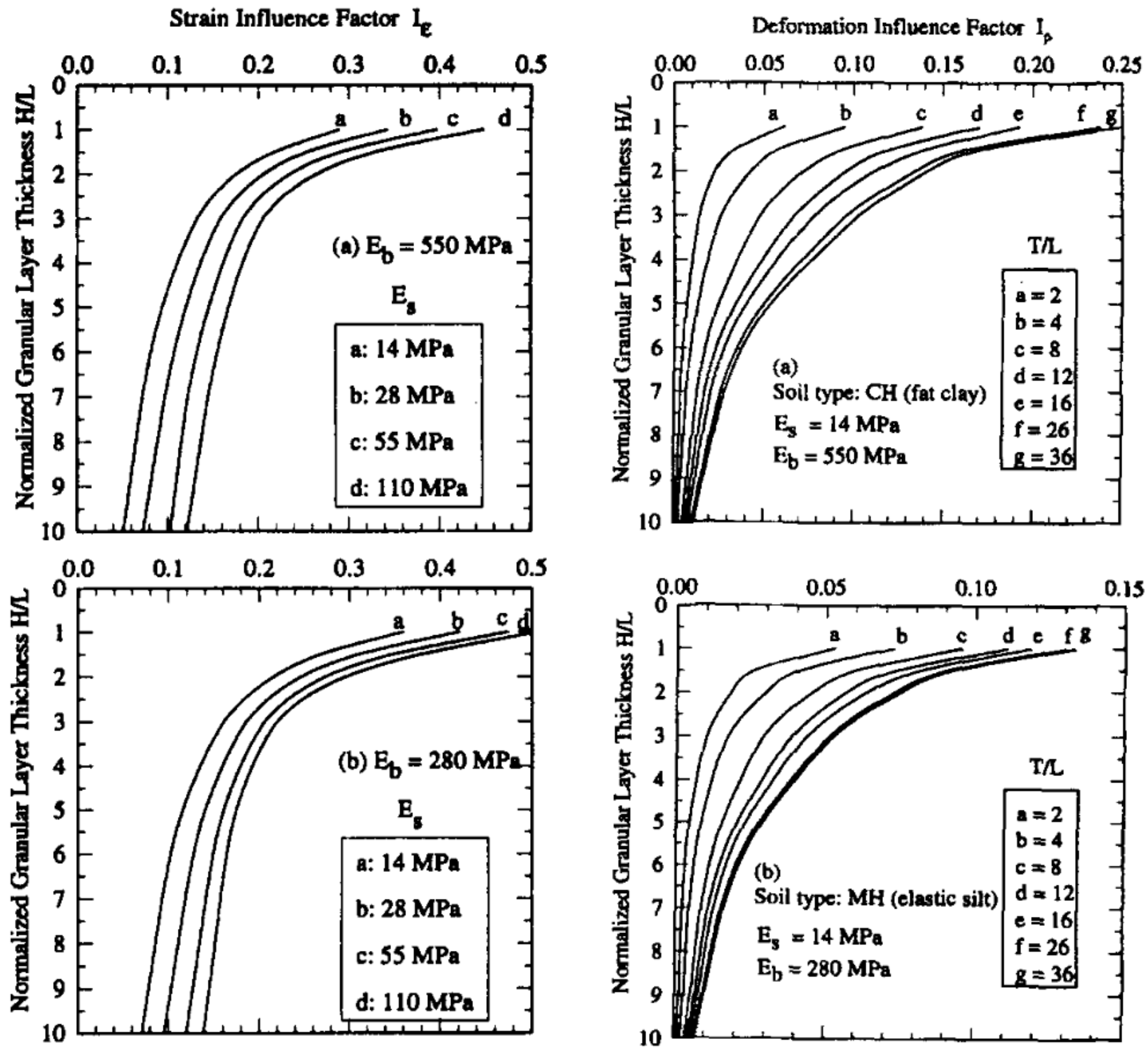

(a) (b)

Figure 2.10: Design Charts Used to Prevent (a) Progressive Shear Failure and (b) Excessive Plastic Deformation (Li and Selig, 1998a).

2.6.5. UIC Design Method

The Union Internationale des Chemins de Fer (UIC) created a set of guidelines for the construction of ballasted substructures in the UIC Code 719R (UIC, 2008). According to UIC, a substructure comprises a ballast layer, a blanket layer, and a prepared subgrade overlying the natural subgrade soil. The combined thickness of the track bed layers is determined by considering the subgrade soil type and bearing capacity, traffic characteristics, frost protection, track configuration and quality, and the type of tie and tie spacing. The subgrade is classified into four categories where QS0 describes soils unfit for use as subgrade material, QS1 represents poor subgrade soils with minimum California Bearing Ratios (CBR) between 1 and 3, QS2 defines average subgrade soils with a minimum CBR of 5, and QS3 represents good quality soils with a minimum CBR between 10 and 17. UIC 719R provides a table that summarizes the minimum required track bed layer thicknesses based on the aforementioned factors to ensure the constructed ballasted substructure provides the appropriate bearing capacity and sufficiently shields frost susceptible subgrade soils from freezing temperatures.

2.6.6. Sayeed and Shahin (2018a) Method

Drawing on the findings of Burrow et al. (2007) who concluded that railroad tracks using foundations designed using the most up-to-date design methods such as Li and Selig's (1998a) required frequent maintenance, Sayeed and Shahin (2018a, 2018b) modified the Li and Selig method. Sayeed and Shahin (2018a, 2018b) based their work on three-dimensional finite element simulations of an 80m-long track structure in which the ballast and subgrade are modeled separately using the Mohr-Coulomb and linear elastic constitutive models respectively. Cyclic loading is applied to the track structure numerically by simulating the passage of a standard passenger train on the modeled track section as moving loads. This remedies a common shortcoming of most design methods whereby subgrade stresses are calculated based on static loads only, thereby neglecting the dynamic nature of train loads. As a modified version of the Li and Selig method, the Sayeed and Shahin method proposes two sets of design charts developed to select the granular layer thickness required to preclude progressive shear failure and excessive plastic deformation of the subgrade. Examples of the design charts provided by Sayeed and Shahin (2018a) are presented in Figure 2.11.

2.7. Geogrid Reinforcement of Railroad Ballast

The development of vertical deformations in the ballast layer stems from the densification of the ballast aggregate during cyclic loading along with the lateral spread of the particles made possible, in part, by the lack of appreciable lateral confinement of the ballast aggregate. Excessive ballast deformations have a detrimental effect on track alignment and compromises track safety and riding quality. This is generally addressed by either imposing speed restrictions on affected track sections or undertaking of expensive periodic ballast maintenance operations such as tamping or stone-blowing. Given the elevated cost of maintenance operations, there exists a strong incentive to reinforce ballast layers to improve their performance and minimize their operating costs.

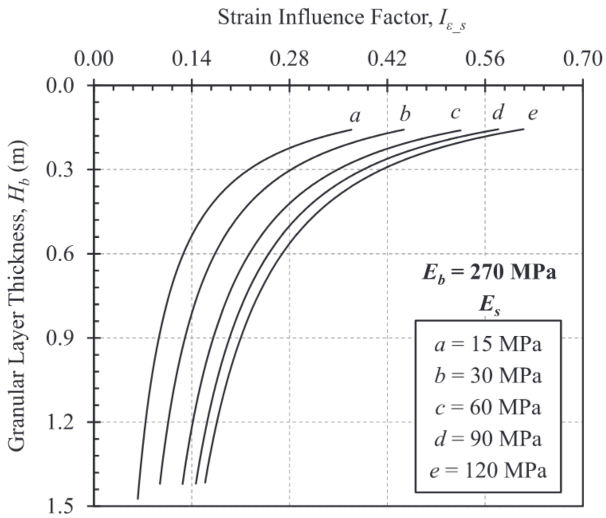

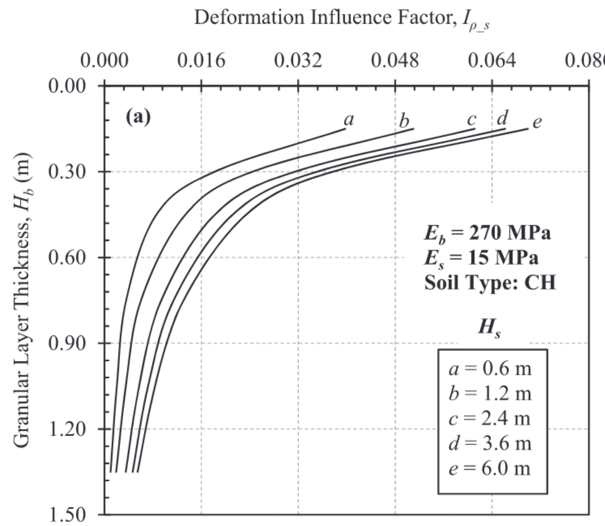

(a) (b)

Figure 2.11: Design Charts Used to Select the Granular Layer Thickness Required to Prevent (a) Progressive Shear Failure and (b) Excessive Plastic Deformation in the Subgrade (adapted from Sayeed and Shahin (2018a)).

It is in this context that geogrids are being used to reinforce railroad ballast. A geogrid is a polymeric material generally made of either polypropylene (PP), polyester (PET), or high-density polyethylene (HDPE). Its structure consists of large openings called apertures bordered by orthogonal ribs as shown in Figure 2.12. A geogrid reinforces unbound aggregate materials like railroad ballast by leveraging its open structure and allowing the surrounding soil particles to strike through its plane and become wedged in its apertures, effectively forming a semi-rigid mat that confines the unbound aggregate. The inclusion of a geogrid in railroad ballast helps minimize its deformation, reduces lateral spreading, mitigates ballast breakage, and increases the track's bearing capacity.

2.7.1. Geogrid-Ballast Interaction Mechanism

The inclusion of a geogrid in a layer of railroad ballast improves the granular layer's mechanical properties by precluding the development of extensional strains in the soil as shown in Figure 2.13 (Jewell et al., 1984). This is achieved by leveraging the geogrid's high tensile strength and stiffness through a stress transfer occurring at the geogrid-ballast interface that results in the geosynthetic resisting the tensile stresses the soil is unable to bear (Lopes, 2021). This stress transfer hinges on the formation of a strong ballast-geogrid interlock stemming from the interpenetration of ballast particles into the geogrid's apertures that transforms the two materials into a semi-rigid medium that confines the granular material. Stresses may be mobilized along the geogrid-ballast interface through either or a combination of two relative soil movements. The first consists of the direct sliding of a mass of ballast particles above the geogrid interlocked with other ballast particles while the second represents the relative pullout motion of the geogrid with respect to the surrounding ballast particles (Jewell, 1988; Lopes, 2021).

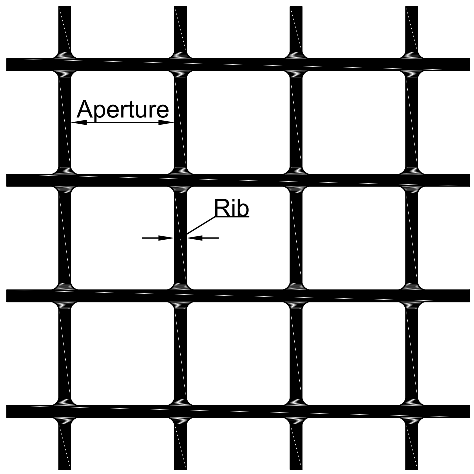

Figure 2.12: Open Structure of a Typical Biaxial Geogrid.

The geogrid-ballast interaction is strongly affected by the physical and mechanical properties of the ballast aggregate and the mechanical properties, shape, and geometry of the geogrid. A geogrid may interact with railroad ballast through the following three mechanisms (Jewell et al., 1984; Lopes, 2021):

- Skin friction: shear between the ballast particles and the geogrid's plane surface
- Soil-soil friction: shearing of the ballast located above the geogrid over ballast particles wedged in the geogrid's apertures
- Passive thrust against on the geogrid's bearing members

In the case of direct sliding, the geogrid-ballast interface shear strength (T) stems from soil-soil friction ($T_{s\text{-}s}$) and skin friction (T_s) (Lopes, 2021):

$$T = T_s + T_{s-s} \tag{2.6}$$

$$T_s = a_s W L \sigma_n' \tan \delta \tag{2.7}$$

$$T_{s-s} = (1 - a_s) W L \sigma_n' \tan \phi' \tag{2.8}$$

Where W and L are the width and length of the geogrid, a_s is the fraction of the geogrid that is solid, δ is the reinforcement interface's friction angle, φ is the soil's friction angle, and σ'_n is the effective normal stress on the interface.

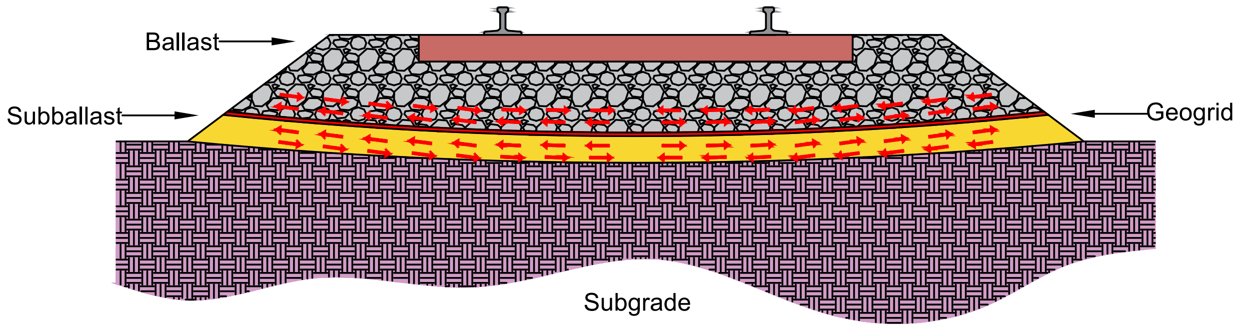

Figure 2.13: Geogrid Placed at the Ballast/Subballast Interface Limiting the Development of Tensile Stresses in the Ballast Layer.

If a pullout movement of the geogrid occurs along the geogrid-ballast interface, the interface shearing resistance is primarily derived from skin friction on both sides of the geogrid and passive thrust of ballast particles against the geogrid's bearing members (T_p) (Lopes, 2021):

$$T = 2T_s + T_p \tag{2.9}$$

$$T_p = \frac{L}{S} a_b W B \sigma'_p \tag{2.10}$$

Where S, B, and a_b are the distance between geogrid bearing members, thickness of the geogrid ribs, and fraction of the width of the geogrid available for bearing respectively, and σ'_p is the effective passive stress.

2.7.2. Behavior of Geogrid-Reinforced Ballast

Bathurst and Raymond (1986, 1987) performed large-scale model experiments called ballast box tests in which a 300mm-thick ballast layer was constructed in a rigid container to investigate the behavior of geogrid-reinforced ballast. Several experiments were conducted during which a geogrid was placed at depths ranging from 50 to 200mm below the tie and where the support conditions below the ballast layer were varied to simulate the presence of subgrades with California Bearing Ratios (CBR) of ∞, 39, and 1. Bathurst and Raymond (1986, 1987) found that a geogrid reduces the rate at which track settlement develops under cyclic loading, particularly in cases where the underlying subgrade is soft, with the tie settlement in the geogrid-reinforced layer being 50% smaller than that of the unreinforced layer after 100,000 load cycles. The authors also stated that geogrids located closer to the tie yield a greater settlement reduction than geogrids located deeper in the ballast layer.

Similar experiments conducted by Gobel et al. (1994) revealed that reinforcing a ballasted substructure with a geogrid increases the substructure's bearing capacity and reduces track settlement. They recommended the geogrid be placed at the subballast-subgrade interface for maximum settlement reductions. Small-scale ballast box tests and finite element simulations carried out by Raymond (2002) and Raymond and Ismail (2003) echoed the findings of Bathurst and Raymond (1987) by demonstrating that geogrids decrease track settlement by 13-30% and that maximum settlement reductions are obtained when the underlying soil strata is soft.

McDowell and Stickley (2006) sought to determine whether reinforcing ballast with a geogrid could allow the use of weaker ballast aggregate while maintaining satisfactory track performance. After running several ballast box tests, in which geogrids were placed at depths of 100 and 200mm beneath the tie in a 300mm-thick ballast layer, the authors reported that geogrids do not provide much improvement when reinforcing weak ballast aggregate but translate into substantially improved mechanical properties when reinforcing strong ballast particles. The use of geogrids is also shown to lead to marginal increases in ballast stiffness and decreases in ballast breakage while the tie settlement is considerably minimized. McDowell and Stickley (2006) recommended placing a geogrid 200mm under the tie for optimal performance.

Sharpe et al. (2006) and Fernandes et al. (2008) performed field tests in which a geogrid was placed below a 400mm-thick ballast layer and geotextiles and geogrids were incorporated at the ballast/subballast and subballast/subgrade interfaces along different track sections respectively. Sharpe et al. (2006) reported an increase in trackbed stiffness following the placement of a geogrid below the ballast layer even on track sections supported by subgrades described as being only slightly soft. Fernandes et al. (2008) indicated that similar track performance is obtained regardless of the type of geosynthetic used and demonstrated that the use of geosynthetic reinforcement decreases the substructure's compressibility, laterally confines the granular layers, and significantly reduces ballast breakage. They further commented that geotextiles are more likely to suffer considerable mechanical damage during their service life and as such recommended using geogrids to reinforce the granular layers of a substructure. These observations were echoed by the field tests performed by Indraratna et al. (2010) in Bulli, NSW, Australia where a geocomposite comprising a geogrid and a geotextile was laid at the interface between a 150mm-thick subballast and a 300mm-thick ballast layer along track sections with fresh ballast aggregate and recycled ballast aggregate. The results showed that the inclusion of a geocomposite below a fresh ballast layer yields 30% and 50% reductions in vertical and lateral deformations in the ballast layer respectively. In the track sections consisting of recycled ballast aggregate, the geocomposite achieves 9% and 17% reductions in vertical and lateral deformations in the ballast layer respectively.

A comprehensive laboratory study using large-scale model tests was conducted by Brown et al. (2007) to identify the key factors that impact the performance of geogrid-reinforced ballast. Biaxial geogrids with stiffnesses ranging from 825 to 1,260MN/m and aperture sizes ranging from 32 to 100mm were placed 250mm below the base of the tie in 300mm-thick ballast layers supported either by a stiff subgrade or a subgrade with a 30MPa stiffness. Brown et al. (2007) observed that there exists a range of optimal geogrid stiffness with an increase in stiffness from 825 to 1,060MN/m yielding a 68.7% reduction in settlement and an increase from 1,225 to 1,260MN/m causing the tie settlement to increase by 92%. The authors commented that the geogrid aperture size wields an important influence on the ability of geogrids to stabilize railroad ballast and identified aperture sizes ranging from 60 to 80mm as being the most conducive to maximum settlement reduction. Geogrids are also observed to be more effective at minimizing tie settlement for a soft subgrade.

To determine whether geogrids could be used to stabilize fouled ballast, Indraratna et al. (2011) conducted direct shear tests on geogrid-reinforced clean ballast and fouled ballast with void contamination indices of 20%, 40%, 70%, and 95% under normal stresses of 15, 27, 51, and 75kPa. In general, the inclusion of geogrids leads to an increase in the ballast's shear strength and a reduction in its dilation at all normal stresses. The greatest increase in shear strength occurs in the clean ballast aggregate while the increasing presence of fouling material in fouled ballast specimens decreases the benefits derived from the geogrid's presence. Additional direct shear tests performed on fresh ballast aggregate by Indraratna et al. (2012) sought to investigate the effect of the geogrid aperture size on the geosynthetic's ability to reinforce railroad ballast. They assessed the effect of the geogrid aperture size (A) on ballast shear strength by normalizing it by the ballast's mean particle diameter (D_{50}) thereby defining the A/D_{50} ratio. The authors defined three ranges of the A/D_{50} ratio based on their effect on the geogrid-ballast interlock. A/D_{50} ratios smaller than 0.95 were labeled as the feeble interlock zone where the geogrid apertures are too small to allow the formation of a strong interlock. The optimum interlock zone was defined as A/D_{50} ratios ranging from 0.95 to 1.20 and consists of geogrid aperture sizes yielding the most effective reinforcement of railroad ballast. Geogrids possessing aperture sizes giving A/D_{50} ratios in excess of 1.20 fall into the diminishing interlock zone where satisfactory geogrid interlock still occurs albeit at a decreasing effectiveness with increasing aperture size.

Large-scale cyclic load tests performed by Indraratna et al. (2013) examined the impact of geogrid reinforcement on the lateral deformation response and degradation of railroad ballast. Geogrids were placed either at the ballast/subballast interface or 65, 130, and 195mm above the subballast. Two geogrids with square apertures, one with rectangular apertures, and one with triangular apertures were used in the experiment. Ballast samples were observed to experience a rapid increase in vertical and lateral deformation during the initial 50,000 load cycles while the inclusion of geogrids leads to a settlement reduction of 58% and a decrease in ballast breakage by 53% compared with the unreinforced condition. The authors noted that geogrids can reduce the displacement of ballast particles located within a certain zone extending above and below the geosynthetic called the geogrid influence zone (GIZ). The extent of the GIZ along with the magnitude of the reduction in lateral ballast deformation are both functions of the geogrid aperture size and geogrid placement depth.

Similar experiments performed by Hussaini et al. (2015, 2016) assessed the effect of geogrids on the deformation response and degradation of railroad ballast under cyclic loading for vertical stresses of 460kPa and 230kPa. The presence of geogrids minimizes particle breakage compared to the unreinforced case by up to 53% which the authors attributed to the geogrid creating a non-displacement boundary at the ballast/geogrid interface that confines the ballast aggregate. It was also seen that increasing the vertical stress from 230kPa to 460kPa results in an increase in settlement and particle breakage but that the extent of the geogrid influence zone remains the same regardless of the applied vertical stress.

Sweta and Hussaini (2020, 2022) performed ballast box tests to study the effect of geogrids on the deformation response, resilient modulus, and damping of railroad ballast subjected to 250,000 load cycles applied at frequencies of 10, 20, 30, and 40Hz. The authors reported that the lateral and vertical deformations and breakage of unreinforced ballast increases non-linearly with an increase in frequency from 10 to 40Hz. The reductions in lateral and vertical ballast deformations derived from the inclusion of geogrids compared to the unreinforced case decrease with increasing frequency. At a frequency of 10Hz, maximum reductions in lateral and vertical ballast deformations amount to 59% and 43% respectively. These drop to 49% and 35% at 20Hz, 45% and 33% at 30Hz, and 33% and 27% at 40Hz. The ballast's resilient modulus increases following the placement of a geogrid, with maximum increases of 25.8%, 21.4%, 17%, and 11% being recorded at loading frequencies of 10, 20, 30, and 40Hz respectively. It was also found that the inclusion of a geogrid in railroad ballast increases the granular material's damping ratio, with maximum increases in the damping ratio of 36%, 22%, 15%, and 10.42% occurring at loading frequencies of 10, 20, 30, and 40Hz respectively.

Sadeghi et al. (2020, 2023) examined the effectiveness of geogrids in improving the mechanical properties of sand-fouled ballast using direct shear tests and ballast box tests. In the direct shear tests, geogrids were used to reinforce clean ballast and ballast contaminated with 6, 12, 18, 24, 30, and 36% of sand. Three different biaxial geogrids with square apertures of 24×24mm, 34×34mm, and 46×46mm were used in the experiments. Sand contamination of railroad ballast triggers reductions in shear strength and friction angle of up to 33% and 23% respectively while the incorporation of geogrids successfully mitigates the effects of fouling, resulting in shear strength increases of up to 25% compared with the unreinforced condition. In their ballast box tests, the authors compared the behavior of clean ballast with ballast contaminated with 7, 14, 24, and 36% of sand subjected to 100,000 load cycles. The authors indicated that optimum geogrid performance is obtained with an aperture size of 34×34mm which consistently leads to smaller tie settlement, reduces particle breakage, and increases the ballast layer's stiffness. Reinforcing clean and fouled ballast with geogrids also minimizes ballast breakage. The optimum placement depth is found to be 200mm beneath the tie as the authors found it results in a higher ballast stiffness, smaller tie settlement, and reduced ballast breakage than in the case where the geogrid is placed 100mm below the tie. Sadeghi et al. (2020, 2023) further stated that the inclusion of geogrids in clean and fouled ballast decreases the ballast's damping ratio owing to the stiffening effect of the geogrid-ballast interlock that causes a reduction in energy dissipation.

2.7.3. Factors Affecting the Performance of Geogrid-Reinforced Ballast

The mechanical behavior of geogrid-reinforced ballast subjected to cyclic loading is influenced by both the characteristics of the geogrid and the behavior of the granular material itself, as detailed in Section 2.2.4. The efficacy of geogrid reinforcement is predicated on its ability to form a robust mechanical interlock with the surrounding granular material. This interlock allows the geogrid to effectively confine ballast, thereby enabling it to withstand tensile stresses that the ballast cannot resist. Research has shown that the performance of a geogrid embedded in ballast is contingent upon its aperture size, its placement depth, and the compressibility of the underlying subgrade.

2.7.3.1. Geogrid Aperture Size

The effectiveness of the geogrid-ballast interlock is strongly tied to the ability of ballast particles to strike through the geogrid's plane and become wedged in its apertures. As such, the relationship between the geogrid aperture size (A) and the size of the surrounding ballast particles, often described by their mean particle diameter (D_{50}), is crucial in the development of the interlock. For a given size of ballast particles, excessively small geogrid apertures prevent ballast particles from interpenetrating into the geosynthetic's openings thereby precluding the formation of a stable interlock. On the other hand, geogrid apertures that are too large in comparison with the size of the surrounding soil particles may be detrimental to the effectiveness of the interlock, offering a lower confinement and reduced reinforcement benefits to the soil. To effectively compare the geogrid aperture size to the diameter of the surrounding ballast particles, Indraratna et al. (2012) defined the A/D_{50} ratio. Table 2.2 summarizes some of the recommendations on the A/D_{50} ratio available in the literature.

A comprehensive research campaign conducted at the University of Nottingham (Brown, Brodrick, et al., 2007; Brown, Kwan, et al., 2007; McDowell et al., 2006; McDowell & Stickley, 2006) examined the key geogrid parameters that affect the performance of geogrid-reinforced ballast. McDowell et al. (2006) used the discrete element method (DEM) to simulate pullout tests on geogrids with A/D_{50} ratios of 0.9, 1.1, 1.4, and 1.6 embedded in railroad ballast. Their results indicated that an A/D_{50} ratio of 1.4 generated the greatest pullout force in the smallest displacement while A/D_{50} ratios of 1.1 and 1.6 performed similarly. Additionally, ballast box tests conducted by

Brown et al. (2007) investigated the behavior of ballast reinforced with geogrids with *A/D_{50}* ratios of 0.64, 0.76, 1.0, 1.30, 1.80, and 2.0. The use of geogrids with small apertures resulted in the formation of a shear plane along the geogrid-ballast interface caused by the lack of interlock between the two materials. Based on considerations of tie settlement reductions in geogrid-reinforced ballast, the authors recommended using *A/D_{50}* ratios ranging from 1.20 to 1.60.

Table 2.2: Recommended Geogrid Aperture Size Ratios.

Author(s)	Experiment(s)	Types of Geogrids	Recommended A/D_{50}	Observations
McDowell et al. (2006)	Pullout Test (DEM)	A/D_{50}: 0.9, 1.1, 1.4, 1.6	1.4	-A/D_{50} of 1.4 mobilizes the highest pullout force in the smallest displacement -A/D_{50} of 1.1 and 1.6 yield similar performances -A/D_{50} of 0.9 has a low pullout resistance
Brown et al. (2007)	Ballast Box Test	A/D_{50}: 0.64, 0.76, 1, 1.3, 1.8, 2	1.2-1.6	-Formation of a shear plane at the geogrid level due to lack of interlock when aperture size is too small
Indraratna et al. (2013)	Ballast Box Test	A/D_{50}: 0.6, 1.08, 1.21, 1.85	1.21	-A/D_{50} ratio affects optimum placement depth -A/D_{50}<0.95 is most effective at the ballast/subballast interface -A/D_{50}>0.95 is most effective 65mm above the subballast
Hussaini et al. (2015, 2016)	Ballast Box Test	A/D_{50}: 0.6, 1.08, 1.21, 1.85	1.21	-A/D_{50}=1.21 most effective at minimizing ballast settlement
Hussaini & Sweta (2020, 2021), Sweta & Hussaini (2020)	Ballast Box Test Direct Shear Test	A/D_{50}: 0.63, 0.83, 0.93, 0.95, 1.54	0.93	-Role of A/D_{50} in reducing lateral displacement evident near geogrid location - A/D_{50} of 0.93 is most effective at minimizing lateral and vertical deformation, and increasing resilient modulus
Sadeghi et al. (2020, 2023)	Direct Shear Test Plate Load Test Ballast Box Test	A/D_{50}: 0.83, 1.17, 1.59	1.17	-Greatest shear strength increase and reduction of particle settlement and rotation in fouled ballast when A/D_{50} is 1.17 - A/D_{50}=1.17 yields greatest decrease in ballast damping ratio

Indraratna et al. (2012) performed ballast box tests on geogrid-reinforced ballast and divided the *A/D_{50}* ratio into three ranges: *A/D_{50}* < 0.95 as the feeble interlock zone, 0.95 < *A/D_{50}* < 1.20 as the optimum interlock zone, and *A/D_{50}* > 1.20 as the diminishing interlock zone. The relevance of these ranges was illustrated by ballast box tests conducted by Indraratna et al. (2013) who reported an *A/D_{50}* ratio of 1.21 is the most effective at minimizing ballast deformations while in general, using an A/D_{50} ratio greater than 0.95 for geogrids embedded in ballast yields satisfactory performance. The authors added that an A/D_{50} ratio smaller than 0.95 is most effective in cases where the geogrid is laid at the ballast/subballast interface. These observations were echoed by the ballast box tests carried out by Hussaini et al. (2015, 2016). Similar findings were reported by Hussaini and Sweta (2020) who indicated, upon performing direct shear tests and ballast box tests on geogrid-reinforced ballast, that there exists a threshold limit of the A/D_{50} ratio beyond a geogrid becomes unable to arrest the lateral movement of ballast particles due to their free movement within its apertures. Ballast box tests conducted by Sadeghi et al. (2023) identified an optimum A/D_{50} ratio of 1.17 as it led to the greatest decrease in ballast settlement and damping ratio.

2.7.3.2. Geogrid Placement Depth

Various recommendations exist on the optimum placement depth of geogrids in a ballast layer. Bathurst and Raymond (1987) and Raymond and Ismail (2003) stated that geogrids located at depths of 50 to 100mm beneath the ties are the most effective at minimizing tie settlement. However, for practical reasons, they recommended geogrids be placed at least 150mm below the ties. Indraratna et al. (2013) and Hussaini et al. (2015, 2016) showed that the reinforcing effect of a geogrid in terms of minimizing particle movement is maximum in its immediate vicinity and quickly decreases with increasing vertical distance from its location. They found a placement depth of 130mm above the subballast is most effective at minimizing ballast deformation but recommended geogrids be placed 65mm above the subballast for practical reasons. Additionally, Gedela and Karpurapu (2021) reported that geogrids placed 125mm below the ties are the most effective at reducing tie settlement. Some of the recommended values of the geogrid placement depth found in the literature are summarized in Table 2.3.

2.7.3.3.Subgrade Strength

The compressibility of the subgrade supporting the ballasted substructure is a factor that dictates the performance of geogrids embedded in railroad ballast. Bathurst and Raymond (1987) and Brown et al. (2007) showed the ability of geogrids to minimize track settlement increases with a decrease in subgrade strength. Yu et al. (2019) conducted triaxial tests on ballast/subballast/subgrade assemblies reinforced with geogrids and reported that considerable reductions in settlement are achieved by the geogrids when the subgrade is weak while only minor settlement decreases are recorded when the subgrade is firm. A finite element modeling parametric study investigating the performance of geosynthetic-reinforced ballasted substructures done by Jiang and Nimbalkar (2019) highlighted the contribution of the subgrade strength to the geogrid's reinforcing action. Their work revealed that subgrade deformation impacts the geogrid's reinforcement mechanisms by triggering the deformation of the track substructure, thereby mobilizing tensile stresses in the reinforcement. As such, enhanced geogrid performance is observed in track substructures resting on softer subgrades.

Table 2.3: Recommended Geogrid Placement Depth for Optimum Reinforcement of Railroad Ballast.

Author(s)	Experiment(s)	Tested Geogrid Depths	Optimum Depth	Observations
Bathurst et al. (1986, 1987)	Ballast Box Test	50mm, 100mm, 150mm, 200mm	200mm	-Maximum settlement reduction at placement depths of 50 and 100mm -50 and 100mm are not feasible in the field due to disturbance from maintenance works
Raymond (2002), Raymond & Ismail (2003)	Cyclic Load Test & FEM	D_r/B: 0.18 – 0.9	D_r/B: 0.18 – 0.6	-Effect of reinforcement negligible when $D_r/B > 0.6$ -Benefit of geogrid becomes more pronounced with high number of loading cycles
McDowell & Stickley (2006)	Ballast Box Test	100mm, 200mm	200mm	-Better performance in terms of settlement with a geogrid depth of 200mm
Chen et al. (2012)	Ballast Box Test (DEM)	100mm, 150mm, 200mm, 250mm	200mm	-Geogrid is found to limit lateral ballast displacement within 50mm above and below its location
Indraratna et al. (2013), Hussaini et al. (2015, 2016)	Ballast Box Test	130mm, 195mm, 260mm, 325mm	260mm	-Geogrid most effective at limiting ballast vertical and lateral strains and ballast breakage at depth of 260mm
Sadeghi et al. (2023)	Ballast Box Test	100mm, 200mm	200mm	-Geogrid at 200mm results in smaller settlement, higher ballast stiffness, and lower ballast breakage

2.8. Summary

This literature review begins by examining the structure and components of conventional ballasted railway tracks, emphasizing the key role played by railroad ballast. It then explores the forces exerted on the ballast layer by passing trains, setting the stage for an analysis of how ballast responds to cyclic loading. The review delves into the resilient and permanent deformation characteristics of ballast under repeated loads, considering various factors influencing its behavior such as the stress level, loading frequency, number of load cycles, moisture content, ballast morphology, and the ballast density and gradation. Further, the review addresses the geotechnical challenges inherent to ballasted railroad tracks, focusing on issues stemming from the ballast and subgrade layers. It then transitions to evaluating the strategies employed to design ballasted track foundations. In the progression towards improved railway track performance, the literature review shifts focus to the behavior of geogrid-reinforced ballast. It provides a discussion on how geogrid inclusions impact ballast performance, guided by an analysis of relevant factors.

Preface to Chapter 3

Canadian ballasted railway tracks are exposed to significant seasonal temperature fluctuations. Changes in ambient air temperature may be felt up to a depth of 10m in soil structures, with the first 2m of soil experiencing the greatest temperature changes and the shallowest 300mm exhibiting daily temperature variations (Murray & Farrar, 1988; Xiao et al., 2021, 2022). Since the geogrids used to reinforce railroad ballast are generally placed at shallow depths beneath the ties that seldom exceed 300mm, they are likely to be affected by variations in ambient air temperature. Geogrids are typically manufactured from polymeric materials called thermoplastics which possess temperature-dependent mechanical properties. Their behavior is characterized by a brittle response to loading at low temperatures that contrasts with an increasing ductility observed at elevated temperatures. Therefore, this raises the question of assessing how polymeric geogrids behave at different temperatures.

In this chapter, this query is addressed by performing single-rib tensile tests on specimens of a biaxial geogrid and a geogrid composite consisting of a geogrid heat-bonded to a geotextile at temperatures ranging from -30ºC to 40ºC and -30ºC to 20ºC respectively. The methodology employed to run the experiments is first reviewed. The results are then analyzed by dissecting the tensile load–strain response of both materials. The failure patterns observed in both materials at different temperatures are finally examined and related to the geogrids' mechanical behavior.

Chapter 3: Effect of Temperature on the Mechanical Properties of Two Polymeric Geogrid Materials†

Abstract

Understanding the tensile behavior of geosynthetic reinforcement materials at different temperatures is essential for the design of reinforced soil structures in seasonally cold regions. This study describes a series of tensile tests performed on two polypropylene geogrid materials, namely a biaxial geogrid and a geogrid composite. A total of 84 tests were performed in an environmental chamber with temperatures as low as -30°C and as high as +40°C. The response of each material is examined over the range of investigated temperatures to evaluate the effect of temperature changes on the tensile strength of the two geogrid materials. The response of the biaxial geogrid is found to be sensitive to temperature variations, with samples tested at low temperatures exhibiting brittle behavior characterized by high rupture strength and small ultimate strain while samples tested at elevated temperatures displayed ductile behavior with large elongation at failure and comparatively small rupture strength. Similar response was found for the geogrid composite, however, the rupture strength seemed to be less sensitive to temperature changes. The modes of failure observed at each temperature are examined based on photographic evidence taken during the experiments.

Keywords: Geosynthetics, Geogrid, Tensile loading, Temperature effect, Mechanical properties

---

†A version of this manuscript was published in *Geosynthetics International.*

3.1. Introduction

Geogrids are polymeric materials commonly used to reinforce and stabilize earth structures. They are typically made from three different types of polymers, i.e., polypropylene (PP), high-density polyethylene (HDPE), and polyester (PET). Polymeric materials used to manufacture geogrids are predominantly thermoplastics that exhibit a temperature-dependent behavior that ranges from being soft and flexible at high temperatures to brittle at low temperatures (Koerner, 2005; McGown et al., 2004; Ward & Sweeney, 2004). The temperature at which major changes occur in the mechanical properties of these materials is called the glass transition temperature (T_g). Below its glass transition temperature, a polymeric material behaves in a rigid and brittle fashion while it becomes more rubbery when temperatures exceed T_g (Jackson & Dhir, 1996; Koerner et al., 1993; McGown et al., 2004).

While geogrids are usually embedded within earth structures, the ambient temperature fluctuations experienced by earth structures translate into temperature variations within the reinforcement layer (D. I. Bush, 1990; Segrestin & Jailloux, 1988; Zarnani et al., 2011). Segrestin and Jailloux (1988) developed a numerical model to evaluate the temperature change within a geosynthetics-reinforced earth structure as a result of seasonal temperature changes. They determined that outside temperature changes could be felt up to a depth of 10m in earth structures and that geosynthetics were likely to experience temperature-induced changes in their mechanical properties (Segrestin & Jailloux, 1988). This observation was echoed by Zarnani et al. (Zarnani et al., 2011) and Kim & Kim (Kim & Kim, 2020) who respectively studied the effects of soil temperature changes on geogrid strains placed in a reinforced embankment and in a geosynthetic-reinforced railway subgrade. Their respective findings revealed geogrid deformations are sensitive to soil temperature changes and geogrid strains increase with increasing soil temperature and decrease with decreasing temperature.

As shown in Table 3.1, several studies have been conducted to investigate the influence of temperature on the mechanical properties of geosynthetics. Calhoun (Calhoun, 1972) sought to determine how temperature affects the tensile strength of geotextiles and concluded that their strength is insensitive to temperature changes based on grab tensile tests on geotextiles performed at temperatures ranging from -18°C to 82°C. Zornberg et al. (Zornberg et al., 2004) conducted a series of wide-width tensile tests on woven PP geotextiles at temperatures ranging from 24°C to

60°C. They reported that the geotextiles' tensile strength decreases while the ultimate strain increases with increasing temperature. Henry and Durell (Henry & Durell, 2007) performed wide-width tensile and puncture tests on clean and moistened PP geotextiles at low temperatures and observed that the tensile strength of dry geotextiles decreases with decreasing temperature while that of wet geotextiles increases due to the stiffening effect of ice and soil fines present on the geotextile samples. They noted that both the dry and wet geotextiles elongate less at low temperatures and that a clear behavioral change occurs between 0°C and -20°C which corresponds to the range of T_g of polypropylene (Henry & Durell, 2007).

Karademir and Frost (Karademir & Frost, 2014) subjected individual PP filaments taken from a needle-punched non-woven geotextile to tensile tests at temperatures ranging from 20°C to 50°C. Their experiments revealed that increasing temperatures translate into reduced tensile strength, modulus of elasticity, stiffness, and yield strength. Additionally, Koda et al. (Koda et al., 2018) performed wide-width tensile tests on a woven PP geotextile at 20°C, 50°C, and 80°C. They determined that a rise in temperature leads to a reduction in strength and an increase in ultimate strain, with the tensile strength at 80°C being 34% smaller than that at 20°C.

Analogous research efforts have been dedicated to investigating the temperature dependence of polymeric geogrids. Kongkitkul et al. (Kongkitkul et al., 2012) performed tensile tests on PP, PET, and HDPE geogrids at temperatures ranging from 30°C to 50°C. They showed that geogrids experienced a reduction in tensile strength with increasing temperature and that HDPE geogrids were the most sensitive to temperature changes, followed by the PP and PET geogrids. Similarly, Chantachot et al.(Chantachot et al., 2016, 2017, 2018) carried out tensile tests on uniaxial HDPE and biaxial PP geogrids (2016), on an HDPE geogrid (2017), and on PP, PET, and HDPE geogrids (Chantachot et al., 2018) under increasingly high temperatures ranging from 30°C to 50°C. They demonstrated that an increase in temperature manifested itself in a greater ultimate strain in the PP geogrid while that of the HDPE geogrid remained unchanged. Kasozi et al. (Kasozi et al., 2014) conducted tensile tests at elevated temperatures on a uniaxial HDPE geogrid in a bid to determine how a rise in temperature would affect its performance and reported that the HDPE geogrid loses strength with increasing temperature. Li et al. (G. Li et al., 2018) studied the temperature dependence of polypropylene by performing tensile tests on dog-bone PP samples at temperatures ranging from -30°C to 110°C and indicated that the samples' modulus of elasticity decreases with increasing temperature. Additionally, Aryiama et al. (Ariyama et al., 1997) showed that the modulus of elasticity and tensile strength of PP samples decrease at elevated temperatures after subjecting the samples to tensile tests at temperatures ranging from 25°C to 70°C.

An attempt to characterize the behavior of geogrids at low temperatures was made by Wang et al. (E. L. Wang et al., 2008) who performed creep tests on a uniaxial HDPE geogrid over a temperature range of -35°C to 20°C and observed that geogrids developed smaller strains at low temperatures. Likewise, Bonthron and Jonsson (Bonthron & Jonsson, 2017) conducted tensile tests on one PET geogrid and four PP geogrids at temperatures ranging from -20°C to 20°C. They concluded that geogrids generally become stiffer at low temperatures, exhibiting greater tensile strength and smaller ultimate strain compared to the reference temperature.

Geosynthetics have temperature-dependent properties and may exhibit a wide range of behavior depending on the temperatures they are exposed to (D. I. Bush, 1990; Cuelho et al., 2005; Han & Jiang, 2013; Koerner et al., 1992; McGown et al., 2004). As such, it is critical to characterize the mechanical behavior of geosynthetics over the range of temperatures they may be exposed to during their service life. The objective of this study is to investigate the effect of temperature on the tensile strength of a large aperture biaxial PP geogrid and biaxial PP geogrid composite, i.e., biaxial geogrid heat-bonded to a non-woven polyester geotextile, designed to reinforce ballasted railway embankments in seasonally cold regions (Bhat & Thomas, 2015; Bhat & Tomas, 2017).

Table 3.1: Summary of Previous Research on the Effect of Temperature on the Mechanical Properties of Geosynthetics.

Author(s)	Year	Type of Geosynthetic	Temperature Range	Measured Properties	Results
Calhoun	1972	PP Geotextile	-18°C to 82°C	-Tensile Strength	Tensile strength is not affected by temperature
Ariyama et al.	1997	PP Samples	25°C to 70°C	-Tensile Strength -Modulus of Elasticity	Tensile strength and modulus of elasticity decrease at elevated temperatures
Zornberg et al.	2004	PP Geotextile	24°C to 60°C	-Tensile Strength -Elongation	Higher temperatures lead to smaller tensile strengths and greater strains
Henry and Durell	2007	PP Geotextile	-54°C to 20°C	-Tensile Strength -Elongation -Puncture Strength	Tensile strength of dry geotextile decreased while that of wet geotextile increased with decreasing temperature. Lower ultimate strain at low temperature
Wang et al.	2008	HDPE Geogrid	-35°C to 20°C	-Creep -Strain	Smaller strains at lower temperatures
Kongkitkul et al.	2012	PP, PET, HDPE Geogrids	30°C to 50°C	-Tensile Strength -Elongation	Higher temperatures translate into lower tensile strain and greater ultimate strain. HPDE is the most sensitive to temperature changes, followed by PP and PET
Karademir and Frost	2014	PP Geotextile	20°C to 50°C	-Tensile Strength -Modulus of Elasticity -Stiffness	Reduction in tensile strength, modulus of elasticity, and stiffness with increasing temperature
Kasozi et al.	2014	HDPE Geogrid	30°C to 60°C	-Tensile Strength -Elongation	Greater temperatures lead to lower tensile strength and greater ultimate strain
Chantachot et al.	2016, 2017, 2018	HDPE and PP Geogrids	30°C to 50°C	-Tensile Strength -Elongation	PP, PET, and HDPE geogrids experience strength loss with increasing temperature. Only PP and PET geogrids exhibit greater strains
Bonthron & Jonsson	2017	PET and PP Geogrids	-20°C to 20°C	-Tensile Strength -Elongation	Geogrids become stiffer at low temperatures, developing a greater tensile strength and smaller ultimate strain
Koda et al.	2018	PP Geotextile	20°C to 80°C	-Tensile Strength -Elongation	Rise in temperature leads to smaller tensile strength and greater ultimate strain
Li et al.	2018	PP Samples	-30°C to 110°C	-Modulus of Elasticity	Modulus of elasticity is max at the lowest temperature and consistently decreases with increasing temperature

3.2. Experimental Program

This study aims to examine the effect of temperature on the tensile strength of a large aperture biaxial PP geogrid used to reinforce railway ballast and a biaxial PP geogrid composite designed to stabilize weak subgrades underlying railway ballast (see Figure 3.1).

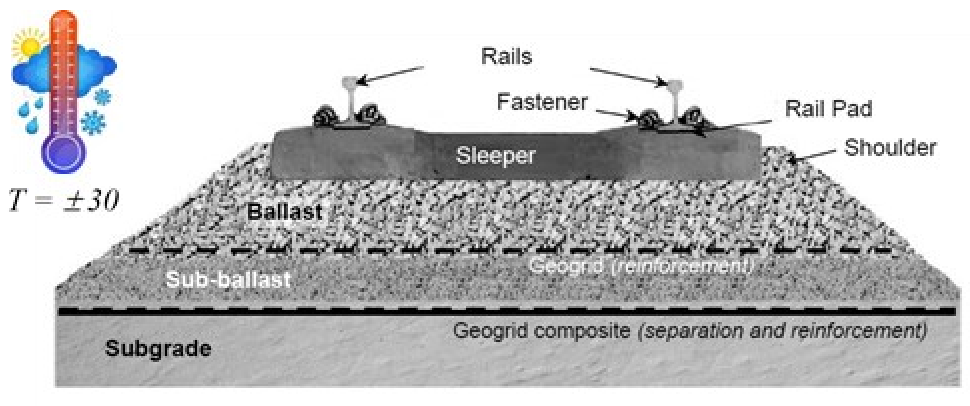

Figure 3.1: Example of a Typical Installation of Different Reinforcement Layers Within a Railway Embankment.

Given the respective location of the two geosynthetics within the embankment and the wide range of temperatures railway embankments built in seasonally cold regions are exposed to (Desbrousses & Meguid, 2021; H. Liu et al., 2012), tensile tests conducted at a single standard temperature may not yield results sufficient to characterize the tensile behavior of the geogrid and the geogrid composite over their full range of service temperatures. As such, a series of single-rib tensile tests are performed on single-rib samples of each material in accordance with Method A of ASTM D6637 (ASTM, 2015) over a given range of temperatures. Tensile tests are conducted on single-rib samples of the biaxial PP geogrid at temperatures ranging from -30°C to 40°C at 10°C increments while geogrid composite samples are exposed to testing temperatures ranging from -30°C to 20°C. A total of six samples of each material are tested at each investigated temperature. It is noteworthy that the range of testing temperatures for the geogrid composite is kept between -30°C and 20°C as the material is found to deform excessively at temperatures exceeding 20°C, leading to slippage between the sample and the test clamps.

3.2.1. Tested Materials

Two types of geosynthetics used in railroad construction are tested in this study. The first is a large aperture biaxial polypropylene geogrid and the second is a biaxial polypropylene geogrid heat-bonded to a non-woven polyester geotextile. The properties of each material as reported by the manufacturer are given in Table 3.2 and are labeled as Machine Direction/Cross-Machine Direction. The biaxial PP geogrid and the geogrid composite are shown in Figure 3.2 and Figure 3.3 respectively. Every sample used in this study was taken from the same roll of each material.

Table 3.2: Minimum Average Roll Value Properties for the Biaxial Geogrid and Biaxial Geogrid Composite (Titan Environmental Containment, 2020, 2021).

Property	Biaxial Geogrid	Biaxial Geogrid Composite
Material	Polypropylene	Geogrid: Polypropylene Geotextile: Polyester
Ultimate Tensile Strength	30/30 kN/m	30/30 kN/m
Tensile Strength at 2% Strain	11/11 kN/m	12/12 kN/m
Tensile Strength at 5% Strain	21/21 kN/m	22/22 kN/m
Ribs/m	17	25
Aperture Size	57/57 mm	38/38 mm
Rib Thickness	1.8/1.2 mm	2.3/1.5 mm

3.2.2. Testing Equipment

The single-rib tensile tests were performed using an MTS Insight electromechanical testing system equipped with a 5kN load cell. Wedge action grips with serrated jaws were used to clamp the single-rib samples during the experiments and were connected to the load frame by means of extension rods. To perform tensile tests at different temperatures, a temperature chamber was installed within the loading frame such that the grips and the tested samples could remain in a temperature-controlled environment throughout the tests. A schematic diagram and a photograph of the test setup are shown in Figure 3.4.

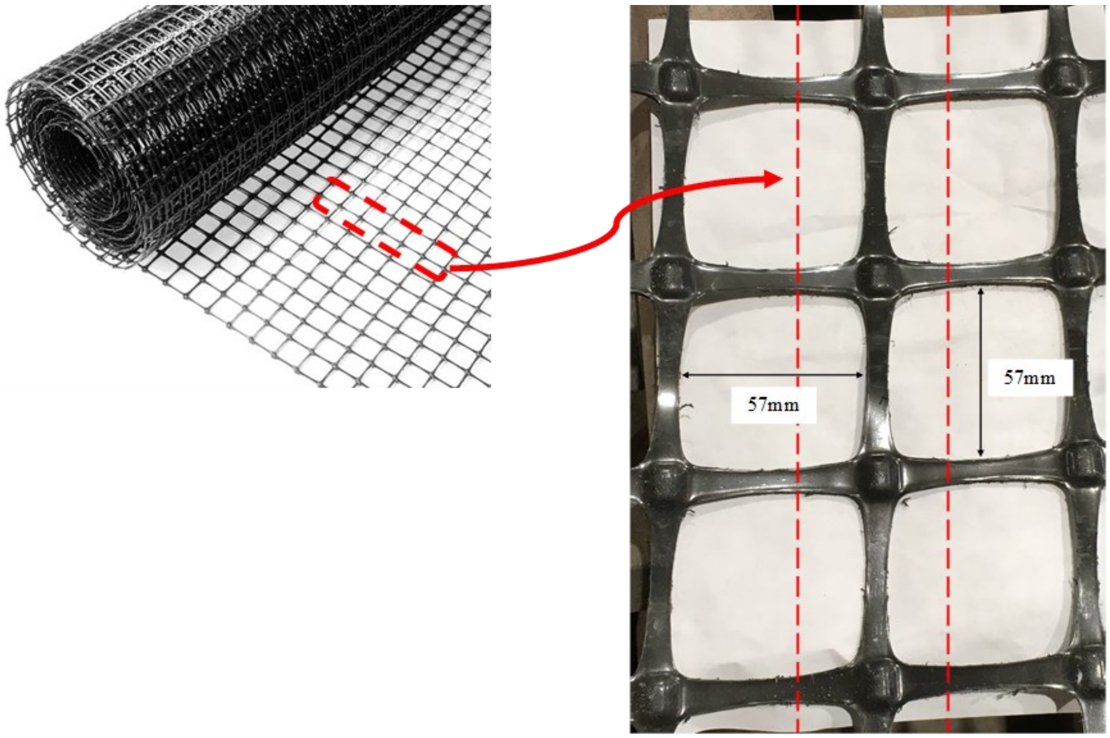

Figure 3.2: Large Aperture Biaxial PP Geogrid (Roll Figure Adapted from Civils and Utilities (2024)).

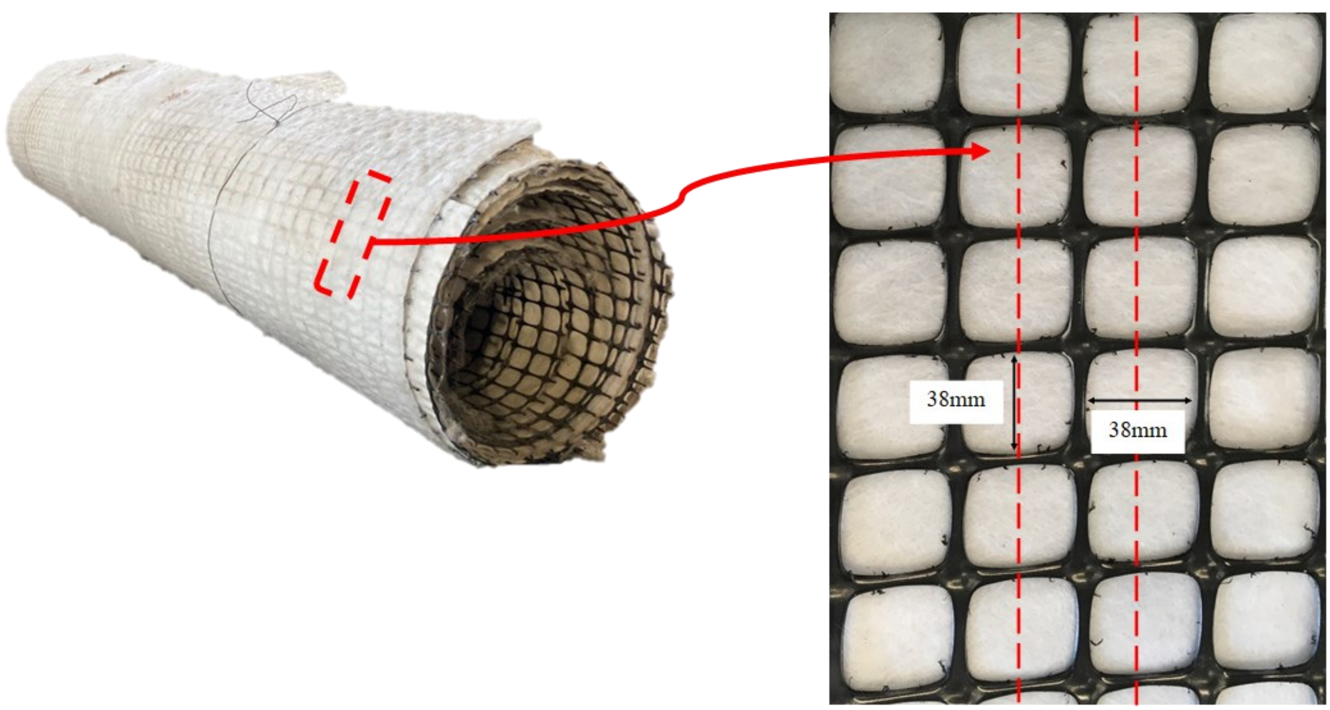

Figure 3.3: Biaxial Geogrid Composite.

The temperature chamber used in this study was a Thermcraft medium-range laboratory oven with heating and cooling capabilities equipped with a heating system, a circulating air blower, a built-in thermocouple, and a cryogenic cooling system connected to a tank of liquid nitrogen. The circulating air blower operated at all times to ensure homogeneous temperature distribution within the chamber. The laboratory oven's temperature was controlled by an analog temperature controller connected to the oven's built-in thermocouple.

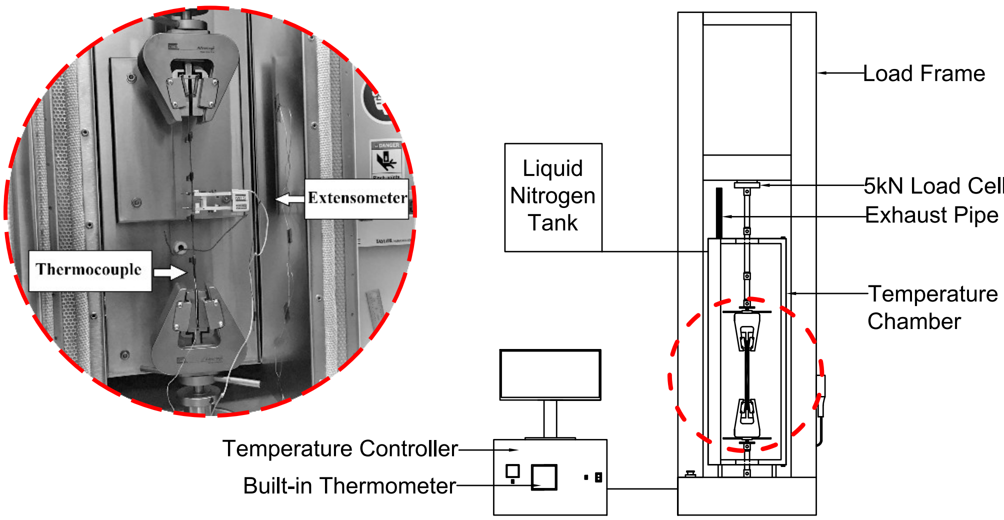

Figure 3.4: Diagram of the Test Set Up Used to Perform Tensile Tests in a Temperature-Controlled Environment.

An MTS 632.11F-90 clip-on extensometer with a gauge length of 25mm was used to monitor the sample elongation throughout the tests. It has a range of operating temperatures of -100°C to 150°C and the variations in the calibration factor are negligible over the range of temperatures used in this study. The testing system was operated using the MTS Elite software suite. A thermocouple was taped to the surface of each sample and to one of the chamber's walls to monitor the temperature difference between the sample's surface and the chamber in real-time. The time required for each sample to reach a stable initial temperature varied depending on the target temperature. Testing was initiated once the sample's surface temperature had reached the desired testing temperature.

3.3. Test Results and Discussion

3.3.1. Biaxial Geogrid

Figure 3.5 shows the average load-strain relationship measured for single-ribs of the biaxial PP geogrid tested at temperatures that range from -30°C to +40°C with 10°C increments.

The geogrid was first tested at a reference temperature of 20°C as prescribed by ASTM D6637 to establish a set of reference properties and compare them to the values reported by the manufacturer. A mean ultimate tensile strength of 33.54kN/m was obtained and compares well with the minimum average roll value (MARV) ultimate tensile strength of 30.00kN/m reported by the manufacturer as shown in Table 3.2.

The load-strain curves in Figure 3.5 indicate that the geogrid's tensile behavior is temperature-sensitive. At room temperature (+20ºC), the tested sample reached an ultimate load of 33.6 kN/m at about 14% strain. When the temperature increases above 20°C, the load-strain relationships retain a shape akin to that at the reference temperature but display markedly lower rupture strengths and greater ultimate strains. The initial slope of the load-strain curves at elevated temperatures is also noticeably lower than the one at the reference temperature, suggesting that the geogrid loses stiffness at higher temperatures. Conversely, the load-strain relationships at temperatures below 20°C occupy the upper part of the plot and exhibit increasingly greater rupture strengths and smaller ultimate strains as the temperature decreases. The initial slope of the load-strain curves at low temperatures is greater than that at 20°C, hinting at a stiffer geogrid response to tensile loads with decreasing temperature. The ultimate strength was found to incrementally increase to 37.6, 41, 43.7, and 44.7 kN/m when the temperature decreased from +20ºC to +10, 0, -10, and -20. It is noteworthy that the load-strain relationships at -20°C and -30°C are almost identical.

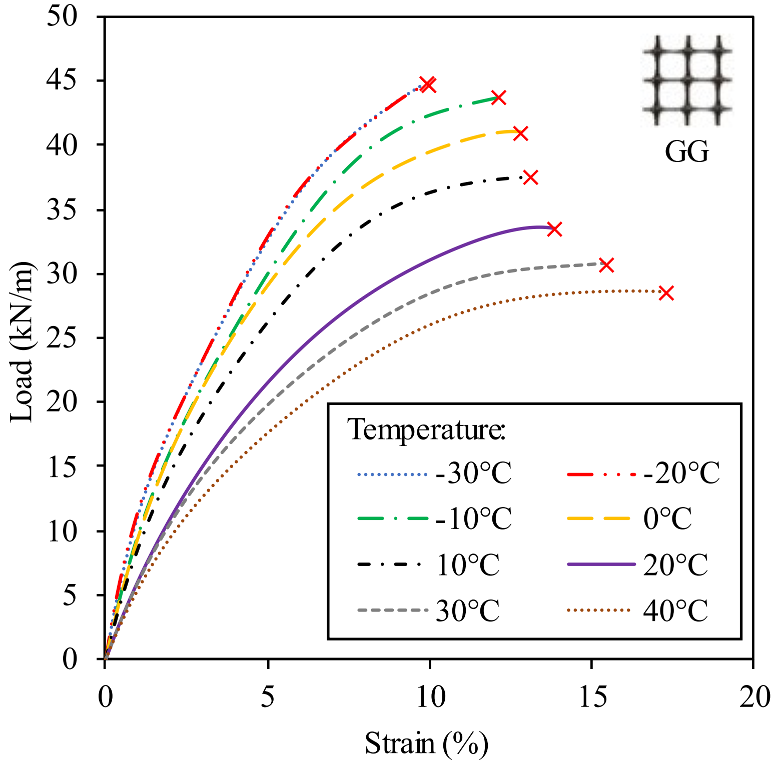

Figure 3.5: Average Load-Strain Relationship for the Geogrid at Temperatures Ranging from -30ºC to 40ºC.

3.3.1.1. Effect of Temperature on the Strength at Failure

The average rupture strengths at each investigated temperature are summarized in Table 3.3 and normalized against the rupture strength at 20°C in Figure 3.6. The results demonstrate that temperature has a notable effect on the rupture strength of the tested geogrid. Low temperatures generally translate into high rupture strengths compared to that at the reference temperature and geogrids exposed to high temperatures experience a strength loss. Over the range of tested temperature, the maximum increase in rupture strength occurred at -30°C where the reported tensile strength was about 33.7% greater than the reference value. Conversely, the maximum decrease in tensile strength happened at 40°C where the maximum tensile strength mobilized by the geogrid was about 14.8% smaller than the reference value. Figure 3.6 reveals that the rate of change in tensile strength is not constant throughout the range of tested temperatures. Indeed, the rupture strength seems to increase almost linearly from 40°C to -10°C, but the rate of change in strength decreases significantly between -10°C and -20°C and becomes almost non-existent between -20°C and -30°C with the rupture strength at -30°C being only 0.36% greater than the one at -20°C. This suggests that an important transition occurs in the geogrid's behavior around -10°C. This could be attributed to reaching polypropylene's glass transition temperature, which is usually between 0°C and -20°C (Henry & Durell, 2007). A similar phenomenon was observed by Henry and Durell (2007) who performed wide-width tensile tests on PP geotextiles at low temperatures and noticed a clear change in the geotextile's behavior between 0°C and -20°C.

Table 3.3: Temperature-Induced Changes in Rupture Strength (T_{ult})

Temperature (°C)	T_{ult} (kN/m)	% Change
-30	44.85	33.69
-20	44.69	33.21
-10	43.76	30.46
0	41.03	22.29
10	37.58	12.03
20	33.55	0.00
30	30.77	-8.29
40	28.60	-14.76

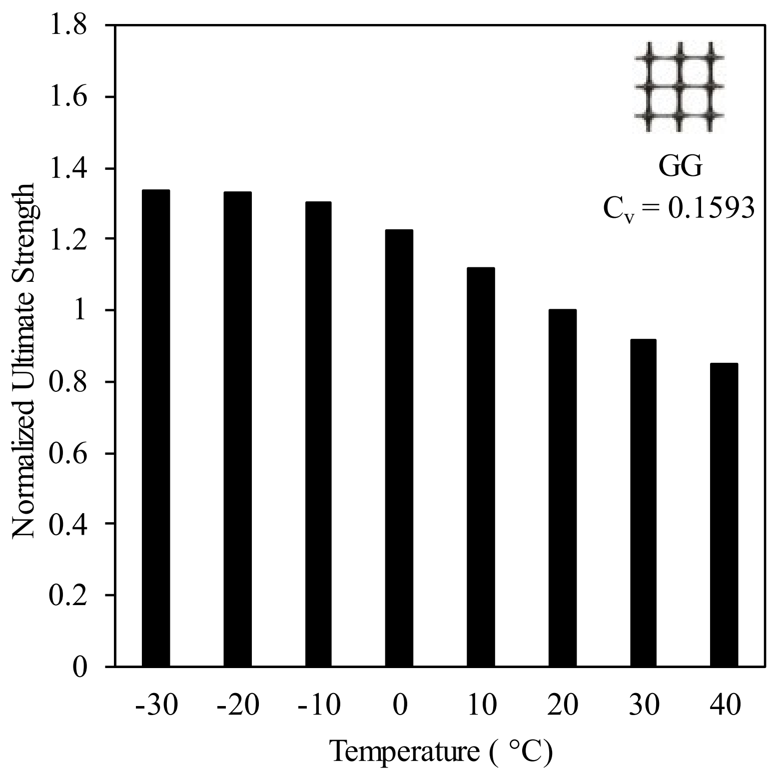

Figure 3.6: Effect of Temperature on the Normalized Rupture Strength of the Geogrid (T_{ult}/T_{ult20}).

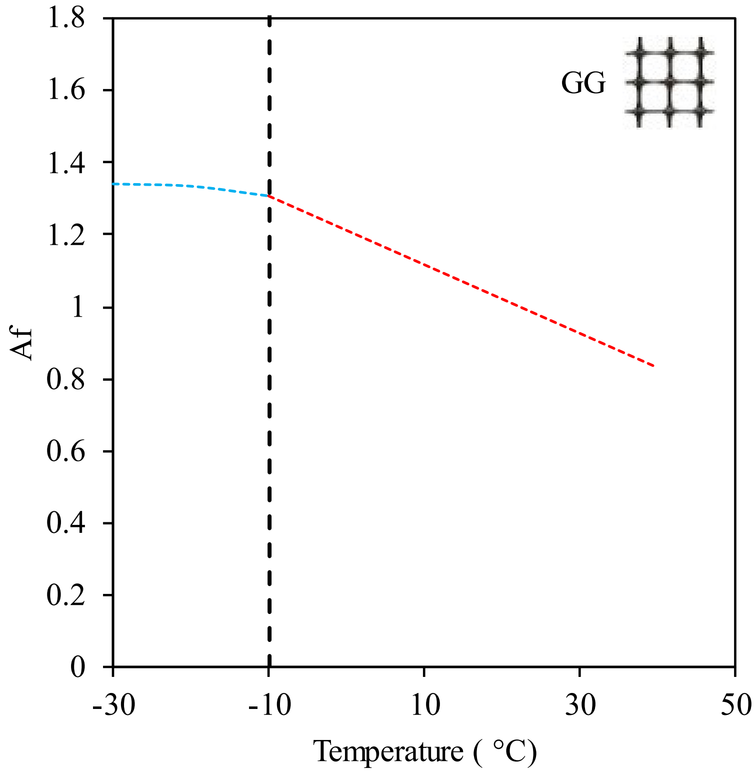

Figure 3.7: (a) Normalized Rupture Strength of the Geogrid vs. Temperature, (b) A^f from -10°C to 40°C, (c) A^f from -30°C to -10°C, (d) A^f over the Range of Investigated Temperatures.

Linear and polynomial regression were performed to characterize the relationship between the geogrid's normalized tensile strength and temperature in terms of the temperature effect parameter A^f as defined in Kongkitkul et al. (2012) and Chantachot et al. (Chantachot et al., 2018). A^f is the ratio between the rupture strength (T_{ult}) at a given temperature and the rupture strength ($T_{ult20^{\circ}C}$) at the reference temperature. The relationship between the normalized rupture strength and temperature from -10°C to 40°C was successfully described using a linear equation (Eq. 3.1). However, the relationship between -30°C and -10°C was more adequately represented using a quadratic expression (Eq. 3.2). The temperature effect parameter A^f is given by the following equations and summarized in Figure 3.7 in which the solid curves refer to the experimental data while the dashed ones represent Equations 3.1 and 3.2.

For -10°C < T < 40°C:

$$\frac{T_{ult}}{T_{ult20}} = A^f = -0.00942 \times T[°C] + 1.21092 \tag{3.1}$$

For -30°C < T < -10°C:

$$\frac{T_{ult}}{T_{ult20}} = A^f = -0.00011 \times T[°C]^2 - 0.00617 \times T[°C] + 1.25423 \tag{3.2}$$

To quantify the effect of temperature on the geogrid's stiffness, the tensile strength at 2% strain of the geogrid at each temperature is normalized against a reference value obtained at 20°C and is plotted in Figure 3.8. The tensile strength mobilized at 2% strain considerably increased at temperatures below 20°C and experienced a reduction at temperatures exceeding 20°C, demonstrating that for the same displacement, the geogrid developed greater tensile stress values at low temperatures, which emphasizes the increasingly brittle response of the material with decreasing temperature.

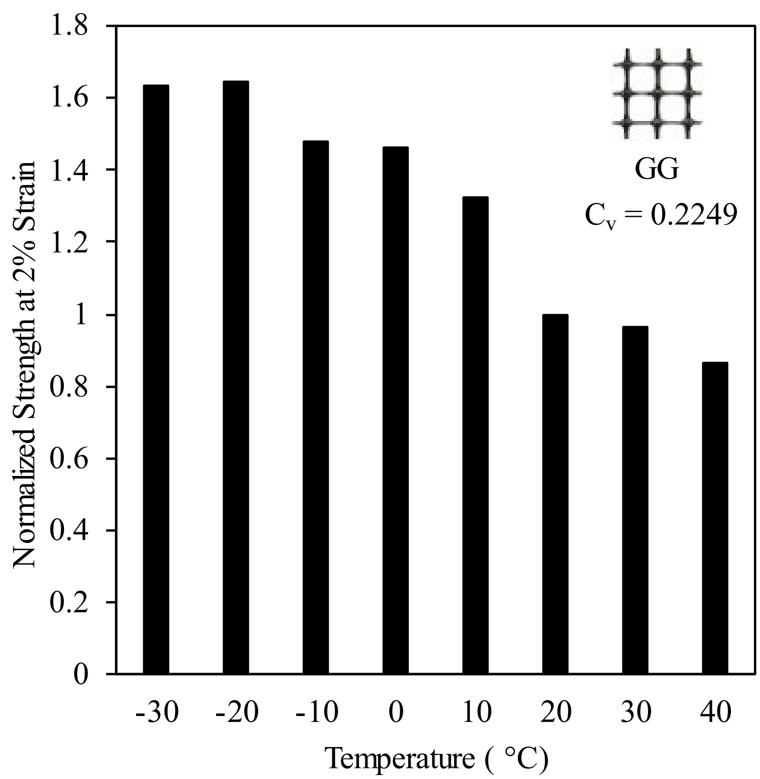

Figure 3.8: Effect of Temperature on the Normalized Tensile Strength of the Geogrid at 2% Strain ($T_{2\%}/T_{2\%20}$).

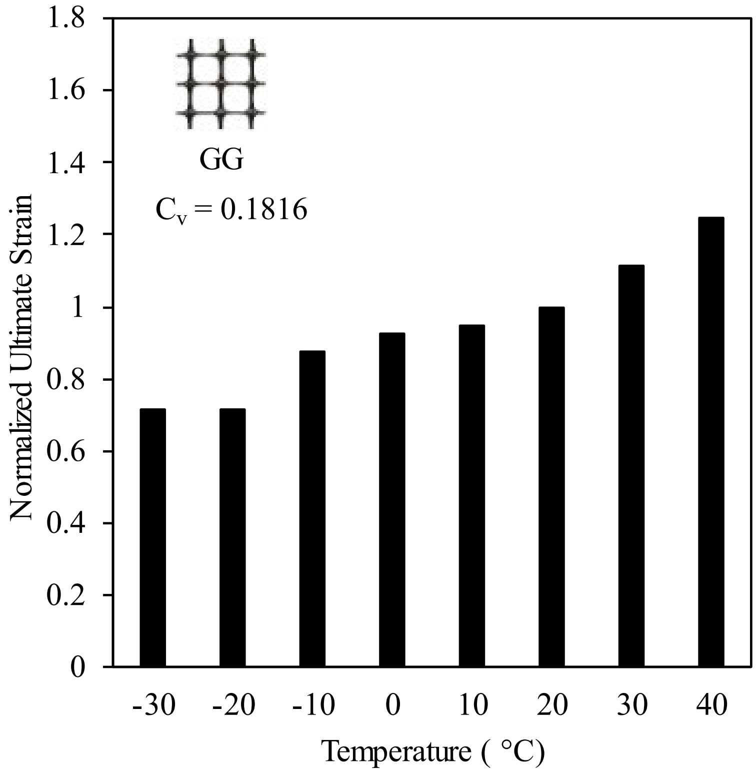

Figure 3.9: Variations in Normalized Ultimate Strain with Temperature for the Geogrid Material.

3.3.1.2. Effect of Temperature on the Ultimate Strain

Figure 3.9 shows the variations in normalized ultimate strain with changes in temperature. The normalized ultimate strain is obtained by dividing the ultimate strain at a given temperature by the strain at the reference temperature, i.e., 20°C. The ultimate strain follows a trend opposite to that of the rupture strength, with its value increasing with an increase in temperature. The minimum ultimate strain occurs at -30°C and the maximum is at 40°C, with the strain at 40°C being almost 75% greater than the one at -30°C. It is noteworthy that the ultimate strain at -30°C and -20°C are found to be very similar and that a substantial strain increase occurs at -10°C, further confirming the observation that considerable behavioral changes take place in the geogrid at that temperature. The rate of strain increase between -10°C and 10°C is relatively low but picks up considerably from 10°C to 40°C. The changes in ultimate strain along with the observed differences in tensile strength at each temperature demonstrate that the geogrid becomes more ductile at elevated temperatures and loses some of its load-carrying capacity and that the reverse occurs at lower temperatures, where the geogrid's behavior is characterized by a stiff and brittle response to tensile loads.

3.3.1.3. Failure Patterns

Testing the PP geogrid at temperatures ranging from -30°C to 40°C revealed that the material exhibits not only changing mechanical properties but also different modes of failure as temperatures vary. In every tensile test, failure happened as one of the junctions within the test gauge length broke. Figure 3.10a to 10f show the various failure modes of the geogrid's junctions at different temperatures. At 20°C (Figure 3.10d), the junction split in half after the single-rib sample had experienced plastic deformation. As the temperature was increased to 30°C and 40°C (Figure 3.10e and Figure 3.10f respectively), the geogrid became more ductile and elongated more before failing. This additional ductility meant that the material behaved in a more viscous manner, with the junctions exhibiting significant distortion at failure. However, no particular damage was observed in the ribs neighboring the failed junction. At lower temperatures, the geogrid became stiffer and gradually lost its ability to elongate when subjected to tensile loads. At 0°C, the single-rib samples deformed significantly less than at 20°C and exhibited a more brittle and sudden failure. The samples started to have what seemed to be fibers popping out of the sides of their ribs when the tensile load increased up to failure. A similar phenomenon was observed at -10°C and -30°C (Figure 3.10b and Figure 3.10a respectively), with the failure becoming even more brittle and sudden with more fibers crumbling from the sides of the single rib samples as the temperature was decreased.

The observed failure patterns along with the recorded load-displacement responses coincide with the transition from ductile to brittle behaviour that occurs when the temperature drops below polypropylene's glass transition temperature (T_g). Polypropylene being a semi-crystalline thermoplastic, its molecules have a very limited ability to reorient themselves at temperatures below its T_g, giving it a hard and brittle behaviour akin to that the geogrid displayed between -30°C to -10°C characterized by high tensile strength, low ultimate strain, and relatively negligible junction deformation along with fibre spalling at failure. On the other hand, once polypropylene is exposed to temperatures exceeding its T_g, its molecules have a greater ability to reorient themselves, giving it a more flexible and ductile behaviour similar to that of the geogrid between 0°C and 40°C.

(a) -30°C

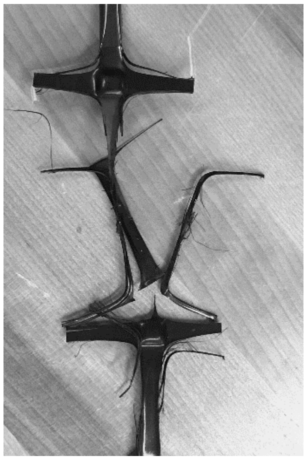

(b) -10°C

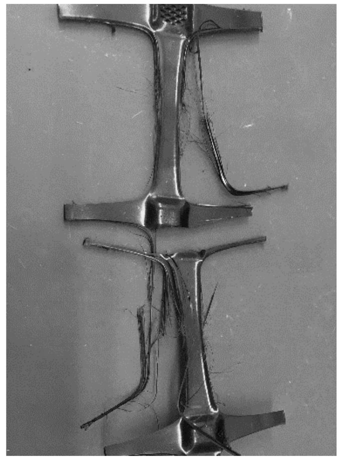

(c) 0°C

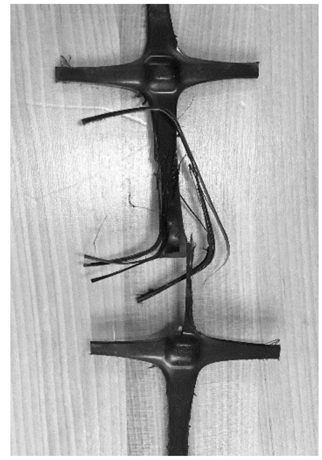

(d) 20°C

(e) 30°C

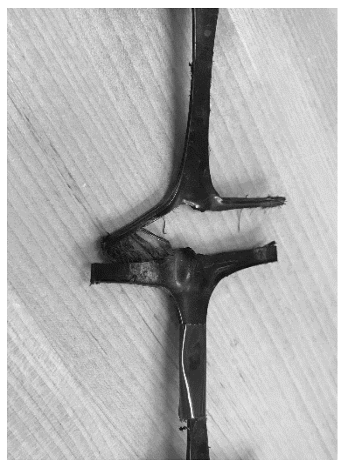

(f) 40°C

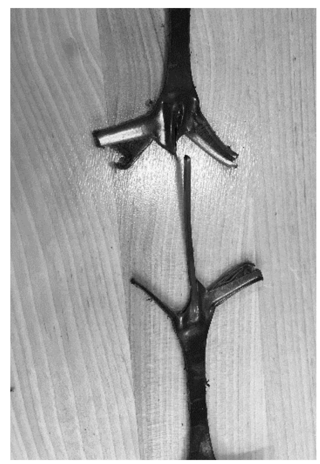

Figure 3.10: Failure Modes of the Geogrid at (a) -30°C, (b) -10°C, (c) 0°C, (d) 20°C, (e) 30°C, and (f) 40°C.

3.3.2. Biaxial PP Geogrid Composite

Figure 3.11 shows the average load-strain relationships obtained from tensile load tests performed on the geogrid composite at temperatures ranging from -30°C to 20°C. The average load-strain relationships indicate that the ultimate strain is sensitive to temperature variations, with samples tested at low temperatures exhibiting a significantly lower strain at failure than samples tested at higher temperatures. The rupture strength however seems to be relatively insensitive to temperature changes, with only minor strength variations being observed over the range of tested temperatures. The general shape of the load-strain curves shows that the geogrid composite develops a more brittle response to tensile loads as the surrounding temperature decreases. The single-rib tensile tests performed at the reference temperature recommended by ASTM D6637, i.e., 20°C, gave a mean ultimate tensile strength of 37.59kN/m which is in good agreement with the MARV ultimate tensile strength of 30.00kN/m reported by the manufacturer. The geogrid composite was tested in an effort to characterize its overall load-displacement response at various temperatures. The recorded variations of ultimate tensile strength and strain suggest its composite nature leads to a load-displacement response that is dissimilar to that of the PP geogrid alone.

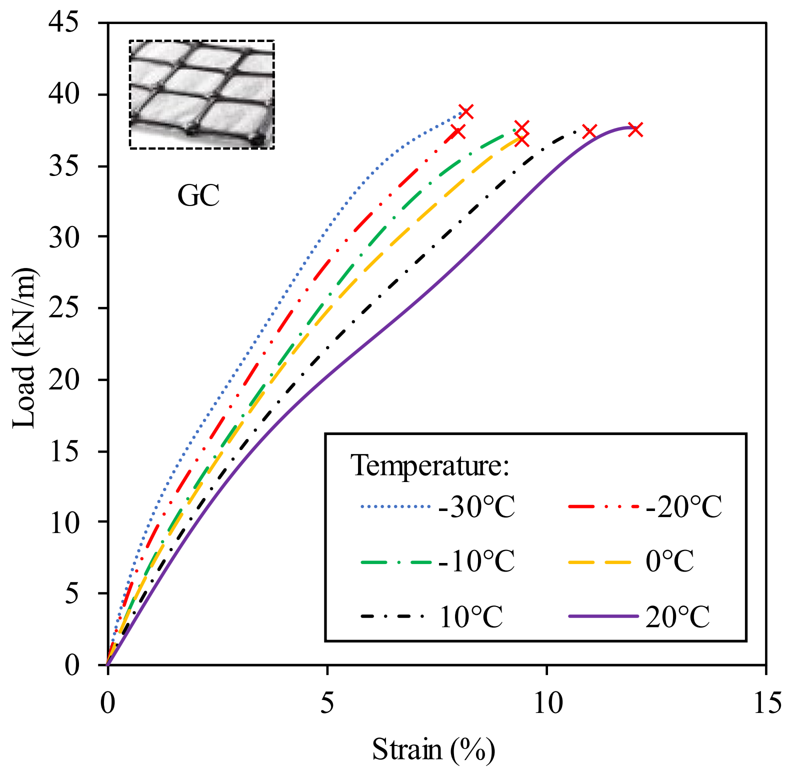

Figure 3.11: Average Load-Strain Relationships for the Geogrid Composite at Different Temperatures.

3.3.2.1. Effect of Temperature on the Tensile Strength at Failure

The changes in normalized rupture strength with temperature are depicted in Figure 3.12 and the rupture strength at each temperature along with the percentage change in strength with respect to the reference temperature are listed in Table 3.4. Contrary to the trend observed with the biaxial

PP geogrid, the investigated geogrid composite shows insignificant temperature-induced changes in rupture strength, with maximum difference occurring at -30°C where the rupture strength is found to be about 3.4% greater than at 20°C. The rupture strength remained relatively constant over the entire range of the investigated temperatures. This may be attributed to the geogrid being heat-bonded to a polyester geotextile.

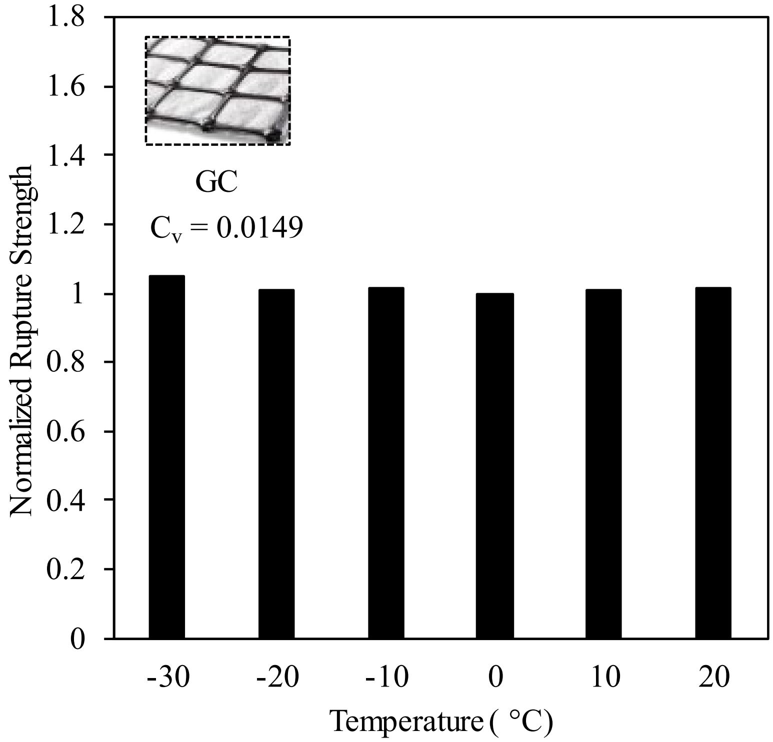

Figure 3.12: Normalized Rupture Strength of the Geogrid Composites at Each Tested Temperature.

Table 3.4: Rupture Strength (T_{ult}) at Temperatures Ranging from -30°C to 20°C.

Temperature (°C)	T_{ult} (kN)	% Change
-30	38.91	3.38
-20	37.52	-0.32
-10	37.70	0.16
0	37.11	-1.41
10	37.51	-0.36
20	37.64	0.00

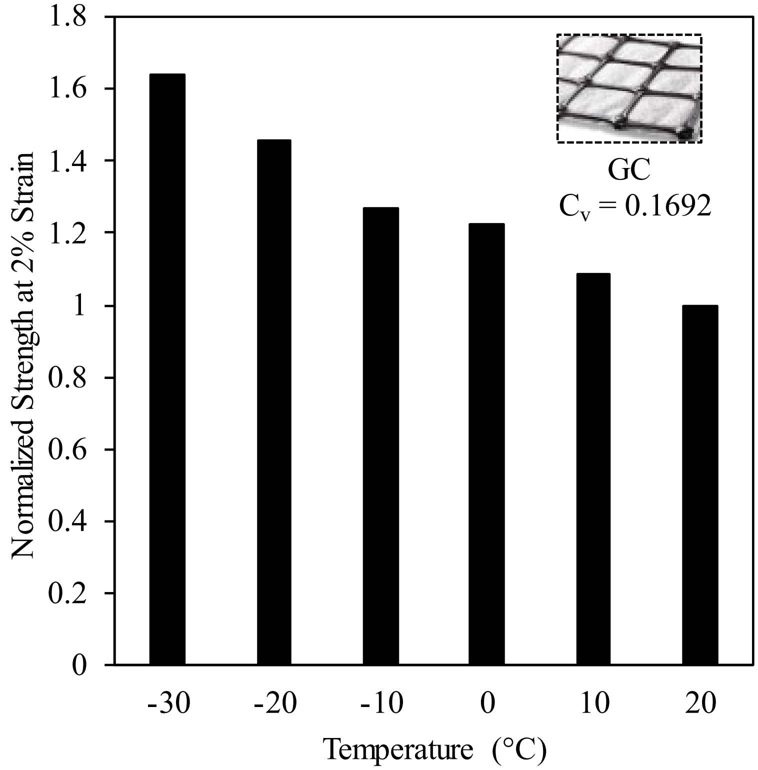

Figure 3.13: Normalized Tensile Strength of the Geogrid Composite at 2% Strain at Each Tested Temperature.

The bond between the geogrid and the geotextile allows for the tensile strength of both materials to be simultaneously mobilized. Jeon (2016) indicated that when a geogrid composite is subjected to tensile load, the geogrid tends to fail before the geotextile as observed in the geogrid composite used in this study. Given that the tensile strength of the large aperture biaxial geogrid described in the previous section exhibited a clear temperature-dependent response, it is expected that a load transfer mechanism develops through the bond between the geogrid and the non-woven polyester geotextile which prevents the geogrid from developing greater tensile strengths at low temperatures. However, the geogrid composite still fails at smaller strains at low temperatures due to the geogrid's increasingly brittle behavior.

Additionally, Figure 3.13 shows the variations in the composite's normalized tensile strength at 2% strain with temperature. The mobilized tensile strain continually increased as the temperature decreased, indicating an increasingly stiff response of the geogrid composite at cold temperatures.

3.3.2.2. *Effect of Temperature on the Ultimate Strain*

Figure 3.14 shows the sensitivity of the normalized strain to changes in temperature. While it was previously observed that the geogrid composite's rupture strength was relatively insensitive to temperature, the material exhibits markedly different elongation properties at different temperatures. The samples tested at 20°C had the highest strain at failure amongst all tested samples. Decreasing temperatures had the effect of reducing the material's ability to deform under increasing tensile load. The lowest strains were recorded at -20°C and -30°C. The smallest strain was 33.7% smaller than the one at 20°C.

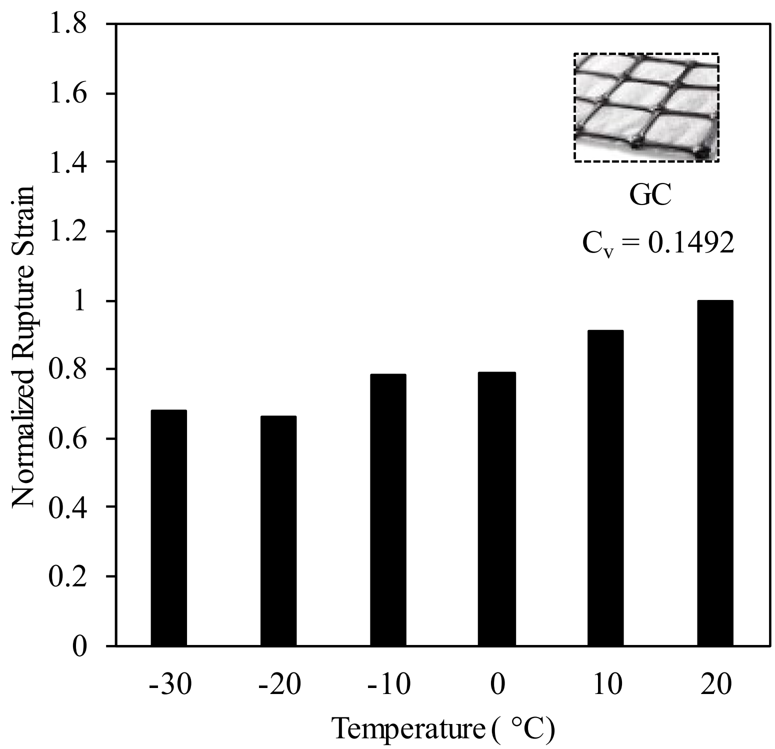

Figure 3.14: Normalized Ultimate Strain of the Geogrid Composite at Temperatures Ranging from -30°C to 20°C.

3.3.2.3. *Failure Modes*

Figure 3.15a through 3.15f shows the different junction failure patterns observed at every tested temperature for the geogrid composite. Every tensile test conducted during this experimental campaign ended with failure of a geogrid junction within the test gauge length. At the reference temperature (Figure 3.15f), the junction failed by splitting and little damage was observed in the rest of the sample. Similar behavior was also observed at 10°C (Figure 3.15e). However, at lower temperatures, as the material became more brittle, the junction failed more suddenly, and the rest of the sample appeared to sustain damage during testing by having fibers popping out of the ribs' sides. The fibrous appearance of the failed samples became increasingly clear with decreasing temperature as demonstrated by Figure 3.15a to d. The evolution of failure patterns with temperature echoes the findings of section 3.3.1.3 whereby the samples tested at low temperatures ranging from -30°C to -10°C exhibited considerably smaller ultimate strains (see Figure 3.12) and significant fiber spalling along their ribs compared to samples tested at 10°C and 20°C. This emphasizes the behavioral transition that takes place when the testing temperature exceeds the PP geogrid's T_g as the material becomes increasingly able to deform under loads.

3.4. Conclusions

The goal of this study was to investigate the effect of temperature on the mechanical properties of a large aperture biaxial PP geogrid and a biaxial PP geogrid composite used to reinforce and stabilize ballasted railway embankments in seasonally cold regions. The major conclusions drawn from the current study are as follows:

- The ultimate tensile strength and strain of the biaxial PP geogrid were found to be sensitive to temperature changes. A rise in temperature beyond the reference value (20°C) resulted in a reduction in tensile strength and a rise in ultimate strain, while smaller ultimate strains and greater tensile strengths were observed as the temperatures were lower below 20°C. The maximum ultimate strain was recorded at 40°C with a value of about 17% along with the minimum tensile strength which was about 15% smaller than the reference one. Conversely, the smallest ultimate strain (about 10%) occurred at -30°C along with the maximum tensile strength which was about 34% greater than the one measured at 20°C
- A pronounced transition in the biaxial PP geogrid's response to tensile loads was observed at temperatures below -10°C. The rupture strength increased almost linearly between -10°C and 40°C but varied insignificantly between -20°C and -30°C. The ultimate strain exhibited a similar trend, with only minor changes being reported between -20°C and -30°C. Such behavioral changes may be attributed to the testing temperature dipping below the glass transition temperature of polypropylene and the corresponding transition from ductile to brittle behavior

- The ultimate tensile strength of the geogrid composite was relatively insensitive to temperature changes while its ultimate strain decreased with the decrease in temperature. The maximum ultimate strain was recorded at 20°C with a value of 12.0% while the minimum ultimate strain occurred at -30°C with a value of 8.2%
- The responses of both the biaxial PP geogrid and biaxial PP geogrid composite to tensile loads were considerably affected by temperature variations, indicating that properties determined by standard tests performed at room temperature do not capture the full extent of a polymeric material's range of tensile behavior. Geogrids destined to be placed in earth structures constructed in regions known to have distinct and pronounced seasonal climatic changes should be tested over a range of temperatures representative of those they would be exposed to during their service life
- Additional tests are needed to quantify the individual effect of the geogrid and geotextile on the mechanical behavior of the geogrid composite

(a) -30°C

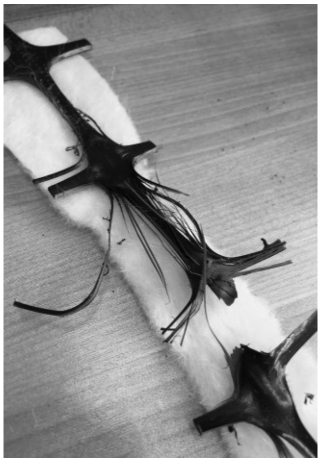

(b) -20°C

(c) -10°C

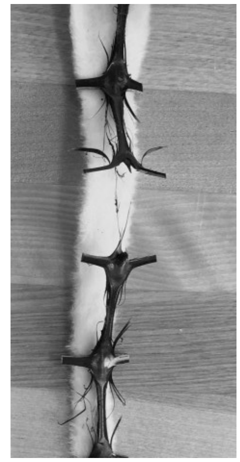

(d) 0°C

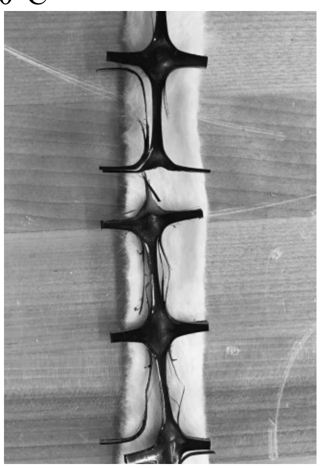

(e) 10°C

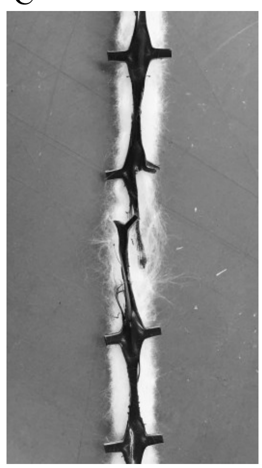

(f) 20°C

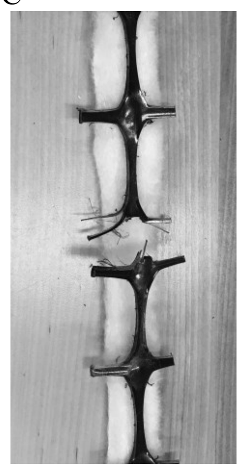

Figure 3.15: Failure Modes for the Geogrid Composite at (a) -30°C, (b) -20°C, (c) -10°C, (d) 0°C, (e) 10°C, and (f) 20°C.

Preface to Chapter 4

The reinforcing ability of a geogrid embedded in a ballast layer is influenced by several factors, including the size of its apertures, its placement depth, and the compressibility of the underlying subgrade. While existing experimental research has suggested that geogrids are particularly beneficial for ballast layers supported by weak subgrades, the nuanced interplay between the subgrade strength, geogrid placement depth, and their combined impact on tie settlement remains underexplored. This chapter presents large-scale ballast box tests performed to investigate the effects of subgrade strength and geogrid placement depth on the behavior of geogrid-reinforced ballast subjected to cyclic loading.

A total of thirteen experiments are conducted on both unreinforced and reinforced 300mm-thick ballast layers. Reinforced ballast layers feature a geogrid placement at a depth of either 150mm, 200mm, or 250mm beneath the tie. The geogrid used in the ballast box test is the same as the large-aperture biaxial geogrid that was tested in Chapter 3. Three different artificial subgrades are used in the experiments to simulate California Bearing Ratios (CBRs) of 25, 13, and 5. A model tie is placed on top of each ballast layer and subjected to 40,000 load cycles. During each experiment, a suite of sensors that includes a load cell and linear variable displacement transducers is used to monitor the load applied to the tie and its settlement response. The performance of unreinforced and geogrid-reinforced ballast layers across different subgrades is then analyzed and compared.

Chapter 4: Experimental Investigation of the Effects of Subgrade Strength and Geogrid Location on the Cyclic Response of Geogrid-Reinforced Ballast†

Abstract

This study aims to investigate how the subgrade strength and location of a geogrid within a ballast layer affect the geosynthetic's ability to stabilize railroad ballast. To do so, a total of thirteen large-scale cyclic load tests are performed on unreinforced tie-ballast assemblies and on tie-ballast assemblies reinforced with a geogrid placed at a depth of 150mm, 200mm, and 250mm to compare the mechanical behavior of unreinforced ballast with that of geogrid-reinforced ballast. The results suggest that the compressibility of the subgrade supporting a geogrid-reinforced tie-ballast assembly plays a crucial role in determining the geogrid's reinforcing efficiency. In cases where a geogrid-reinforced ballast layer is supported by a competent subgrade, the geogrid's performance appears insensitive to its placement depth. However, the geogrid's location wields an increasingly significant influence over its ability to stabilize railroad ballast as the underlying subgrade becomes softer, with geogrids placed in closer to the loaded area outperforming those located deeper in the ballast layer. The inclusion of geogrids in railroad ballast leads to reductions in the tie's permanent and resilient settlement which vary depending on the geogrid's location and subgrade compressibility. However, the tie-ballast assemblies' damping ratio appears to be insensitive to the presence of geogrids.

Keywords: Ballast; Subgrade; Geogrid; Tie Settlement; Cyclic Loading, Ballast Box Test

---

†A version of this manuscript was published in the *International Journal of Geosynthetics and Ground Engineering.*

4.1. Introduction

The stability of ballasted railroad tracks depends to a great degree on the performance of the ballasted track structure that supports train traffic (Fischer, 2022). A ballasted track structure may be divided into a superstructure that comprises the rail-tie assembly and an underlying multi-layer geotechnical system called the substructure which is composed of the ballast, subballast, and subgrade layers and provides a bearing platform on which the superstructure rests, thereby playing a crucial role in preserving the level of track alignment required to maintain safe track riding conditions.

The ballast layer is the uppermost stratum in the substructure and consists of an unbound assembly of hard, angular, crushed rocks. Its primary functions include supporting traffic-induced loads while safely transferring them down to the underlying soil layers, maintaining satisfactory horizontal and vertical track alignment, and providing ample void space to allow for fast drainage and accommodate the presence of fine materials in the layer (Desbrousses & Meguid, 2021, 2022; Indraratna, Salim, et al., 2011; Selig & Sluz, 1978; Selig & Waters, 1994). As it is located directly beneath the ties, the ballast layer is exposed to high dynamic loads that are responsible for the development of considerable non-recoverable deformations in the layer, making it one of the main sources of settlement in ballasted railway tracks.

The deformations that arise in the ballast layer are governed by the material's unbound and discrete nature, its generally low levels of lateral confinement, and the train loads it is subjected to. At the onset of cyclic loading in newly laid tracks, the loosely packed ballast aggregate coupled with the absence of appreciable lateral confinement foster conditions that are conducive to a rapid buildup of non-recoverable vertical and lateral deformations in the ballast layer as individual ballast particles move and slide past another to rearrange into a more stable and denser packing in response to the repeated application of train loads (Bruzek et al., 2016; Indraratna et al., 2005; Lackenby et al., 2007; Malisetty et al., 2022; Q. Sun et al., 2014, 2019; Sussmann et al., 2012; Thakur et al., 2013). The densification of the ballast layer leads to the formation of a strong interlock between the ballast particles that are now tightly wedged against each other, resulting in an increase in the layer's stiffness and a reduction in the rate at which settlement accumulates under further cyclic loading as the granular assembly behaves almost elastically during loading-unloading cycles.

Over time and due to sustained exposure to cyclic train loading, the ballast aggregate degrades and individual particles break down into finer ones. This generation of smaller particles contributes to the progressive filling of the void space in the layer in a process known as fouling. Fouled ballast possesses a lower shear strength and poorer drainage capabilities compared to fresh ballast and as such is prone to accumulating settlement at an increasing rate when subjected to cyclic train loading, potentially leading to even more subsidence, particularly in cases where the subgrade is made of fine-grained soils with low shear strength and high plasticity that are vulnerable to developing large deformations under cyclic loading (Kashani et al., 2017, 2018; D. Li et al., 2015).

The development of excessive deformations in the ballast layer has an adverse effect on the track alignment and leads to a degradation in track safety and riding quality. This usually prompts either the imposition of speed limits on affected track sections or the scheduling of costly periodic ballast maintenance operations such as tamping or stone-blowing to correct track alignment issues (Anderson & Key, 2000; Chrismer & Davis, 2000; Touqan et al., 2020). Tamping is the most common ballast maintenance operation and consists of lifting the ties while inserting tamping tines into the ballast layer to simultaneously squeeze and vibrate the aggregate under the ties to restore an acceptable track level. Although this method is initially effective at correcting track geometry issues, its benefits are offset by the fact that it loosens, disturbs, and damages the ballast material which typically experiences a period of rapid settlement accumulation following the resumption of train traffic (D'Angelo et al., 2018; Sol-Sánchez et al., 2016). On the other hand, stone-blowing is an alternative to tamping whereby the ties are lifted while a set volume of gravel is pneumatically injected under the ties. Since stone-blowing does not disturb the underlying ballast bed, only minor deformations occur once train traffic resumes on affected track sections (Anderson & Key, 2000; D'Angelo et al., 2018). Given the elevated cost of maintenance operations, alternatives, such as the inclusion of geogrid reinforcement in the ballast layer, are being used to improve the in-service performance of railroad ballast and curtail its operating costs (Fischer, 2022; Luo, Zhao, Cai, et al., 2023a; Marx et al., 2023; Prasad & Hussaini, 2022).

A geogrid is used to reinforce ballast thanks to its ability to develop a strong mechanical interlock with the surrounding particulate matter, forming a semi-rigid mat that laterally confines the granular assembly to minimize its deformations (Indraratna, Ngo, et al., 2011). The performance of a geogrid embedded in railroad ballast is a function of its aperture size, its placement depth, and the compressibility of the underlying subgrade soil. The size of a geogrid's apertures (A) in comparison with that of the surrounding soil particles, generally represented by the mean particle diameter (D_{50}), must be sufficiently large to allow the ballast particles to strike through its plane for a strong interlock to form. Experiments conducted on geogrid-reinforced ballast have indicated that an optimal interlock is achieved with an A/D_{50} ratio of 0.95-1.20 while A/D_{50} ratios in excess of 1.20 yield adequate reinforcement (Hussaini et al., 2015, 2016; Hussaini & Sweta, 2020; Indraratna et al., 2012, 2013; Sweta & Hussaini, 2019, 2020, 2022).

Similarly, large-scale cyclic loading experiments performed on geogrid-reinforced ballast samples have demonstrated that a geogrid is more effective at stabilizing railroad ballast when placed closer to the bottom of the ties (Bathurst et al., 1986; Bathurst & Raymond, 1987; Brown, Kwan, et al., 2007). However, a geogrid must also be placed sufficiently deep within the ballast bed so as not to interfere with potential ballast operations that generally affect the layer's upper 100-150mm. This has led to the recommendation that geogrids should be placed at least 150mm below the base of the ties. Additionally, experimental and numerical modeling works on geogrid-reinforced ballast have highlighted that the strength of the subgrade supporting a reinforced ballasted substructure wields a considerable influence over the type of benefit derived from reinforcing ballast with geogrids, with geogrids being reported to be more effective at reducing track settlement in tracks supported by weak subgrades (Bathurst et al., 1986; Bathurst & Raymond, 1987; Yu et al., 2019). However, most experimental studies conducted to date have been limited to comparing the behavior of geogrid-reinforced ballast samples supported by a stiff subgrade to a soft subgrade without capturing how different subgrade strengths affect the performance of geogrid-reinforced ballast.

As such, this paper focuses on studying the relationship between the performance of a geogrid embedded in a ballast layer, its placement depth, and the strength of the underlying subgrade. To do so, a series of large-scale ballast box tests is performed on unreinforced and geogrid-reinforced tie-ballast assemblies resting on different subgrades to compare the behavior of railroad ballast under various conditions and capture its sensitivity to the presence of geogrid reinforcement. The parameters monitored during the experiments include the tie's permanent settlement, its resilient deflection, the tie support stiffness, and the ballast's damping ratio.

4.2. Methodology

4.2.1. Materials

4.2.1.1. Ballast

Crushed granite aggregate quarried in St-Hippolyte, Quebec (Canada) screened to conform with an AREMA No. 4 grading (see Figure 4.1) typical of mainline ballast material is used in the experiments presented in this paper. The aggregate's physical properties are summarized in Table 4.1 and conform with the relevant recommended limiting values for ballast material outlined in AREMA's *Manual for Railway Engineering* (AREMA, 2010). In every experiment, a new 300mm-thick layer of railroad ballast is constructed in the ballast box in three 100mm-thick lifts compacted to a target unit weight of 15.7kN/m^3 using an Exen EKCA handheld vibrating plate compactor. The compactor applies a 30.1kgf over a 120×150mm area at a frequency of 133Hz. The compactor is passed over six 150mm-wide strips running in the direction of the 1,290mm-long side of the box for 30 seconds on each strip, resulting in a total compaction time of 3 minutes per lift. A ballast thickness of 300mm is chosen to reflect the typical depth of ballast layers in standard gage tracks in North America (AREMA, 2010).

4.2.1.2. Geogrid

In the reinforced ballast box tests, ballast layers are reinforced with a biaxial polypropylene geogrid designed to stabilize ballast aggregate in railroad applications. The geogrid is manufactured such that it possesses thick integral nodes, thick ribs, and large square apertures to allow for the development of a strong mechanical interlock with the surrounding coarse ballast aggregate. The geogrid's physical and mechanical properties are summarized in Table 4.2 (Desbrousses et al., 2021; Titan Environmental Containment, 2020). A new geogrid sheet is used for every reinforced ballast box test. To prevent the geogrid from warping around the edges of the box, every sheet is trimmed to a size of 700×1,030mm.

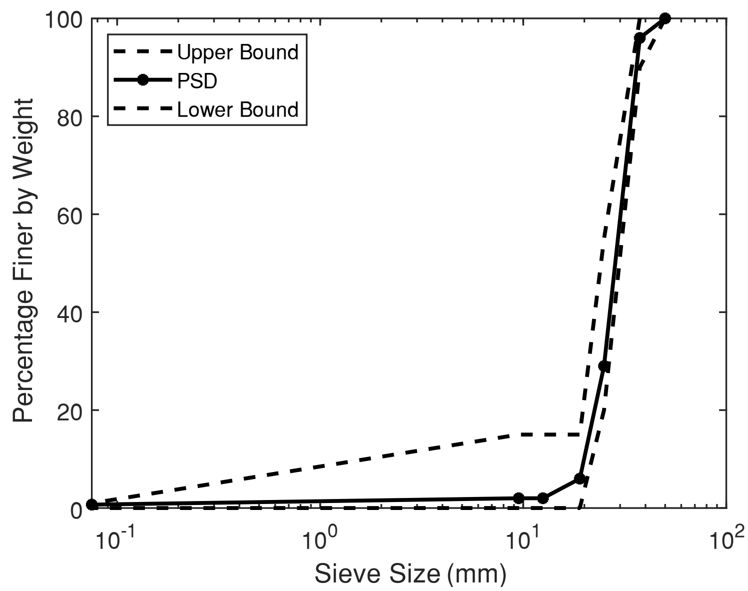

Figure 4.1: Particle Size Distribution of the Granite Aggregate Used in the Ballast Box Tests.

Table 4.1: Properties of the Crushed Granite Aggregate.

Properties	Value
Flat and Elongated Particles (ASTM D4791)	0%
Flat Particles (ASTM D4791)	3%
Los Angeles Abrasion (ASTM C535)	32.8%
Dry Bulk Specific Gravity (ASTM C127)	2.741
Loose Bulk Density (ASTM C29)	1,400 kg/m^3
Compacted Bulk Density (ASTM C29)	1,600 kg/m^3

4.2.1.3. Artificial Subgrades

To simulate the presence of different subgrades below the ballast layer and capture their effect on the tie's settlement, the box's bottom steel plate is covered with one of three assortments of elastomer pads each with its own compressibility. The compressibility of each rubber mat combination is expressed as an equivalent soil strength by performing a California Bearing Ratio (*CBR*) test on the mats following the procedure outlined in ASTM D1883 (ASTM, 2005). The three artificial subgrades used in this study have *CBR* readings of 25, 13, and 5 and are herein referred to as the competent, fair, and soft subgrades respectively while the condition where the box's bottom steel plate alone is used to provide a bearing platform to the overlying ballast layer is referred to as the stiff subgrade. The properties of each artificial subgrade are summarized in

Table 4.3. It is noteworthy that the nomenclature used to describe subgrade soils (i.e., stiff, competent, fair, and soft) is chosen so as to conveniently convey the difference in compressibility between the four artificial subgrades considered in this experimental campaign.

Table 4.2: Physical and Mechanical Properties of the Biaxial Geogrid (Desbrousses et al., 2021; Titan Environmental Containment, 2020).

Aperture Size (mm)	Ribs/m	Rib Thickness (mm)	Tensile Strength (kN/m)		
			Ultimate	5% Strain	2% Strain
57/57	17	1.8/1.2	30/30	21/21	11/11

Note: Properties are reported as Minimum Average Roll Values (MARV) in the Machine Direction / Cross-Machine Direction.

Table 4.3: Rubber Mat Properties.

Subgrade	Stiff	Competent	Fair	Soft
CBR	∞	25	13	5
Material	Steel Plate	12.7mm-thick 60A Neoprene Rubber Mat	12.7mm-thick 40A Neoprene Rubber Mat	12.7mm-thick 40A Neoprene Rubber Mat + 25.4mm-thick 60A Neoprene Rubber Mat

4.2.2. Experimental Setup

A series of ballast box tests is conducted by constructing 300mm-thick ballast layers in a ballast box with plan dimensions of 915×1,290mm and a depth of 600mm (see Figure 4.2). The ballast box consists of an outer rigid frame composed of welded hollow steel sections that create a central enclosure lined on the edges with 38mm-thick plywood sheets covered with smooth sheet metal fixed to the outer frame and a steel plate at the bottom. Upon placing and compacting the ballast sample in the ballast box, a model tie consisting of a steel I-beam with plan dimensions of 301×203mm and a hollow steel section bolted to its top is placed above the 300mm-deep ballast bed to transmit the desired cyclic compressive loads to the granular assembly.

The ballast box is located below a 1,780kN-capacity load frame that supports a cyclic loading apparatus comprising an 85kN pneumatic actuator, a load cell, an electronic pressure regulator, a PID controller, and a function generator. The cyclic loading machine is used to deliver cyclic loading to the model tie following a sine wave with an amplitude of 10.5kN and load extrema of 3.5kN and 24.5kN at a frequency of 0.8Hz for a total of 40,000 load cycles during a given test. The applied loads give rise to minimum and maximum stresses of 57.3kPa and 400kPa respectively at the tie-ballast interface.

The instrumentation used to monitor the tie's behavior as it is subjected to the applied cyclic loads involves a 50kN load cell, four linear variable displacement transducers (LVDTs), and a data acquisition system that logs the sensors' data at a frequency of 100Hz. The four LVDTs are placed at each corner of the tie's top surface such that its average settlement may be computed at each load cycle.

A total of thirteen ballast box tests are performed during the experimental campaign presented in this paper. Four experiments consist of testing unreinforced tie-ballast assemblies resting on the stiff, competent, fair, and soft subgrades to establish a reference behavior against which the performance of geogrid-reinforced ballast samples is compared. For each artificial subgrade, three geogrid-reinforced ballast box tests are conducted in which a single geogrid layer is embedded in the ballast bed at depths of 150mm, 200mm, and 250mm below the tie's base. A summary of the experiments discussed in this study is provided in Table 4.4.

Table 4.4: Test Summary.

Test No.	*CBR*	Condition	Reinforcement Depth
1	∞ (Steel Plate)	Unreinforced	N/A
2	25	Unreinforced	N/A
3		Reinforced	150mm
4			200mm
5			250mm
6	13	Unreinforced	N/A
7		Reinforced	150mm
8			200mm
9			250mm
10	5	Unreinforced	N/A
11		Reinforced	150mm
12			200mm
13			250mm

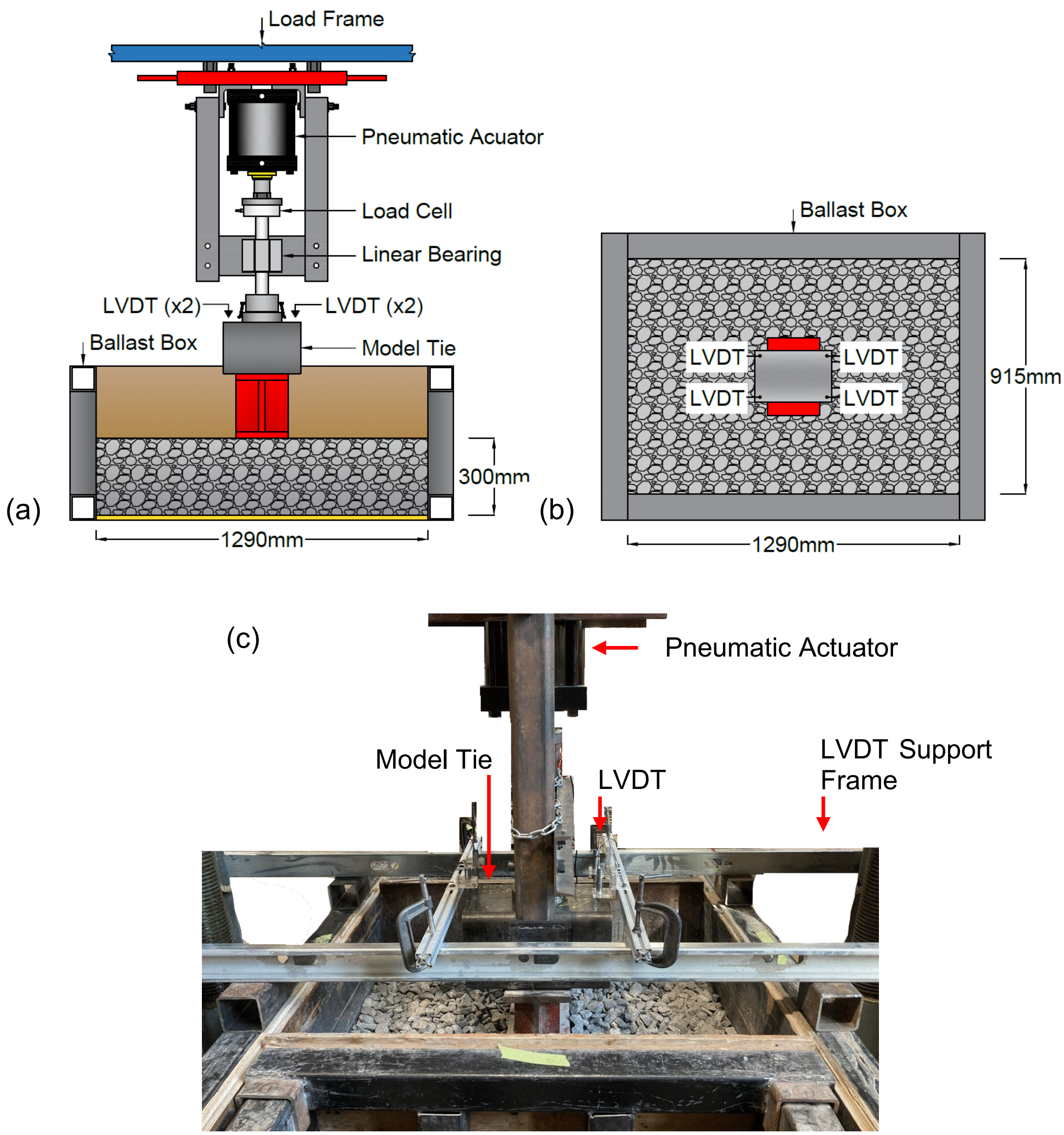

Figure 4.2: (a) Pneumatic Cyclic Loading Apparatus and its Ballast Box, (b) Plan View of the Ballast Box, (c) Laboratory Set Up.

4.3. Results

4.3.1. Permanent Settlement

The tie settlement curves recorded during the unreinforced ballast box tests performed over the stiff, competent, fair, and soft subgrades are shown in Figure 4.3a. The experimental data for each support condition is also represented by a power model (Equation 4.1) akin to that put forward by Indraratna et al. (Indraratna et al., 2000, 2006) in which the tie's settlement (S) is expressed as a function of the number of load cycles (N), the permanent tie deflection after the first load cycle (a), and a coefficient (b) determined from non-linear regression analysis:

$$S = a \times N^b \tag{4.1}$$

The results presented in Figure 4.3a indicate that the subgrade's strength wields a considerable influence on the development of permanent ballast deformations and consequently of the tie's settlement, with the presence of weaker subgrades below the ballast translating into the tie experiencing greater subsidence. The settlement response of each ballast sample is characterized by a rapid accumulation of permanent vertical deformation at the onset of cyclic loading caused by ballast particles sliding and moving past one another as the initially loosely packed granular assembly rearranges into a more stable packing. The densification of the ballast layer gives rise to the formation of a tight interlock between neighboring ballast particles that are now wedged against each other. The interlock leads to an increase in the ballast layer's stiffness and correspondingly contributes to reducing the rate at which settlement builds up as the granular layer behaves in an almost elastic fashion during individual loading-unloading cycles. This trend is clearly observable in the ballast sample supported by a stiff subgrade ($CBR = \infty$) in which the tie experiences the majority of its settlement within the first 10,000 load cycles while only marginal increases in settlement occur in response to further cyclic loading. However, the presence of softer subgrades below the ballast impacts the rate at which the tie settlement develops, with the tie resting on ballast layers supported by the competent, fair, and soft subgrades experiencing 75.1%, 71.9%, and 68.7% of their respective total subsidence after 10,000 load cycles compared to 85.5% for the tie-ballast assembly supported by the stiff subgrade. The total tie settlement recorded in each sample also reflects the variations in subgrade compressibility, with the tie resting on the stiff, competent, fair, and soft subgrades experiencing a total settlement of 4.62mm, 12.10mm, 24.46mm, and 35.02mm respectively at the end of the 40,000 load cycles.

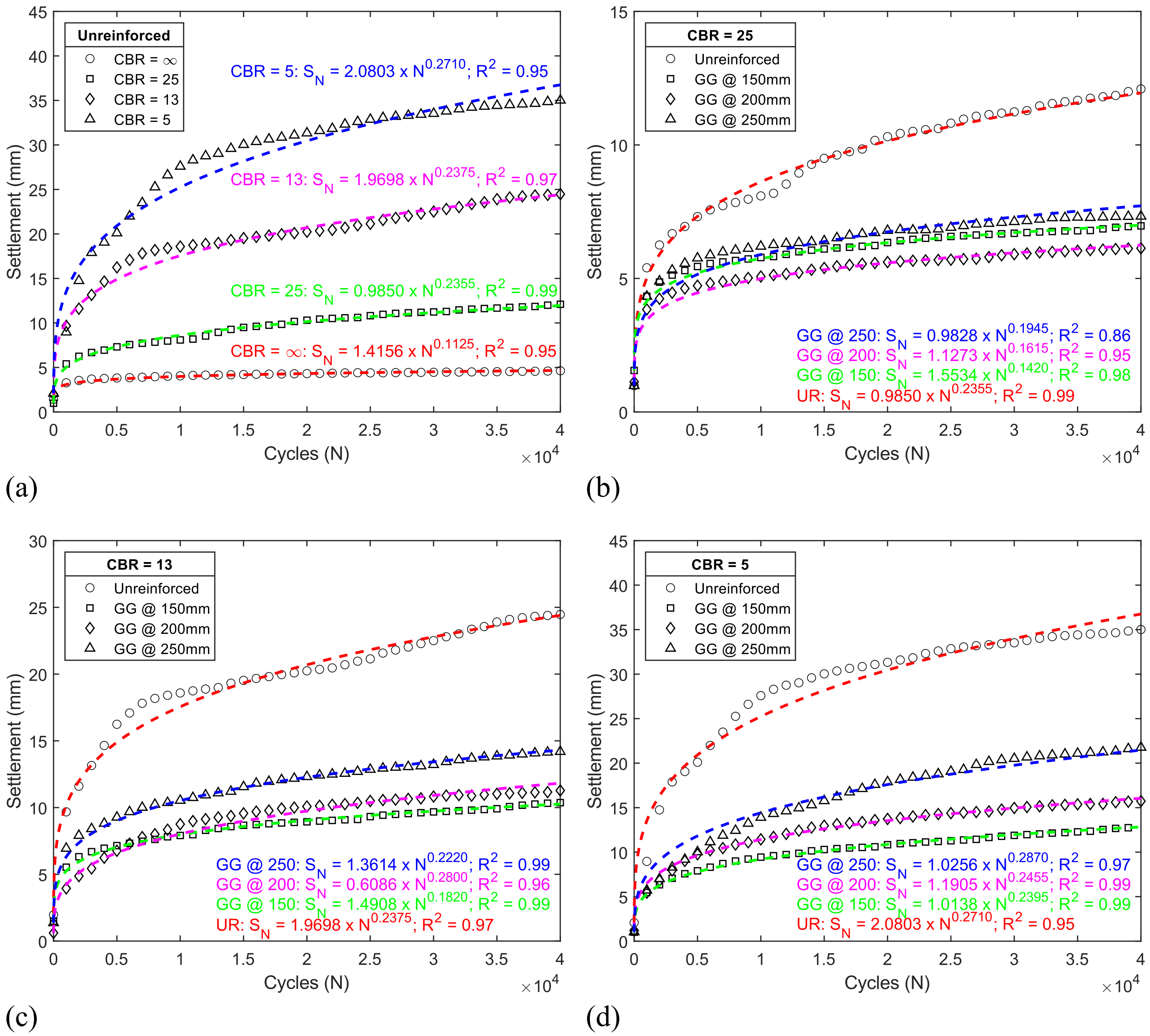

Figure 4.3: Tie Settlement Curves Recorded in (a) Unreinforced Ballast Samples and Geogrid-Reinforced Ballast Layers Supported by the (b) Competent, (c) Fair, and (d) Soft Subgrades.

Figure 4.3b, c, and d display the settlement curves of ties supported by geogrid-reinforced ballast layers resting on the competent, fair, and soft subgrades respectively. For ballast layers supported by the competent subgrade (*CBR* = 25), the tie settlement curves indicate that although the inclusion of a geogrid in the granular assembly successfully reduces the magnitude of the tie's settlement, its performance appears to be insensitive to its placement depth. The tie exhibits a similar response to cyclic loading in the three reinforced tests and experiences similar settlements regardless of the geogrid's location in the ballast bed, with the marginal discrepancies that occur between the reinforced settlement curves shown in Figure 4.3b being considered to be within the range of test repeatability.

The results observed in reinforced ballast layers supported by the fair subgrade (*CBR* = 13) contrast those obtained with the competent subgrade as the geogrid's relative insensitivity to its placement depth appears to vanish with the presence of a softer subgrade. Figure 4.3c shows the variations in tie settlement observed in geogrid-reinforced ballast beds supported by the fair subgrade. The results suggest that the ability of a geogrid to minimize tie settlement becomes sensitive to its placement depth in the ballast layer, with the geogrid placed 150mm below the tie exhibiting a superior ability to reduce the tie's subsidence compared to the geogrids located 200mm and 250mm below the tie. It is noteworthy that the geogrids placed at depths of 150mm and 200mm are markedly more efficient at minimizing ballast deformation than the geogrid placed deeper in the ballast layer.

The trends that materialized in geogrid-reinforced ballast beds supported by the fair subgrade are exacerbated by the presence of an even softer subgrade (i.e., soft subgrade with a *CBR* of 5) as shown in Figure 4.3d. The tie settlement curves recorded in geogrid-reinforced ballast samples are characterized by pronounced differences that are attributed to the geogrid's location within the ballast bed. The geogrid placed at the shallowest depth is the most effective at reducing the tie's settlement, followed by the geogrids placed at depths of 200mm and 250mm respectively. The data shown in Figure 4.3d highlights that as the subgrade becomes weaker, the geogrid's location within the ballast layer becomes a key factor that determines its ability to stabilize railroad ballast as the settlement reduction achieved by a geogrid decreases as it is located farther away from the loaded area, i.e., the tie's base.

To put the observations drawn from the results displayed in Figure 4.3a to d into perspective, the settlement reduction achieved by each geogrid is represented by the settlement reduction factor (R_t) (Shin et al., 2002) computed using Equation 4.2 and plotted in Figure 4.4 and 4.5a to d.

$$R_t = 100 \times \frac{S_{UR} - S_{GG}}{S_{UR}} \tag{4.2}$$

Where S_{UR} is the tie settlement recorded in the unreinforced ballast sample for a given subgrade and S_{GG} is the tie settlement observed in a given geogrid-reinforced ballast layer supported by the same subgrade.

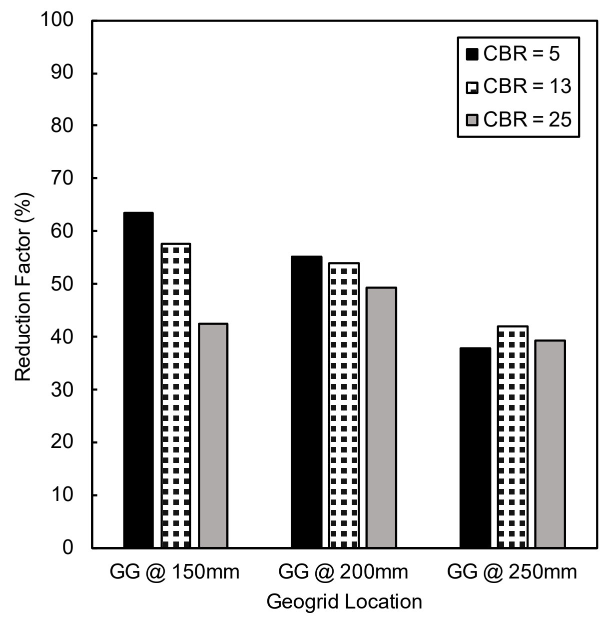

Figure 4.4: Final Tie Settlement Reduction Factors in Geogrid-Reinforced Ballast Layers.

The data plotted in Figure 4.4 reveals that the subgrade strength wields a considerable influence on the relationship between a geogrid's placement depth and its ability to minimize ballast deformations. All geogrids placed 250mm below the base of the tie generate similar reduction factors of approximately 40% regardless of the subgrade type. The subgrade strength starts to produce a difference in reduction factors for geogrids located at a depth of 200mm. While the geogrid reinforcing the ballast bed supported by the competent subgrade yields a reduction factor of 41.97% that shows very little difference compared to the one obtained with a geogrid placed at 250mm for the same subgrade, the geogrids reinforcing the ballast layers supported by the fair and soft subgrades give rise to reduction factors of 53.84% and 57.59% respectively that correspond to increases of 4.55% and 15.19% compared to the geogrids placed at a depth of 250mm. Similarly, geogrids placed 150mm below the tie display a behavior that is highly sensitive to the compressibility of the underlying subgrade. As observed with the geogrid located 200mm below the tie, the geogrid placed at a depth of 150mm in the ballast layer supported by the competent subgrade does not yield a reduction factor that differs from those produced by the geogrids located at 250mm, and 200mm. On the other hand, placing the geogrid at a depth of 150mm in the ballast bed resting on the fair subgrade results in a greater reduction factor of 55.05% compared to 53.84% and 49.29% for the geogrids located at depths of 200mm and 250mm. A similar, although more pronounced, trend occurs in the ballast layer supported by the soft subgrade with the geogrid placed at 150mm resulting in a reduction factor of 63.40% compared to 57.59% and 42.40% when placed at depths of 200mm and 250mm respectively. Additionally, these observations are supported by Figures 3.5a, b, c, and d which show the reduction factors obtained in every single reinforced ballast layer after 10,000, 20,000, 30,000, and 40,000 load cycles respectively. The figures indicate that throughout the ballast box tests, the greatest reduction factors occur in ballast samples supported by the weakest subgrades reinforced with a geogrid located as close to the tie's base as possible. The figures further illustrate the influence of the subgrade's strength on a geogrid's ability to reduce ballast deformations with the geogrids placed at 150mm and 200mm in ballast layers supported by the fair and soft subgrades being wrapped with reduction factor contours greater than or equal to 50% throughout the entire test duration while the geogrids placed at 250mm and those reinforcing ballast supported by the competent subgrade consistently have the lowest reduction factors.

In terms of practical implications, Figures 4.4 and 4.5 suggest that when geogrids are used to reinforce ballast layers supported by stiff subgrades, they can be placed at the ballast-subballast interface or deep within the ballast layer as their placement depth does not wield a significant influence on their ability to reinforce the granular material. On the other hand, in cases where ballast layers supported by weaker subgrades are to be reinforced with geogrids, placing the geogrids above the ballast-subballast interface and closer to the tie's base is desirable as their ability to stabilize ballast is a function of their proximity to the loaded area.

4.3.2. Resilient Settlement

The tie's resilient settlement is defined as the difference between the tie's maximum and minimum settlements during a given load cycle and provides a measure of its elastic rebound. Figure 4.6a displays the variations of the tie's resilient deflection in unreinforced ballast samples resting on the stiff, competent, fair, and soft subgrades. The resilient deformation is highly sensitive to changes in subgrade compressibility with the tie tested on the stiff subgrade experiencing a resilient deflection of 0.36mm at the end of the 40,000 load cycles compared to 0.59mm, 0.81mm, and 0.86mm for the competent, fair, and soft subgrades. For every subgrade, the evolution of the tie's resilient settlement follows a similar pattern whereby the tie first exhibits a high resilient deflection followed by a sharp decrease during the first 10,000 load cycles as the initially loose ballast assembly densifies under the action of repeated loads before reaching a dense stable state which manifests itself by having the resilient deformation reach a stable plateau.

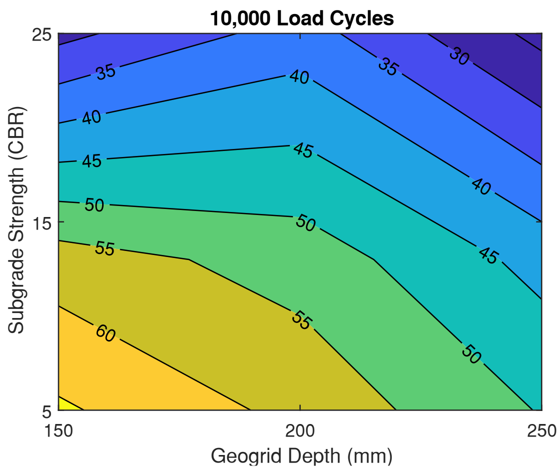

(a)

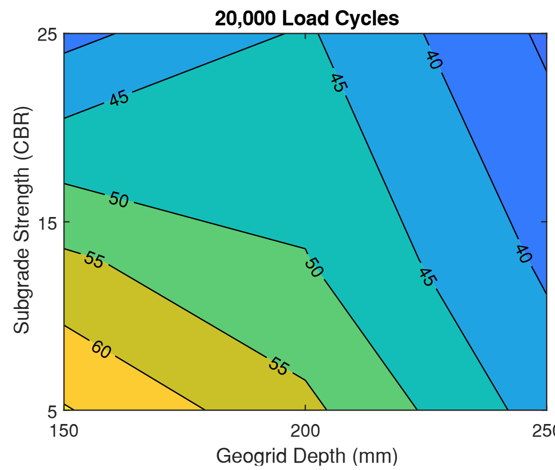

(b)

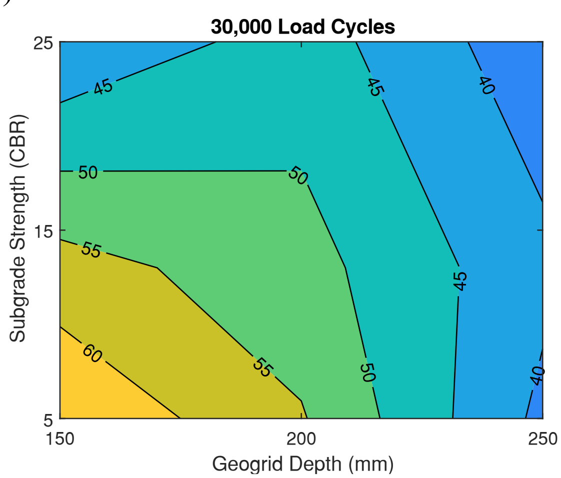

(c)

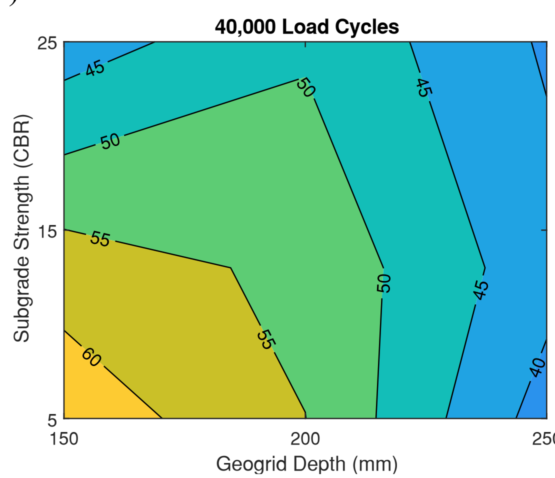

(d)

Figure 4.5: Evolution of the Reduction Factor Generated by a Geogrid as a Function of its Placement Depth and the Subgrade Strength after (a) 10,000, (b) 20,000, (c) 30,000, and (d) 40,000 Load Cycles.

Figure 4.6b, c, and d show the variations in the tie's resilient settlement recorded in unreinforced and geogrid-reinforced ballast samples supported by the competent, fair, and soft subgrades respectively. In all three figures, the inclusion of a geogrid in ballast samples is seen to translate into a reduction of the tie's resilient deformation. This reduction is attributed to the formation of a mechanical interlock between the geogrid and the surrounding aggregate. As ballast particles become wedged in the geogrid's apertures, the ballast-geogrid interface acts as a non-displacement boundary that laterally confines the granular assembly, thereby increasing its stiffness and decreasing the recoverable settlement it experiences under cyclic loading.

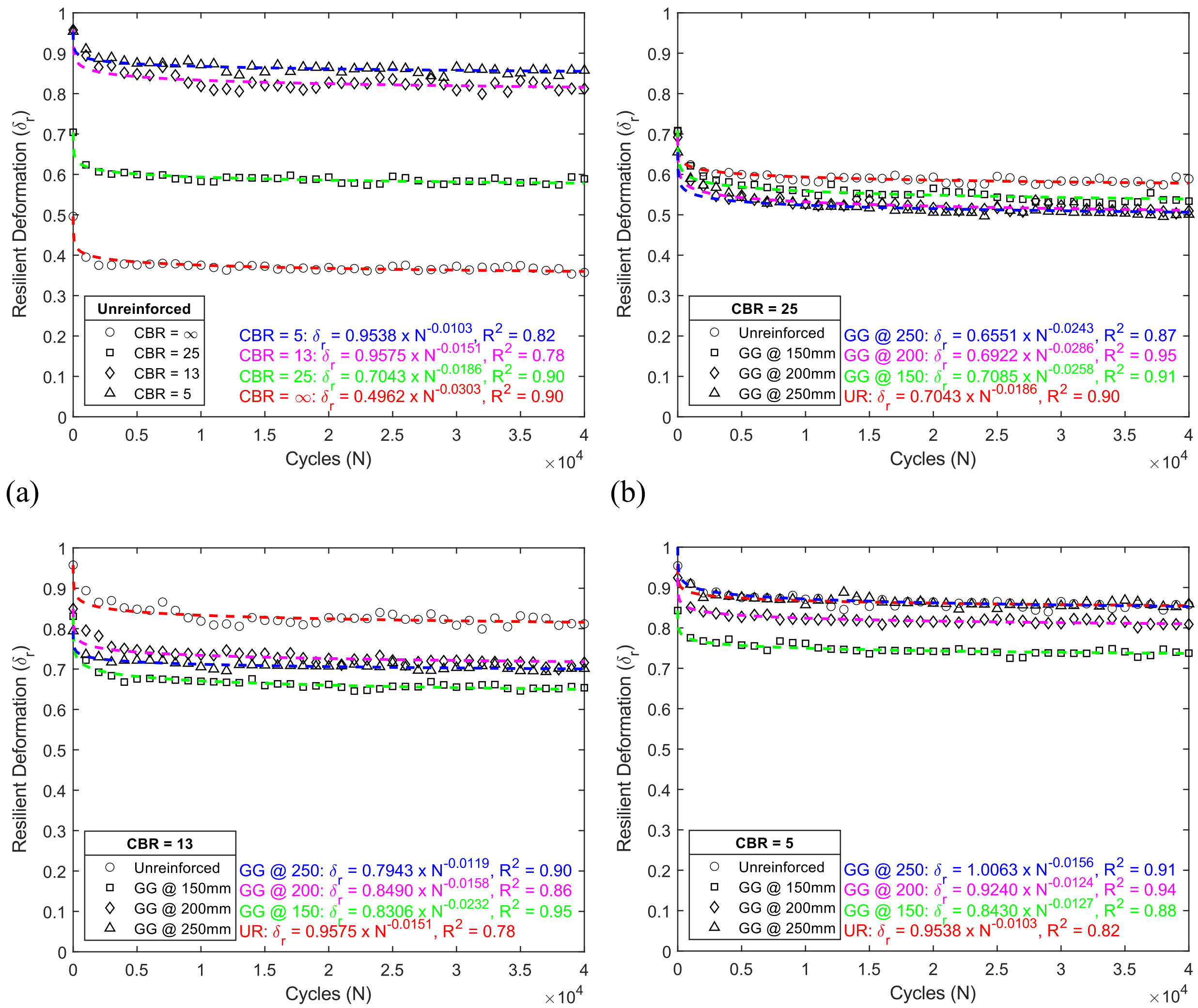

(c) (d)

Figure 4.6: Variations in the Tie's Resilient Deformation Recorded in (a) Unreinforced Ballast Samples and Geogrid-Reinforced Ballast Layers Supported by the (b) Competent, (c) Fair, and (d) Soft Subgrades.

The variations in tie resilient deflection recorded over the competent subgrade (Figure 4.6b) reflect the findings drawn from the settlement curves for the same subgrade shown in Figure 4.3b. The inclusion of a geogrid in the ballast layer minimizes the magnitude of the tie's resilient deflection throughout the entire 40,000 load cycles. However, the performance of a given geogrid appears to be marginally sensitive to its placement depth as the geogrids placed at depths of 150mm, 200mm, and 250mm give rise to similar reductions in resilient settlement.

The changes in the tie's resilient settlement observed in ballast layers supported by the fair subgrade (Figure 4.6c) point to the fact that a softer support condition fosters an environment in which a geogrid's placement depth becomes a factor that determines its ability to reinforce railroad ballast. The geogrid located 150mm below the base of the tie achieves the greatest reduction in resilient deflection while the ones located at depths of 200mm and 250mm lead to a smaller decrease in resilient settlement. The observation is further substantiated by the results obtained during ballast box tests with the soft subgrade (Figure 4.6d) in which a marked difference exists between the tie's resilient deflection in ballast samples reinforced with geogrids located at different depths. The greatest reduction in resilient settlement takes place in the ballast sample reinforced with the geogrid placed 150mm below the tie followed by the one where the geogrid is embedded at a depth of 200mm. It is worth noting that the geogrid located 250mm into the ballast layer does not offer any appreciable decrease in the tie's resilient deflection as it displays a resilient settlement curve akin to that of the unreinforced tie-ballast assembly.

4.3.3. Tie Support Stiffness

The tie support stiffness (K) is calculated by dividing the load amplitude (ΔP) by the tie's resilient deflection (δ_r) during a given load cycle as shown in Equation 4.3 (Abadi et al., 2018; Grossoni et al., 2016; C. Shi et al., 2021):

$$K = \frac{\Delta P}{\delta_r} \tag{4.3}$$

The evolution of the tie's support stiffness in unreinforced ballast samples supported by the stiff, competent, fair, and soft subgrades is shown in Figure 4.7a. The variations in tie support stiffness reflect the trends observed in the tie's permanent and resilient deflections whereby the initially loose state of the ballast layer and its progressive densification and stiffening during the first 10,000 load cycles translate into the support stiffness experiencing a period of rapid increase followed by a period where it remains almost unchanged under further cyclic loading as the denser granular assembly behaves almost elastically. Similar to the resilient deflection, the support stiffness is highly sensitive to the subgrade strength, with the highest stiffness being recorded in the ballast layer supported by the stiff subgrade followed by ballast samples resting on the competent, fair, and soft subgrades respectively.

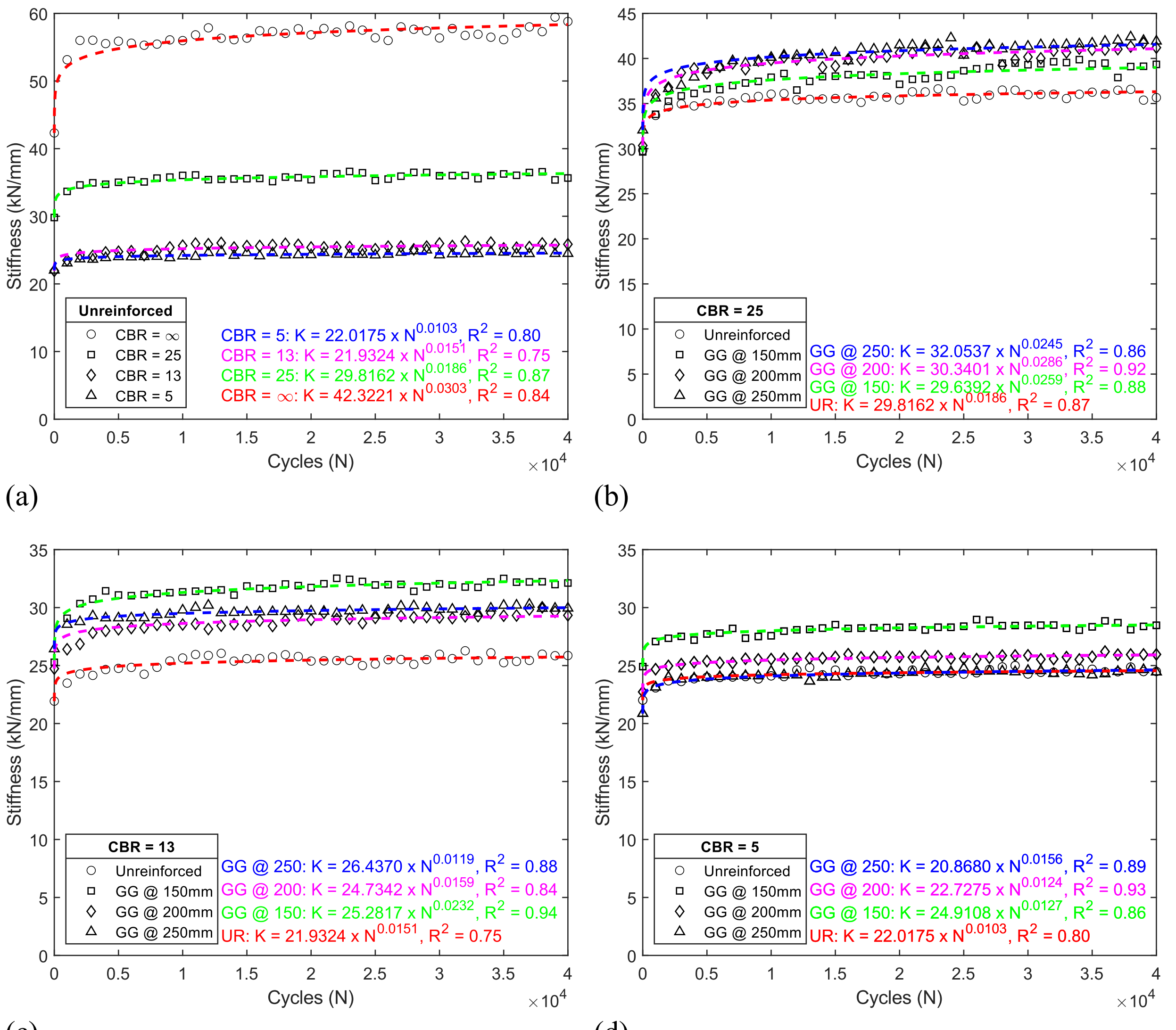

Figure 4.7: Variations in Tie Support Stiffness Recorded in (a) Unreinforced Ballast Samples and Geogrid-Reinforced Ballast Layers Supported by the (b) Competent, (c) Fair, and (d) Soft Subgrades.

The inclusion of geogrids in ballast layers generates an increase in the tie support stiffness owing to the development of a mechanical interlock between the geogrid and the surrounding particulate medium. As ballast particles become wedged in the grid’s apertures, the ballast layer is subjected to greater lateral confinement that minimizes the granular assembly’s proclivity to deform when exposed to cyclic loading and translates into the geogrid-reinforced ballast offering a greater support stiffness to the overlying tie.

Figure 4.7b shows the evolution of the tie support stiffness in geogrid-reinforced and unreinforced ballast layers supported by the competent subgrade. Placing a geogrid in ballast samples results in tie support stiffnesses that consistently exceed that recorded in the unreinforced sample due to the ensuing reduced resilient deflection. However, the stiffness of geogrid-reinforced ballast supported by the competent subgrade appears to be independent of the reinforcement's location in the granular assembly, echoing the findings reported for the tie's permanent and resilient deflections.

A geogrid's propensity to increase the support stiffness of ballast assemblies becomes increasingly tied to its placement depth as the strength of the underlying subgrade decreases. The support stiffnesses observed in geogrid-reinforced and unreinforced ballast layers supported by the fair subgrade are displayed in Figure 4.7c. Although all reinforced ballast layers have higher stiffness than the unreinforced ballast sample, a notable difference exists between the ballast assembly reinforced with a geogrid located 150mm below the tie and those where the geogrid is at depths of 200mm and 250mm. Specifically, the ballast layer with a geogrid placed at a depth of 150mm has a greater stiffness compared to the other two layers that exhibit similar stiffnesses. The observation that the subgrade strength plays a role in determining whether the geogrid's location wields an influence on its impact on the ballast stiffness is further substantiated by the variations in support stiffness in unreinforced and geogrid-reinforced ballast layers resting on the soft subgrade shown in Figure 4.7d. The ballast layer reinforced with a geogrid placed at a depth of 150mm experiences the greatest stiffness increase of all the reinforced samples, culminating in a stiffness that is 16.3% higher than that of the unreinforced sample at the end of the test. The ballast sample reinforced with a geogrid placed at a depth of 200mm develops a smaller increase in its support stiffness, resulting in a stiffness that is 6% greater than in the unreinforced case at the end of the test. In contrast, placing a geogrid 250mm below the tie does not appear to affect the support stiffness, as the ensuing stiffness is akin to that obtained in the unreinforced ballast layer.

4.3.4. Damping Ratio

Railroad ballast exhibits a hysteretic behavior when subjected to cyclic loading which is characterized by the storage and dissipation of energy during a given loading-unloading cycle. In the experiments presented herein, the energy dissipation in railroad ballast stems from the plastic rearrangement of the soil fabric that takes place as individual ballast particles rearrange in response to the application of external loads. The ballast's propensity to dissipate energy during cyclic loading is examined experimentally by analyzing the hysteresis loops generated during a given ballast box test to compute the damping ratio (D_r) for each load cycle using Equation 4.4 as per ASTM D3999 (ASTM, 1996):

$$D_r = \frac{A_{Loop}}{4\pi A_T} \tag{4.4}$$

Where A_{Loop} is the area bounded by the hysteresis loop for a given cycle and A_T is the area contained within the shaded triangle shown in Figure 4.8. The area contained within a given hysteresis loop provides a measure of the energy dissipated by the material during a given load cycle while the shaded triangle represents the maximum elastic energy that may be stored per unit volume of the material. It is important to emphasize that the damping ratios calculated in this paper are a function of the ballast's properties (as well as any geogrid inclusion that may be embedded in it) and the underlying subgrade.

Figure 4.9a displays the variations in damping ratio in unreinforced ballast samples tested over the stiff, competent, fair, and soft subgrades. In general, the damping ratio of a given test initially has a high value at the beginning of a test and experiences a sharp drop within the first 10,000 load cycles followed by a stage where it decreases at a much lower rate. This echoes the observations made in Figure 4.3a and Figure 4.6a where the onset of cyclic loading consistently leads to either the settlement or resilient deflection varying significantly due to the plastic rearrangement of the ballast's fabric followed by either property varying in a more stable fashion. The damping ratios of the unreinforced tie-ballast assemblies exhibit a strong sensitivity to the presence of a compressible subgrade with the damping ratio over the stiff subgrade reaching a value of 0.029 at the end of the ballast box test against 0.071, 0.074, and 0.078 in unreinforced experiments performed over the competent, fair, and soft subgrades respectively.

The inclusion of geogrid reinforcement in ballast layers supported by the competent subgrade results in a small reduction in damping ratio compared to the unreinforced case as shown in Figure 4.9b, with only minor differences in damping ratio being recorded between each reinforced test. However, the experiments performed in reinforced-ballast samples supported by the fair and soft subgrades (Figure 4.9c and d respectively) indicate that negligible reductions in damping ratio occur as a consequence of reinforcing railroad ballast with a geogrid, regardless of its placement depth. Bearing in mind that the results displayed in Figures 3.9a to d are a reflection of the ballast/subgrade assembly's propensity to dissipate energy during cyclic loading, the data suggests that a geogrid only generates marginal reductions in the damping ratio and that the energy dissipated by the ballast/subgrade assembly is mainly a function of the subgrade's strength.

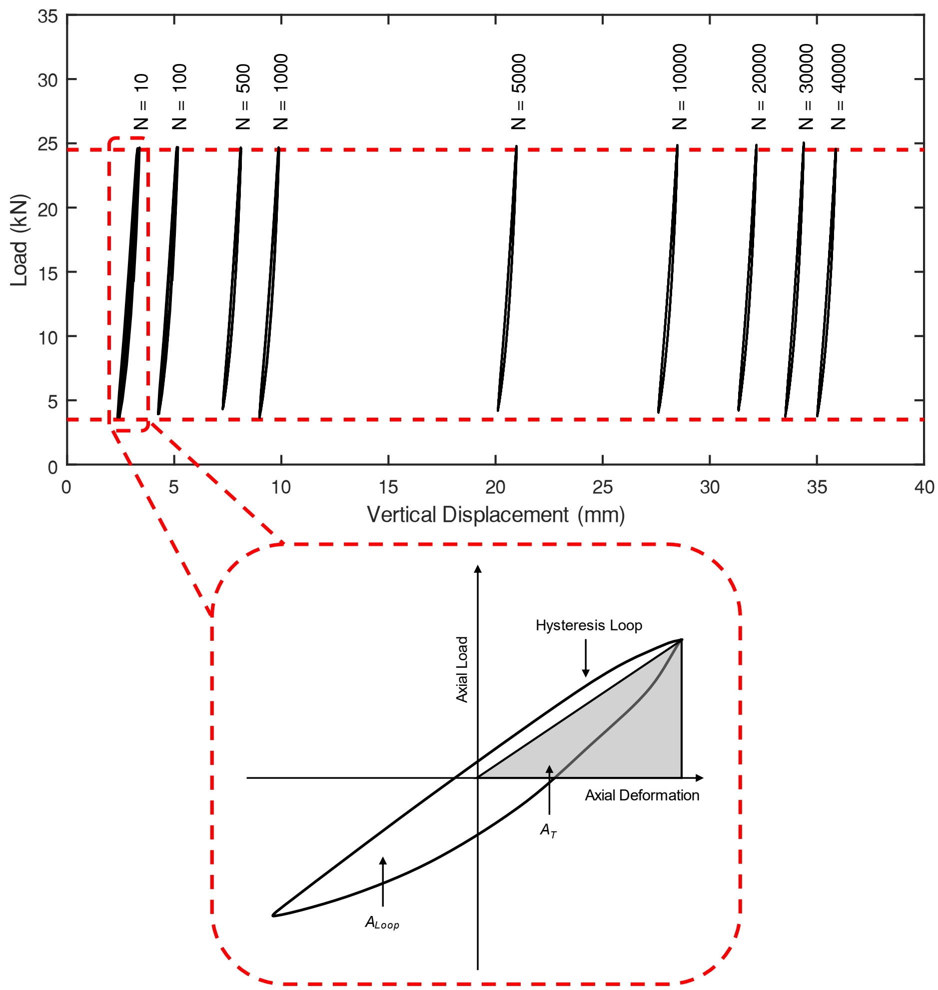

Figure 4.8: Hysteresis Loops Recorded during the Ballast Box Test Performed on the Unreinforced Tie-Ballast Assembly Supported by the Soft Subgrade and the Areas Used to Evaluate its Damping Ratio.

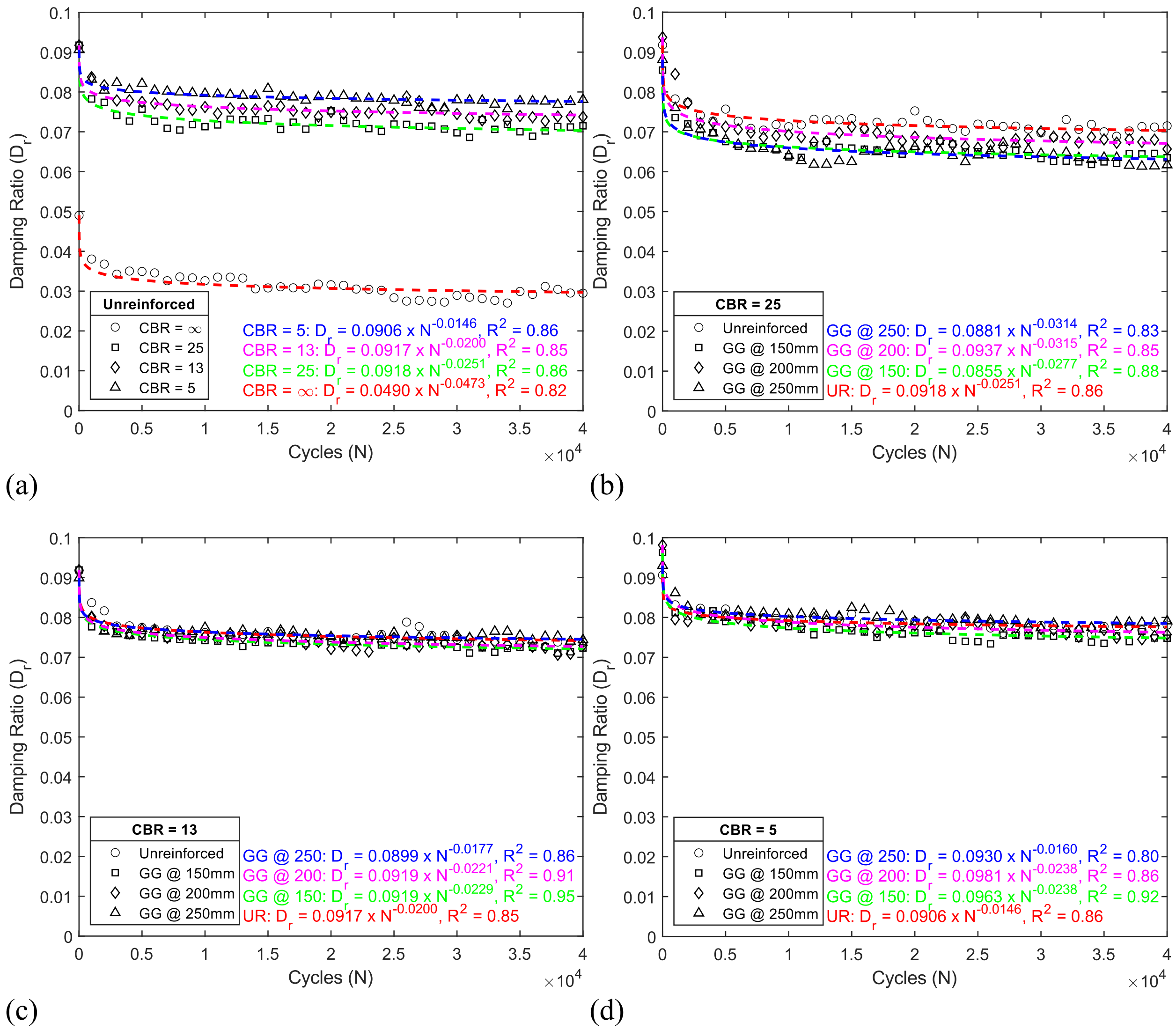

Figure 4.9: Evolution of the Ballast-Subgrade Assembly’s Damping Recorded in (a) Unreinforced Ballast Samples and Geogrid-Reinforced Ballast Layers Supported by the (b) Competent, (c) Fair, and (d) Soft Subgrades.

4.3.5. Limitations

The results presented in this paper are influenced by the fact that elastomer pads were used to simulate the presence of different subgrades below the tie-ballast assembly. Unlike natural soils, the rubber mats may not sustain permanent plastic deformations under cyclic loading. As such, while they provided different degrees of resiliency to the overlying ballast which allowed the granular material to exhibit different deformation behaviors, the pads’ response to cyclic loading remained the same throughout the experiments and may not fully represent the behavior of natural subgrades. It is noteworthy that the loading frequency and the relatively low number of load cycles used in the ballast box tests may not be an actual representation of typical train traffic loading while the box's rigid boundaries may not allow for the physical modeling of low levels of lateral confinement. Additionally, the impact of geogrid inclusions on the ballast suffusion potential should be assessed. The detachment and transport of fine particles within railroad ballast may potentially induce internal instability in the ballast layer (K. Liu et al., 2021). Hence, additional research is necessary to investigate how geogrids influence the potential for suffusion in reinforced ballast samples.

4.4. Conclusions

This study focuses on evaluating the effect of the subgrade strength on the ability of geogrids to reinforce railroad ballast when placed at different locations below the tie. To do so, a total of thirteen ballast box tests are conducted on unreinforced and geogrid-reinforced ballast samples subjected to cyclic loading. The key findings of the experimental campaign are as follows:

- The subgrade strength wields a considerable influence on the type of reinforcement benefit derived from embedding a geogrid in railroad ballast
- For ballast layers supported by a competent subgrade, the use of geogrid reinforcement leads to a reduction in tie settlement that remains relatively the same regardless of the geogrid's placement depth
- A geogrid's placement depth becomes increasingly important when the reinforced ballast layer rests on the fair or soft subgrade, with geogrids located closer to the tie being more effective at minimizing the tie's settlement. While this trend is observable in reinforced ballast samples supported by the fair subgrade, the effect of the geogrid's location is particularly pronounced in reinforced tie-ballast assemblies resting on the soft subgrade
- The reductions in resilient settlement produced by geogrids follow the trends observed for the tie's permanent settlement whereby geogrid-reinforced ballast layers resting on a competent subgrade display similar resilient deformations regardless of the reinforcement's location while reinforced tie-ballast assemblies supported by weaker subgrades exhibit reductions in resilient deformation that are strongly influenced by the geogrid's location, with shallower placement depths resulting in the greatest reductions

- Embedding a geogrid in a ballast layer enhances the track support stiffness. For ballast layers resting on the competent subgrade, the geogrid location appears to have a marginal impact on the ensuing increase in stiffness. The geogrid's placement depth becomes increasingly important, however, when the strength of the underlying subgrade decreases, with geogrids located closer to the bottom of the tie leading to greater stiffness increases compared to those situated deeper within the ballast layer
- The damping ratio appears to be relatively insensitive to the presence of geogrid reinforcement with only minor differences in damping being observed between unreinforced and geogrid-reinforced tie-ballast assemblies. The damping ratio is primarily affected by the strength of the underlying subgrade

Preface to Chapter 5

The experimental work presented in Chapter 4 suggests that the geogrid placement depth becomes a crucial factor as the underlying subgrade weakens. In ballast layers supported by softer subgrades, geogrids located closer to the bottom of the tie appear to be more effective at minimizing ballast deformations compared to their counterparts placed at greater depths. This in turn translates into shallow geogrid placement depths resulting in smaller tie settlements and greater tie support stiffnesses as the subgrade strength decreases. Although the ballast box tests provide valuable information on the macroscale repercussions of reinforcing ballast with geogrids, little to no information may be obtained from such experiments regarding the interaction between the geogrids and ballast particles. As such, it is practically impossible to observe the particle scale manifestations of the observed macroscale phenomena induced by incorporating a geogrid in a layer of ballast subjected to cyclic loading.

To remedy this shortcoming, a three-dimensional discrete element model of the ballast box test featuring a 300mm-thick ballast layer is developed, calibrated, and introduced in Chapter 5. The model is first used to explore the impact of the geogrid placement depth on the micromechanical behavior of geogrid-reinforced ballast. Geogrid depths of 50mm, 100mm, 150mm, 200mm, and 250mm are considered in the simulations. The behavior of the geogrid-reinforced ballast assemblies is then compared to that of an unreinforced ballast layer by analyzing the motion of ballast particles in each layer, the transmission of loads in each granular assembly through interparticle contacts, and the dissipation of energy in each ballast bed. Upon delving into the effects of the geogrid placement depth at the particulate level, the scope of the parametric study is expanded to investigate the influence of the geogrid aperture size and geogrid stiffness on the cycle loading response of geogrid-reinforced ballast. The geogrid aperture size is varied such that it yields a range of geogrid aperture size (A) to mean ballast particle diameter (D_{50}) ratio of 1.09 to 2.91. The geogrid stiffness, on the other hand, is taken to reflect the spectrum of geogrid tensile strength at 2% strain at temperatures ranging from -30ºC to 40ºC observed in the experiments discussed in Chapter 3, giving stiffnesses ranging from 18.00kN/m to 9.54kN/m.

Chapter 5: The Effects of Geogrid Characteristics on the Mechanical Response of Reinforced Ballast under Cyclic Loading: A Discrete Element Study†

Abstract

This study presents an investigation into the mechanical behavior of geogrid-reinforced ballast subjected to cyclic loading focusing on the macro- and micromechanical features of the geogrid-ballast interaction mechanism. Key areas of interest include the effects of geogrid placement depth, aperture size, and stiffness on the motion of ballast particles, formation of contact force chains, and energy dissipation. A three-dimensional discrete element model, calibrated with experimental data, simulates ballast box tests performed on 300mm-thick ballast layers reinforced by geogrids placed at depths ranging from 50mm to 250mm below the tie. The findings reveal that geogrids located within the upper 150mm of the ballast layer significantly reduce tie settlement by minimizing particle movement, creating well-connected soil structures, and decreasing energy dissipation. Upon identifying 150mm as the optimal geogrid placement depth, a parametric study evaluates the impact of the geogrid aperture size (A) and stiffness on the behavior of geogrid-reinforced ballast. The geogrid aperture size (A) is varied to give aperture size to ballast diameter (D) ratios ranging from 1.09 to 2.91 while the geogrid's stiffness ranges from 9.54kN/m to 18.00kN/m. Results indicate that A/D ratios greater than or equal to 1.45 are required for geogrids to perform satisfactorily while stiffness appears to wield a negligible influence on the response of geogrid-reinforced ballast.

Keywords: Reinforced Ballast; Soft Subgrade; Aperture Size; Geogrid Stiffness; Discrete Element Modeling.

---

†A version of this manuscript is currently under review in *Transportation Infrastructure Geotechnology*.

5.1. Introduction

Railroad tracks are generally supported by a ballasted substructure that consists of a three-layer soil system composed of a ballast layer overlying a subballast layer resting on a subgrade (D. Li et al., 2015; Selig & Waters, 1994). The ballast bed consists of large, uniformly graded, angular crushed rocks. Being at the top of the substructure, the ballast layer serves as a bearing platform for the track superstructure that supports the train loads and distributes them to the underlying soil strata, maintains satisfactory track alignment, and provides swift water drainage and resilience against large dynamic train loads (J. Chen, Vinod, et al., 2022; Dahlberg, 2001; Desbrousses & Meguid, 2021). Despite its critical role in ensuring track alignment, the ballast layer is widely recognized as one of the main vectors of track settlement (D'Angelo et al., 2018; Desbrousses & Meguid, 2022; Kumar et al., 2019; Selig & Waters, 1994; K. Wang et al., 2020). Being an unbound material subjected to low lateral confinement (Indraratna et al., 2005; Lackenby et al., 2007; Thakur et al., 2013), ballast deforms considerably at the onset of cyclic loading due to the rearrangement of its particles to reach a denser soil structure (Malisetty et al., 2022). Sustained exposure to repeated train loads also leads to the wear and tear of ballast particles, thereby reducing the material's shear strength and contributing, in the long run, to further deformations in the ballast bed (Q. Gu et al., 2022; Sol-Sánchez et al., 2016).

As such, geogrids are increasingly utilized to mitigate deformation in railroad ballast layers, leveraging their open structure characterized by large apertures bordered by orthogonal ribs to form a robust mechanical interlock with the surrounding ballast particles. This reinforcement mechanism has been explored experimentally through a variety of test methods such as the direct shear test (Indraratna et al., 2012; Sadeghi et al., 2020; Sweta & Hussaini, 2018, 2019; Tutumluer et al., 2012), pullout test (C. Chen et al., 2013), triaxial test (Mishra et al., 2014; Qian et al., 2015, 2018; Yu et al., 2019), ballast box test (Bathurst & Raymond, 1987; Desbrousses et al., 2023; Hussaini et al., 2015, 2016; Indraratna et al., 2013; S. Liu et al., 2016; McDowell & Stickley, 2006; Sadeghi et al., 2023), and field/full-scale tests (Esmaeili, Zakeri, et al., 2017; Fernandes et al., 2008; Indraratna et al., 2010; Luo, Zhao, Cai, et al., 2023b). Experimental research has shown that the performance of a geogrid embedded in ballast is contingent upon its aperture size and placement depth as well as the strength of the underlying subgrade. Cyclic loading ballast box tests (Bathurst et al., 1986; Bathurst & Raymond, 1987; Desbrousses et al., 2023; Indraratna et al., 2013) have demonstrated that geogrids placed closer to the bottom of the ties significantly reduce vertical and lateral ballast deformations, with the geogrid position wielding an increasingly important influence as subgrades become weaker (Desbrousses et al., 2023). The geogrid aperture size has been shown to be the backbone of the geogrid-ballast interlock, with direct shear tests and ballast box tests performed by Indraratna et al. (2012, 2013) and Sadeghi et al. (2020, 2023) indicating that optimal geogrid reinforcement is achieved when the ratio between the geogrid's aperture size (A) and the ballast's mean particle diameter (D_{50}) lies between 0.95 and 1.20, resulting in maximum reductions in vertical and lateral ballast deformation. Other researchers, such as Brown et al. (2007), revealed that adequate geogrid reinforcement is obtained for A/D_{50} ratios ranging from 1.20 to 1.60. Qian et al. (2015, 2018) and Mishra et al. (2014) performed large-scale triaxial tests on geogrid-reinforced ballast and reported that a robust geogrid-ballast interlock is the root cause of the observed increase in ballast shear strength.

In a laboratory setting, analyzing the mechanical behavior of geogrid-reinforced ballast typically relies on observable macroscale processes, such as the evolution of tie settlement. However, these experiments often fall short in capturing the intricate microscale interactions that occur within a geogrid-ballast system due to the practical difficulties associated with observing micromechanical processes. To address this gap, researchers have turned to the discrete element method (DEM) (Cundall & Strack, 1979) to explore the behavior of geogrid-reinforced ballast from a particulate perspective. Studies conducted by McDowell et al. (2006), Ferellec and McDowell (2012), and Chen et al. (2013, 2014) have employed DEM to simulate pullout and triaxial tests, modeling ballast particles as rigid assemblies of bonded spheres to capture their irregular shape and representing geogrids as strings of bonded, overlapping spheres. Their findings shed light on the geogrid deformations that take place during pullout testing and highlight the contribution of the geogrid-ballast interlock to pullout resistance by analyzing the interparticle contact force chains. Further applications of the discrete element method in modeling geogrid-reinforced ballast include the work of Ngo et al. (2014, 2016) who simulated direct shear tests on geogrid-reinforced ballast. By delving into the micromechanical features of the geogrid-ballast interaction, they reported that the incorporation of geogrids in ballast results in an increase in the number of interparticle contacts compared to an unreinforced ballast sample. They further indicated that geogrids affect the formation of contact force chains during shearing. Gao and Meguid (2018) simulated bearing capacity tests on geogrid-reinforced crushed limestone aggregate and concluded that the inclusion of geogrids increases bearing capacity while minimizing particle rotation. Luo et al. (2023) assessed the performance of a geogrid placed at the ballast/subballast interface during cyclic loading and found that the presence of a geogrid translates into an increase in the ballast's coordination number, reduces particle rotation, decreases the mean interparticle contact force, and minimizes the tie settlement. Chen et al. (2023) focused on evaluating the effect of the geogrid aperture size on the geosynthetic's ability to minimize ballast pocket formation and recommended geogrids with 40×40mm apertures be placed beneath the ballast layer to mitigate the growth of ballast pockets and minimize tie settlement. Similarly, Feng et al. (2023) and Wang et al. (2024) simulated direct shear tests on geogrid-reinforced aggregate to identify the optimum A/D_{50} ratio. Their results pointed to a more localized shear strain in geogrid-reinforced aggregate during shearing, with the geogrid supporting most of the applied shear load. They advocated for geogrids with high flexural rigidity and an A/D_{50} ratio of 2.53 for optimal geogrid performance based on analyses of contact force chains, energy dissipation, and particle movement. However, few studies have investigated the effect of a geogrid's placement depth, aperture size, and stiffness on the micromechanical behavior of a geogrid-reinforced ballast assembly subjected to cyclic loading.

Therefore, in this paper, a three-dimensional discrete element model is developed to simulate cyclic loading ballast box tests performed on a 300mm-thick layer of railroad ballast and delve into the micromechanical causes of observable macroscopic phenomena such as tie settlement. The model's contact model parameters are calibrated using results from triaxial tests conducted on railroad ballast and geogrid tensile and aperture stability modulus tests. This study then explores the kinematics of ballast assemblies reinforced with geogrids positioned at varying depths ranging from 50 to 250mm below the tie. The influence of the geogrid's aperture size (*A*) and stiffness is then assessed by varying the geogrid aperture size to ballast diameter ratio (*A/D*) from 1.09 to 2.91 and the geogrid's stiffness from 9.54kN/m to 18.00kN/m.

5.2. Overview of the Experimental Campaign

Desbrousses et al. (2023) performed a series of large-scale ballast box tests to investigate the effect of subgrade strength and geogrid placement depth on the deformation behavior of railroad ballast subjected to cyclic loading. In each experiment, a 300mm-thick layer of railroad ballast was constructed in three 100mm-thick lifts compacted to an approximate unit weight of 15.7kN/m^3 in a ballast box with plan dimensions of 1,290mm by 915mm and a height of 600mm. The ballast aggregate used in the experiments consisted of crushed granite aggregate screened to conform to an AREMA No. 4 gradation. Upon constructing the granular assembly, a model tie with plan dimensions of 203×301mm was placed above the compacted ballast layer. A cyclic compressive load with a mean value of 14kN and an amplitude of 10.5kN was applied to the tie at a frequency of 0.8Hz following a sinusoidal waveform for a total of 40,000 repetitions using a pneumatic cyclic loading apparatus developed by Desbrousses and Meguid (2023b). The load delivered to the tie was monitored by a load cell mounted on the pneumatic cyclic loading apparatus while the tie's settlement was recorded by linear variable displacement transducers. The presence of compressible subgrades below the constructed ballast layers was considered by lining the bottom of the box with one of three rubber mats representing artificial subgrades with equivalent California Bearing Ratio (CBR) readings of 25, 13, and 5. For each subgrade condition, four ballast box tests were performed with one being conducted on an unreinforced ballast layer while the remaining three were done on geogrid-reinforced ballast assemblies. The geogrid embedded in the ballast layers was a large aperture biaxial polypropylene geogrid with thick nodes and ribs designed to stabilize coarse unbound aggregates like railroad ballast. The geogrid had square apertures with a center-to-center size of 57mm and an ultimate tensile strength of 30kN/m (Desbrousses et al., 2021; Desbrousses & Meguid, 2023a; Titan Environmental Containment, 2020). The effect of temperature on the geogrid's tensile strength was investigated by Desbrousses et al. (2021, 2023a) who performed in-isolation tensile tests on specimens of the geogrid in a temperature-controlled environment at temperatures ranging from -30 to 40ºC. The geogrid's tensile strength at 2% strain and ultimate tensile strength at temperatures ranging from -30 to 40ºC are summarized in Table 5.1.

For each subgrade, an experiment was performed for geogrid placement depths of 250mm, 200mm, and 150mm below the base of the tie. A diagram of the experimental setup used by Desbrousses et al. (2023) is provided in Figure 5.1. The key findings of Desbrousses et al.'s laboratory tests indicated that the subgrade strength wields a considerable influence on the ability of geogrids to reinforce railroad ballast and abate tie settlement. Results demonstrated that geogrid inclusions resulted in similar attenuation of the tie settlement in ballast assemblies supported by a competent subgrade. However, the ability of geogrids to reduce tie settlement showed an increasing sensitivity to the geosynthetic's placement depth as the subgrade became weaker, with geogrids located closer to the tie yielding the highest reductions in tie settlement.

Table 5.1: Mechanical Properties of the Large Aperture Biaxial Polypropylene Geogrid.

	Temperature (°C)							
	-30	-20	-10	0	10	20	30	40
Tensile strength at 2% strain (kN/m)	18.00	18.11	16.28	16.12	14.61	11.01	10.62	9.54
Ultimate tensile strength (kN/m)	44.85	44.69	43.76	41.03	37.58	33.55	30.77	28.60

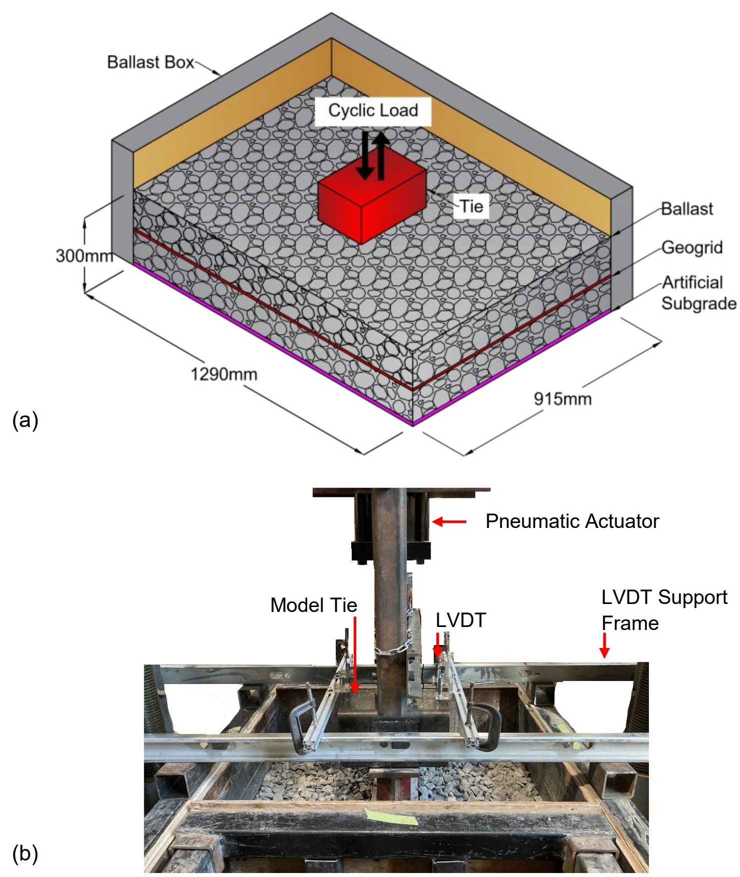

Figure 5.1: (a) Schematic diagram of the ballast box test and (b) laboratory setup used by Desbrousses et al. (2023) [Adapted from Desbrousses et al. (2023) with permission].

5.3. Discrete Element Modeling of Geogrid-Reinforced Railroad Ballast

The experimental work conducted by Desbrousses et al. (2023) provided insights into the macroscale behavior of tie-ballast assemblies subjected to cyclic loading. This included examining the tie's permanent and resilient settlement, along with the evolution of the ballast layer's stiffness and damping ratio during cyclic loading. However, it was practically impossible to shed light on the particulate-level processes driving these macroscale phenomena. To address this, the current study employs the distinct element method (DEM) using Itasca's three-dimensional *Particle Flow Code* (*PFC 3D* (Itasca, 2022)) to investigate the micromechanical aspects of geogrid-ballast interactions that influence the macroscale behavior of geogrid-reinforced ballast. Unlike the continuum assumption used in finite element modeling, DEM allows for a highly discontinuous material such as railroad ballast to be modeled as an assembly of irregularly shaped particles. Particle motion is then calculated using Newton's second law by a time integration approach akin to the central difference method. The interactions between particles are governed by contact models which are particle-interaction laws that rely on sets of contact model parameters to determine the forces arising at particle contacts.

5.3.1. Railroad Ballast

In discrete element simulations, particle shape wields a significant influence on the simulated material's bulk behavior. For railroad ballast, researchers commonly use spheres (Gao & Meguid, 2018; Guo, Zhao, Markine, Shi, et al., 2020), polyhedrons (Bian et al., 2020; W. Chen et al., 2023; Eliáš, 2014; Qian et al., 2018; Tutumluer et al., 2012), or clumps (assemblies of overlapping spheres) (J. Chen, Vinod, et al., 2022; J. Ferellec & McDowell, 2010; H. Li & McDowell, 2018; Luo, Zhao, Bian, et al., 2023; Suhr & Six, 2017, 2020, 2022), to represent ballast particles. While spheres are simple and computationally efficient, they fall short of realistically representing ballast particles. Indeed, their round shape fails to accurately capture the angular nature of ballast aggregate which leads to limited contact interlocking, increased particle rotation, and the normal component of contact forces passing through the centroid of each sphere without causing a moment (Gao & Meguid, 2018; Guo, Zhao, Markine, Jing, et al., 2020; O'Sullivan, 2011). This in turn underestimates the shear strength of ballast assemblies and overestimates tie settlement. Polyhedrons and clumps, in contrast, can more accurately depict the irregular shapes of ballast particles. A clump is a rigid assembly of overlapping spheres of various sizes and positions, allowing for complex non-smooth, non-convex, and non-spherical particle shapes to be modeled while using the contact detection and resolution algorithms used for regular spheres (O'Sullivan, 2011). By representing more complex particle geometries, clumps develop a greater degree of contact interlocking than spheres and normal contact forces may impact a moment to clumps since the normal force vector and the vector from the contact point to a clump's centroid may not be collinear. On the other hand, polyhedrons use complex triangular meshes for surface definition to represent a given particle shape. One major limitation of polyhedrons is that most discrete element codes, including *PFC 3D*, require polyhedrons to be convex thereby omitting the concavity seen in actual ballast particles (Tolomeo & McDowell, 2022). This convexity implies that a polyhedron may only share a single contact with a neighboring polyhedron, unlike clumps which can share multiple contact points with neighboring clumps. This gives clumps an enhanced ability to resist rotation and contributes to the formation of a more stable soil structure whereas polyhedrons tend to underestimate the shear strength of railroad ballast (Tolomeo & McDowell, 2022).

In this study, the irregular shapes of ballast particles are replicated using the clump logic in *PFC 3D*. This involves scanning a real ballast particle, converting this scan into a 3D triangulated mesh, and then using *PFC 3D*'s *Bubble Pack Algorithm* to create a clump by filling the volume enclosed by the triangular mesh with overlapping spheres of varying size as shown in Figure 5.2. The clumps created in this study match the volume of a sphere with a diameter (D) of 27.5mm which corresponds to the mean diameter of the ballast aggregate used in Desbrousses et al.'s experiments (Desbrousses et al., 2023).

The linear contact model is used to describe the interactions between the clumps that represent ballast particles. Figure 5.2c gives a description of the linear contact model's rheological components which provide the behavior of an infinitesimal linear-elastic and frictional interface that carries a force. When two particles contact, the overlap that develops between the two pieces gives rise to a normal and a tangential force that are functions of the linear stiffness of the normal and tangential springs. Slip between contacting particles is permitted by imposing a Coulomb limit on the shear force.

To simulate the behavior of railroad ballast, the linear contact model's parameters are calibrated by simulating three large-scale triaxial tests conducted by Suiker et al. (2005) on AREMA No. 4 ballast. The triaxial tests were performed on cylindrical ballast samples with a diameter of 254mm and a height of 645mm (see Figure 5.3a) at confining pressures of 10.3kPa, 41.3kPa, and 69.8kPa. Suiker et al. reported their results by computing the stress ratio $-(q/p)$ and the deviatoric strain (κ), where q is the deviatoric stress invariance and p is the hydrostatic stress invariant. The aforementioned variables are computed as follows:

$$q = |\sigma_1 - \sigma_3| = \sigma_d \quad (5.1)$$

$$p = \frac{1}{3}(\sigma_1 + 2\sigma_3) \quad (5.2)$$

$$\kappa = \frac{2}{3}|\epsilon_1 - \epsilon_3| \quad (5.3)$$

Where σ_1 is the major principal stress, σ_3 is the minor principal stress, σ_d is the deviatoric stress, ϵ_1 is the major principal strain, and ϵ_3 is the minor principal strain.

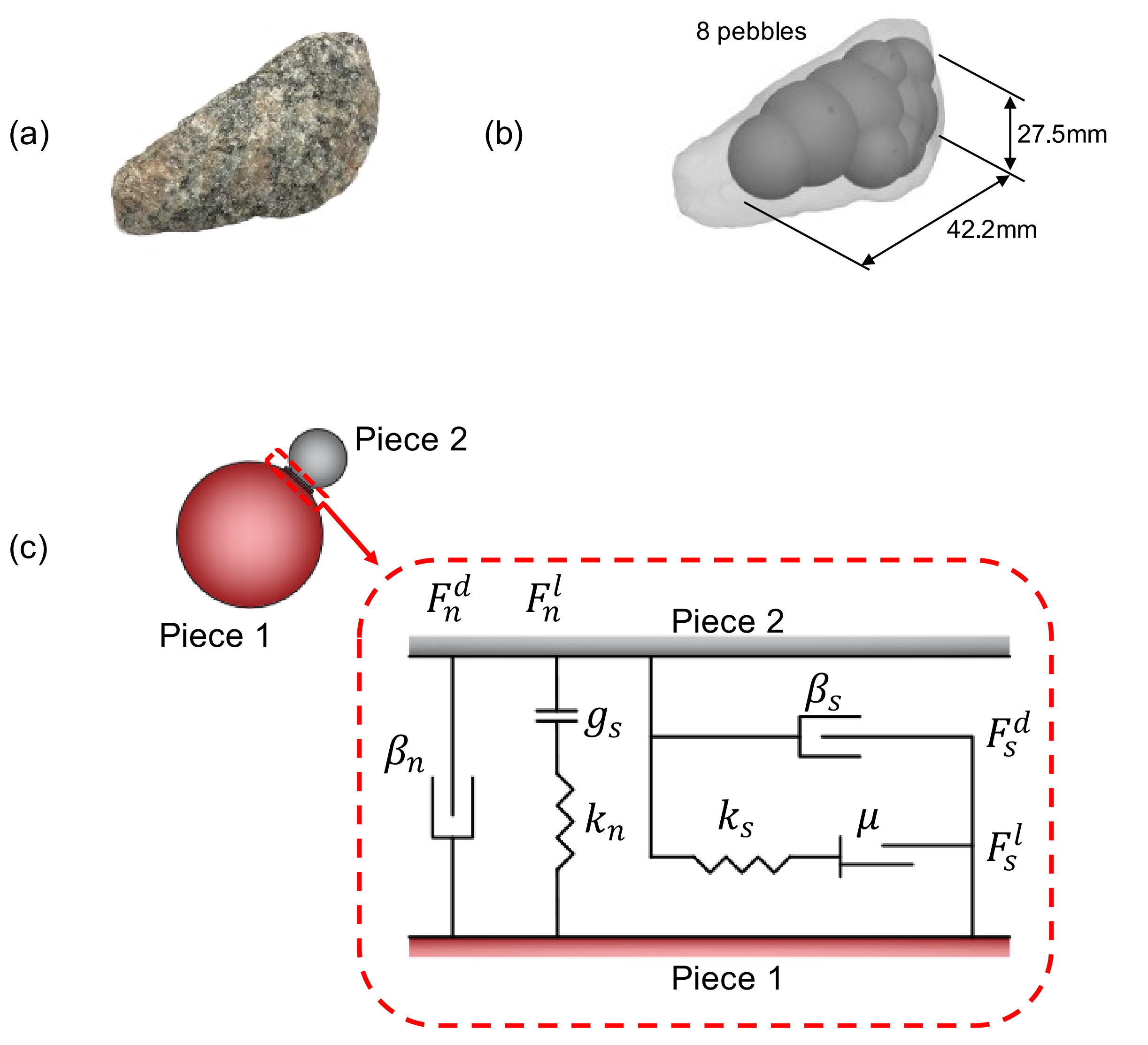

Figure 5.2: Modeling Ballast Particles using the Clump Logic: (a) Ballast Particle, (b) PFC 3D Clump, and (c) Linear Contact Model and its Rheological Components.

The contact model parameters are determined by trial and error such that the simulated triaxial tests match the experimental results. The contact parameters are set using the deformability method, whereby the stiffness of the normal and tangential linear springs is defined by the effective modulus (E^*) and the normal-to-shear stiffness ratio (κ^*) using the following relationships:

$$k_n = \frac{AE^*}{L} \tag{5.4}$$

$$\kappa^* = \frac{k_n}{k_s} \tag{5.5}$$

Where:

$$A = \pi r^2 \tag{5.6}$$

$$r = \begin{Bmatrix} \min\left(R^{(ball\ 1)}, R^{(ball\ 2)}\right), & ball - ball \\ R^{ball}, & ball - facet \end{Bmatrix} \tag{5.7}$$

$$L = \begin{Bmatrix} R^{(ball\ 1)} + R^{(ball\ 2)}, & ball - ball \\ R^{(ball\ 1)}, & ball - facet \end{Bmatrix} \tag{5.8}$$

And R denotes the radius of the contacting balls.

The deformability method was derived to relate the modulus of elastic (E) and Poisson's ratio (v) of a homogeneous, isotropic, and well-connected granular assembly undergoing small-strain deformations to the normal (k_n) and shear spring (k_s) stiffnesses of the linear contact model (Itasca Consulting Group Inc., 2024). The assembly's modulus of elasticity (E) is related to the effective modulus (E^*), with an increase in E translating into an increase in E^*. Similarly, the assembly's Poisson's ratio (v) is related to the normal-to-shear stiffness ratio (κ^*), with the Poisson's ratio increasing with the normal-to-shear stiffness ratio up to a limiting positive value.

The results obtained experimentally are compared with the results from the DEM triaxial tests in Figure 5.3b to c. The discrete element simulations exhibit a reasonable agreement with the experimental data, giving an effective modulus E^* of 325MPa, a normal-to-shear stiffness ratio (κ^*) of 1, and a friction coefficient (μ) of 0.55. The contact model parameters are summarized in Table 5.2. It is noteworthy that the contact model parameters (E^*, κ^*, and μ) were selected following a trial-and-error approach to obtain the closest possible match with the available experimental data.

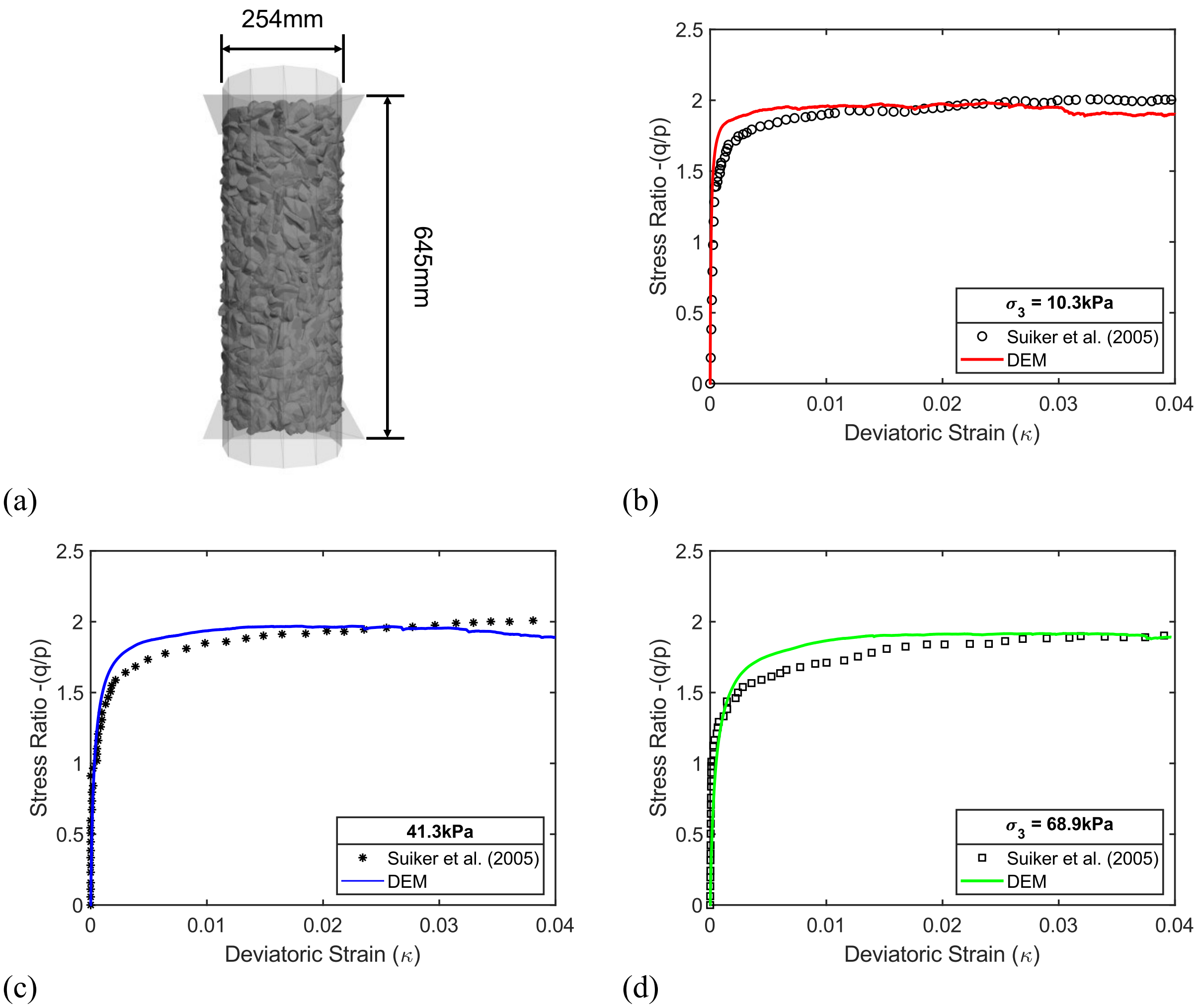

Figure 5.3: (a) Simulating the triaxial tests performed by Suiker et al. (2005) and comparing the experimental data with the discrete element simulations at confining pressures of (b) 10.3kPa, (c) 41.3kPa, and (d) 68.9kPa.

5.3.2. Geogrid

To capture the micromechanical features of the geogrid-ballast interaction mechanisms numerically, the large aperture biaxial polypropylene geogrid used by Desbrousses et al. (2023) in their experimental work is modeled. The geogrid's discrete element model is created following the grid generation procedure developed by Stahl et al. (2014) and Itasca (2019) in which geogrids are modeled as strings of overlapping spheres joined by linear parallel bonds as shown in Figure 5.4. The linear parallel bond contact model provides the behavior of two interfaces and simulates the presence of cementing material between two contacting particles. The first interface is analogous to the linear contact model insofar as it carries a force, does not resist relative particle rotation, and permits slippage by applying a Coulomb limit on the shear force. The second interface, called the parallel bond, acts in tandem with the first one. It establishes an elastic interaction between contacting particles that transmits both a force and a moment through a set of elastic springs distributed over the contact plane. The parallel bond contact parameters are defined using the deformability method whereby the bond's normal and tangential spring stiffnesses ($\overline{k_n}$ and $\overline{k_s}$) are characterized by the bond effective modulus ($\overline{E^*}$) and the bond normal-to-shear stiffness ratio ($\overline{\kappa^*}$) where:

$$\overline{k_n} = \frac{\overline{E^*}}{L} \tag{5.9}$$

$$\overline{k_s} = \frac{\overline{k_n}}{\overline{\kappa^*}} \tag{5.10}$$

$$L = \begin{Bmatrix} R^{(ball\ 1)} + R^{(ball\ 2)}, & ball - ball \\ R^{(ball\ 1)}, & ball - facet \end{Bmatrix} \tag{5.11}$$

Table 5.2: Contact Model Parameters Used for the Ballast Particles and the Box's Walls.

Parameter	**Value**
Clumps (Ballast)	
Particle density ρ (kg/m^3)	2,741
Effective modulus E^* (MPa)	325
Normal-to-shear stiffness ratio κ^*	1
Friction coefficient μ	0.55
Facets (Side Walls)	
Effective modulus E^* (MPa)	325
Normal-to-shear stiffness ratio κ^*	1
Friction coefficient μ	0.55
Facets (Bottom Wall)	
CBR = 25	
Normal and shear stiffnesses k_n, k_s (N/m)	1×10^6
Friction coefficient μ	0.55
CBR = 5	
Normal and shear stiffnesses k_n, k_s (N/m)	2×10^5
Friction coefficient μ	0.55

The linear parallel bond contact model parameters are calibrated by simulating a single-rib tensile test, a multi-rib tensile test, and an aperture stability modulus test and comparing the results with the tensile test data published by Desbrousses et al. (2021, 2023a) and the aperture stability modulus provided by the geogrid's manufacturer (Titan Environmental Containment, 2020). Given that the parallel bond provides the behavior of a linear elastic cementing material between contacting particles, the viscoelastic behavior typically displayed by polymeric geogrids may not be captured in the simulated tensile tests. As such, the contact model parameters are calibrated to match the geogrid's tensile strength at 2% strain due to the almost linear relationship between force and elongation exhibited by the biaxial geogrid during tensile testing (Gao & Meguid, 2018; Han et al., 2012; McDowell et al., 2006; N. T. Ngo et al., 2014). The single-rib and multi-rib tensile tests are simulated to comply with the requirements outlined in ASTM D6637 Method A and B respectively.

The simulated geogrid consists of thick longitudinal and transverse ribs composed of fifteen overlapping spheres with a radius of 3mm. The nodes are represented by larger spheres with a radius of 3.5mm each surrounded by eight smaller node balls with a radius of 1.75mm to give the junction the required torsional stiffness. The geogrid specimen used in the single-rib tensile test simulation is 285mm long and comprises six junctions thereby closely matching the dimensions of the geogrid specimens used in the tensile tests performed by Desbrousses et al. (2021, 2023a). Similarly, the multi-rib geogrid specimens used in the multi-rib tensile test simulation are 285mm long and 228mm wide, having six junctions in the direction of testing as shown in Figure 5.4. Both the single-rib and multi-rib tensile tests are performed by fully restraining the motion of the bottom rib of the tested sample and applying a constant velocity corresponding to a strain rate of 10% strain/min in the testing direction to the topmost rib or rib junction. The results from the numerical tensile tests are compared with the available experimental data for geogrids tested at room temperature (20ºC) in Figure 5.5a and b. In order to investigate the effect of geogrid stiffness on the grid's ability to stabilize railroad ballast, additional tensile tests are simulated and compared with the geogrid's 2% strain tensile strength determined at -30, -10, 10, 20, and 40ºC by Desbrousses et al. (2021, 2023a). The corresponding contact model parameters are summarized in Table 5.3. It is noteworthy that the linear parallel bond contact model's effective modulus E^* is set to a very low value to preclude the development of large contact forces between the geogrid's overlapping spheres.

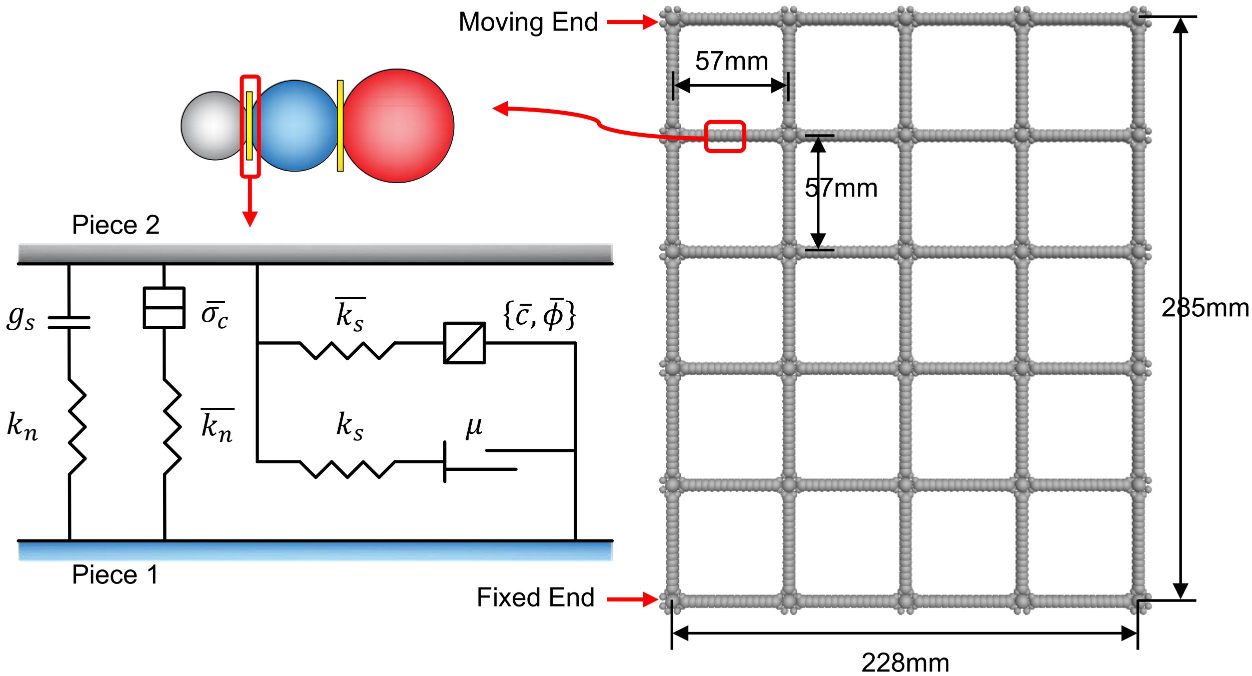

Figure 5.4: Discrete Element Model of the Biaxial Geogrid Showing the Boundary Conditions Used in the Multi-Rib Tensile Test and the Rheological Components of the Linear Parallel Bond Contact Model.

The modeled geogrid's torsional stiffness is assessed by simulating an aperture stability modulus test following the procedure outlined in ASTM D7864 in which a square geogrid sample is generated and clamped along its four outer edges as shown in Figure 5.6a. The central junction is then subjected to a twisting moment (M_t) of 2N.m by applying a force (F) to each of the four ribs emanating from the junction at points located at a distance (r) of 12.7mm +/- 1mm away from it. The geogrid's torsional stiffness (k_t) is then calculated by dividing the twisting moment (M_t) by the resulting rotation (θ_t) as follows:

$$k_t = \frac{M_t}{\theta_t} \tag{5.12}$$

Table 5.3: Contact Model Parameters Used for the Biaxial Geogrid.

Parameter	**Value**
Geogrid	
Particle density ρ (kg/m^3)	950
Effective modulus E^* (MPa)	1×10^{-8}
Normal-to-shear stiffness ratio κ^*	1
Tensile strength $\bar{\sigma}_c$ (MPa)	1×10^{14}
Cohesion $\bar{c}$ (MPa)	1×10^{14}
T=-30ºC	
Bond effective modulus $\overline{E^*}$ (MPa)	750
Bond normal-to-shear stiffness ratio $\overline{k^*}$	1
T=-10ºC	
Bond effective modulus $\overline{E^*}$ (MPa)	680
Bond normal-to-shear stiffness ratio $\overline{k^*}$	1
T=10ºC	
Bond effective modulus $\overline{E^*}$ (MPa)	610
Bond normal-to-shear stiffness ratio $\overline{k^*}$	1
T=20ºC	
Bond effective modulus $\overline{E^*}$ (MPa)	465
Bond normal-to-shear stiffness ratio $\overline{k^*}$	1
T=40ºC	
Bond effective modulus $\overline{E^*}$ (MPa)	400
Bond normal-to-shear stiffness ratio $\overline{k^*}$	1

For the chosen contact model parameters, the application of a twisting moment of 2N.m caused a rotation of 2.67º (see Figure 5.6b), giving a torsional stiffness of 0.748N.m/deg which closely matches the 0.75N.m/deg reported by the geogrid's manufacturer (Titan Environmental Containment, 2020). The contact model parameters used for the geogrid are presented in Table 5.3. It is noteworthy that a low value (1×10^{-8}MPa) is assigned to the effective modulus component of the linear parallel bond contact model. This is necessary to preclude the development of large tensile forces in the parallel bonds caused by the occurrence of linear contact forces stemming from the overlap between contacting geogrid spheres (Stahl et al., 2014).

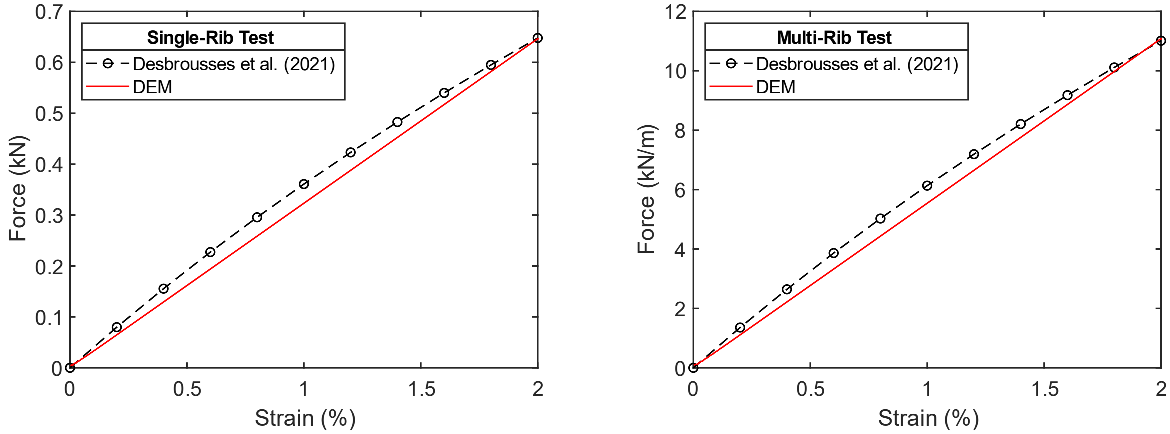

(a) (b)

Figure 5.5: Comparing Experimental Data Obtained by Desbrousses et al. (2021) with the Discrete Element Simulations of the (a) Single-Rib and (b) Multi-Rib Tensile Tests.

5.3.3. Ballast Box and Geogrid-Ballast Assemblies

A ballast box with plan dimensions identical to those used by Desbrousses et al. (2023) in their experiments is created in *PFC 3D* using facets. The linear contact model is used to characterize the interactions between the ballast particles and the box's side walls using the same contact parameters (i.e., E^* and μ) as those used for the ballast particles. Assigning identical contact model parameters to the clumps and facets is commonly used in DEM simulations of ballast box tests (C. Chen et al., 2012, 2015; H. Li & McDowell, 2020, 2018; Lim & McDowell, 2005). A 300mm-thick ballast layer is then generated in six 50mm-thick lifts using the Improved Multi-Layer Compaction Method (IMCM) developed by Lai et al. (2014) and used in multiple discrete element studies to generate geogrid-reinforced soil samples (J. Chen, Bao, et al., 2022; Gao & Meguid, 2018; Lai et al., 2014). The sample generation process takes place in a gravity-free environment with the friction coefficient set to zero for the clumps and the facets.

The first lift is created by generating a cloud of non-overlapping clumps in the box and compressing it using a rigid platen until the desired porosity is reached, at which point the model is cycled to equilibrium. The second lift is then generated in a similar fashion, compressed above the first lift using a second rigid platen, and cycled to equilibrium at which point the wall separating the two lifts is deleted and the model is cycled to equilibrium again. The process is repeated until the desired height of the ballast layer is reached. When a geogrid is to be incorporated in the ballast layer and its placement depth is attained during the sample generation process, a geogrid with plan dimensions of 1,000×700mm is created within a sleeve consisting of two rigid walls to preclude contacts between the grid and the surrounding clumps during the generation process. The grid balls are then fixed such that they may not translate nor rotate. A subsequent ballast layer is then created above the geogrid, compressed to the desired porosity, and cycled to equilibrium. The geogrid's protective sleeve is then removed, allowing it to come into contact with the surrounding ballast particles. Once the ballast sample is fully generated, gravity is turned on, the coefficient of friction for the clumps, facets, and geogrid balls is set to its final value, the geogrid balls are freed such that the geogrid may deform freely within the ballast sample, and the model is cycled to equilibrium. A tie with plan dimensions of 203×301mm is then placed at the top of the compacted granular assembly. The sample generation process is illustrated in Figure 5.7.

To simulate the presence of subgrades with equivalent California Bearing Ratios (CBR) of 25 and 5 beneath the ballast layer, the normal and shear contact stiffnesses of the ballast box's bottom facets are modified. The contact stiffness values are calibrated and validated by simulating the first twenty load cycles of the unreinforced ballast box tests performed by Desbrousses et al. on ballast layers supported by subgrades with CBRs of 25 and 5. This involved subjecting unreinforced ballast layers to cyclic loading with a mean compressive load of 14kN, a loading amplitude of 10.5kN, and a frequency of 0.8Hz and monitoring the tie settlement response obtained numerically and comparing it with the available experimental data. The spring stiffness values assigned to the box's bottom wall are summarized in Table 5.2.

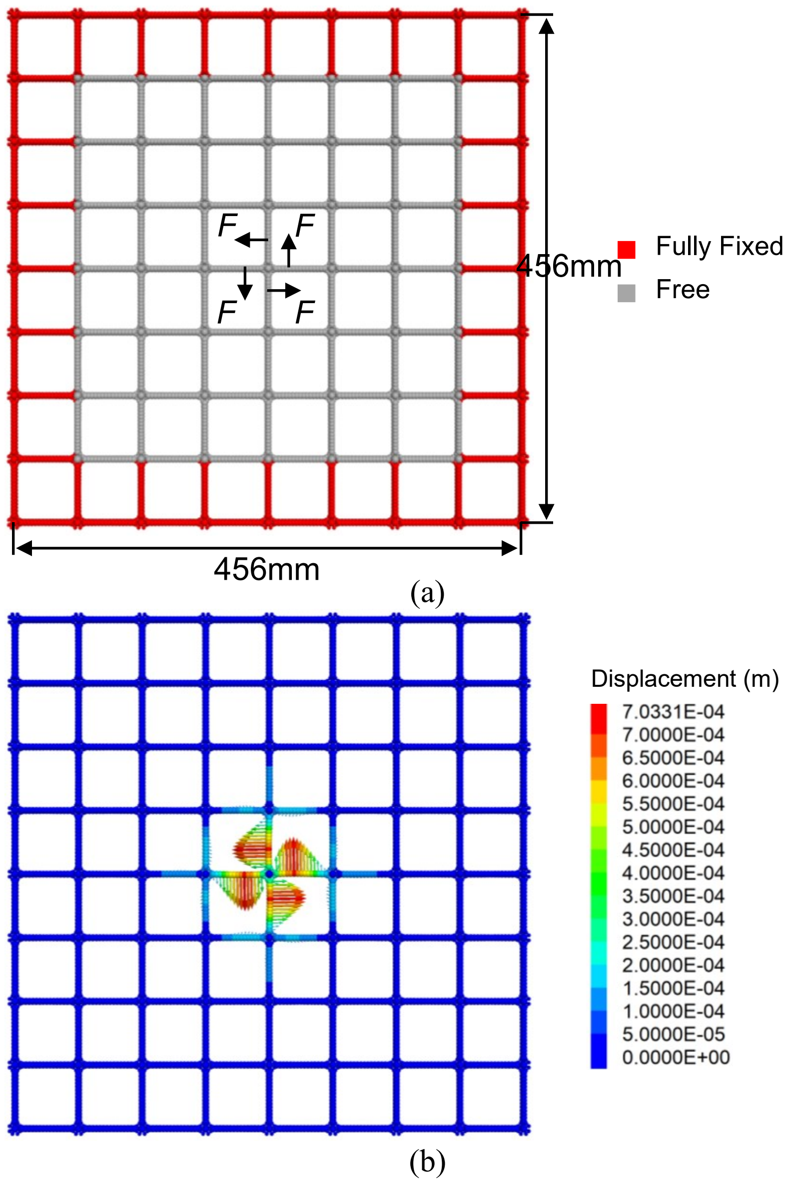

Figure 5.6: (a) Boundary Conditions Used in the Aperture Stability Modulus Test and (b) Displacement of the Geogrid Ribs Following the Application of the Twisting Moment.

5.3.4. Simulation Summary

In this study, each ballast box simulation involves the application of cyclic loading to the tie for twenty load cycles at a frequency of 10Hz with a mean load of 14kN and a load amplitude of 10.5kN. Two subgrade conditions are considered, with CBRs of 25 and 5. For each subgrade, six ballast box tests are carried out: one with an unreinforced ballast layer and five with geogrid-reinforced ballast assemblies, where the geogrid is placed at depths ranging from 50 to 250mm below the tie, in 50mm intervals. This setup is chosen to assess how different geogrid placement depths affect the mechanical properties of geogrid-reinforced ballast. Upon investigating the effect of the geogrid placement depth, the influence of the geogrid aperture size (A) and geogrid stiffness are studied. The geogrid aperture size is varied from 30×30mm to 80×80mm, giving rise to aperture-size-to-ballast-diameter (A/D) ratios from 1.09 to 2.91 while the geogrid stiffness is set to values ranging from 9.54 to 18.00kN/m. An overview of the simulations presented in this paper is provided in Table 5.4.

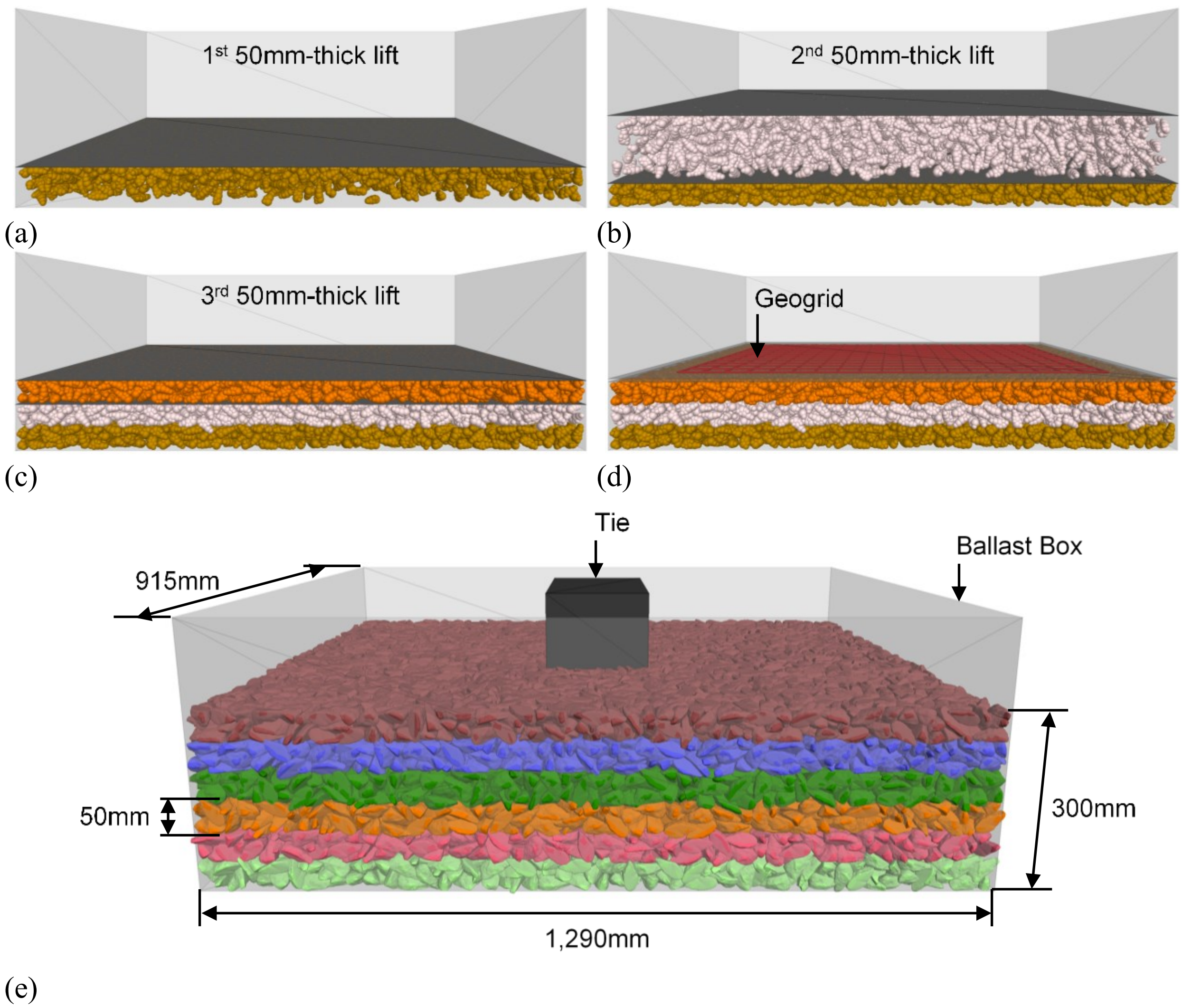

Figure 5.7: Sample Generation Procedure Using the Improve Multi-Layer Compaction Method (IMCM) Showing the (a) Generation of the First 50mm-Thick Lift, (b) Creation of the Second Lift, (c) Compaction of the Third Lift, (d) Incorporation of a Geogrid 150mm Above the Box, and (e) Compacted 300mm-Thick Ballast Layer.

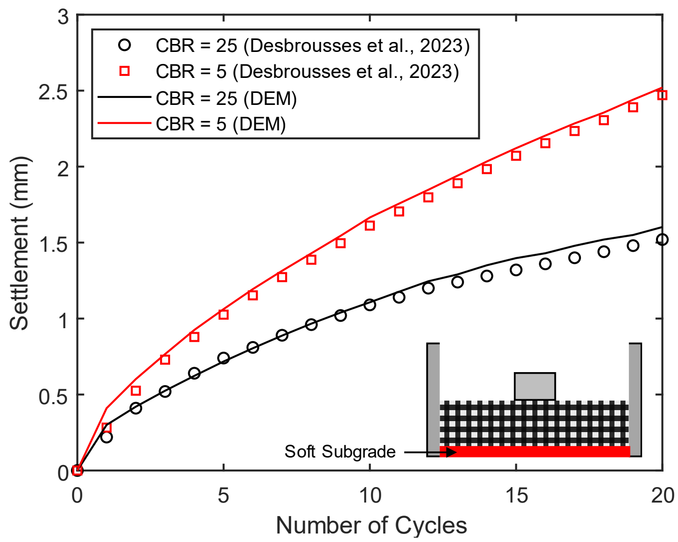

Figure 5.8: Calibrating the Box's Bottom Wall's Spring Stiffness to Simulate the Presence of Subgrades with CBRs of 25 and 5 Below the Ballast Layer.

Table 5.4: Simulation Summary.

Subgrade Strength (CBR)	Geogrid Depth (mm)	A/D Ratio	Geogrid Stiffness (kN/m)
25	50, 100, 150, 200, 250	2.07	11.01
5	50, 100, 150, 200, 250	2.07	11.01
5	150	1.09, 1.45, 1.82, 2.07, 2.55, 2.91	11.01
5	150	2.07	18.00, 16.28, 14.61, 11.01, 9.54

It is imperative to clarify that the primary objective of these simulations is not to replicate the exact outcomes observed in Desbrousses et al.'s experimental work. Instead, the discrete element simulations presented herein are exploratory in nature and are strategically designed to delve into the intricate micromechanical features of ballast-geogrid interactions. All micromechanical contact parameters employed in these simulations have been rigorously calibrated using existing experimental data, ensuring a robust and realistic representation of the physical behavior of the materials involved. The focus of this study is on qualitatively examining the underlying mechanisms influencing the behavior of geogrid-reinforced ballast under cyclic loading, particularly in terms of particle displacement, rotation, velocity, and the development of interparticle contacts. Deliberate variations in the loading frequency and the number of load cycles, allow for a broader exploration of simulation scenarios, thereby enhancing the study's scope while keeping the simulation time within reasonable limits.

5.4. Results and Analysis

5.4.1. Macroscopic Behavior

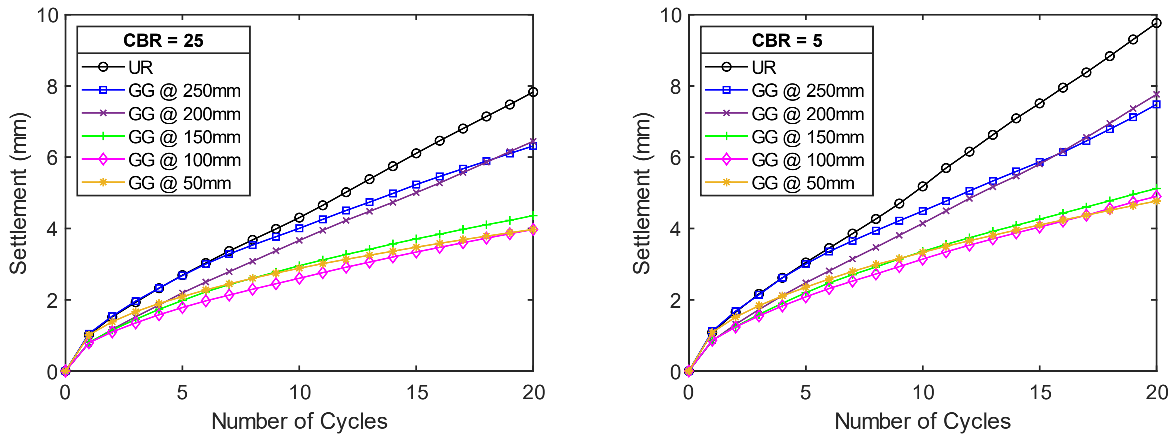

(a) (b)

Figure 5.9: Accumulation of Tie Settlement in Unreinforced and Geogrid-Reinforced Ballast Layers Supported by a Subgrade with a CBR of (a) 25 and (b) 5.

The macroscale response of ballast layers supported by subgrades with a CBR of 25 and 5 is investigated by analyzing the evolution of the tie's settlement shown in Figure 5.9a and b respectively. In ballast box tests performed over a competent subgrade (CBR of 25), the largest tie settlement takes place in the unreinforced ballast layer, culminating at a value of 7.83mm after twenty load cycles. The tie's permanent displacement decreases following the introduction of a geogrid in the ballast layer, although this reduction is sensitive to the geosynthetic's placement depth. At the end of the twenty load cycles, the tie resting on ballast assemblies reinforced with geogrids placed at depths of 200mm and 250mm settles by 6.45mm and 6.31mm respectively, which represents respective settlement reductions of 17.67% and 19.34% compared to the unreinforced case. Incorporating a geogrid at a shallower location in the ballast layer, i.e., 50mm, 100mm, and 150mm beneath the tie, leads to markedly smaller tie settlements of 3.97mm, 3.97mm, and 4.36mm, representing settlement reductions of 49.23%, 49.26%, and 44.27% respectively compared to the unreinforced ballast layer.

Greater tie settlements invariably develop in ballast layers supported by a weaker subgrade (CBR of 5) as illustrated by Figure 5.9b. Similar to the trends observed in the ballast beds overlying a subgrade with a CBR of 25, the maximum tie settlement occurs in the unreinforced ballast assembly, reaching a total value of 9.76mm. The reduction in tie settlement generated by the placement of a geogrid in the ballast layer exhibits features akin to those encountered in ballast box tests performed on a more competent subgrade. Geogrids placed deep into the ballast layer, i.e., 200mm and 250mm below the tie, are less effective at minimizing the tie's settlement compared with geogrids positioned within the layer's upper 150mm. The lowest reductions in tie settlement of 23.37% and 20.38% are obtained in ballast assemblies reinforced with geogrids located 250mm and 200mm beneath the tie respectively. However, incorporating geogrids at depths of 50mm, 100mm, and 150mm results in respective tie settlement reductions of 51.15%, 49.81%, and 47.55%. It is also noteworthy that, on average, greater reductions in tie subsidence are achieved by geogrids when the underlying subgrade is weak.

The settlement curves shown in Figure 5.9 indicate that not all ballast layers exhibit the same rate of settlement growth as the number of load cycles increases. Indeed, the unreinforced ballast layers along with the ones reinforced with geogrids placed 200mm and 250mm below the tie possess a steeper rate of settlement accumulation than that of geogrid-reinforced ballast beds where geogrids are located in the upper 150mm. To examine this pattern, the incremental non-recoverable vertical tie displacement recorded in ballast assemblies supported by subgrades with a CBR of 25 and 5 is plotted in Figure 5.10a and b respectively.

Figure 5.10a and b indicate that all ballast samples initially undergo significant residual settlement following the application of the first load cycle. This is then followed by a progressive decline in the rate at which residual settlement accumulates under further cyclic loading. Interestingly, ballast beds reinforced with geogrids positioned at depths of 50mm, 100mm, and 150mm see their incremental residual tie settlement stabilize as the number of cycles increases. This suggests that these layers gradually reach a stable state in which the large initial tie subsidence was caused by significant rearrangements of the soil fabric as ballast particles moved and slid past each other to form a denser state. However, this phenomenon is not observable in the unreinforced ballast layers nor the ballast beds reinforced with geogrids located 200mm and 250mm under the tie. The incremental tie settlement in these three cases fluctuates as cyclic loading continues, particularly in the case of a weak subgrade (CBR of 5). These variations suggest that considerable rearrangement of the soil fabric keeps occurring as cyclic loading continues and hint at the fact that these ballast assemblies are likely to experience a sustained accumulation of residual tie settlement under further repeated loading while simultaneously highlighting the superior settlement-abating ability of geogrids situated within the upper 150mm of the ballast layers.

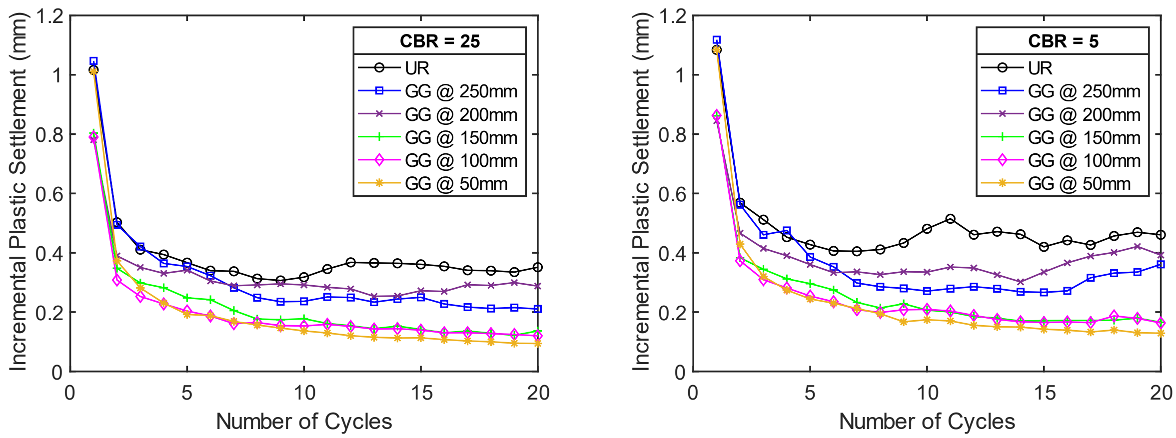

(a) (b)

Figure 5.10: Variations in the Incremental Tie Settlement with Cyclic Loading in Unreinforced and Geogrid-Reinforced Ballast Layers Supported by a Subgrade with a CBR of (a) 25 and (b) 5.

The results presented in Figure 5.9 and 5.10 illustrate the macroscopic manifestations of the incorporation of biaxial geogrids in 300mm-thick ballast layers. The deformation response of geogrid-reinforced ballast is particularly sensitive to the placement depth of geogrid reinforcement, with geogrids positioned closer to the tie yielding greater reductions in tie settlement. Additionally, although greater settlement magnitudes are recorded in ballast assemblies resting on a subgrade with a CBR of 5, similar deformation patterns develop ballast samples supported by the two subgrades considered in this section.

In the following sections, a microscopic analysis is conducted to explore the micromechanical behavior of unreinforced and geogrid-reinforced ballast subjected to cyclic loading. A particular emphasis is placed on investigating the impact of geogrids on the ballast particles' translational and rotational motion, coordination number, contact orientation, and the energy dissipated through frictional sliding during cyclic loading. For the sake of brevity and given the similar patterns observed in ballast layers supported by subgrades with CBRs of 25 and 5, the analysis is confined to the ballast box tests performed over a subgrade with a CBR of 5.

5.4.2. Microscale Response

5.4.2.1. Particle Displacement Vectors

To study the reinforcing mechanisms involved in the behavior of geogrid-reinforced ballast, the motion of the ballast particles contained in the ballast box is examined. The total displacement vectors of ballast particles in the unreinforced and geogrid-reinforced ballast box tests obtained during the twentieth load cycle are plotted at the same scale in Figure 5.11a to f.

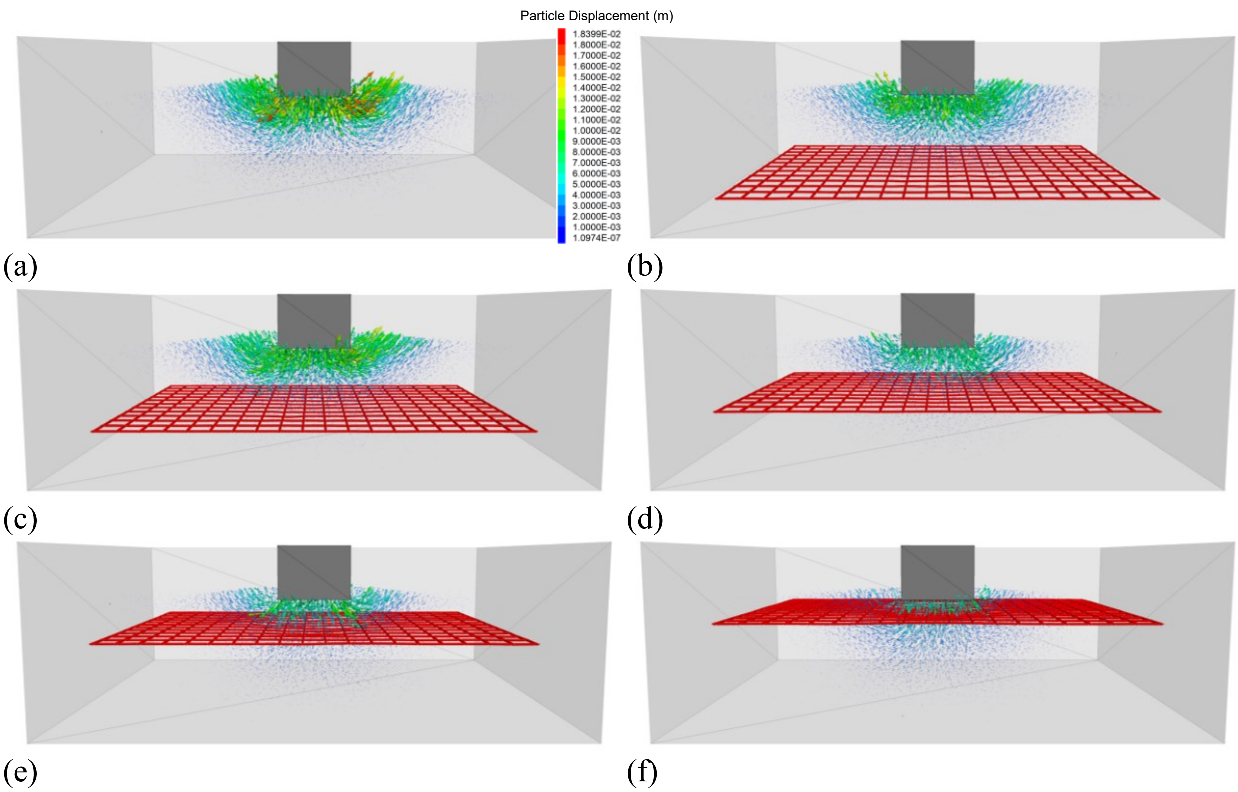

Figure 5.11: Total Displacement Vectors (in Meters) Plotted at the Same Scale during the Twentieth Load Cycle in the (a) Unreinforced Ballast Layer and Geogrid-Reinforced Ballast Layers with Geogrids Located at Depths of (b) 250mm, (c) 200mm, (d) 150mm, (e) 100mm, and (f) 50mm.

The displacement vectors provide a first glimpse into the micromechanical processes involved in the evolution of the tie settlement observed in Figure 5.9. Among all the ballast box experiments, the tie resting on the unreinforced ballast layer experiences the highest cumulative settlement. Figure 5.11a illustrates the effect of this subsidence at the particle level, where the displacement vectors of the particles are noticeably larger than those in geogrid-reinforced ballast assemblies.

Furthermore, the most significant particle displacements occur in the layer's upper half. Directly beneath the tie, ballast aggregates primarily exhibit vertical movements, while particles on the tie's sides predominantly displace laterally. In contrast, the lower half of the ballast assembly experiences comparatively smaller particle displacements. This indicates the existence of an active zone, marked by substantial particle movement within the top 150mm of the ballast layer, and a stable zone in the lower half, characterized by minimal particle movement.

Incorporating geogrids at depths of 250mm and 200mm, as shown in Figure 5.11b and c, results in modest decreases in the magnitude of the particle displacement vectors. Substantial particle movement persists in the ballast bed's upper half, with notable lateral displacements in particles adjacent to the tie. While the geogrids do mitigate particle motion, the reduction is somewhat limited, aligning with the observed accumulation of tie settlement in Figure 5.9b.

Figure 5.11d to f highlight the impact of the geogrid placement depth on tie settlement. Figure 5.11d demonstrates that positioning a geogrid 150mm beneath the tie significantly alters the particle displacement vectors, changing both the magnitude and direction of particle movement. The most noticeable shifts occur around the tie, with reduced lateral displacements compared to both the unreinforced ballast bed and samples with geogrids at depths of 200mm and 250mm. This suggests that the closer the geogrid is to the active zone, the more effectively it curtails particle movement, particularly limiting lateral displacements. Figure 5.11e and f, illustrating ballast layers reinforced with geogrids placed at depths of 100mm and 50mm respectively, support this observation. A notable trend emerges whereby as the geogrid is placed nearer to the tie, there is a progressive decrease in the magnitude of the displacement vectors, especially in lateral movements, reaching a peak efficacy with the geogrid positioned 50mm below the tie.

From a practical perspective, the observed reductions in lateral particle displacement can be tied to the lateral flow of ballast particles observed in typical ballasted tracks. Railroad ballast is essentially a self-supporting material that is generally exposed to low confining pressures (i.e., 5-40kPa) (Hussaini et al., 2015; Hussaini & Sweta, 2021; Indraratna et al., 2005; Lackenby et al., 2007; Thakur et al., 2013). The absence of lateral resisting forces allows ballast particles to spread laterally when subjected to cyclic loading, leading to an increase in track deformation and ballast degradation (Hussaini et al., 2016; Indraratna et al., 2005; Selig & Waters, 1994). Analyzing the lateral displacement of ballast particles in the simulated ballast box tests demonstrates the ability of geogrids to laterally confine unbound granular materials like ballast through the formation of a geogrid-ballast interlock that resists the particles' lateral movement. This reduction in lateral displacement then translates into the tie undergoing a smaller total settlement.

5.4.2.2. Particle Translational and Rotational Motion

Figure 5.12 illustrates the average particle velocity across the height of each 300mm-thick ballast layer. In every scenario, particle velocity increases steadily from the base of the box up to 150mm, aligning with the stable zone of minimal particle displacement observed in Figure 5.11a to f. Above 150mm, the average particle velocity increases significantly, corresponding to the active zone of intense particle displacement. The unreinforced ballast layer shows the highest particle velocities throughout its height compared to the geogrid-reinforced granular assemblies, peaking at 5.51mm/s near the top.

For layers with geogrids at 200mm and 250mm depths, the pattern of particle velocity change is similar to that of the unreinforced layer, albeit with lower overall magnitudes. Below 150mm, velocities in these layers are nearly identical. Above this height, both layers exhibit a substantial increase in average particle velocity, with the layer containing a geogrid at 200mm showing a slightly higher maximum velocity of 5.26mm/s compared to 3.76mm/s for the layer reinforced with a geogrid placed at a depth of 250mm.

The velocity profiles of ballast assemblies reinforced with geogrids placed at shallower depths (150mm, 100mm, and 50mm) are markedly different from the previously mentioned layers. In the stable zone, particle velocities remain almost constant up to around 150mm across all three layers. However, in the active zone, the increase in particle velocity is less pronounced than in both the unreinforced layer and layers with geogrids placed at depths of 200mm and 250mm. The layers with geogrids at 100mm and 150mm shown similar velocity increases, with maximum velocities of 2.00mm/s and 1.76mm/s respectively occurring near the top. The layer with a geogrid situated 50mm under the tie exhibits only slight increases in velocity in the active zone, reaching a peak of 0.97mm/s. This reduced velocity increase in the active zone for ballast layers with geogrids at depths of 50mm, 100mm, and 150mm indicates the effectiveness of geosynthetics in stabilizing the ballast aggregate, preventing its excessive displacement and thereby minimizing the resulting tie settlement.

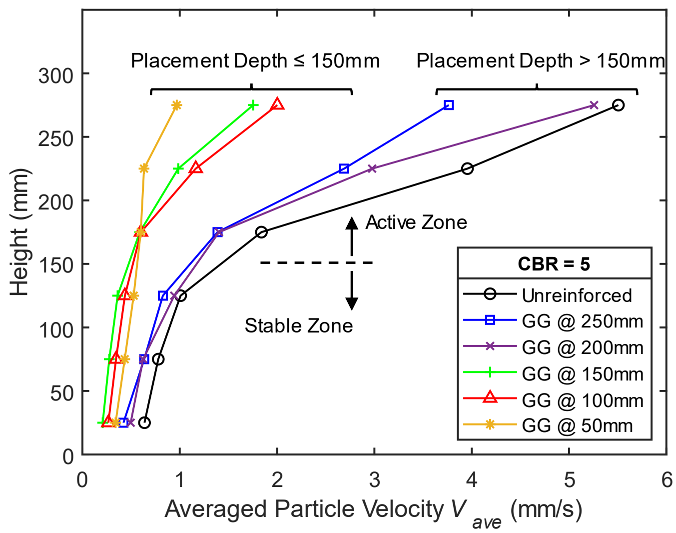

(a)

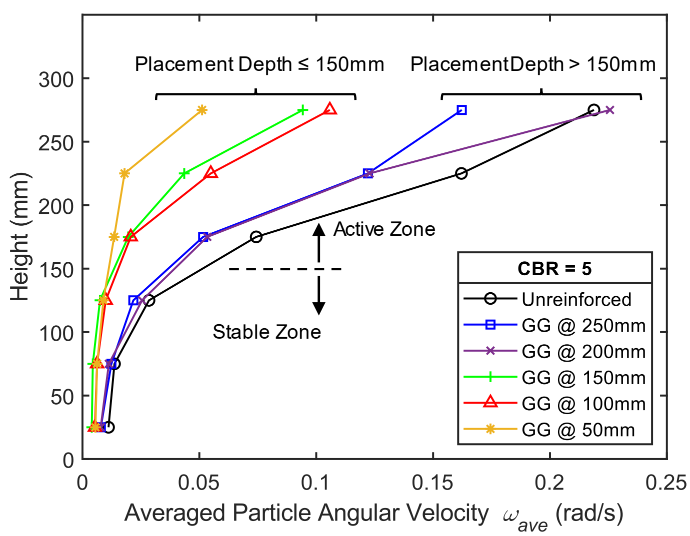

(b)

Figure 5.12: (a) Variation of the Average Particle Velocity with Depth as a Function of the Geogrid Placement Depth and (b) Effect of the Geogrid Location on the Variation of Average Particle Angular Velocity with Depth.

The inclusion of geogrids in the ballast assemblies impacts the rotational motion of ballast particles. Figure 5.12b presents the evolution of the average angular velocity of ballast particles along the height of each layer. In the unreinforced ballast layer, a noticeable uptick in angular velocity starts at a height of 125mm, escalating sharply in the active zone. Ballast layers with geogrids located at depths of 200mm and 250mm exhibit similar patterns with relatively constant angular velocities in the stable zone followed by a rapid increase with height in the active zone. Peak angular velocities in the unreinforced layer and those reinforced with geogrids at 250mm and 200mm reach 0.22rad/s, 0.16rad/s, and 0.23rad/s respectively.

On the other hand, ballast layers with geogrids at 150mm, 100mm, and 50mm demonstrate considerably lower angular velocities. These layers maintain nearly uniform angular velocities in the stable zone. In the active zone, the layers with geogrids at 150mm and 100mm display similar trends of angular velocity increase, reaching maximums of 0.09rad/s and 0.11rad/s respectively. The layer with a geogrid placed 50mm beneath the tie shows the smallest increase in angular velocity within the active zone, peaking at 0.05rad/s. This indicates a more pronounced effect of geogrids at shallower depths in mitigating the rotational motion of ballast particles.

5.4.2.3. Contact Force Chains

Under cyclic loading, ballast particles reorganize to bear the applied loads, transmitting forces via interparticle contacts that create a complex network of force chains. As Radjai et al. (1997, 1998) and Thornton and Antony (1998) stated, these contacts may be divided into two subnetworks: a strong network with forces (F_c) larger than the average contact force ($\overline{F_c}$), and a weak contact network carrying forces smaller than the average contact force. The strong contact network, mainly aligned with the deviator stress direction, consists of continuous force chains that provide the bulk of the soil's shear strength (Lai et al., 2014; Y. Liu & Yan, 2023). Conversely, the weak network forces are usually perpendicular to the strong network and support the stability of strong force chains (J. Liu et al., 2020; Minh et al., 2014). Chen et al. (2022) further classified the strong contact network in geogrid-reinforced soils under monotonic loading into three types: Type I ($\overline{F_c} \leq F_c < 2\overline{F_c},$), Type II ($2\overline{F_c} \leq F_c < 3\overline{F_c}$), and Type III ($F_c \geq 3\overline{F_c}$), noting that Type III contacts play an important role in stress dispersion and load transfer, both vertically to the soil's support and horizontally to Type I and II contacts (J. Chen, Bao, et al., 2022).

Figure 5.13a to f depict the contact force networks in both unreinforced and geogrid-reinforced ballast layers during the twentieth load cycle. Contact forces are represented by cylinders, with thicker ones indicating greater forces. Each network comprises a weak contact network and three strong contact subnetworks (Type I, II, and III) based on the classification proposed by Chen et al. (2022). Across all samples, Type III forces exhibit a primarily vertical orientation and are located beneath the tie, correlating with the direction of the applied compressive load. Meanwhile, Type I and II contacts are oriented more laterally, consistent with Chen et al.'s findings. The unreinforced ballast layer exhibits the highest mean contact force of 12.59N, while the incorporation of geogrids generally reduces the average contact force, with the lowest one being recorded in the layer reinforced with a geogrid at a depth of 150mm.

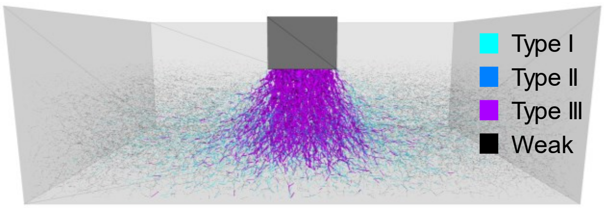

(a) Mean force: 12.59N
Max force: 1,003.45N

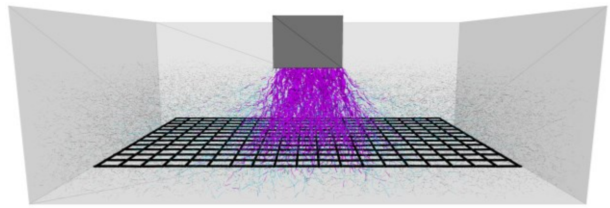

(b) Mean force: 12.05N
Max force: 1,239.36N

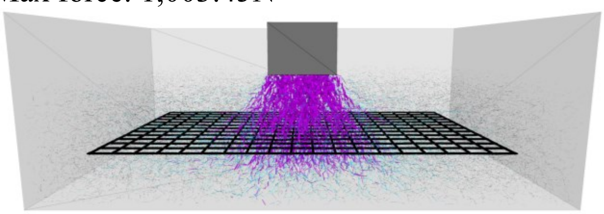

(c) Mean force: 11.94N
Max force: 1,851.87N

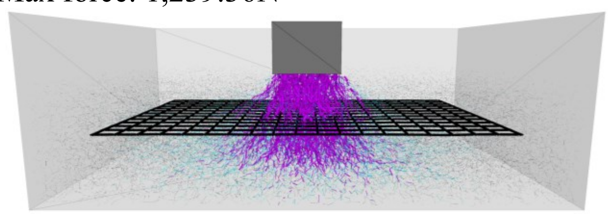

(d) Mean force: 11.24N
Max force: 904.81N

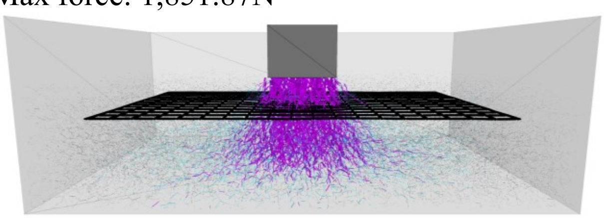

(e) Mean force: 11.69N
Max force: 1,036.19N

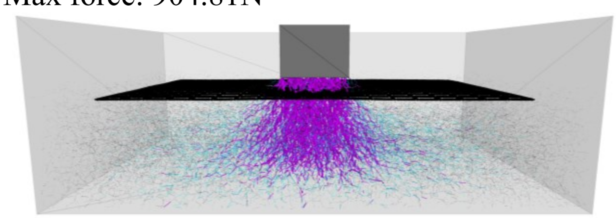

(f) Mean force: 12.04N
Max force: 855.81N

Figure 5.13: Contact Force Chains During the Twentieth Load Cycle in (a) Unreinforced and Reinforced Ballast Layers with a Geogrid Located at a Depth of (b) 250mm, (c) 200mm, (d) 150mm, (e) 100mm, and (f) 50mm.

The impact of the geogrid placement depth on the average Type III contact force within select ballast layers is examined in Figure 5.14. For clarity, the figure only includes the contact force variations of the unreinforced ballast layer and layers with geogrids positioned at depths of 250mm, 150mm, and 50mm. The unreinforced layer exhibits the greatest average Type III contact forces throughout its entire height, ranging from 139.14N at the bottom to 245.13N at the top. Adding a geogrid reduces these contact forces, with deeper placement depths (e.g., 250mm) resulting in smaller force reductions. On the other hand, shallower placements depth of 150mm and 50mm show more significant decreases in average contact forces. This finding reflects the effect of the geogrid location on the geogrid-induced reductions in tie settlement and particle velocity observed in Figure 5.9b and Figure 5.12a and b.

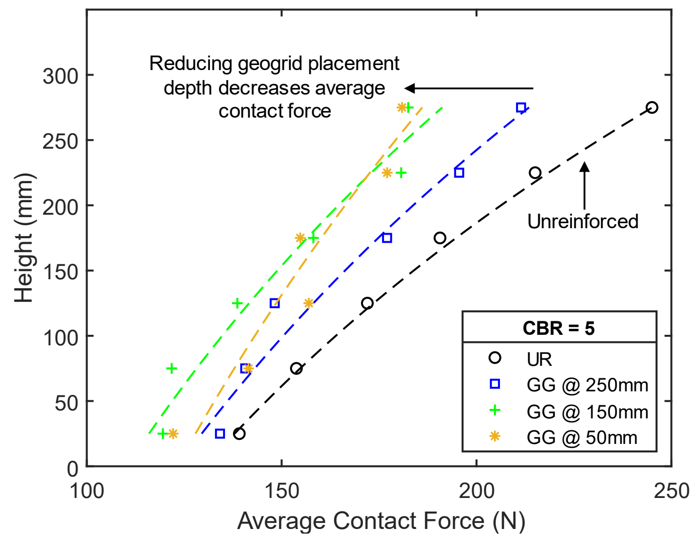

Figure 5.14: Effect of Geogrid Placement Depth on the Variations in Average Contact Force among Type III Contacts in Unreinforced and Geogrid-Reinforced Ballast Assemblies.

The forces transmitted at interparticle contacts are affected by the ballast layer's microstructure and its number of contacts. The number of contacts per particle in a granular assembly is described by the coordination number (CN) which gives a measure of the average number of contacts per particle and packing intensity at the particle level. It is defined as $CN = 2N_c/N_p$ where N_c is the number of contacts in the granular system and N_p is the number of particles (O'Sullivan, 2011). The coordination number affects the macroscopic behavior and stability of granular materials, with a high coordination number being associated with an increased stability and stiffness, enhanced load transfer ability, and reduced potential for particle breakage (Fei & Narsilio, 2020; X. Gu et al., 2014; Luo, Zhao, Bian, et al., 2023; Minh & Cheng, 2013; O'Sullivan, 2011; Ouadfel, 1998).

Figure 5.15 tracks the changes in coordination number across all ballast samples during cyclic loading. A common pattern emerges whereby each layer shows a marked reduction in its coordination number after the first load cycle followed by a gradually decreasing reduction with successive load cycles. The unreinforced layer possesses the lowest coordination number and experience a sustained reduction of its CN during cyclic loading, indicating a weaker particle interconnectivity. This translates into a more deformable soil structure and results in the emergence of higher interparticle contact forces as evidenced by the data plotted in Figure 5.14. By the end of cyclic loading, its coordination number reaches a value of 6.36. In contrast, ballast assemblies with geogrids at depths of 250mm and 200mm exhibit smaller CN decreases than their unreinforced counterpart. Their initial sharp decline in CN transitions to gradual reductions, ending with a CN of 6.55 in both layers.

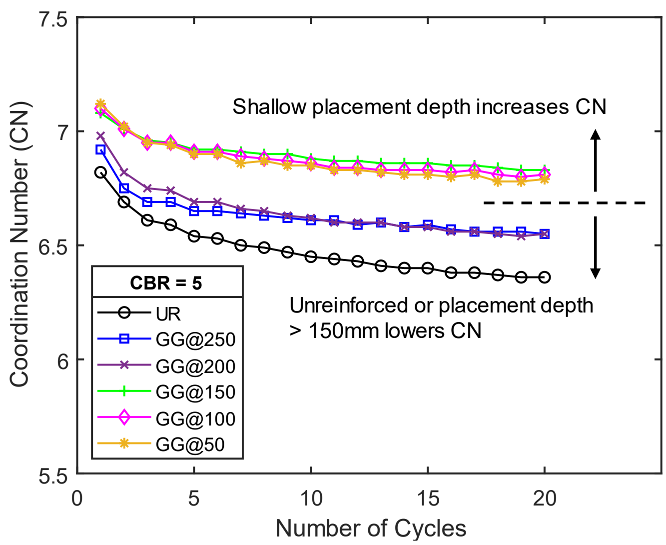

Figure 5.15: Evolution of the Coordination Number during Cyclic Loading in Unreinforced and Geogrid-Reinforced Ballast Layers.

The CN values further reflect the efficacy of geogrids at depths of 150mm and above. Ballast layers with geogrids positioned 150mm, 100mm, and 50mm beneath the tie display minimal changes in their coordination number, reaching final values of 6.78, 6.76, and 6.74 respectively. These higher coordination numbers suggest enhanced particle connectivity, leading to a more stable and stiffer soil structure. Consequently, these layers are more resistant to the applied loads and exhibit reduced interparticle forces (Figure 5.14), potentially indicating a reduced potential for particle breakage.

5.4.2.4. Energy Dissipation

Applying a cyclic compressive load to a ballast assembly through a tie is a process that involves the storage, transformation, and dissipation of energy. External energy is input into the system through the motion of the tie. This energy is then transformed into mechanical energy (E_m), which is a combination of mechanical body energy (E_{mb}) and mechanical contact energy (E_{mc}) expressed as follows (J. Chen, Bao, et al., 2022):

$$E_m = E_{mb} + E_{mc} \tag{5.13}$$

$$E_{mb} = E_{pot} + E_{kin} + E_{damp} \tag{5.14}$$

$$E_{mc} = E_k + E_\mu + \overline{E_k} \tag{5.15}$$

Where E_{pot} is the potential energy, E_{kin} is the kinetic energy, E_{damp} is the energy dissipated by non-viscous damping, E_k is the strain energy stored in the linear springs, E_μ is the energy dissipated by frictional slip, and $\overline{E_k}$ is the strain energy stored in the parallel bond springs (applicable to models where geogrids are present).

In the discrete element simulations presented in this paper, energy dissipation may occur through non-viscous damping and interparticle frictional sliding once the contact's frictional strength is exceeded. To investigate the effect of geogrids on the dissipation of energy at the contact level, the cumulative energy dissipated through frictional slip is tracked during the simulations. The energy dissipated by frictional slip E_μ is expressed as follows:

$$E_\mu = E_\mu - \frac{1}{2}\left(\left(\boldsymbol{F}_s^l\right)_0 + \left(\boldsymbol{F}_s^l\right)\right).\boldsymbol{\Delta\delta}_s^{\boldsymbol{\mu}} \tag{5.16}$$

Where:

$$\boldsymbol{\Delta\delta}_s^{\boldsymbol{\mu}} = \boldsymbol{\Delta\delta}_s - \boldsymbol{\Delta\delta}_s^{\boldsymbol{k}} = \boldsymbol{\Delta\delta}_s - \left(\frac{\boldsymbol{F}_s^l - \left(\boldsymbol{F}_s^l\right)_0}{k_s}\right) \tag{5.17}$$

And $\left(\boldsymbol{F}_s^l\right)_0$ is the linear shear force at the beginning of the timestep, $\boldsymbol{\Delta\delta}_s$ is the adjusted relative shear displacement increment, and $\boldsymbol{\Delta\delta}_s^{\boldsymbol{k}}$ and $\boldsymbol{\Delta\delta}_s^{\boldsymbol{\mu}}$ are the shear displacement's elastic and slip component respectively.

The cumulative energy dissipated through frictional slip in the unreinforced ballast layer and ballast beds reinforced with geogrids located at depths of 150mm, 100mm, and 50mm is illustrated in Figure 5.16. Although a similar amount of energy is dissipated in all ballast layers during the first load cycle, the unreinforced ballast layer experiences a sustained growth in the energy dissipated through interparticle sliding during the twenty load cycles, reaching a total of 162.33J at the end of the ballast box test. The ballast assemblies reinforced with geogrids located in the layers' upper 150mm display reduced tendencies to dissipate energy through frictional sliding.

This is attributed to their better-connected soil structure and the confining effects of the geogrids, which effectively restrains particle movement. Following the first load cycle, the reinforced layers register gradually smaller increases in energy dissipated through frictional slip under additional cyclic loading. At the end of the text, the total energy dissipated in the layers reinforced with geogrids located 150mm, 100mm, and 50mm beneath the tie amount to 102.33J, 105.76J, and 107.63J respectively. It is noteworthy that although the results for the ballast layers reinforced with geogrids positioned 250mm and 200mm below the tie are not presented in Figure 5.16 for brevity, a total of 135.13J and 139.31J respectively is dissipated in each layer, providing an intermediate performance compared to the layers where geogrids are placed closer to the tie.

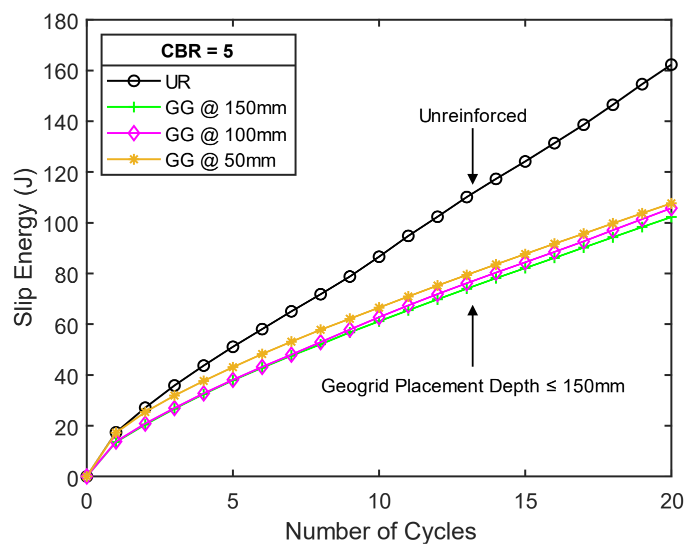

Figure 5.16: Energy Dissipated by Frictional Sliding in the Unreinforced and Reinforced Ballast Layers with Geogrids Located at Depths of 150mm, 100mm, and 50mm.

5.4.3. Geogrid Response

The deformation profiles of geogrids at various depths in ballast layers during the application of the twentieth load cycle are plotted in Figure 5.17a to e. The geogrid positioned 50mm below the tie (Figure 5.17a) exhibits the most notable deformation, characterized by a significant depression at its center directly beneath the tie. This depression aligns with the downward movement of ballast particles observed under the tie as shown in Figure 5.11. In contrast, the ribs surrounding the central area of the geogrid exhibit upward movement, which is consistent with the displacement of ballast aggregates adjacent to the tie. As the geogrid placement depth increases (100mm, 150mm, 200mm, and 250mm in Figure 5.17b to e), the central depression beneath the tie decreases in magnitude. It is noteworthy that the ribs surrounding the centrally depressed area of the grid shift from an upward to a lateral displacement pattern. Additionally, the geogrids placed 200mm and 250mm beneath the tie show markedly reduced deflections, indicating a lesser degree of reinforcement mobilization compared to shallower geogrids.

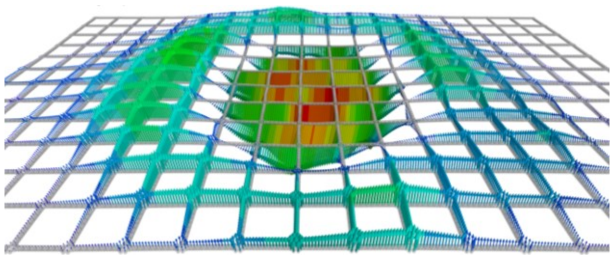

(a) Placement depth: 50mm
Maximum displacement: 5.65mm

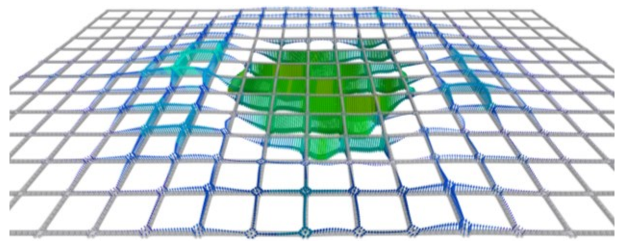

(b) Placement depth: 100mm
Maximum displacement: 4.21mm

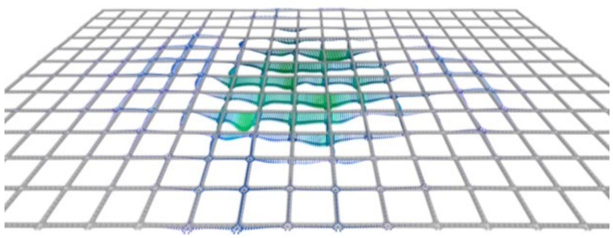

(c) Placement depth: 150mm
Maximum displacement: 2.52mm

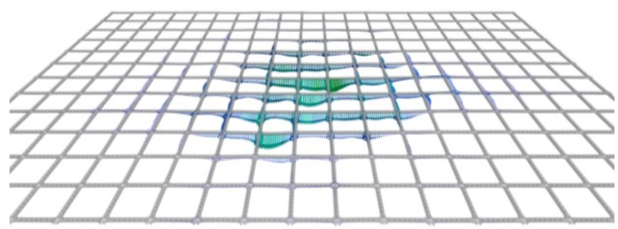

(d) Placement depth: 200mm
Maximum displacement: 2.50mm

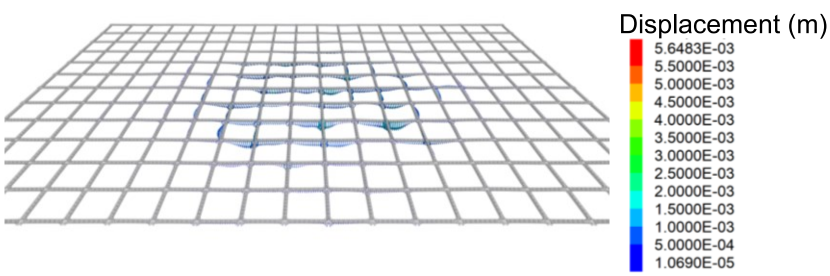

(e) Placement depth: 250mm
Maximum displacement: 1.41mm

Figure 5.17: Total Displacement Vectors (in meters) of the Parallel-Bonded Balls Drawn at the Same Scale for the Geogrids Placed at Depths of (a) 50mm, (b) 100mm, (c) 150mm, (d) 200mm, and (e) 250mm.

The deformation of each geogrid causes strain energy ($\overline{E_k}$) to be stored in the parallel-bonded contacts linking the spheres that make up each reinforcement. The parallel bond strain energy is given by:

$$\overline{E_k} = \frac{1}{2}\left(\frac{\overline{F_n}^2}{\overline{k_n}\bar{A}} + \frac{\|\overline{\boldsymbol{F_s}}\|^2}{\overline{k_s}\bar{A}} + \frac{\overline{M_t}^2}{\overline{k_t}\bar{J}} + \frac{\|\overline{\boldsymbol{M_b}}\|^2}{\overline{k_n}\bar{I}}\right) \tag{5.18}$$

Where $\overline{F_n}$ and $\overline{\boldsymbol{F_s}}$ are the normal and shear components of the parallel-bond force, $\overline{M_t}$ and $\overline{\boldsymbol{M_b}}$ are the twisting and bending moment components of the parallel-bond moment, and $\bar{I}$ and $\bar{J}$ are the moment of inertia and polar moment of inertia of the parallel bond cross-section respectively.

The parallel bond strain energy is tracked during the application of cyclic loading to each geogrid-reinforced ballast assembly to provide a scalar index of the load being carried by each geogrid. The evolution of the parallel bond strain energy of each geogrid is plotted in Figure 5.18. The geogrid located 50mm beneath the tie stores the most strain energy, a consequence of its proximity to the loaded area and the substantial displacement of its ribs. After the initial load cycle, this geogrid carries 37% of the strain energy it stored during the twentieth load cycle which amounts to 2.60J. This is a marked difference compared to the strain energies stored in the other geogrids.

In the initial phases of loading, the geogrids positioned 100mm and 150mm below the tie show similar magnitudes of stored strain energy. However, as cyclic loading progresses, the geogrid at 100mm demonstrates a continuous increase in stored strain energy, surpassing that of the 150mm geogrid. By the twentieth load cycle, the strain energies stored in these geogrids are 2.27J and 1.82J respectively. Reflecting their respective deformation profiles, the geogrids situated deeper in the ballast layer at depths of 200mm and 250mm, store significantly lower magnitudes of strain energy. These two geogrids exhibit comparable amounts of stored strain energy until the fifth load cycle. Beyond this point, the geogrid at 200mm begins to store more strain energy than its counterpart at 250mm, finishing the cyclic load tests with strain energies of 1.41J and 1.14J, respectively.

This analysis of strain energy storage aligns with the deformation profiles observed in each geogrid and highlights the relationship between the geogrid placement depth and its ability to stabilize railroad ballast. The decrease in strain energy stored in the geogrids’ parallel bonds with increasing depth underscores the diminishing mobilization of reinforcements placed deeper in the ballast layer.

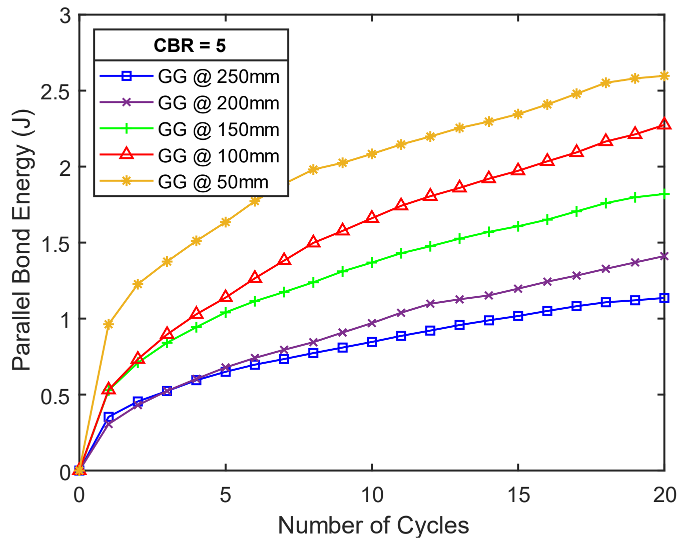

Figure 5.18: Accumulation of Strain Energy Stored in the Geogrid's Parallel Bond Springs during Cyclic Loading.

5.5. Parametric Study

Simulating the behavior of geogrid-reinforced ballast layers subjected to cyclic loading where geogrids are placed at depths ranging from 50mm to 250mm beneath the tie demonstrates that ballast particles that are the most disturbed by the application of cyclic loading are overwhelmingly located within the upper 150mm of the ballast bed. Correspondingly, geogrids situated within the upper half of the 300mm-thick ballast layers exhibit superior tie settlement-abating abilities due to the formation of an interlock with the surrounding aggregates that restrains particle motion and creates a well-connected soil structure.

Although geogrids located 50mm and 100mm beneath the tie perform their reinforcing functions satisfactorily, their placement depths are not practically desirable in the context of ballasted railway substructures as they would interfere with common ballast maintenance operations such as tamping. As such, in the framework of the simulations discussed herein, the optimum geogrid placement depth is set at 150mm below the base of the tie to achieve the maximum reduction in tie settlement while simultaneously being practically feasible.

To explore in-depth the parameters that influence the behavior of geogrid-reinforced ballast, a parametric study is conducted in which the geogrid stiffness and geogrid aperture size are varied. In both cases, the geogrid placement depth is kept constant at 150mm. The geogrid stiffness is changed to represent the biaxial geogrid's tensile strength at 2% strain at temperatures of -30, -10, 10, 20, and 40ºC reported by Desbrousses et al. (2021). The effect of the geogrid's aperture size ratio is also investigated by varying the aperture size (*A*) to 30×30mm, 40×40mm, 50×50mm, 57×57mm, 70×70mm, and 80×80mm while keeping the geogrid's tensile strength at 2% strain constant. When divided by the ballast particle's diameter (*D*) of 27.5mm, the aperture sizes give aperture size ratios (*A/D*) of 1.09, 1.45, 1.82, 2.07, 2.55, and 2.91.

5.5.1. Effect of Geogrid Aperture Size Ratio

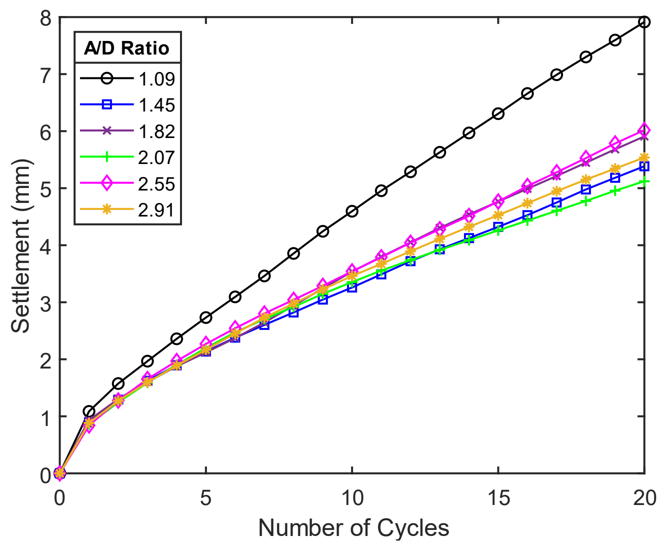

Figure 5.19: Effect of the Geogrid Aperture Size Ratio (*A/D*) on the Evolution of the Tie Settlement in Ballast Layers Reinforced with a Geogrid Located 150mm Beneath the Tie.

Figure 5.19 shows the effect of the geogrid aperture size on the accumulation of tie settlement during twenty load cycles in ballast layers reinforced with geogrids placed 150mm beneath the tie with aperture size ratios ranging from 1.09 to 2.91. A geogrid with an *A/D* of 1.09 results in considerable tie settlement, reaching 7.91mm after twenty load cycles. This is significantly higher than the 5.12mm settlement observed with the original 57mm geogrid (*A/D* = 2.07) and is comparable to the tie settlement in the unreinforced ballast bed (see Figure 5.9b). Incrementally increasing the aperture size ratio to 1.45 reduces tie settlement by 32%, achieving a final subsidence of 5.38mm. Further increasing *A/D* to 1.82 results in a slightly higher tie settlement of 5.91mm. The lowest tie settlement recorded is with the original 57mm aperture geogrid (*A/D* =

2.07). Increasing the *A/D* ratio to 2.55 and 2.91 results in gradual increases in tie settlement, with final values of 6.02mm and 5.54mm, respectively.

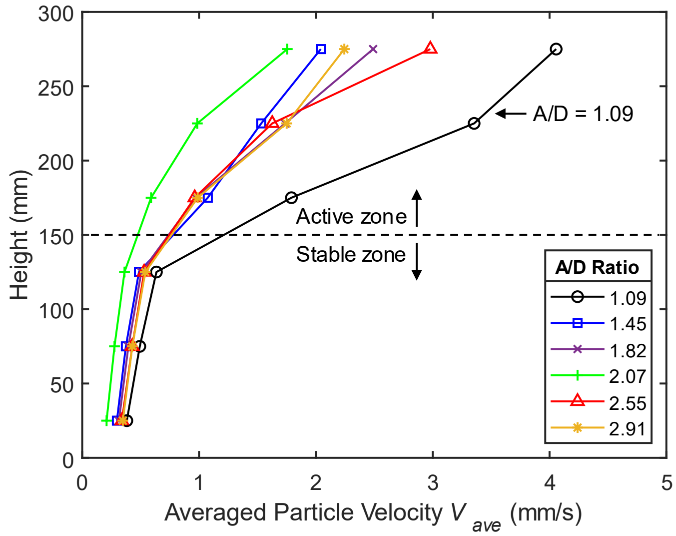

(a)

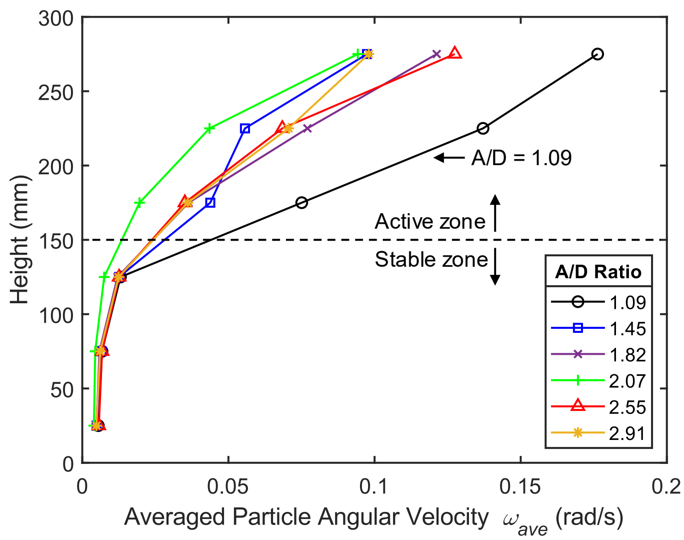

(b)

Figure 5.20: Effect of the Geogrid Aperture Size Ratio (*A/D*) on the (a) Average Particle Velocity and (b) Average Particle Angular Velocity.

To delve into the micromechanical implications of changing the geogrid opening size, the variations in particle translational and rotational velocity with depth along the ballast layer are plotted in Figure 5.20a and b respectively. Both figures stress the inadequacy of an *A/D* ratio of

1.09, as evidenced by the sharp increases in both translational and angular velocities of ballast particles that take place around the geogrid's location. This suggests that the geogrid's small opening size hinders the formation of a stable interlock with the surrounding ballast, which splits the layer into two halves and promotes excessive particle rotation and translation above the geogrid. In contrast, *A/D* of 1.45 and up lead to marked reductions in both particle velocities, indicating a more effective stabilization of the ballast and a correspondingly lower tie settlement.

Figure 5.21, which displays the tie plotted settlement against aperture size, corroborates the findings presented in this subsection. The 30mm aperture geogrid is deemed unsuitable for reinforcing the simulated ballast due to its small opening size. However, apertures ranging from 40mm to 80mm demonstrate satisfactory performance. The observed trend suggests that an aperture size of approximately 60mm (*A/D* of 2.18) could be optimal for minimizing tie settlement in the context of the mono-sized ballast particles considered in the simulations.

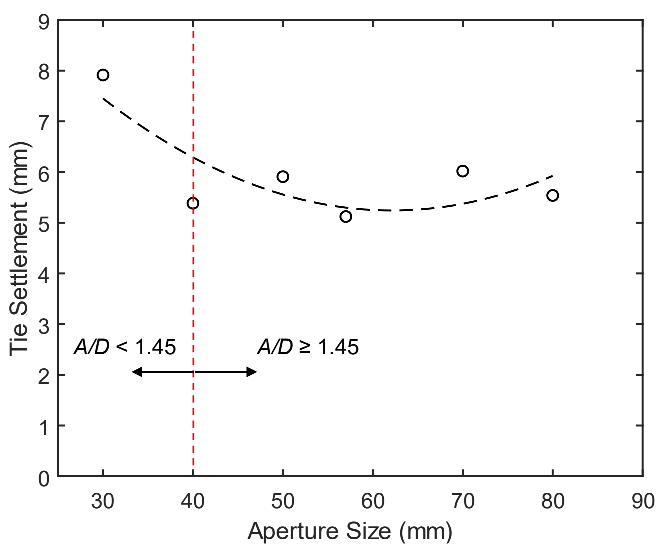

Figure 5.21: Optimum Size of the Geogrid's Apertures Based on Total Tie Settlement Considerations.

5.5.2. Effect of Geogrid Stiffness

The effect of changing geogrid stiffness is investigated by simulating geogrids with a tensile strength at 2% strain that matches the values recorded by Desbrousses et al. (2021, 2023a) when performing tensile tests on samples of the biaxial geogrid at temperatures of -30, -10, 10, 20, and 40ºC. This tensile strength variation aims to understand the influence of geogrid stiffness on tie settlement, energy dissipation by frictional sliding, and the strain energy stored in the geogrids' parallel bond springs. The geogrids are all embedded in the ballast layers at a depth of 150mm below the tie. Table 5.5 summarizes the findings for total tie settlement, cumulative slip energy, and parallel bond strain energy for each geogrid stiffness during the twentieth load cycle.

The results indicate a relative insensitivity of the tie settlement to the geogrid's tensile strength at 2% strain. Tie subsidence values of 5.13mm, 4.96mm, 4.90mm, 5.12mm, and 5.14mm are recorded for geogrid stiffnesses of 18.00kN/m, 16.28kN/m, 14.61kN/m, 11.01kN/m, and 9.54kN/m, respectively. This is supported by the consistency of cumulative energy dissipated by frictional slip across samples reinforced with geogrids of different stiffnesses, with values ranging narrowly between 98.72J and 102.38J.

In contrast, the strain energy stored in the geogrids' parallel bond springs is markedly dependent on the geosynthetic's tensile strength at 2% strain. The greatest amount of strain energy is observed in geogrids with the lowest stiffnesses, as they offer the least resistance to deformation. Consequently, the highest bond strain energy during the twentieth load cycle is recorded in the geogrid with a stiffness of 9.54kN/m, while the lowest is associated with the geogrid having a stiffness of 18.00kN/m.

Table 5.5: Effect of Geogrid Stiffness on the Tie Settlement, Energy Dissipated by Frictional Sliding, and Parallel Bond Strain Energy after Twenty Load Cycles.

Temperature (^oC)	-30	-10	10	20	40
Geogrid Stiffness (kN/m)	18.00	16.28	14.61	11.01	9.54
Tensile Modulus at 2% Strain (kN/m)	900	814	730.5	550.5	477
Settlement (mm)	5.13	4.96	4.90	5.12	5.14
Slip Energy (J)	100.95	100.22	98.72	102.24	102.38
Bond Strain Energy (J)	1.52	1.61	1.69	1.82	1.94

5.6. Discussion

In the previous sections, the results illustrate the influence of geogrid placement depth, aperture size ratio, and stiffness on the deformation behavior of geogrid-reinforced ballast subjected to cyclic loading. Geogrids positioned at depths ranging from 50 to 150mm yield the most significant reductions in tie settlement, attributed to their ability to confine ballast particles through the development of a geogrid-ballast interlock. This confinement leads to reduced particle movement and total slip energy, along with an increase in the average coordination number, indicating more interconnected soil structures. However, the efficacy of geogrid reinforcement wanes at greater placement depths (200 and 250mm), resulting in increased tie settlements, more pronounced particle movement, and lower coordination numbers.

Further analysis reveals that the aperture size of geogrids is critical for the effective reinforcement of the mono-sized ballast (diameter of D = 27.5mm) considered in the simulations. An aperture size (A) of 30×30mm (A/D = 1.09) proves too small and impedes the formation of a stable ballast-geogrid interlock. This contributes to the formation of a displacement plane at the geogrid level that splits the ballast layer in two, with substantial particle movement occurring above the geogrid. Optimal tie settlement reduction is observed for A/D ratios greater than or equal to 1.45. Interestingly, variations in geogrid stiffness, ranging from a tensile strength at 2% strain of 18.00 to 9.54kN/m, have a lesser impact on ballast reinforcement compared to the aperture size, with similar tie settlement outcomes across the stiffness range.

Studies summarized in Table 5.6 explored the impact of geogrid placement depth and aperture size on the performance of geogrid-reinforced ballast. Cyclic load tests conducted on geogrid-reinforced ballast (Bathurst et al., 1986; Bathurst & Raymond, 1987; C. Chen et al., 2012; Desbrousses et al., 2023; Indraratna et al., 2013) have indicated that geogrids placed closer to the bottom of the ties are more effective in reducing tie settlement. Guidelines on the use of geogrids for ballast reinforcement provided by AREMA (2010) further state that geogrids may be placed within the ballast layer to reduce the rate of track settlement. This aligns with the findings presented in this paper which demonstrate notable settlement reductions with geogrids positioned within the upper 150mm of the ballast layer. It is important to note that it is generally advised to place geogrids at a depth of at least 150mm below the tie (Das, 2016) to prevent interference with common ballast maintenance operations such as tamping, which tend to disturb the upper 100mm of the ballast layer (Bathurst & Raymond, 1987; Guo et al., 2021; Offenbacher et al., 2021; S. Shi et al., 2022).

The role of the geogrid aperture size in enhancing ballast reinforcement has been investigated through various testing methods, including direct shear tests (Indraratna et al., 2012; Indraratna, Ngo, et al., 2011; Sadeghi et al., 2020; Sweta & Hussaini, 2018), pullout tests (C. Chen et al., 2013), triaxial tests (Mishra et al., 2014; Qian et al., 2015), and variants of the ballast box tests

(Hussaini et al., 2015, 2016; Indraratna et al., 2013; Sadeghi et al., 2023). Indraratna et al. (2012, 2013) and Hussaini et al. (2015, 2016) studied the effect of the A/D_{50} ratio between a geogrid's aperture size (A) and the ballast's mean particle diameter (D_{50}) using direct shear tests and cyclic load tests on the behavior of geogrid-reinforced ballast. They reported that optimum geogrid reinforcement is achieved for A/D_{50} ratios ranging from 0.95 to 1.20 while acceptable reinforcement exists for ratios in excess of 1.20. Other studies, such as the cyclic load tests performed by Brown et al. (2007) and the pullout tests conducted by Chen et al. (2013), recommend using greater A/D_{50} ratios in the range of 1.2 to 1.6 for optimal reinforcement. On the other hand, AREMA (2010) indicates that using geogrids with an aperture size in excess of 43mm results in optimal geogrid performance, irrespective of the ballast particle size. The results drawn from the simulations discussed herein echo the findings of Brown et al. (2007) and AREMA's recommendations (AREMA, 2010) by demonstrating effective geogrid performance for aperture size ratios greater than 1.45.

Regarding the geogrid stiffness, AREMA recommends using geogrids with a minimum tensile modulus at 2% strain of 277×474kN/m (machine × cross-machine directions) for adequate performance in railroad ballast. Brown et al. (2007) further stated that increasing geogrid stiffness leads to better ballast reinforcement provided that sufficient overburden pressure exists above the geosynthetic. The parametric study presented in this paper is consistent with the AREMA guidelines, suggesting that adequate geogrid performance is achieved with geogrid tensile moduli at 2% strain in excess of 474kN/m.

Table 5.6: Summary of Studies Investigating the Effect of Geogrid Placement Depth and Aperture Size.

Author(s)	Experiment	Ballast Thickness	Geogrid Depth	Geogrid Aperture Size	Optimum Depth	Optimum Aperture	Observations
Bathurst et al. (1986, 1987)	Ballast box test	300mm	50, 100, 150, 200mm	46×46mm	200mm	N/A	-Minimum tie settlement at geogrid depths of 50 and 100mm -Preferred placement depth at 200mm due to practical considerations
McDowell & Stickley (2006)	Ballast box test	300mm	100, 200mm	39×39mm, 65×65mm	200mm	65mm	-Smaller tie settlement is obtained with a geogrid aperture size of 65mm and a depth of 200mm
McDowell et al. (2006)	Pullout test (DEM)	N/A	N/A	A/D_{50}: 0.9, 1.1, 1.4, 1.6	N/A	A/D_{50}: 1.4	-Lowest pullout resistance for A/D_{50}: 0.9 -Maximum pullout force for A/D_{50}: 1.4 -Similar pullout forces for $1.1< A/D_{50}<1.6$
Brown et al. (2007)	Ballast box test	300mm	250mm	A/D_{50}: 0.64, 0.76, 1, 1.3, 1.8, 2	N/A	A/D_{50}: 1.2-1.6	-Shear plane develops at the geogrid level if apertures are too small
Indraratna et al. (2013), Hussaini et al. (2015, 2016)	Process simulation test	325mm	130, 195, 265, 325mm	A/D_{50}: 0.6, 1.08, 1.21, 1.85	265mm	A/D_{50}: 1.21	-Geogrids reduce ballast breakage and lateral spreading -Geogrids with A/D_{50} >0.95 are suitable for reinforcing ballast -Optimum geogrid location is 65mm above subballast
Chen et al. (2013, 2014)	Pullout test	N/A	N/A	32, 40, 65, 75mm	N/A	65mm	-Geogrid aperture size is more influential than geogrid stiffness and rib thickness for geogrid-ballast interlock -Triangular geogrid is better at interacting and confining ballast -Small geogrid apertures prevent interlocking
Chen et al. (2012)	Ballast box test (DEM)	300mm	50, 100, 150, 200, 250mmm	65mm	200mm	N/A	-Best depth of the geogrid is 100mm followed by 150 and 200mm -Triangular grid interlock better with ballast -Resilient behavior is not affected by presence of geogrid
Hussaini & Sweta, Sweta & Hussaini (2020, 2021, 2018, 2020, 2022)	Process simulation test Direct shear test	380mm	Ballast/subballast interface	A/D_{50}: 0.63, 0.83, 0.93, 0.95, 1.54	N/A	A/D_{50}: 0.93	-Role of aperture size is striking around the geogrid location in terms of lateral spreading -Recommended aperture sizes suitable for geogrid at ballast/subballast interface
Esmaeili et al. (2017)	Single-tie push test Track panel displacement test	450mm	250, 350mm	40×40mm	250mm	N/A	-Increase in lateral track resistance caused by geogrid decreases with increasing geogrid placement depth
Sadeghi et al. (2020, 2023)	Direct shear test Ballast box test	450mm	250, 350mm	A/D_{50}: 0.83, 1.17, 1.59	350mm	A/D_{50}: 1.17	- A/D_{50}: 1.17 with a placement depth of 200mm yields optimum reinforcement in sand-fouled ballast giving a stiffer layer, with less settlement and particle breakage - A/D_{50}: 1.17 increases ballast's shear strength in direct shear test due to superior interlock with ballast
Indraratna et al. (2020)	Impact test	300mm	100, 200, 300mm	A/D_{50}: 1.2	200mm	N/A	-Maximum reduction in ballast axial and radial strain achieved by geogrid placed 100mm above subballast -Maximum reduction in ballast breakage achieved by geogrid placed at a depth of 100mm
Li et al. (2024)	Impact test	400mm	300, 350mm	A/D_{50}: 1.4	300mm	N/A	-Optimum geogrid placement depth is 100mm above subballast to minimize axial and lateral ballast deformations

5.7. Conclusions

This paper presents the findings of three-dimensional discrete element simulations of ballast box tests to examine the deformation behavior of geogrid-reinforced ballast subjected to cyclic loading. The study includes a parametric study that explores the effect of the geogrid's placement depth, *A/D* ratio, and stiffness on the response of geogrids embedded in ballast. Results are analyzed by initially studying the macroscale behavior of reinforced ballast assemblies through the evolution of the tie's settlement during cyclic loading. The analysis then delves into the microscale processes, such as particle motion, formation of contact force chains, and energy dissipation, that contribute to the observed macroscale response to cyclic loading. The key highlights of this study are as follows:

- The tie settlement is highly sensitive to the geogrid placement depth, with geogrids situated 50 to 150mm below the tie resulting in the most significant reductions in tie subsidence compared with the unreinforced ballast layer. The reinforcing efficiency of geogrids wanes at greater depths, leading to less pronounced reductions in tie settlement
- The superior performance of geogrids located 50 to 150mm beneath the tie is attributed to the formation of a robust geogrid-ballast interlock that confines the granular material. This translates into smaller particle movement developing in the granular assembly following the application of cyclic loading which considerably decreases the cumulative energy dissipated through interparticle frictional sliding. The inclusion of geogrids leads to ballast layers being better connected as evidenced by geogrid-reinforced ballast beds possessing greater coordination numbers than in the unreinforced case
- The aperture size of a geogrid is a critical factor in the reinforcement of ballast. The parametric study indicates that an *A/D* ratio of 1.09 is ineffective. Its use leads to increased particle movement in the ballast layer and a corresponding increase in tie settlement. In contrast, *A/D* ratios equal to or greater than 1.45 are found to yield optimal reinforcement
- Variations in geogrid stiffness caused by temperatures ranging from -30 to 40ºC have a negligible influence on the performance of geogrid-reinforced ballast with similar tie settlements being observed across the range of geogrid stiffnesses considered in this paper

This study, while informative, is limited by the simulation of a finite number of load cycles and the use of mono-sized, unbreakable ballast particles. As such, future research should extend the number of simulated load cycles, incorporate a broader range of particle sizes, and consider particle breakage to gain a more comprehensive understanding of the long-term performance of geogrid-reinforced ballast.

Chapter 6: Critical Discussion

6.1. Introduction

The research inquiry central to this thesis pertains to identifying the effects of key geogrid characteristics on the behavior of geogrid-reinforced ballast. The review of the existing literature on geogrid-reinforced ballast presented in Chapter 2 suggests that the ability of a geogrid to reinforce ballast hinges on its interlock with the surrounding granular material. This interaction fosters a mechanical bond between the geogrid and the ballast particles that is considerably influenced by critical geogrid attributes such as its aperture size, stiffness, and placement depth, as well as the strength of the underlying subgrade. It is therefore essential to evaluate how variations in geogrid stiffness, aperture size, and placement depth impact the response of geogrid-reinforced ballast subjected to cyclic loading. It is also imperative to map out the relationship between the geogrid placement depth and the subgrade strength and its effect on the geosynthetic's ability to stabilize ballast. It is further noteworthy that ballasted railway tracks in Canada are exposed to large seasonal temperature variations which may be felt up to a depth of 10m in earth structures. As geogrids are generally placed at shallow depths in ballasted track substructures, they are likely to be affected by fluctuations in ambient temperature. Since geogrids are typically made of polymeric materials with temperature-dependent properties, it is crucial to identify how temperature affects the properties of geogrids used to reinforce railroad ballast.

The effect of temperature on the mechanical properties of a biaxial geogrid designed to reinforce railroad ballast and a geogrid composite is investigated by performing in-isolation single-rib tensile tests in a temperature chamber. In these experiments, single-rib geogrid specimens are brought to tensile failure at temperatures ranging from -30ºC to 40ºC. The results underscore the temperature dependence of the two geogrid materials' ultimate tensile strength and stiffness, which are parameters commonly used in the design of reinforced earth structures. A series of large-scale ballast box tests is then conducted to investigate the effect of geogrid placement depth and subgrade strength on the behavior of geogrid-reinforced ballast. In this experimental campaign, 300mm-thick ballast layers supported by subgrades with CBRs of 25, 13, and 5 are reinforced with geogrids placed at depths of 150, 200, and 250mm below the tie. Finally, the experimental data collected during the ballast box tests and single-rib geogrid tensile tests are used to calibrate and develop a three-dimensional discrete element model of the ballast box tests. Discrete element simulations are carried out to explore the micro-mechanical features of the ballast-geogrid interaction mechanism. A parametric study is also conducted to determine how changes in geogrid aperture size and geogrid stiffness akin to those obtained in the single-rib tests affect the ability of a geogrid to reinforce ballast.

Single-rib tensile test results highlight that the biaxial geogrid is sensitive to temperature changes. It displays a ductile behavior at elevated temperatures and a brittle behavior at lower temperatures which trickles down into the geogrid possessing a greater stiffness at cold temperatures. Ballast box tests reveal that the behavior of the same geogrid embedded in railroad ballast is a function of its placement depth and the compressibility of the underlying subgrade. Although the geogrid's location in a 300mm-thick ballast layer is relatively insignificant when the subgrade is strong, a weaker subgrade translates into shallower placement depths allowing the geosynthetic to stabilize ballast aggregate more effectively. Finally, the discrete element simulations show that geogrids placed at depths smaller than or equal to 150mm under the tie are the most effective at minimizing tie settlement due to their presence in the upper portion of the ballast layer where particles displace the most. Additionally, an A/D_{50} ratio greater than or equal to 1.45 is required for geogrids to effectively stabilize railroad ballast while the geogrid stiffness changes recorded during the single-rib tensile tests appear to have a negligible impact on the behavior of geogrid-reinforced ballast.

6.2. Exploring the Impact of Temperature on the Tensile Strength of Geogrids

Chapter 3 describes single-rib tensile tests aiming to investigate the behavior of a biaxial geogrid and a geogrid composite at temperatures ranging from -30ºC to 40ºC and -30ºC to 20ºC respectively. The biaxial geogrid is found to be highly sensitive to temperature variations. Upon raising the temperature from 20ºC to 40ºC, the geosynthetic develops larger ultimate strains while mobilizing a lower ultimate tensile strength at failure, suggesting an increasingly ductile behavior at elevated temperatures. Conversely, lowering the testing temperature below 20ºC triggers an increase in ultimate tensile strength at failure accompanied by a decrease in ultimate tensile strain. It is noteworthy that the ultimate tensile strength remains constant at temperatures below -10ºC. Temperature changes also affect the geogrid's stiffness at 2% and 5% strain, which are parameters often used in the design of geosynthetic-reinforced earth structures (Kim & Kim, 2020). At elevated temperatures, the geogrid's stiffness decreases while it increases at lower temperatures.

These results are consistent with the findings reported by Wang et al. (2008), Bonthron and Jonsson (2017), and Shokr et al. (2022) who observed that geogrids become increasingly brittle as temperatures drop below 20ºC. Studies investigating the tensile strength of geogrids at elevated temperatures echo the results in Chapter 3, with Kasozi et al. (2014), Kongkitkul et al. (2012), and Chantachot et al. (2016, 2017, 2018) highlighting that polymeric geogrids exhibit ductile responses to loading at elevated temperatures.

The behavior of the geogrid composite contrasts with that of the biaxial geogrid insofar as its ultimate tensile strength is relatively insensitive to temperatures ranging from -30ºC to 20ºC. The material does, however, display an increasingly brittle behavior as the temperature decreases given that its ultimate strain gets smaller. Interestingly, the composite's tensile strength at 2% and 5% strain shows a marked reaction to temperature changes. These two parameters consistently increase as the testing temperature decreases, although similar values are recorded at -20ºC and -30ºC. These findings are consistent with a study undertaken by Jarjour and Meguid (2023) who sought to explore the effect of temperature on the mechanical properties of dry and moist samples of a geogrid composite similar to the one tested in Chapter 3. Their work showed that a decrease in temperature below 20ºC increases the composite's stiffness and ultimate tensile strength, with moist samples displaying a greater rate of strength increase due to the presence of water. Increasing the temperature above 20ºC leads to lower tensile strengths being recorded.

The effect of temperature on the behavior of geosynthetic-reinforced soil (GRS) structures has been investigated by several researchers, primarily in the case of GRS retaining walls. Field tests and numerical modeling work on geosynthetic-reinforced embankments have shown that variations in ambient air temperature may be felt up to a distance of 10m into the soil away from an exposed surface (Segrestin & Jailloux, 1988; Zarnani et al., 2011). The most significant changes in soil temperatures, however, have been shown to take place within the first 2m while the upper 300mm of soil experience daily temperature fluctuations (Murray & Farrar, 1988; Xiao et al., 2021, 2022). Murray and Farrar (1988) monitored the seasonal temperature changes in a geotextile-reinforced earth retaining wall in Waltham Cross, UK over seven years. They pointed out that although temperature fluctuations produce minor variations in the short-term tensile strength of the geotextile, sustained exposure to temperature changes may lead to serious long-term stability implications due to its effect on the geotextile's degradation and creep. Similar concerns were relayed by Kasozi et al. (2014) who studied the performance of a geogrid-stabilized earth wall in Las Vegas, NV. Kasozi et al. (2014) argued that owing to the geogrid' temperature-dependent behavior, sustained exposure to elevated temperatures may degrade the geogrid's tensile strength and create uncertainty over its long-term performance. Additionally, Yarivand et al. (2017) investigated the performance of geosynthetic-reinforced soil bridge abutments exposed to fire and concluded that subjecting geogrids to high temperatures increases the lateral displacement of the bridge abutments. Similarly, Xiao et al. (2021, 2022) performed a case study on 52 GRS walls in China and indicated that exposure to complex environmental conditions, including temperature changes, contributed to the degradation of polypropylene strips used to reinforce a wall that failed. This observation was supported by 1/3 scaled experiments on GRS walls subjected to temperature cycles conducted by Cui et al. (2022) who found that geogrid strains change in function of the ambient temperature which impacts the walls' deformation.

Given that geogrids reinforcing ballast layers are typically located within approximately 300mm of a soil surface exposed to air, seasonal temperature changes are likely to have an impact on their mechanical properties and behavior. Although the experiments discussed herein provide information on the effect of temperature on the tensile strength of two geogrids, the results are obtained only from in-isolation tensile tests. This underscores the primary limitation of this experimental campaign whereby the effect of temperature on the in-service performance of geogrids embedded in railroad ballast is not captured. Additional experimental work is therefore needed to explore how temperature fluctuations affect the performance of geogrid-reinforced ballast and assess whether sustained exposure to temperature variations compromises the stability of reinforced ballast layers.

This could be achieved by performing model tests on a scaled-down model of a ballasted track structure similar to those conducted by Chawla and Shahu (2016a, 2016b) in a temperature-controlled environment. Upon selecting a scale for the models, the soil materials, geogrids, and track superstructure components would have to be scaled down and built accordingly. Soil layers could then be instrumented with earth pressure cells, thermocouples, and settlement pegs to monitor their stress, temperature, and deformation. Geogrids could be equipped with strain gauges and thermocouples while linear variable displacement transducers could be placed on the rails to measure their settlement while cyclic loading is applied. Data collected during the experiments could then be used to develop and calibrate numerical models to perform parametric studies and paint a clearer picture of the effect of temperature on the performance of geogrid-reinforced ballast.

6.3. Understanding the Interplay Between Geogrid Placement Depth, Subgrade Strength, and the Behavior of Geogrid-Reinforced Ballast

The stabilization of ballast by geogrids, which mitigates track settlement, is influenced by both the geogrid's placement depth in the granular layer and the compressibility of the underlying subgrade. The relationship between these two variables is investigated by performing ballast box tests. These experiments involve embedding geogrids at varying depths of 150, 200, and 250mm within 300mm-thick ballast layers supported by subgrades with CBRs of 25, 13, and 5. The key contribution of this study highlights that the subgrade strength determines how the depth at which the geogrid is placed affects the performance of reinforced ballast. As the subgrade strength diminishes, the geogrid's placement depth becomes increasingly critical for ballast stabilization. For softer subgrades, positioning the geogrid closer to the tie results in a more significant reduction in tie settlement compared to deeper placement depths. Indeed, in cases where the ballast is supported by a robust subgrade, the reduction in settlement is approximately 40% across all geogrid locations. Contrastingly, the presence of weaker subgrades with CBRs of 13 and 5 translates into settlement reductions of 42%, 54%, and 58% and 38%, 55%, and 63% for geogrid placement depths of 250, 200, and 150mm respectively.

The observations made in this study are in line with the work of Bathurst and Raymond (1987) who conducted large-scale ballast box tests. They indicated that the greatest tie settlement reductions are achieved by geogrids located 50 to 100mm below the ties. However, they recommended placement depths greater than or equal to 150mm be used in practice to avoid interfering with ballast maintenance operations. Their work further highlighted that greater settlement reductions are achieved by geogrids reinforcing ballast layers supported by soft subgrades. These observations were reflected in the experimental and numerical modeling work of Raymond (2002) and Raymond and Ismail (2003). Brown et al. (2007) and Chen et al. (2012) performed large-scale cyclic load tests on geogrid-reinforced ballast and used discrete element modeling to simulate them. Although they concluded that it is more beneficial to reinforce ballast with geogrids when the underlying subgrade is soft, they found that a placement depth of 250mm below the tie leads to the greatest tie settlement reduction. This echoes the findings of McDowell and Stickley (2006) who carried out ballast box tests on geogrid-reinforced ballast and determined that a geogrid placement depth of 200mm under the tie results in a smaller tie settlement compared to a depth of 100mm. Comparable results were obtained by Sadeghi et al. (2023) who concluded that embedding a geogrid 100mm above the subballast gives rise to a greater tie settlement reduction than at a depth of 200mm above the subballast.

The relationship between subgrade strength and geogrid placement depth manifests itself in a similar fashion in its effect on the tie's resilient settlement and support stiffness. In ballast layers supported by a competent subgrade (CBR of 25), similar reductions in the tie's resilient settlement compared to the unreinforced case are obtained regardless of the geogrid location. This is reflected in similar tie support stiffness increases being recorded in these layers. With the presence of softer subgrades below the ballast layer, a new trend emerges whereby geogrids placed closer to the tie produce a greater reduction in resilient settlement than those located deeper in the granular layer. A mirror image of the trend makes itself manifest in the tie support stiffness whereby the greatest increases in tie support stiffness are recorded in layers where geogrids are placed closer to the bottom of the tie. This observation contrasts with the work of Bathurst and Raymond (1987) who indicated that while the resilient settlement is sensitive to the subgrade compressibility, the presence of geogrids does not bring about appreciable changes in the tie's elastic rebound. Brown et al. (2007) drew an analogous conclusion after performing ballast box tests and suggested that the resilient settlement is primarily controlled by the stiffness of the ballast/subgrade assembly. However, Sadeghi et al. (2023) observed that the inclusion of geogrids in railroad ballast leads to an increase in the tie support stiffness in both clean and fouled ballast layers, with geogrids located 100m above the subballast yielding slightly higher stiffnesses than those placed 200mm above the subballast. These findings are supported by the work of Sweta and Hussaini (2020, 2022) who performed ballast box tests in which geogrids are laid at the ballast/subballast interface and reported that the inclusion of geogrids increases the ballast layer's resilient modulus, indicating an increase in the ballast's stiffness.

The results presented in Chapter 4 also highlight the effect of subgrade strength and geogrid placement depth on the ballast layer's damping ratio. In unreinforced ballast beds, the damping ratio is sensitive to subgrade strength, with damping ratios increasing with decreasing subgrade strength. Ballast layers supported by the competent subgrade (CBR of 25) experience small reductions in their damping ratio following the inclusion of geogrids, with the placement depth wielding a negligible impact on the damping ratio. The damping ratio of ballast beds supported by softer subgrades (CBR of 13 and 5), on the other hand, appears to be insensitive to the presence of geogrids. Conflicting information regarding the effect of geogrids on the damping ratio of ballast layers exists in the literature. Sweta and Hussaini (2022) observed that the inclusion of geogrids at the ballast/subballast interface produces an increase in the ballast/subballast assembly's damping ratio after conducting ballast box tests. This alludes to the fact that geogrid-reinforced ballast layers could have a more pronounced proclivity to dissipate energy under cyclic loading. However, this finding is contradicted by Sadeghi et al. (2023) who performed ballast box tests and determined that reinforcing ballast with geogrids is accompanied by a decrease in the ballast's damping ratio. The authors attributed that reduction in damping ratio to the ballast/geogrid interlock and the corresponding confinement of the unbound aggregate material by the geogrid. This in turn restricts the motion of ballast particles, resulting in a stiffer ballast layer and less energy being dissipated during cyclic loading.

The experimental campaign discussed herein has several shortcomings. First, the presence of compressible subgrades below the ballast layers is considered by placing rubber mats of varying compressibility at the bottom of the ballast box. Although these mats provide different degrees of resiliency to the overlying granular layer, they do not sustain the plastic deformations natural soils would experience when subjected to cyclic loading. The presence of actual soft soils under the ballast layer may be an additional source of plastic deformation in the substructure that may drive further particle rearrangement in the ballast layer along with additional track settlement. Second, constructing ballast layers in a rectangular soil container may not accurately depict the typical geometry of ballast layers and imposes boundary conditions on the ballast samples that might deviate from those found in the field. Finally, a relatively small number of load cycles and a low loading frequency are used in the experiments, which may not represent typical train loading conditions.

Future research avenues include using a more powerful loading system to apply cyclic loading for a greater number of load cycles and vary the loading frequency as well as the magnitude of the applied loads. This would provide valuable information on the effect of loading frequency and magnitude on the behavior of geogrid-reinforced ballast. Additionally, a subballast layer may be constructed below the ballast layer to better represent the track substructure. This would allow earth pressure cells to be installed below the subballast and at the ballast/subballast interface to monitor the distribution of stresses in unreinforced and geogrid-reinforced ballast/subballast assemblies. The geogrids embedded in ballast may also be instrumented with strain gauges to gain insights into the geosynthetic's response to cyclic loading.

6.4. Influence of Geogrid Aperture Size, Stiffness, and Placement Depth: A Discrete Element Study

The exploration of tie settlement, both permanent and resilient, and the associated changes in ballast stiffness and damping ratio through ballast box tests, as described in Chapter 4, yields valuable information on the macroscale implications of reinforcing ballast with geogrids. Nevertheless, it is practically impossible to gather information on the intricate ballast/geogrid interactions that occur at the particulate level experimentally. To remedy this shortcoming, a three-dimensional distinct element model (DEM) of the ballast box tests is developed. This model serves as a foundation for a parametric study aiming to delve into the multifaceted features of the ballast/geogrid interaction mechanism. Building on the conclusions drawn in Chapter 4, which indicated an enhancement in a geogrid's ability to reinforce ballast at shallow placement depths, the geogrid placement depth is first varied from 50mm to 250mm. The focus of the parametric study subsequently shifts towards examining the impact of geogrid properties on the performance of reinforced ballast. This is achieved by first changing the geogrid aperture size across a spectrum from 40mm to 80mm in 10mm increments, resulting in A/D_{50} ratios spanning from 1.09 to 2.91. The geogrid stiffness is then varied, with values ranging from 9.54kN/m to 18.00kN/m. These stiffness values correspond to the geogrid's tensile strength at 2% strain obtained at temperatures ranging from -30ºC to 40ºC as discussed in Chapter 3.

Changing the geogrid placement depth from 50mm to 250mm, in 50mm increments, corroborates findings from Chapter 4, highlighting that geogrids positioned closer to the tie significantly reduce tie settlement. Simulations further suggest that geogrids placed 50mm and 100mm under the tie exhibit an enhanced ability to stabilize ballast. An analysis of ballast particle motion unveils the existence of two distinct zones within the ballast layer. The bottom 150mm of the layer, designated as the stable zone, exhibits marginal changes in particle velocity following the application of cyclic loading. Conversely, particles in the upper 150mm, termed the active zone, experience considerable disturbances from cyclic loading, causing particle velocities to increase significantly along the height of the ballast layer. A similar division of the ballast layer was proposed by Chen et al. (2022) who noticed that the average velocity of ballast particles decreases with depth in the ballast layer with the highest particle velocities occurring within the upper 40% of the ballast layer.

The existence of two regimens of particle displacement sheds light on the role of the geogrid placement depth as discussed in Chapter 4 and revisited in Chapter 5. Geogrids situated at shallow depths (≤150mm) beneath the tie fall within the active zone, where ballast particles undergo the most significant displacements due to cyclic loading. The establishment of an interlock between the ballast aggregate and the geogrid in this region substantially curtails particle displacement due to the confinement effect from the geogrid and consequently leads to a decrease in tie subsidence. In contrast, geogrids placed within the stable zone are less effective at reinforcing ballast as they cannot stabilize the particles that displace the most. This finding is supported by observations of energy dissipation via interparticle sliding in geogrid-reinforced ballast assemblies. Ballast layers with geogrids in the active zone display a more pronounced reduction in energy dissipation compared to those with geogrids in the stable zone, highlighting the importance of the geogrid placement depth.

The inclusion of a geogrid in a ballast layer has repercussions on the load transfer mechanism that develops in the granular assembly through interparticle contacts. The average number of contacts per particle, described by the coordination number (CN), is particularly sensitive to the presence and placement depth of a geogrid. The unreinforced ballast layer possesses the smallest coordination number followed by ballast assemblies with geogrids placed in the stable zone. Conversely, geogrids situated within the active zone lead to higher coordination numbers. Changes in coordination numbers have a strong bearing on the mechanical behavior of a granular assembly since higher coordination numbers describe a more stable and less mobile granular material than smaller CNs (Ouadfel, 1998; Ouadfel & Rothenburg, 2001). As such, given that load transmission in granular assemblies is accomplished through interparticle contacts, ballast layers with a higher coordination number have smaller average interparticle contact forces which may correlate to a reduced potential for particle breakage (Fei & Narsilio, 2020; X. Gu et al., 2014; Minh & Cheng, 2013; Niu et al., 2023). This is reflected by analyzing the contact force chains that support the applied loads in the unreinforced and reinforced ballast beds. The high coordination numbers observed in ballast layers with geogrids placed in the active zone translate into these granular assemblies having smaller average strong contact forces compared to the unreinforced ballast layer and layers with geogrids located in the stable zone. Comparable observations were reported by Luo et al. (2023) who indicated that the inclusion of a geogrid at the ballast/subballast interface results in an increase in the ballast layer's coordination number and a reduction in the average interparticle contact force compared to an unreinforced ballast/subballast assembly.

Exploring the micromechanical behavior of geogrid-reinforced ballast layers subjected to cyclic loading complements the key features of the experimental campaign described in Chapter 4. The role of the geogrid placement depth in stabilizing railroad ballast and minimizing tie settlement becomes apparent owing to the shift in the ballast's micromechanical response to cyclic loading it induces. Due to the existence of an active zone in the upper half of ballast layers, geogrids embedded in that region confine the particles experiencing the greatest displacements in response to applied loads. Coupled with an increase in the average coordination number, this improves the granular layer's stability and reduces the resulting tie settlement. Looking at the deeper end of the placement depth spectrum, geogrids embedded within the stable zone of a ballast layer have a reduced ability to minimize tie settlement as they cannot stabilize the volume of ballast particles that is the most disturbed by the applied loads.

Shifting the focus of the parametric study to geogrid characteristics such as the geosynthetic's aperture size and stiffness emphasizes the role of the geogrid itself and provides a different perspective on the behavior of geogrid-reinforced ballast. The geogrid aperture size, described by the A/D_{50} ratio, plays a critical role in fostering an environment conducive to optimal ballast/geogrid interaction. Geogrids with an A/D_{50} ratio smaller than 1.45 are unable to properly reinforce railroad ballast, giving rise to excessive tie settlement. Their apertures are excessively small in comparison with the mean diameter of the surrounding ballast particles. This prevents ballast particles from striking through the geogrids' plane and becoming wedged in their apertures. Instead, a preferential plane of slippage is formed along the geogrid interface which drives additional particle rearrangement and contributes to the development of substantial tie settlement. However, A/D_{50} ratios in excess of 1.45 promote the formation of a stable interlock between a geogrid and the surrounding ballast particles which translates into the tie experiencing a reduced subsidence. Previous studies investigating the role of the geogrid aperture size reported comparable findings to the ones presented in Chapter 5. Indraratna et al. (2012, 2013), Hussaini et al. (2015, 2016), and Sadeghi et al. (2023) indicated that optimal geogrid/ballast interlock is achieved for A/D_{50} ratios ranging from 0.95 to 1.20 while A/D_{50} ratios greater than 1.20 also allow the formation of stable ballast/geogrid interlocks. However, Brown et al. (2007) and Chen et al. (2013) recommended using greater A/D_{50} ratios in the range of 1.2 to 1.6.

Interestingly, the geogrid stiffness does not appear to wield much influence over the response of geogrid-reinforced ballast. Comparable tie settlements and levels of energy dissipated through frictional slip are recorded in ballast layers reinforced with geogrids possessing stiffnesses ranging from 18.00kN/m to 9.54kN/m. The results suggest that temperature-induced changes in the geogrid's stiffness do not cause significant fluctuations in the geogrid's ability to stabilize ballast, thereby partially addressing one of the research gaps identified in Chapter 3. This is particularly relevant in the context of climate change in Canada, with Bush and Lemmen (2019) reporting that mean air temperatures in Canada are projected to increase by 1.5ºC to 2.3ºC from 2031 to 2050. The results presented in the parametric study may suggest that geogrids embedded in ballasted substructures may perform their functions satisfactorily while exposed to rising temperatures.

Beyond the results presented here, it is important to acknowledge the limitations of the simulations, which stem from a variety of factors. First, rigid uncrushable mono-sized clumps are used to model ballast aggregate. This does not capture the typical range of ballast particle sizes commonly found in conventional mainline ballast aggregate. Additionally, the breakage and degradation of ballast particles is not simulated which may have an influence on the deformation behavior of railroad ballast under cyclic loading and precludes evaluating whether the inclusion of geogrids minimizes ballast particle breakage. The simulations are also limited by the small number of loading cycles applied to the ballast layers.

Future research could include using a particle size distribution closer to that found in mainline ballast and simulating breakable ballast particles to explore the micromechanical interactions between geogrids and ballast particles of varying sizes and evaluate whether the presence of geogrids minimizes ballast particle breakage. Coupled discrete-finite element modeling could be employed to study the behavior of geogrid-reinforced ballasted substructures in which railroad ballast would be modeled using discrete elements while the underlying subballast and subgrade layers would be simulated using finite element modeling. Additionally, more ties should be included in the model and moving train loads simulated to investigate the impact of principal stress rotation in reinforced ballast layers.

6.5. Conclusions

This thesis aims to explore the behavior of geogrid-reinforced ballast, with a particular focus on key geogrid characteristics and their impact on the performance of ballast under cyclic loading. In Canada, railway tracks are generally exposed to significant seasonal temperature fluctuations that potentially affect soils at depths up to 10m below the ground surface. Given their polymeric nature and placement within 300mm of the ballast layer's top, geogrids are susceptible to these temperature variations, which may induce changes in their mechanical behavior. Single-rib tensile tests have shown that geogrids exhibit temperature-dependent properties, which in turn influence key design attributes such as their tensile strength at 2% and 5% strain. Investigations into the performance of geogrids embedded in ballast through ballast box tests highlighted that the effect of the geogrid placement depth is dictated by the subgrade strength, with shallower placement depths proving more beneficial in reducing tie settlement for softer subgrades. Distinct element modeling provided further insight, identifying two distinct zones within a ballast layer under cyclic loading. The first is an active zone, located in the layer's upper 150mm, which experiences significant particle displacements due to cyclic loading while the second is a stable zone, found in the layer's bottom 150mm, characterized by minimal particle velocity changes caused by cyclic loading. As such, positioning a geogrid within the active zone substantially diminishes particle movement due to the ballast/geogrid interlock and its confining effect, thereby significantly lowering tie settlements. In contrast, geogrids in the passive zone offer limited stabilization since they are away from the zone of active particle displacement. The simulations also delved into how geogrid aperture size and stiffness influence the behavior of reinforced ballast. They revealed that an A/D_{50} ratio of at least 1.45 is necessary for effective ballast/geogrid interlocking. Moreover, variations in geogrid stiffness, akin to those induced by temperature changes between -30ºC and 40ºC, appear to have a marginal impact on the geogrid's ability to curtail tie subsidence.

Chapter 7: Conclusions

7.1. General Conclusions

This thesis aims to explore the influence of geogrid characteristics on the performance of geogrid-reinforced ballast. Single-rib tensile tests are first conducted in a temperature-controlled controlled environment on two geogrid materials to characterize their response at temperatures ranging from -30ºC to 40ºC. A series of ballast box tests is subsequently performed on geogrid-reinforced ballast layers. These experiments are designed to study the interplay between the subgrade strength and geogrid placement depth and their impact on the behavior of ballast exposed to cyclic loading. Finally, the distinct element method is used to run numerical simulations that offer insights into the micromechanical aspects of the interactions between ballast and geogrid. In addition, a parametric study is undertaken to evaluate how changes in geogrid stiffness and aperture size contribute to a geogrid's ability to reinforce ballast. The salient conclusions of this thesis are summarized below.

In Chapter 3, the two geogrid materials are found to exhibit temperature-dependent mechanical properties. The polypropylene biaxial geogrid behaves in a ductile fashion at elevated temperatures with increasingly small ultimate tensile strengths being mobilized at increasingly large ultimate strains. On the contrary, the geogrid's response to tensile loading becomes more brittle at lower temperatures with greater ultimate tensile strengths being reached at smaller ultimate strains. The effect of temperature changes is also observed in the geogrid's tensile strength at 2% and 5% strain, where both strengths increase at lower temperatures and decrease as temperatures rise. The response of the geogrid composite to temperature changes mirrors this pattern to a certain degree. While its ultimate strain diminishes at lower temperatures, its ultimate tensile strength appears to be insensitive to temperature changes. However, both its tensile strength at 2% and 5% strain increase in response to temperature drops.

The experimental campaign presented in Chapter 4 suggests that the subgrade strength dictates the influence of a geogrid's placement depth in a ballast layer. In ballast beds supported by a competent subgrade, embedding a geogrid 150, 200, and 250mm beneath the tie results in comparable reductions in the tie's permanent and resilient settlement. Similar increases in the tie support stiffness are also observed across the placement depth spectrum. However, a new trend emerges as the subgrade strength decreases. In ballast layers supported by a fair subgrade, the largest reductions in permanent and resilient settlement are achieved by the geogrid located 150mm beneath the tie, followed by those placed at depths of 200 and 250mm. Correspondingly, the geogrid placed 150mm under the tie is the most effective at increasing the tie support stiffness. The differences between geogrid placement depths are further magnified in ballast layers supported by the soft subgrade. Interestingly, the ballast's damping ratio appears to be relatively insensitive to the presence of geogrids and is instead found to be primarily a function of the subgrade's strength.

Expanding on the experimental findings from Chapter 4, Chapter 5 discusses the development of a three-dimensional ballast box test model using the distinct element method. This model offers insight into the micromechanical processes that influence the behavior of geogrid-reinforced ballast. The simulations indicated that ballast particles in a 300mm-thick layer follow two distinct displacement patterns. Particles in the layer's upper 150mm show significant movement due to cyclic loading, with their velocity diminishing as depth increases. Conversely, particles in the lower half of the layer exhibit minimal displacement. This indicates why geogrids placed at shallow depths more effectively stabilize ballast as they interlock with and confine the ballast particles that displace the most. Additionally, the simulations highlight that the use of geogrids increases the ballast layer's coordination number and reduces the average interparticle contact force, especially when the geogrids are placed at shallower depths. The model also illustrates that an A/D_{50} ratio greater than or equal to 1.45 is required for geogrids to achieve an effective interlock with and reinforce ballast particles. Interestingly, the simulations suggest that variations in geogrid stiffness caused by temperature changes from -30ºC to 40ºC as discussed in Chapter 3, have a marginal impact on the geogrid capacity to stabilize ballast.

7.2. Recommendations for Future Work

The work discussed in this thesis offers a limited assessment of the behavior of geogrid-reinforced ballast. Potential future research avenues on this topic include expanding the scope of the experimental campaigns presented herein and leveraging experimental data to develop and calibrate more sophisticated numerical models. The main suggestions for expanding the scope of this research are:

- Experimentally investigate the behavior of geogrids embedded in railroad ballast, subjected to cyclic train loading, and exposed to temperature fluctuations
- Conduct an experimental campaign on scaled-down models to assess the performance of a geosynthetic-reinforced ballasted substructure with a geogrid located in the ballast layer and a geogrid composite placed at the subballast/subgrade interface
- Modify the ballast box test to include a subballast layer and instrument the ballast/subballast assembly along with any geogrid placed in it to monitor the evolution of stresses in the soil media and capture the strains that develop in the geosynthetic
- Using geogrid samples recovered at the end of ballast box tests, assess whether geogrids suffer from strength degradation as a result of their use in soil and exposure to cyclic loading. Additionally, investigate whether their placement depth and the subgrade strength have any effect on potential strength degradations
- Expand the scope of the DEM simulations to include a wider range of ballast particle sizes, consider ballast particle breakage, and investigate the effect of principal stress rotation on the behavior of geogrid-reinforced ballast
- Use coupled discrete element-finite element modeling to explore the deformations and stress distribution that develop in geogrid-reinforced ballasted substructures subjected to cyclic loading
- Consider dynamic elements such as the heat transfer process in a geogrid-reinforced ballasted structure and explore how non-uniform temperature fluctuations affect the stability of reinforced ballast
- Expand the experimental and numerical modeling campaigns to capture the effect of projected temperature changes in Canada over the coming decades on the behavior of geogrid-reinforced ballast
- Extend experimental investigations to investigate how geogrid-reinforced ballasted substructures respond to changes in pore water pressure and ice formation

References

Abadi, T., Pen, L. L., Zervos, A., & Powrie, W. (2018). Improving the performance of railway tracks through ballast interventions. *Proceedings of the Institution of Mechanical Engineers, Part F: Journal of Rail and Rapid Transit*, *232*(2), 337–355. https://doi.org/10.1177/0954409716671545

Alva-Hurtado, J. E., & Selig, E. T. (1981). *Permanent Strain Behavior of Railroad Ballast*. 10th International Conference on Soil Mechanics and Foundation Engineering, Stockholm.

Anderson, W. F., & Key, A. J. (2000). Model Testing of Two-Layer Railway Track Ballast. *Journal of Geotechnical and Geoenvironmental Engineering*, *126*(4), 317–323. https://doi.org/10.1061/(ASCE)1090-0241(2000)126:4(317)

AREMA. (2010). *Manual for Railway Engineering*. AREMA.

Ariyama, T., Mori, Y., & Kaneko, K. (1997). Tensile properties and stress relaxation of polypropylene at elevated temperatures. *Polymer Engineering & Science*, *37*(1), 81–90. https://doi.org/10.1002/pen.11647

ASTM. (1996). ASTM D3999-91 Standard Test Methods for the Determination of the Modulus and Damping Properties of Soils using the Cyclic Triaxial Apparatus. *Annual Book of ASTM Standards*, *4*(Reapproved). https://doi.org/10.1520/D3999-11

ASTM. (2005). ASTM D1883-07: Standard Test Method for CBR (California Bearing Ratio) of Soils in Place. *ASTM Standard Guide*, *04*(May), 21–24. https://doi.org/10.1520/D1883-21

ASTM. (2015). *ASTM D6637 / D6637M-15, Standard Test Method for Determining Tensile Properties of Geogrids by the Single or Multi-Rib Tensile Method* (pp. 435–440). ASTM. https://doi.org/10.1520/D6637_D6637M-15

Barksdale, R. D., & Itani, S. Y. (1989). Influence of Aggregate Shape on Base Behavior. *Transportation Research Record*.

Bathurst, R. J., & Raymond, G. P. (1987). Geogrid reinforcement of ballasted track. *Transportation Research Record*, *1153*, 8–14.

Bathurst, R. J., Raymond, G. P., & Jarrett, P. M. (1986). Performance of Geogrid-Reinforced Ballast Railroad Track Support. *Third International Conference on Geotextiles*, *80*, 43–48.

Bhat, S., & Thomas, J. (2015). Design and construction of a geosynthetic reinforced pavement on weak subgrade. In Canadian Geotechnical Society (Ed.), *Canadian Geotechnical*

Conference & Canadian Permafrost Conference (pp. 1–5). Canadian Geotechnical Society.

Bhat, S., & Tomas, J. (2017). Railroad Subgrade Stabilization using Biaxial Geogrid-Geotextile Composite – A Case Study. In L. Paredes, J. P. Gourc, V. Valdebenito, W. Mondaca, & C. Binvignat (Eds.), *First International Conference on Technology and Application of Geotextiles* (pp. 1–7). Gecamin.

Bian, X., Huang, H., Tutumluer, E., & Gao, Y. (2016). "Critical particle size" and ballast gradation studied by Discrete Element Modeling. *Transportation Geotechnics*, *6*, 38–44. https://doi.org/10.1016/j.trgeo.2016.01.002

Bian, X., Li, W., Qian, Y., & Tutumluer, E. (2020). Analysing the effect of principal stress rotation on railway track settlement by discrete element method. *Geotechnique*, *70*(9), 803–821. https://doi.org/10.1680/jgeot.18.P.368

Bonthron, B., & Jonsson, C. (2017). *Geogrids in cold climate*. Lulea University of Technology.

Bourgonje, T., & Diercks, S. A. (2011). Rehabilitation of Canadian National Railway Track Servicing Oil Sands in Northern Alberta. *AREMA*.

Brough, M. J., Ghataora, G. S., Stirling, A. B., Madelin, K. B., Rogers, C. D. F., & Chapman, D. N. (2003). Investigation of railway track subgrade. I: In-situ assessment. *Proceedings of the Institution of Civil Engineers - Transport*, *156*(3), 145–154. https://doi.org/10.1680/tran.2003.156.3.145

Brown, S. F. (1974). Repeated Load Testing of a Granular Material. *Journal of the Geotechnical Engineering Division*, *100*(7).

Brown, S. F. (1996). Soil mechanics in pavement engineering. *Géotechnique*, *46*(3), 383–426. https://doi.org/10.1680/geot.1996.46.3.383

Brown, S. F., Brodrick, B. V., Thom, N. H., & McDowell, G. R. (2007). The Nottingham railway test facility, UK. *Proceedings of the Institution of Civil Engineers - Transport*, *160*(2), 59–65. https://doi.org/10.1680/tran.2007.160.2.59

Brown, S. F., Kwan, J., & Thom, N. H. (2007). Identifying the key parameters that influence geogrid reinforcement of railway ballast. *Geotextiles and Geomembranes*, *25*(6), 326–335. https://doi.org/10.1016/j.geotexmem.2007.06.003

Bruzek, R., Stark, T. D., Wilk, S. T., Thompson, H. B., & Sussmann, T. R. (2016). Fouled Ballast Definitions and Parameters. *2016 Joint Rail Conference*, *April*. https://doi.org/10.1115/JRC2016-5725

Burrow, M. P. N., Bowness, D., & Ghataora, G. S. (2007). A comparison of railway track foundation design methods. *Proceedings of the Institution of Mechanical Engineers, Part F: Journal of Rail and Rapid Transit*, *221*(1), 1–12. https://doi.org/10.1243/09544097JRRT58

Bush, D. I. (1990). Variation of long-term design strength of geosynthetics in temperatures up to 40 C. In Balkema (Ed.), *Proceedings of the Fourth International Conference on Geotextiles, Geomembranes, and Related Products* (pp. 673–676). Balkema.

Bush, E., & Lemmen, D. S. (2019). *Canada's Climate Change Report*. Government of Canada.

Calhoun, C. C. (1972). *Development of design criteria and acceptance specifications for plastic filter cloths*. US Army Engineer Waterways Experiment Station.

Canadian National Railway. (2015). *Engineering Specifications for Industrial Tracks*.

Chantachot, T., Kongkitkul, W., & Tatsuoka, F. (2016). Load-strain-time behavours of two polymer geogrids affected by temperature. *International Journal of GEOMATE*, *10*(3), 1869–1876. https://doi.org/10.21660/2016.21.5192

Chantachot, T., Kongkitkul, W., & Tatsuoka, F. (2017). Effects of temperature on elastic stiffness of a HDPE geogrid and its model simulation. *International Journal of GEOMATE*, *12*(32), 94–100. https://doi.org/10.21660/2017.32.6620

Chantachot, T., Kongkitkul, W., & Tatsuoka, F. (2018). Effects of temperature rise on load-strain-time behaviour of geogrids and simulations. *Geosynthetics International*, *25*(3), 287–303. https://doi.org/10.1680/jgein.18.00008

Chawla, S., & Shahu, J. T. (2016a). Reinforcement and mud-pumping benefits of geosynthetics in railway tracks: Model tests. *Geotextiles and Geomembranes*, *44*(3), 366–380. https://doi.org/10.1016/j.geotexmem.2016.01.005

Chawla, S., & Shahu, J. T. (2016b). Reinforcement and mud-pumping benefits of geosynthetics in railway tracks: Numerical analysis. *Geotextiles and Geomembranes*, *44*(3), 344–357. https://doi.org/10.1016/j.geotexmem.2016.01.006

Chen, C., Indraratna, B., McDowell, G., & Rujikiatkamjorn, C. (2015). Discrete element modelling of lateral displacement of a granular assembly under cyclic loading. *Computers and Geotechnics*, *69*, 474–484. https://doi.org/10.1016/j.compgeo.2015.06.006

Chen, C., McDowell, G. R., & Thom, N. H. (2012). Discrete element modelling of cyclic loads of geogrid-reinforced ballast under confined and unconfined conditions. *Geotextiles and Geomembranes*, *35*, 76–86. https://doi.org/10.1016/j.geotexmem.2012.07.004

Chen, C., McDowell, G. R., & Thom, N. H. (2013). A study of geogrid-reinforced ballast using laboratory pull-out tests and discrete element modelling. *Geomechanics and Geoengineering*, *8*(4), 244–253. https://doi.org/10.1080/17486025.2013.805253

Chen, C., McDowell, G. R., & Thom, N. H. (2014). Investigating geogrid-reinforced ballast: Experimental pull-out tests and discrete element modelling. *Soils and Foundations*, *54*(1), 1–11. https://doi.org/10.1016/j.sandf.2013.12.001

Chen, J., Bao, N., & Sun, R. (2022). Three-Dimensional Discrete-Element-Method Analysis of Behavior of Geogrid-Reinforced Sand Foundations under Strip Footing. *International Journal of Geomechanics*, *22*(9), 1–16. https://doi.org/10.1061/(asce)gm.1943-5622.0002543

Chen, J., Vinod, J. S., Indraratna, B., Ngo, N. T., Gao, R., & Liu, Y. (2022). A discrete element study on the deformation and degradation of coal-fouled ballast. *Acta Geotechnica*, *4*. https://doi.org/10.1007/s11440-022-01453-4

Chen, W., Zhang, Y., Wang, C., Xiao, Y., & Lou, P. (2023). Effect of ballast pockets and geogrid reinforcement on ballasted track: Numerical analysis. *Transportation Geotechnics*, *42*, 101108. https://doi.org/10.1016/j.trgeo.2023.101108

Choi, J.-Y., Yun, S.-W., Chung, J.-S., & Kim, S.-H. (2020). Comparative Study of Wheel–Rail Contact Impact Force for Jointed Rail and Continuous Welded Rail on Light-Rail Transit. *Applied Sciences*, *10*(7), 2299. https://doi.org/10.3390/app10072299

Chrismer, S., & Davis, D. (2000). Cost comparisons of remedial methods to correct track substructure instability. *Transportation Research Record*, *1713*, 10–14. https://doi.org/10.3141/1713-02

Civils and Utilities. (2024). *Wrekin SX20 20kN Biaxial Geogrid 4 x 50m Roll* [Civils and Utilities]. https://www.civilsandutilities.com/p/wrekin-sx20-20kn-biaxial-geogrid-4-x-50m-roll-WSX20450

Cuelho, E. V., Perkins, S. W., & Ganeshan, S. K. (2005). Determining Geosynthetic Material Properties Pertinent to Reinforced Pavement Design. In C. W. Schwartz, E. Tutumluer, & L. Tashman (Eds.), *Advances in Pavement Engineering* (pp. 1–12). American Society of Civil Engineers. https://doi.org/10.1061/40776(155)19

Cui, F.-L., Xiao, C.-Z., Wang, F., Wang, Z.-H., Ding, L.-Q., & Tian, W.-L. (2022). Physical Modeling of Temperature Influence on Performance of Geogrid-Reinforced Retaining Walls Considering Backfill Type Effect. *Journal of Cold Regions Engineering*, *36*(3), 04022005. https://doi.org/10.1061/(ASCE)CR.1943-5495.0000282

Cundall, P. A., & Strack, O. D. L. (1979). A discrete numerical model for granular assemblies. *Géotechnique*, *29*(1), 47–65. https://doi.org/10.1680/geot.1979.29.1.47

Dahlberg, T. (2001). Some railroad settlement models—A critical review. *Proceedings of the Institution of Mechanical Engineers, Part F: Journal of Rail and Rapid Transit*, *215*(4), 289–300. https://doi.org/10.1243/0954409011531585

D'Angelo, G., Sol-Sanchez, M., Moreno-Navarro, F., Lo Presti, D., & Thom, N. (2018). Use of bitumen-stabilised ballast for improving railway trackbed conventional maintenance. *Geotechnique*, *68*(6), 518–527. https://doi.org/10.1680/jgeot.17.P.022

Das, B. M. (2016). Use of geogrid in the construction of railroads. *Innovative Infrastructure Solutions*, *1*(1), 15. https://doi.org/10.1007/s41062-016-0017-8

de Paiva, C. E. L., Buck, A. P., & Ferreira, A. (2018). Sub-ballast performance in Brazilian railway infrastructures. *Construction and Building Materials*, *190*, 164–169. https://doi.org/10.1016/j.conbuildmat.2018.09.093

Desbrousses, R. L. E., & Meguid, M. A. (2021). On the analysis and design of reinforced railway embankments in cold climate: A review. In S. Tighe, S. Walbridge, & V. Henderson (Eds.), *CSCE 2021 Annual Conference* (pp. 588–598). Springer.

Desbrousses, R. L. E., & Meguid, M. A. (2022). Effect of subgrade compressibility on the reinforcing performance of railroad geogrids: Insights from finite element analysis. *GeoCalgary 2022*.

Desbrousses, R. L. E., & Meguid, M. A. (2023a). Geogrids in cold climates: Insights from in-isolation tensile tests at low temperatures. In *Geosynthetics: Leading the Way to a Resilient Planet* (pp. 467–473). CRC Press. https://doi.org/10.1201/9781003386889-45

Desbrousses, R. L. E., & Meguid, M. A. (2023b). On the Design of a Pneumatic Cyclic Loading Setup for Geotechnical Testing. In C. G. Society (Ed.), *GeoSaskatoon 2023*. Canadian Geotechnical Society.

Desbrousses, R. L. E., Meguid, M. A., & Bhat, S. (2021). Effect of Temperature on the Mechanical Properties of Two Polymeric Geogrid Materials. *Geosynthetics International*, 1–31. https://doi.org/10.1680/jgein.21.00032a

Desbrousses, R. L. E., Meguid, M. A., & Bhat, S. (2023). Experimental Investigation of the Effects of Subgrade Strength and Geogrid Location on the Cyclic Response of Geogrid-Reinforced Ballast. *International Journal of Geosynthetics and Ground Engineering*, *9*(6), 67. https://doi.org/10.1007/s40891-023-00486-3

Desbrousses, R. L. E., Meguid, M. A., & Bhat, S. (2024a). Discrete Element Study on the Effects of Geogrid Characteristics on the Mechanical Response of Reinforced Ballast Under Cyclic Loading. *Transportation Infrastructure Geotechnology*. https://doi.org/10.1007/s40515-024-00413-7

Desbrousses, R. L. E., Meguid, M. A., & Bhat, S. (2024b). *On the effect of subgrade strength on the performance of geogrid-reinforced ballast*. GeoAmericas 2024, Toronto, ON.

Eliáš, J. (2014). Simulation of railway ballast using crushable polyhedral particles. *Powder Technology*, *264*, 458–465. https://doi.org/10.1016/j.powtec.2014.05.052

Elliott, R. P., & Thornton, S. I. (1986). Resilient Modulus and AASHTO Pavement Design. *Transportation Research Record*.

Esmaeili, M., Aela, P., & Hosseini, A. (2017). Experimental assessment of cyclic behavior of sand-fouled ballast mixed with tire derived aggregates. *Soil Dynamics and Earthquake Engineering*, *98*(September 2016), 1–11. https://doi.org/10.1016/j.soildyn.2017.03.033

Esmaeili, M., Aela, P., & Hosseini, A. (2019). Effect of Moisture on Performance of Mixture of Sand-Fouled Ballast and Tire-Derived Aggregates under Cyclic Loading. *Journal of Materials in Civil Engineering*, *31*(2), 04018377. https://doi.org/10.1061/(asce)mt.1943-5533.0002586

Esmaeili, M., Nouri, R., & Yousefian, K. (2017). Experimental comparison of the lateral resistance of tracks with steel slag ballast and limestone ballast materials. *Proceedings of the Institution of Mechanical Engineers, Part F: Journal of Rail and Rapid Transit*, *231*(2), 175–184. https://doi.org/10.1177/0954409715623577

Esmaeili, M., Zakeri, J. A., & Babaei, M. (2017). Laboratory and field investigation of the effect of geogrid-reinforced ballast on railway track lateral resistance. *Geotextiles and Geomembranes*, *45*(2), 23–33. https://doi.org/10.1016/j.geotexmem.2016.11.003

Fardin Rosa, A., Sacramento Aragão, F. T., & Motta, L. M. G. D. (2021). Effects of particle size distribution and lithology on the resistance to breakage of ballast materials. *Construction and Building Materials*, *267*, 121015. https://doi.org/10.1016/j.conbuildmat.2020.121015

Fei, W., & Narsilio, G. A. (2020). Impact of Three-Dimensional Sphericity and Roundness on Coordination Number. *Journal of Geotechnical and Geoenvironmental Engineering*, *146*(12), 1–7. https://doi.org/10.1061/(asce)gt.1943-5606.0002389

Feng, S. J., & Wang, Y. Q. (2023). DEM simulation of geogrid–aggregate interface shear behavior: Optimization of the aperture ratio considering the initial interlocking states. *Computers and Geotechnics*, *154*(December 2022), 105182. https://doi.org/10.1016/j.compgeo.2022.105182

Ferellec, J., & McDowell, G. (2010). Modelling realistic shape and particle inertia in DEM. *Geotechnique*, *60*(3), 227–232. https://doi.org/10.1680/geot.9.T.015

Ferellec, J.-F., & McDowell, G. R. (2012). Modelling of ballast–geogrid interaction using the discrete-element method. *Geosynthetics International*, *19*(6), 470–479. https://doi.org/10.1680/gein.12.00031

Fernandes, G., Palmeira, E. M., & Gomes, R. C. (2008). Performance of geosynthetic-reinforced alternative sub-ballast material in a railway track. *Geosynthetics International*, *15*(5), 311–321. https://doi.org/10.1680/gein.2008.15.5.311

Fischer, S. (2022). Geogrid reinforcement of ballasted railway superstructure for stabilization of the railway track geometry – A case study. *Geotextiles and Geomembranes*, *50*(5), 1036–1051. https://doi.org/10.1016/j.geotexmem.2022.05.005

Gao, G., & Meguid, M. A. (2018). Effect of particle shape on the response of geogrid-reinforced systems: Insights from 3D discrete element analysis. *Geotextiles and Geomembranes*, *46*(6), 685–698. https://doi.org/10.1016/j.geotexmem.2018.07.001

Gedela, R., & Karpurapu, R. (2021). A Review on the Role of Geosynthetics in Preventing the Excessive Settlement and Mud Pumping of Ballasted Railway Track. In *Lecture Notes in Civil Engineering* (Vol. 86, pp. 715–726). Springer Singapore. https://doi.org/10.1007/978-981-15-6233-4_51

Göbel, C. H., Weisemann, U. C., & Kirschner, R. A. (1994). Effectiveness of a reinforcing geogrid in a railway subbase under dynamic loads. *Geotextiles and Geomembranes*, *13*(2), 91–99. https://doi.org/10.1016/0266-1144(94)90041-8

Grossoni, I., Andrade, A. R., & Bezin, Y. (2016). Assessing the role of longitudinal variability of vertical track stiffness in the long-term deterioration. *The Dynamics of Vehicles on Roads and Tracks - Proceedings of the 24th Symposium of the International Association for Vehicle System Dynamics, IAVSD 2015*, 851–860. https://doi.org/10.1201/b21185-91

Gu, Q., Liu, H., Wu, Y., Luo, Z., & Bian, X. (2022). Evolution of trackbed performance and ballast degradation due to passages of million train wheel axle loads. *Transportation Geotechnics*, *34*(January), 100753. https://doi.org/10.1016/j.trgeo.2022.100753

Gu, X., Huang, M., & Qian, J. (2014). DEM investigation on the evolution of microstructure in granular soils under shearing. *Granular Matter*, *16*(1), 91–106. https://doi.org/10.1007/s10035-013-0467-z

Guo, Y., Marikine, V., & Jing, G. (2022). Railway ballast. In *Rail Infrastructure Resilience: A Best-Practices Handbook*. Elsevier Inc. https://doi.org/10.1016/B978-0-12-821042-0.00021-6

Guo, Y., Markine, V., & Jing, G. (2021). Review of ballast track tamping: Mechanism, challenges and solutions. *Construction and Building Materials*, *300*, 123940. https://doi.org/10.1016/j.conbuildmat.2021.123940

Guo, Y., Xie, J., Fan, Z., Markine, V., Connolly, D. P., & Jing, G. (2022). Railway ballast material selection and evaluation: A review. *Construction and Building Materials*, *344*(June), 128218. https://doi.org/10.1016/j.conbuildmat.2022.128218

Guo, Y., Zhao, C., Markine, V., Jing, G., & Zhai, W. (2020). Calibration for discrete element modelling of railway ballast: A review. *Transportation Geotechnics*, *23*(January), 100341. https://doi.org/10.1016/j.trgeo.2020.100341

Guo, Y., Zhao, C., Markine, V., Shi, C., Jing, G., & Zhai, W. (2020). Discrete element modelling of railway ballast performance considering particle shape and rolling resistance. *Railway Engineering Science*, *28*(4), 382–407. https://doi.org/10.1007/s40534-020-00216-9

Han, J., Bhandari, A., & Wang, F. (2012). DEM Analysis of Stresses and Deformations of Geogrid-Reinforced Embankments over Piles. *International Journal of Geomechanics*, *12*(4), 340–350. https://doi.org/10.1061/(asce)gm.1943-5622.0000050

Han, J., & Jiang, Y. (2013). Use of geosynthetics for performance enhancement of earth structures in cold regions. *Sciences in Cold and Arid Regions*, *5*(5), 517. https://doi.org/10.3724/SP.J.1226.2013.00517

Heath, D., Waters, J., Shenton, M., & Sparrow, R. (1972). Design of Conventional Rail Track Foundations. *Proceedings of the Institution of Civil Engineers*, *51*(2), 251–267. https://doi.org/10.1680/iicep.1972.5952

Henry, K. S., & Durell, G. R. (2007). Cold temperature testing of geotextiles: New, and containing soil fines and moisture. *Geosynthetics International*, *14*(5), 320–329. https://doi.org/10.1680/gein.2007.14.5.320

Heydinger, A. G., Xie, Q., Randolph, B. W., & Gupta, J. D. (1996). Analysis of Resilient Modulus of Dense- and Open-Graded Aggregates. *Transportation Research Record*.

Hicks, R. G. (1970). *Factors Influencing the Resilient Properties of Granular Materials* [Ph.D. Thesis]. University of California Berkeley.

Hicks, R. G., & Monismith, C. L. (1971). Factors Influencing the Resilient Response of Granular Materials. *Highway Research Record*, 15–31.

Huang, H., & Tutumluer, E. (2011). Discrete Element Modeling for fouled railroad ballast. *Construction and Building Materials*, *25*(8), 3306–3312. https://doi.org/10.1016/j.conbuildmat.2011.03.019

Huang, H., Tutumluer, E., & Dombrow, W. (2009). Laboratory characterization of fouled railroad ballast behavior. *Transportation Research Record*, *2117*, 93–101. https://doi.org/10.3141/2117-12

Hussaini, S. K. K. (2013). An experimental study on the deformation behaviour of geosynthetically reinforced ballast. *Ph.D. Thesis*, 240.

Hussaini, S. K. K., Indraratna, B., & Vinod, J. S. (2015). Performance assessment of geogrid-reinforced railroad ballast during cyclic loading. *Transportation Geotechnics*, *2*, 99–107. https://doi.org/10.1016/j.trgeo.2014.11.002

Hussaini, S. K. K., Indraratna, B., & Vinod, J. S. (2016). A laboratory investigation to assess the functioning of railway ballast with and without geogrids. *Transportation Geotechnics*, *6*, 45–54. https://doi.org/10.1016/j.trgeo.2016.02.001

Hussaini, S. K. K., & Sweta, K. (2020). Application of Geogrids in Stabilizing Rail Track Substructure. *Frontiers in Built Environment*, *6*(February), 1–13. https://doi.org/10.3389/fbuil.2020.00020

Hussaini, S. K. K., & Sweta, K. (2021). Investigation of deformation and degradation response of geogrid-reinforced ballast based on model track tests. *Proceedings of the Institution of Mechanical Engineers, Part F: Journal of Rail and Rapid Transit*, *235*(4), 505–517. https://doi.org/10.1177/0954409720944687

Ibrahim, A., Desbrousses, R. L. E., Xu, J., & Meguid, M. A. (2024). Investigation of the mechanical response of recovered geogrids under repeated loading. *Geosynthetics International*. https://doi.org/10.1680/jgein.23.00177

Indraratna, B., Hussaini, S. K. K., & Vinod, J. S. (2013). The lateral displacement response of geogrid-reinforced ballast under cyclic loading. *Geotextiles and Geomembranes*, *39*, 20–29. https://doi.org/10.1016/j.geotexmem.2013.07.007

Indraratna, B., Ionescu, D., & Christie, H. D. (1998). Shear Behavior of Railway Ballast Based on Large-Scale Triaxial Tests. *Journal of Geotechnical and Geoenvironmental Engineering*, *124*(5), 439–449. https://doi.org/10.1061/(ASCE)1090-0241(1998)124:5(439)

Indraratna, B., Ionescu, D., & Christie, H. D. (2000). State-of-the-art Large Scale Testing of Ballast. *Conference on Railway Engineering, 21-23 May 2000*, 208–220.

Indraratna, B., Karimullah Hussaini, Sd. K., & Vinod, J. S. (2012). On The Shear Behavior of Ballast-Geosynthetic Interfaces. *Geotechnical Testing Journal*, *35*(2), 103317. https://doi.org/10.1520/GTJ103317

Indraratna, B., Khabbaz, H., Salim, W., & Christie, D. (2006). Geotechnical properties of ballast and the role of geosynthetics in rail track stabilisation. *Proceedings of the Institution of Civil Engineers - Ground Improvement*, *10*(3), 91–101. https://doi.org/10.1680/grim.2006.10.3.91

Indraratna, B., Lackenby, J., & Christie, D. (2005). Effect of confining pressure on the degradation of ballast under cyclic loading. *Géotechnique*, *55*(4), 325–328. https://doi.org/10.1680/geot.2005.55.4.325

Indraratna, B., Ngo, N. T., & Rujikiatkamjorn, C. (2011). Behavior of geogrid-reinforced ballast under various levels of fouling. *Geotextiles and Geomembranes*, *29*(3), 313–322. https://doi.org/10.1016/j.geotexmem.2011.01.015

Indraratna, B., Ngo, T., Bessa Ferreira, F., Rujikiatkamjorn, C., & Shahkolahi, A. (2020). Laboratory examination of ballast deformation and degradation under impact loads with synthetic inclusions. *Transportation Geotechnics*, *25*, 100406. https://doi.org/10.1016/j.trgeo.2020.100406

Indraratna, B., Nimbalkar, S., Christie, D., Rujikiatkamjorn, C., & Vinod, J. (2010). Field Assessment of the Performance of a Ballasted Rail Track with and without Geosynthetics. *Journal of Geotechnical and Geoenvironmental Engineering*, *136*(7), 907–917. https://doi.org/10.1061/(ASCE)GT.1943-5606.0000312

Indraratna, B., & Salim, W. (2005). *Mechanics of Ballasted Rail Tracks: A Geotechnical Perspective*. Taylor & Francis Group.

Indraratna, B., Salim, W., & Rujikiatkamjorn, C. (2011). *Advanced Rail Geotechnology—Ballasted Track*. CRC Press. https://doi.org/10.1201/b10861

Indraratna, B., Sun, Y., & Nimbalkar, S. (2016). Laboratory Assessment of the Role of Particle Size Distribution on the Deformation and Degradation of Ballast under Cyclic Loading. *Journal of Geotechnical and Geoenvironmental Engineering*, *142*(7), 04016016. https://doi.org/10.1061/(ASCE)GT.1943-5606.0001463

Indraratna, B., Vinod, J. S., & Lackenby, J. (2009). Influence of particle breakage on the resilient modulus of railway ballast. *Geotechnique*, *59*(7), 643–646. https://doi.org/10.1680/geot.2008.T.005

Ionescu, D. (2004). Ballast Degradation and Measurement of Ballast Fouling. *7th Railway Engineering Proceedings*, *July 2004*, p.169-180.

Itasca. (2022). *Particle Flow Code (PFC3D)* [Computer software].

Itasca Consulting Group Inc. (2019). *Pavement Design Package for PFC3D*. Itasca Consulting Group Inc.

Itasca Consulting Group Inc. (2024). *Particle Flow Code 3D (PFC 3D) User Manual*.

Jackson, N., & Dhir, R. K. (1996). *Civil Engineering Materials*. Palgrave MacMillan.

Janardhanam, R., & Desai, C. S. (1983). Three-Dimensional Testing and Modeling of Ballast. *Journal of Geotechnical Engineering*, *109*(6), 783–882. https://doi.org/10.1061/(ASCE)0733-9410(1983)109:6(783)

Jarjour, J., & Meguid, M. A. (2023). Investigating the effect of temperature and water freezing on the response of geogrid composite. *Geosynthetics International*. https://doi.org/10.1680/jgein.23.00078

Jewell, R. A. (1988). The mechanics of reinforced embankments on soft soils. *Geotextiles and Geomembranes*, *7*(4), 237–273. https://doi.org/10.1016/0266-1144(88)90001-5

Jewell, R. A., Milligan, G. W. E., Sarsby, R. W., & Dubois, D. (1984). *Interaction Between Soil and Geogrids.* 18–30.

Jia, W., Markine, V., Guo, Y., & Jing, G. (2019). Experimental and numerical investigations on the shear behaviour of recycled railway ballast. *Construction and Building Materials*, *217*, 310–320. https://doi.org/10.1016/j.conbuildmat.2019.05.020

Jiang, Y., & Nimbalkar, S. (2019). Finite Element Modeling of Ballasted Rail Track Capturing Effects of Geosynthetic Inclusions. *Frontiers in Built Environment*, *5*(May), 1–11. https://doi.org/10.3389/fbuil.2019.00069

Jing, G., & Aela, P. (2020). Review of the lateral resistance of ballasted tracks. *Proceedings of the Institution of Mechanical Engineers, Part F: Journal of Rail and Rapid Transit*, *234*(8), 807–820. https://doi.org/10.1177/0954409719866355

Karademir, T., & Frost, J. D. (2014). Micro-scale tensile properties of single geotextile polypropylene filaments at elevated temperatures. *Geotextiles and Geomembranes*, *42*(3), 201–213. https://doi.org/10.1016/j.geotexmem.2014.03.001

Kashani, H. F., Ho, C. L., & Hyslip, J. P. (2018). Fouling and water content influence on the ballast deformation properties. *Construction and Building Materials*, *190*, 881–895. https://doi.org/10.1016/j.conbuildmat.2018.09.058

Kashani, H. F., & Hyslip, J. P. (2018). Ballast Life and Effective Parameters. *2018 Joint Rail Conference*, V001T01A023. https://doi.org/10.1115/JRC2018-6264

Kashani, H. F., Hyslip, J. P., & Ho, C. L. (2017). Laboratory evaluation of railroad ballast behavior under heavy axle load and high traffic conditions. *Transportation Geotechnics*, *11*, 69–81. https://doi.org/10.1016/j.trgeo.2017.04.002

Kasozi, A. M., Siddharthan, R. V., & Mahamud, R. (2014). MSE wall geogrid tensile strength at high temperature sites. *Environmental Geotechnics*, *3*(1), 4–16. https://doi.org/10.1680/envgeo.13.00073

Kim, U. J., & Kim, D. S. (2020). Load sharing characteristics of rigid facing walls with geogrid reinforced railway subgrade during and after construction. *Geotextiles and Geomembranes*, *48*(6), 940–949. https://doi.org/10.1016/j.geotexmem.2020.08.002

Knutson, R. M., & Thompson, M. R. (1977). Resilient Response of Railway Ballast. *Transportation Research Record*.

Knutson, R. M., & Thompson, M. R. (1978). Permanent-Deformation Behavior of Railway Ballast. *Transportation Research Record*, *5*.

Koda, E., Miszkowska, A., & Kiersnowska, A. (2018). Assessment of the temperature influence on the tensile strength and elongation of woven geotextiles used in landfill. In K. G. Society (Ed.), *11th International Conference on Geosynthetics 2018, ICG 2018* (Vol. 4, pp. 2676–2681). International Geosynthetics Society.

Koerner, R. M. (2005). *Designing with Geosynthetics*. Pearson Education.

Koerner, R. M., Hsuan, Y., & Lord, A. E. (1993). Remaining technical barriers to obtaining general acceptance of geosynthetics. *Geotextiles and Geomembranes*, *12*(1), 1–52. https://doi.org/10.1016/0266-1144(93)90035-M

Koerner, R. M., Lord, A. E., & Hsuan, Y. H. (1992). Arrhenius modeling to predict geosynthetic degradation. *Geotextiles and Geomembranes*, *11*(2), 151–183. https://doi.org/10.1016/0266-1144(92)90042-9

Kongkitkul, W., Tabsombut, W., Jaturapitakkul, C., & Tatsuoka, F. (2012). Effects of temperature on the rupture strength and elastic stiffness of geogrids. *Geosynthetics International*, *19*(2), 106–123. https://doi.org/10.1680/gein.2012.19.2.106

Kumar, N., Suhr, B., Marschnig, S., Dietmaier, P., Marte, C., & Six, K. (2019). Micro-mechanical investigation of railway ballast behavior under cyclic loading in a box test using DEM: effects of elastic layers and ballast types. *Granular Matter*, *21*(4), 1–17. https://doi.org/10.1007/s10035-019-0956-9

Kwan, C. C. J. (2006). *Geogrid Reinforcement of Railway* [Ph.D. Thesis]. University of Nottigham.

Lackenby, J. (2006). *Triaxial behaviour of ballast and the role of confining pressure under cyclic loading* [Ph.D. Thesis]. University of Wollongong.

Lackenby, J., Indraratna, B., McDowell, G., & Christie, D. (2007). Effect of confining pressure on ballast degradation and deformation under cyclic triaxial loading. *Géotechnique*, *57*(6), 527–536. https://doi.org/10.1680/geot.2007.57.6.527

Lai, H. J., Zheng, J. J., Zhang, J., Zhang, R. J., & Cui, L. (2014). DEM analysis of "soil"-arching within geogrid-reinforced and unreinforced pile-supported embankments. *Computers and Geotechnics*, *61*, 13–23. https://doi.org/10.1016/j.compgeo.2014.04.007

Lekarp, F., Isacsson, U., & Dawson, A. (2000a). State of the Art. I: Resilient Response of Unbound Aggregates. *Journal of Transportation Engineering*, *126*(1), 66–75. https://doi.org/10.1061/(ASCE)0733-947X(2000)126:1(66)

Lekarp, F., Isacsson, U., & Dawson, A. (2000b). State of the Art. II: Permanent Strain Response of Unbound Aggregates. *Journal of Transportation Engineering*, *126*(1), 76–83. https://doi.org/10.1061/(ASCE)0733-947X(2000)126:1(76)

Li, C., Gao, R., Hu, Q., & Chen, J. (2024). Effect of the combination of geogrid and rubber granules on the performance of ballast under impact loads. *Granular Matter*, *26*(1), 10. https://doi.org/10.1007/s10035-023-01384-1

Li, D. (2018). 25 years of heavy axle load railway subgrade research at the Facility for Accelerated Service Testing (FAST). *Transportation Geotechnics*, *17*(May), 51–60. https://doi.org/10.1016/j.trgeo.2018.09.003

Li, D., Hyslip, J., Sussmann, T., & Chrismer, S. (2015). *Railway Geotechnics*. CRC Press. https://doi.org/10.1201/b18982

Li, D., & Selig, E. T. (1995). Evaluation of railway subgrade problems. *Transportation Research Record*, *1489*, 17–25.

Li, D., & Selig, E. T. (1998a). Method for Railroad Track Foundation Design. I: Development. *Journal of Geotechnical and Geoenvironmental Engineering*, *124*(4), 316–322. https://doi.org/10.1061/(ASCE)1090-0241(1998)124:4(316)

Li, D., & Selig, E. T. (1998b). Method for Railroad Track Foundation Design. II: Applications. *Journal of Geotechnical and Geoenvironmental Engineering*, *124*(4), 323–329. https://doi.org/10.1061/(ASCE)1090-0241(1998)124:4(323)

Li, D., & Wilk, S. (2021). Recent studies on railway-track substructure at TTCI. *Transportation Safety and Environment*, *3*(1), 36–49. https://doi.org/10.1093/tse/tdaa031

Li, G., Li, J., Wang, J., Feng, J., Guo, Q., Zhou, J., & Mitrouchev, P. (2018). The Effect of Temperature on Mechanical Properties of Polypropylene. In K. Wang, Y. Wang, J. Strandhagen, & T. Yu (Eds.), *Advanced Manufacturing and Automation VII. IWAMA 2017. Lecture Notes in Electrical Engineering* (Vol. 451, Issue 1, pp. 143–149). Springer. https://doi.org/10.1007/978-981-10-5768-7_14

Li, H., & McDowell, G. (2020). Discrete element modelling of two-layered ballast in a box test. *Granular Matter*, *22*(4), 1–14. https://doi.org/10.1007/s10035-020-01046-6

Li, H., & McDowell, G. R. (2018). Discrete element modelling of under sleeper pads using a box test. *Granular Matter*, *20*(2), 1–12. https://doi.org/10.1007/s10035-018-0795-0

Lim, W. L. (2004). Mechanics of Railway Ballast Behaviour. In *Ph.D. Thesis*. University of Nottingham.

Lim, W. L., & McDowell, G. R. (2005). Discrete element modelling of railway ballast. *Granular Matter*, *7*(1), 19–29. https://doi.org/10.1007/s10035-004-0189-3

Liu, H., Niu, F., Niu, Y., Lin, Z., Lu, J., & Luo, J. (2012). Experimental and numerical investigation on temperature characteristics of high-speed railway's embankment in seasonal frozen regions. *Cold Regions Science and Technology*, *81*, 55–64. https://doi.org/10.1016/j.coldregions.2012.04.004

Liu, J., Zhou, W., Ma, G., Yang, S., & Chang, X. (2020). Strong contacts, connectivity and fabric anisotropy in granular materials: A 3D perspective. *Powder Technology*, *366*, 747–760. https://doi.org/10.1016/j.powtec.2020.03.018

Liu, K., Qiu, R., Su, Q., Ni, P., Liu, B., Gao, J., & Wang, T. (2021). Suffusion response of well graded gravels in roadbed of non-ballasted high speed railway. *Construction and Building Materials*, *284*, 122848. https://doi.org/10.1016/j.conbuildmat.2021.122848

Liu, S., Huang, H., Qiu, T., & Kwon, J. (2016). Effect of geogrid on railroad ballast particle movement. *Transportation Geotechnics*, *9*, 110–122. https://doi.org/10.1016/j.trgeo.2016.08.003

Liu, Y., & Yan, Z. (2023). Study on strong contact system by sub-network partitioning method for binary mixtures. *European Journal of Environmental and Civil Engineering*, 1–25. https://doi.org/10.1080/19648189.2023.2268691

Lopes, M. L. (2021). Soil geosynthetic interaction. *ICE Handbook of Geosynthetic Engineering*, 55–79. https://doi.org/10.1680/icehge.65000.045

Luo, Z., Zhao, C., Bian, X., & Chen, Y. (2023). Discrete element analysis of geogrid-stabilized ballasted tracks under high-speed train moving loads. *Computers and Geotechnics*, *159*(March), 105451. https://doi.org/10.1016/j.compgeo.2023.105451

Luo, Z., Zhao, C., Cai, W., Gu, Q., Lin, W., Bian, X., & Chen, Y. (2023a). Full-scale model tests on ballasted tracks with/without geogrid-stabilization under high-speed train loads. *Géotechnique*, *19(6)*, 1–43. https://doi.org/10.1680/jgeot.22.00339

Luo, Z., Zhao, C., Cai, W., Gu, Q., Lin, W., Bian, X., & Chen, Y. (2023b). Full-scale model tests on ballasted tracks with/without geogrid-stabilization under high-speed train loads. *Geotechnique*, 1–15. https://doi.org/10.1680/jgeot.22.00339

Malisetty, R. S., Indraratna, B., Qi, Y., & Rujikiatkamjorn, C. (2022). Shakedown response of recycled rubber-granular waste mixtures under cyclic loading. *Geotechnique*, *1*. https://doi.org/10.1680/jgeot.21.00040

Marx, D. H., Kumar, K., & Zornberg, J. G. (2023). Quantification of geogrid lateral restraint using transparent sand and deep learning-based image segmentation. *Geotextiles and Geomembranes*, *October 2022*. https://doi.org/10.1016/j.geotexmem.2023.04.004

McDowell, G. R., Harireche, O., Konietzky, H., Brown, S. F., & Thom, N. H. (2006). Discrete element modelling of geogrid-reinforced aggregates. *Proceedings of the Institution of Civil Engineers - Geotechnical Engineering*, *159*(1), 35–48. https://doi.org/10.1680/geng.2006.159.1.35

McDowell, G. R., & Stickley, P. (2006). Performance of geogrid-reinforced ballast. *Ground Engineering*, *39*(1), 26–30.

McGown, A., Khan, A. J., & Kupec, J. (2004). The isochronous strain energy approach applied to the load–strain–time–temperature behaviour of geosynthetics. *Geosynthetics International*, *11*(2), 114–130. https://doi.org/10.1680/gein.2004.11.2.114

Minh, N. H., & Cheng, Y. P. (2013). A DEM investigation of the effect of particle-size distribution on one-dimensional compression. *Geotechnique*, *63*(1), 44–53. https://doi.org/10.1680/geot.10.P.058

Minh, N. H., Cheng, Y. P., & Thornton, C. (2014). Strong force networks in granular mixtures. *Granular Matter*, *16*(1), 69–78. https://doi.org/10.1007/s10035-013-0455-3

Mishra, D., Qian, Y., Kazmee, H., & Tutumluer, E. (2014). Investigation of Geogrid-Reinforced Railroad Ballast Behavior Using Large-Scale Triaxial Testing and Discrete Element

Modeling. *Transportation Research Record: Journal of the Transportation Research Board*, *2462*(1), 98–108. https://doi.org/10.3141/2462-12

Murray, R. T., & Farrar, D. M. (1988). Temperature distributions in reinforced soil retaining walls. *Geotextiles and Geomembranes*, *7*(1–2), 33–50. https://doi.org/10.1016/0266-1144(88)90017-9

Navaratnarajah, S. K., & Indraratna, B. (2017). Use of Rubber Mats to Improve the Deformation and Degradation Behavior of Rail Ballast under Cyclic Loading. *Journal of Geotechnical and Geoenvironmental Engineering*, *143*(6), 1–15. https://doi.org/10.1061/(asce)gt.1943-5606.0001669

Ngamkhanong, C., Feng, B., Tutumluer, E., M.A. Hashash, Y., & Kaewunruen, S. (2021). Evaluation of lateral stability of railway tracks due to ballast degradation. *Construction and Building Materials*, *278*, 122342. https://doi.org/10.1016/j.conbuildmat.2021.122342

Ngo, N. T., & Indraratna, B. (2016). Improved Performance of Rail Track Substructure Using Synthetic Inclusions: Experimental and Numerical Investigations. *International Journal of Geosynthetics and Ground Engineering*, *2*(3), 1–16. https://doi.org/10.1007/s40891-016-0065-3

Ngo, N. T., Indraratna, B., & Rujikiatkamjorn, C. (2014). DEM simulation of the behaviour of geogrid stabilised ballast fouled with coal. *Computers and Geotechnics*, *55*, 224–231. https://doi.org/10.1016/j.compgeo.2013.09.008

Ngo, T., Indraratna, B., & Ferreira, F. (2021). Influence of synthetic inclusions on the degradation and deformation of ballast under heavy-haul cyclic loading. *International Journal of Rail Transportation*, *00*(00), 1–23. https://doi.org/10.1080/23248378.2021.1964390

Niu, D., Shi, W., Wang, C., Xie, X., & Niu, Y. (2023). Effect of coordination number of particle contact force on rutting resistance of asphalt mixture. *Construction and Building Materials*, *392*, 131784. https://doi.org/10.1016/j.conbuildmat.2023.131784

Nurmikolu, A. (2012). Key aspects on the behaviour of the ballast and substructure of a modern railway track: Research-based practical observations in Finland. *Journal of Zhejiang University SCIENCE A*, *13*(11), 825–835. https://doi.org/10.1631/jzus.A12ISGT1

Offenbacher, S., Antony, B., Barbir, O., Auer, F., & Landgraf, M. (2021). Evaluating the applicability of multi-sensor equipped tamping machines for ballast condition monitoring. *Measurement*, *172*, 108881. https://doi.org/10.1016/j.measurement.2020.108881

O'Sullivan, C. (2011). Particulate Discrete Element Modelling. In *Particulate Discrete Element Modelling*. https://doi.org/10.1201/9781482266498

Ouadfel, H. (1998). *Numerical Simulations of Granular Assemblies with Three-Dimensional Ellipsoid-Shaped Particles* [Ph.D. Thesis]. University of Waterloo.

Ouadfel, H., & Rothenburg, L. (2001). `Stress-force-fabric' relationship for assemblies of ellipsoids. *Mechanics of Materials*, *33*(4), 201–221. https://doi.org/10.1016/S0167-6636(00)00057-0

Pan, T., Tutumluer, E., & Anochie-boateng, J. (2006). Aggregate Morphology Affecting Resilient Behavior of Unbound Granular Materials. *Transportation Research Record*, 12–20.

Prasad, K. V. S., & Hussaini, S. K. K. (2022). Review of different stabilization techniques adapted in ballasted tracks. *Construction and Building Materials*, *340*(April), 127747. https://doi.org/10.1016/j.conbuildmat.2022.127747

Qian, Y., Mishra, D., Tutumluer, E., Hashash, Y. M. A., & Ghaboussi, J. (2016). Moisture Effects on Degraded Ballast Shear Strength Behavior. *2016 Joint Rail Conference*, V001T01A034. https://doi.org/10.1115/JRC2016-5840

Qian, Y., Mishra, D., Tutumluer, E., & Kazmee, H. A. (2015). Characterization of geogrid reinforced ballast behavior at different levels of degradation through triaxial shear strength test and discrete element modeling. *Geotextiles and Geomembranes*, *43*(5), 393–402. https://doi.org/10.1016/j.geotexmem.2015.04.012

Qian, Y., Tutumluer, E., Hashash, Y. M. A., & Ghaboussi, J. (2022). Triaxial testing of new and degraded ballast under dry and wet conditions. *Transportation Geotechnics*, *34*, 100744. https://doi.org/10.1016/j.trgeo.2022.100744

Qian, Y., Tutumluer, E., Mishra, D., & Kazmee, H. (2018). Triaxial testing and discrete-element modelling of geogrid-stabilised rail ballast. *Proceedings of the Institution of Civil Engineers: Ground Improvement*, *171*(4), 223–231. https://doi.org/10.1680/jgrim.17.00068

Raad, L., Minassian, G. H., & Gartin, S. (1992). Characterization of Saturated Granular Bases Under Repeated Loads. *Transportation Research Record*.

Radjai, F., Wolf, D. E., Jean, M., & Moreau, J.-J. (1998). Bimodal Character of Stress Transmission in Granular Packings. *Physical Review Letters*, *80*(1), 61–64. https://doi.org/10.1103/PhysRevLett.80.61

Radjai, F., Wolf, D. E., Roux, S., Jean, M., & Moreau, J. J. (1997). Force networks in dense granular media. *Powders and Grains*.

Railway Association of Canada. (2018). *Rail Trends*. www.railcan.ca

Railway Association of Canada. (2020). *Rail Trends*. www.railcan.ca

Raymond, G. P. (1978). Design for Railroad Ballast and Subgrade Support. *Journal of the Geotechnical Engineering Division*, *104*(1), 45–60. https://doi.org/10.1061/AJGEB6.0000576

Raymond, G. P. (2002). Reinforced ballast behaviour subjected to repeated load. *Geotextiles and Geomembranes*, *20*(1), 39–61. https://doi.org/10.1016/S0266-1144(01)00024-3

Raymond, G. P., & Diyaljee, V. A. (1979). Railroad Ballast Sizing and Grading. *Journal of the Geotechnical Engineering Division*, *105*(5), 676–681. https://doi.org/10.1061/AJGEB6.0000803

Raymond, G. P., & Ismail, I. (2003). The effects of geogrid reinforcement on unbound aggregates. *Geotextiles and Geomembranes*, *21*(6), 355–380. https://doi.org/10.1016/S0266-1144(03)00044-X

Raymond, G. P., Lamson, S. T., & Law, J. E. (1983). *A review of current track structure design and future track research requirements*. Canadian Institute of Guided Ground Transport.

Raymond, G. P., & Williams, D. R. (1978). Repeated Load Triaxial Tests on a Dolomite Ballast. *Journal of the Geotechnical Engineering Division*, *104*(7), 1013–1029. https://doi.org/10.1061/AJGEB6.0000655

Roustaei, M., & Hendry, M. T. (2023). Frost Action in Canadian Railways: A Review of Assessment and Treatment Methods. *J. Cold Reg. Eng.*, *37*(4).

Sadeghi, J., Tolou Kian, A. R., Ghiasinejad, H., Fallah Moqaddam, M., & Motevalli, S. (2020). Effectiveness of geogrid reinforcement in improvement of mechanical behavior of sand-contaminated ballast. *Geotextiles and Geomembranes*, *48*(6), 768–779. https://doi.org/10.1016/j.geotexmem.2020.05.007

Sadeghi, J., Tolou Kian, A. R., Khanmoradi, A., & Chopani, M. (2023). Behavior of sand-contaminated ballast reinforced with geogrid under cyclic loading. *Construction and Building Materials*, *362*(August 2022), 129654. https://doi.org/10.1016/j.conbuildmat.2022.129654

Sayeed, M. A., & Shahin, M. A. (2018a). Design of ballasted railway track foundations using numerical modelling. Part I: Development. *Canadian Geotechnical Journal*, *55*(3), 353–368. https://doi.org/10.1139/cgj-2016-0633

Sayeed, M. A., & Shahin, M. A. (2018b). Design of ballasted railway track foundations using numerical modelling. Part II: Applications. *Canadian Geotechnical Journal*, *55*(3), 369–396. https://doi.org/10.1139/cgj-2016-0634

Scanlan, K. M. (2018). *Evaluating degraded ballast and track geometry variability along a Canadian freight railroad through ballast maintenance records and ground-penetrating radar* [Ph.D. Thesis]. University of Alberta.

Segrestin, P., & Jailloux, J. M. (1988). Temperature in soils and its effect on the ageing of synthetic materials. *Geotextiles and Geomembranes*, *7*(1–2), 51–69. https://doi.org/10.1016/0266-1144(88)90018-0

Selig, E. T., & Sluz, A. (1978). Ballast and Subgrade Response To Train Loads. *Transportation Research Record*, *694*, 53–60.

Selig, E. T., & Waters, J. M. (1994). *Track Geotechnology and Substructure Management*. Thomas Telford Ltd.

Sharpe, P., Brough, M. J., & Dixon, J. (2006). Geogrid Trials at Coppull Moor on the West Coast Main Line. *1st International Conference on Railway Foundations–RailFound06*, 367–375. https://www.researchgate.net/publication/288559036

Shenton, M. J. (1978). Deformation of Railway Ballast under Repeated Loading Conditions. In *Railroad Track Mechanics and Technology* (pp. 405–425). Elsevier. https://doi.org/10.1016/B978-0-08-021923-3.50025-5

Shi, C., Zhao, C., Yang, Y., Guo, Y., & Zhang, X. (2021). Analysis of Railway Ballasted Track Stiffness and Behavior with a Hybrid Discrete–Continuum Approach. *International Journal of Geomechanics*, *21*(3), 1–10. https://doi.org/10.1061/(asce)gm.1943-5622.0001941

Shi, S., Gao, L., Cai, X., Xiao, Y., & Xu, M. (2022). Mechanical characteristics of ballasted track under different tamping depths in railway maintenance. *Transportation Geotechnics*, *35*, 100799. https://doi.org/10.1016/j.trgeo.2022.100799

Shin, E. C., Kim, D. H., & Das, B. M. (2002). Geogrid-reinforced railroad bed settlement due to cyclic load. *Geotechnical and Geological Engineering*, *20*(3), 261–271. https://doi.org/10.1023/A:1016040414725

Shokr, M., Meguid, M. A., & Bhat, S. (2022). Experimental Investigation of the Tensile Response of Stiff Fiberglass Geogrid Under Varying Temperatures. *International Journal of Geosynthetics and Ground Engineering*, *8*(1). https://doi.org/10.1007/s40891-022-00361-7

Sol-Sánchez, M., Moreno-Navarro, F., & Rubio-Gámez, M. C. (2016). Analysis of ballast tamping and stone-blowing processes on railway track behaviour: The influence of using USPs. *Geotechnique*, *66*(6), 481–489. https://doi.org/10.1680/jgeot.15.P.129

Stahl, M., Konietzky, H., te Kamp, L., & Jas, H. (2014). Discrete element simulation of geogrid-stabilised soil. *Acta Geotechnica*, *9*(6), 1073–1084. https://doi.org/10.1007/s11440-013-0265-0

Suhr, B., & Six, K. (2017). Parametrisation of a DEM model for railway ballast under different load cases. *Granular Matter*, *19*(4), 1–16. https://doi.org/10.1007/s10035-017-0740-7

Suhr, B., & Six, K. (2020). Simple particle shapes for DEM simulations of railway ballast: Influence of shape descriptors on packing behaviour. *Granular Matter*, *22*(2), 1–17. https://doi.org/10.1007/s10035-020-1009-0

Suhr, B., & Six, K. (2022). Efficient DEM simulations of railway ballast using simple particle shapes. *Granular Matter*, *24*(4), 1–19. https://doi.org/10.1007/s10035-022-01274-y

Suiker, A. S. J., Selig, E. T., & Frenkel, R. (2005). Static and Cyclic Triaxial Testing of Ballast and Subballast. *Journal of Geotechnical and Geoenvironmental Engineering*, *131*(6), 771–782. https://doi.org/10.1061/(ASCE)1090-0241(2005)131:6(771)

Sun, Q. D., Indraratna, B., & Nimbalkar, S. (2016). Deformation and Degradation Mechanisms of Railway Ballast under High Frequency Cyclic Loading. *Journal of Geotechnical and Geoenvironmental Engineering*, *142*(1), 04015056. https://doi.org/10.1061/(ASCE)GT.1943-5606.0001375

Sun, Q., Indraratna, B., & Ngo, N. T. (2019). Effect of increase in load and frequency on the resilience of railway ballast. *Geotechnique*, *69*(9), 833–840. https://doi.org/10.1680/jgeot.17.P.302

Sun, Q., Indraratna, B., & Nimbalkar, S. (2014). Effect of cyclic loading frequency on the permanent deformation and degradation of railway ballast. *Geotechnique*, *64*(9), 746–751. https://doi.org/10.1680/geot.14.T.015

Sun, Y., Chen, C., & Nimbalkar, S. (2017). Identification of ballast grading for rail track. *Journal of Rock Mechanics and Geotechnical Engineering*, *9*(5), 945–954. https://doi.org/10.1016/j.jrmge.2017.04.006

Sun, Y., Indraratna, B., & Nimbalkar, S. (2014). Three-dimensional characterisation of particle size and shape for ballast. *Géotechnique Letters*, *4*(3), 197–202. https://doi.org/10.1680/geolett.14.00036

Sussmann, T. R., Ruel, M., & Chrismer, S. M. (2012). Source of Ballast Fouling and Influence Considerations for Condition Assessment Criteria. *Transportation Research Record: Journal of the Transportation Research Board*, *2289*(1), 87–94. https://doi.org/10.3141/2289-12

Sweta, K., & Hussaini, S. K. K. (2018). Effect of shearing rate on the behavior of geogrid-reinforced railroad ballast under direct shear conditions. *Geotextiles and Geomembranes*, *46*(3), 251–256. https://doi.org/10.1016/j.geotexmem.2017.12.001

Sweta, K., & Hussaini, S. K. K. (2019). Behavior evaluation of geogrid-reinforced ballast-subballast interface under shear condition. *Geotextiles and Geomembranes*, *47*(1), 23–31. https://doi.org/10.1016/j.geotexmem.2018.09.002

Sweta, K., & Hussaini, S. K. K. (2020). Effect of geogrid on deformation response and resilient modulus of railroad ballast under cyclic loading. *Construction and Building Materials*, *264*, 120690. https://doi.org/10.1016/j.conbuildmat.2020.120690

Sweta, K., & Hussaini, S. K. K. (2022). Role of particle breakage on damping, resiliency and service life of geogrid-reinforced ballasted tracks. *Transportation Geotechnics*, *37*(July), 100828. https://doi.org/10.1016/j.trgeo.2022.100828

Thakur, P. K., Vinod, J. S., & Indraratna, B. (2013). Effect of confining pressure and frequency on the deformation of ballast. *Geotechnique*, *63*(9), 786–790. https://doi.org/10.1680/geot.12.T.001

Thom, N. H., & Brown, S. F. (1989). The mechanical properties of unbound aggregates from various sources. In *Unbound Aggregates in Roads* (pp. 130–142). Elsevier. https://doi.org/10.1016/B978-0-408-04355-7.50024-8

Thornton, C., & Antony, S. J. (1998). Quasi–static deformation of particulate media. *Philosophical Transactions of the Royal Society of London. Series A: Mathematical, Physical and Engineering Sciences*, *356*(1747), 2763–2782. https://doi.org/10.1098/rsta.1998.0296

Tian, P., Zaman, M. M., & Laguros, J. G. (1998). Gradation and Moisture Effects on Resilient Moduli of Aggregate Bases. *Transportation Research Record: Journal of the Transportation Research Board*, *1619*(1), 75–84. https://doi.org/10.3141/1619-09

Titan Environmental Containment. (2020). *Titan Rail Grid 30* (Issue November, p. 2020).

Titan Environmental Containment. (2021). *Swamp Grid 30* (Issue January, p. 2021).

Tolomeo, M., & McDowell, G. R. (2022). Modelling real particle shape in DEM: a comparison of two methods with application to railway ballast. *International Journal of Rock Mechanics and Mining Sciences*, *159*(December 2021), 105221. https://doi.org/10.1016/j.ijrmms.2022.105221

Touqan, M., Ahmed, A., El Naggar, H., & Stark, T. (2020). Static and cyclic characterization of fouled railroad sub-ballast layer behaviour. *Soil Dynamics and Earthquake Engineering*, *137*(July), 106293. https://doi.org/10.1016/j.soildyn.2020.106293

Transport Canada. (2023). *Rail Jobs*. https://tc.canada.ca/en/corporate-services/jobs-transport-canada/looking-exciting-work-get-job-transportation/rail-jobs

Tutumluer, E., Huang, H., & Bian, X. (2012). Geogrid-Aggregate Interlock Mechanism Investigated through Aggregate Imaging-Based Discrete Element Modeling Approach. *International Journal of Geomechanics*, *12*(4), 391–398. https://doi.org/10.1061/(ASCE)GM.1943-5622.0000113

Tutumluer, E., & Pan, T. (2008). Aggregate Morphology Affecting Strength and Permanent Deformation Behavior of Unbound Aggregate Materials. *Journal of Materials in Civil Engineering*, *20*(9), 617–627. https://doi.org/10.1061/(asce)0899-1561(2008)20:9(617)

UIC. (2008). *Earthworks and track bed for railway lines—UIC 719 R*. Union Internationale des Chemins de Fer.

Usman, K., Burrow, M., & Ghataora, G. (2015). Railway Track Subgrade Failure Mechanisms Using a Fault Chart Approach. *Procedia Engineering*, *125*, 547–555. https://doi.org/10.1016/j.proeng.2015.11.060

Wang, E. L., Xu, E. L., Zhang, B., Zhong, H., Gao, Z. K., & Chang, J. D. (2008). Experimental study on creep properties of plastic geogrid under low temperature. In G. Li, Y. Chen, &

X. Tang (Eds.), *Geosynthetics in Civil and Environmental Engineering—Geosynthetics Asia 2008: Proceedings of the 4th Asian Regional Conference on Geosynthetics* (pp. 70–73). Springer. https://doi.org/10.1007/978-3-540-69313-0_15

Wang, K., Zhuang, Y., Kouretzis, G., & Sloan, S. W. (2020). Shakedown analysis of ballasted track structure using three-dimensional finite element techniques. *Acta Geotechnica*, *15*(5), 1231–1241. https://doi.org/10.1007/s11440-019-00818-6

Wang, L., Meguid, M., & Mitri, H. S. (2021). Impact of ballast fouling on the mechanical properties of railway ballast: Insights from discrete element analysis. *Processes*, *9*(8). https://doi.org/10.3390/pr9081331

Wang, Y.-Q., Feng, S.-J., Zhao, Y., & Zheng, Q.-T. (2024). Microscale analysis of geogrid–aggregate interface cyclic shear behavior using DEM. *Computers and Geotechnics*, *166*, 105973. https://doi.org/10.1016/j.compgeo.2023.105973

Ward, I. M., & Sweeney, J. (2004). *An Introduction to the Mechanical Properties of Solid Polymers*. John wiley & Sons Ltd.

Wu, P., Zhang, F., Wang, J., Wei, L., & Huo, W. (2023). Review of wheel-rail forces measuring technology for railway vehicles. *Advances in Mechanical Engineering*, *15*(3), 168781322311589. https://doi.org/10.1177/16878132231158991

Xiao, C., Cui, F., Ding, L., Wang, F., & Tian, W.-L. (2022). Temperature Distributions in Geogrid-Reinforced Soil Retaining Walls Subjected to Seasonal Freeze–Thaw Cycles. *International Journal of Geomechanics*, *22*(12), 04022234. https://doi.org/10.1061/(ASCE)GM.1943-5622.0002595

Xiao, C., Gao, S., Liu, H., & Du, Y. (2021). Case history on failure of geosynthetics-reinforced soil bridge approach retaining walls. *Geotextiles and Geomembranes*, *49*(6), 1585–1599. https://doi.org/10.1016/j.geotexmem.2021.08.001

Yarivand, A., Behnia, C., Bakhtiyari, S., & Ghalandarzadeh, A. (2017). Performance of geosynthetic reinforced soil bridge abutments with modular block facing under fire scenarios. *Computers and Geotechnics*, *85*, 28–40. https://doi.org/10.1016/j.compgeo.2016.12.004

Yu, Z., Woodward, P. K., Laghrouche, O., & Connolly, D. P. (2019). True triaxial testing of geogrid for high speed railways. *Transportation Geotechnics*, *20*(May), 100247. https://doi.org/10.1016/j.trgeo.2019.100247

Zarnani, S., Scott, J. D., & Sego, D. C. (2011). Effect of soil temperature changes on geogrid strains. *Canadian Geotechnical Journal*, *48*(8), 1287–1294. https://doi.org/10.1139/t11-035

Zornberg, J. G., Byler, B. R., & Knudsen, J. W. (2004). Creep of Geotextiles Using Time–Temperature Superposition Methods. *Journal of Geotechnical and Geoenvironmental Engineering*, *130*(11), 1158–1168. https://doi.org/10.1061/(ASCE)1090-0241(2004)130

Appendix

A.1. Introduction

This appendix provides an in-depth description of the pneumatic cyclic loading apparatus used to perform the ballast box tests described in Chapter 4. The cyclic loading setup along with the soil container were designed and built by the Ph.D. candidate under the supervision of Prof. Meguid. The information contained in this appendix constitutes parts of a paper published in the following conference proceedings:

Desbrousses, R.L.E. and Meguid, M.A. (2023). On the Design of a Pneumatic Cyclic Loading Setup for Geotechnical Testing. *In:* GeoSaskatoon 2023. Canadian Geotechnical Society, Saskatoon, AB.

A.2. Soil Container

One of the objectives of the developed setup is to provide a soil container with an adjustable width that may be changed depending on the specific requirements of the experiment to be conducted, allowing for soil samples and model footings of different dimensions to be tested. As such, a modular box consisting of a rigid outer frame and two movable inner walls is constructed as shown in Figure A.1. The outer frame is composed of two 1,830mm-long, 600mm-tall sides built with welded 4×4in (100×100mm) hollow steel sections (HSS) connected to two 1,575mm-long, 600mm-tall sides by four 2,438mm-long threaded rods tightened at each end with hexagonal nuts. The inner sides of the two 1,830mm-long walls are lined with 1 ½in-thick plywood sheets and thin sheet metal. The outer rigid frame is braced laterally by means of two 2,135mm-long, 4×6in (100×150mm) HSS placed against the outer edge of each 1,830mm-long side and connected to each other with two 2,285mm-long threaded rods. Two 1,290mm-long, 600mm-tall movable sides composed of welded 4×4in HSS lined with 1 ½in-thick plywood sheets and sheet metal (see Figure A.1b) are placed within the outer frame, creating a rectangular trench in the center of the box with a steel plate as its bottom surface in which ballast can be poured. Each movable wall has two hexagonal nuts welded on its back side.

The position of each inner movable wall is adjustable along the box's longitudinal axis by means of eight removable steel spacers placed in holders welded to the back of each movable wall and to the front of the 1,575mm-long sides of the outer rigid frame. Each movable wall is forced into tight contact with the four steel spacers sitting against its back with a tensioning system (see Figure 1c) that consists of two threaded rods screwed into the hexagonal nuts welded to the back of the movable walls going through two 4×6in HSS reacting against the outside edge of the 1,575mm-long sides of the outer rigid frame. The threaded rods are tensioned using washers and hexagonal nuts that are screwed against the 4×6in HSS thereby pulling the movable walls they are attached to toward the outer rigid frame and hence forcing them into tight contact with the spacers. Four sets of steel spacers are made, allowing the box's plan dimensions to be set to 305×1,290mm, 610×1,290mm, 915×1,290mm, and 1,220×1,290mm as shown in Figure A.2.

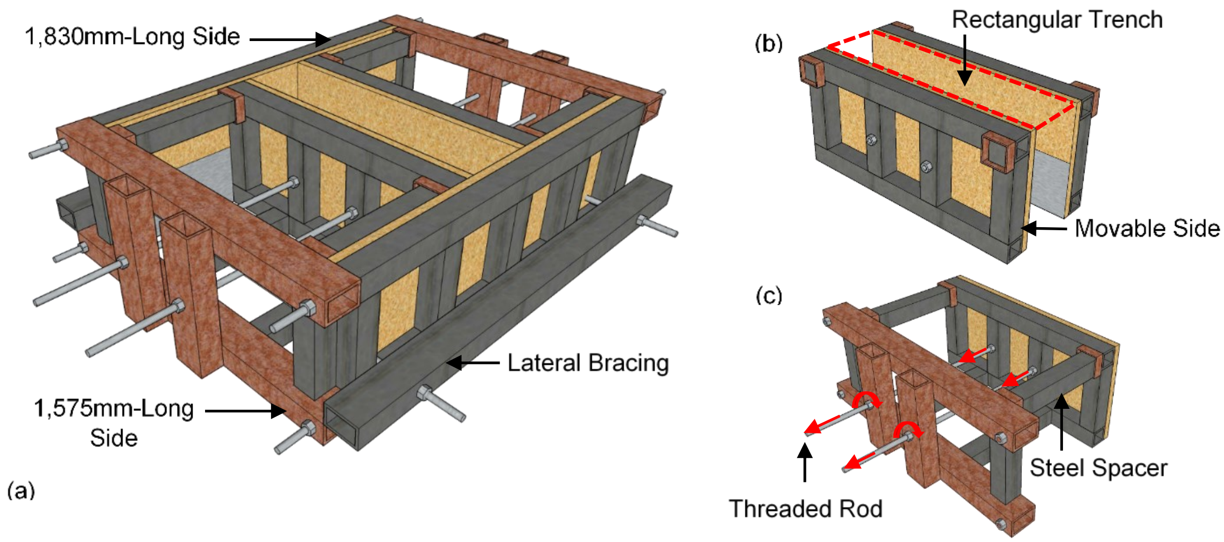

Figure A.1: (a) Overview of the Soil Container, (b) Inner Movable Walls, (c) Tensioning System and Steel Spacers.

A.3. Pneumatic Cyclic Loading Apparatus

Cyclic loading is applied to the ballast samples and their overlying tie or any other soil sample with a model footing built in the soil container by a pneumatic actuator mounted on a 400,000lb (1,780kN)-capacity load frame as shown in Figure A.3. The actuator is a heavy-duty 10in (254mm) bore steel cylinder with a 2½in (63.5mm) diameter piston road and a 6in (150mm) stroke rated to operate at pressures ranging from 5psi (0.03MPa) to 250psi (1.70MPa) with non-lubricated air. The cylinder is powered by compressed air generated by the laboratory's air compressors that supply air at 100psi (0.69MPa), meaning that the actuator is capable of delivering a theoretical maximum compressive force of 34.9kN.

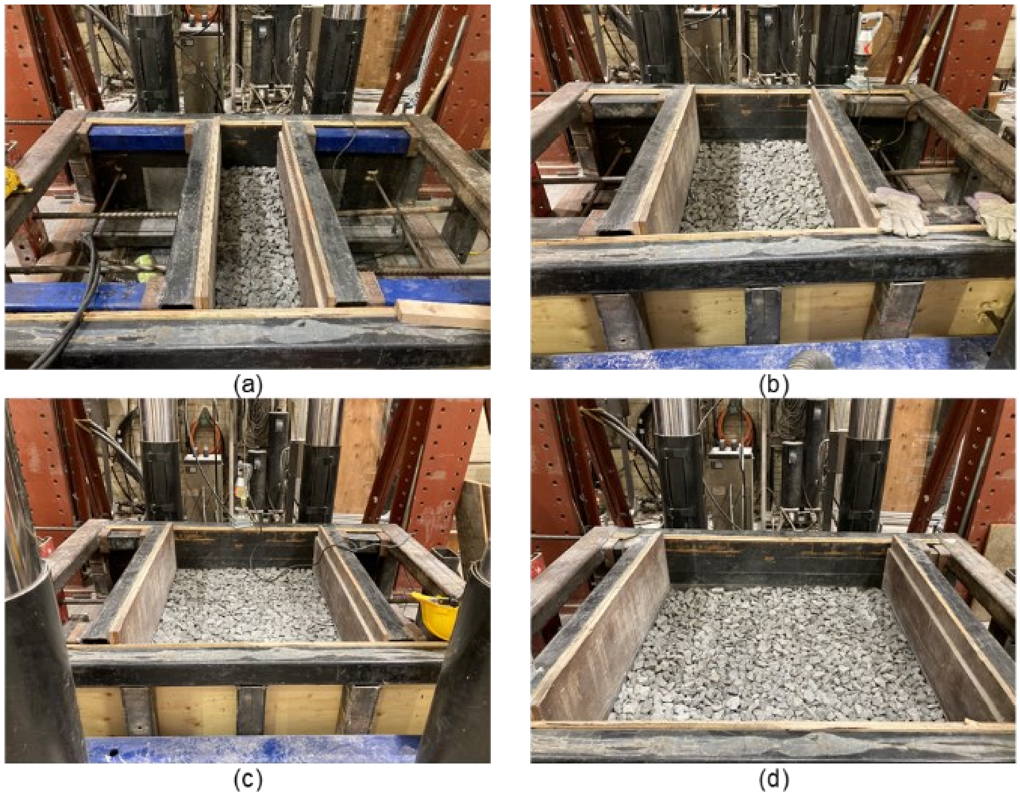

Figure A.2: Soil Container with a Width of (a) 305mm, (b) 610mm, (c) 915mm, and (d) 1,220mm.

A.3.1. Load Measurement and Application

A 50kN load cell is mounted on the end of the actuator's piston rod to measure the load applied to the model tie at any given time during an experiment as shown in Figure A.4. The transfer of the compressive load from the cylinder down to the underlying tie is accomplished through a high-strength, 2in (50.8mm) diameter steel shaft machined to be screwed into the 50kN load cell at its top end and a 6in (150mm) diameter ball joint at its bottom end. The shaft itself passes through a linear bearing supported by an auxiliary frame built around the pneumatic cylinder and bolted to the load frame. The combined presence of the linear bearing and ball joint is necessary to ensure the steel shaft's motion is linear and in line with the center line of both the load cell and pneumatic actuator. Such precautions are needed to prevent the transfer of lateral loads to either the load cell or the cylinder's piston rod during cyclic loading. Indeed, due to the highly discontinuous and random nature of the unbound aggregate underlying the tie, it is likely that the tie will not settle uniformly into the ballast which could result in the tie's top surface being slightly tilted and hence the transfer of lateral loads to the load cell and actuator if the ball joint and linear bearing were not used.

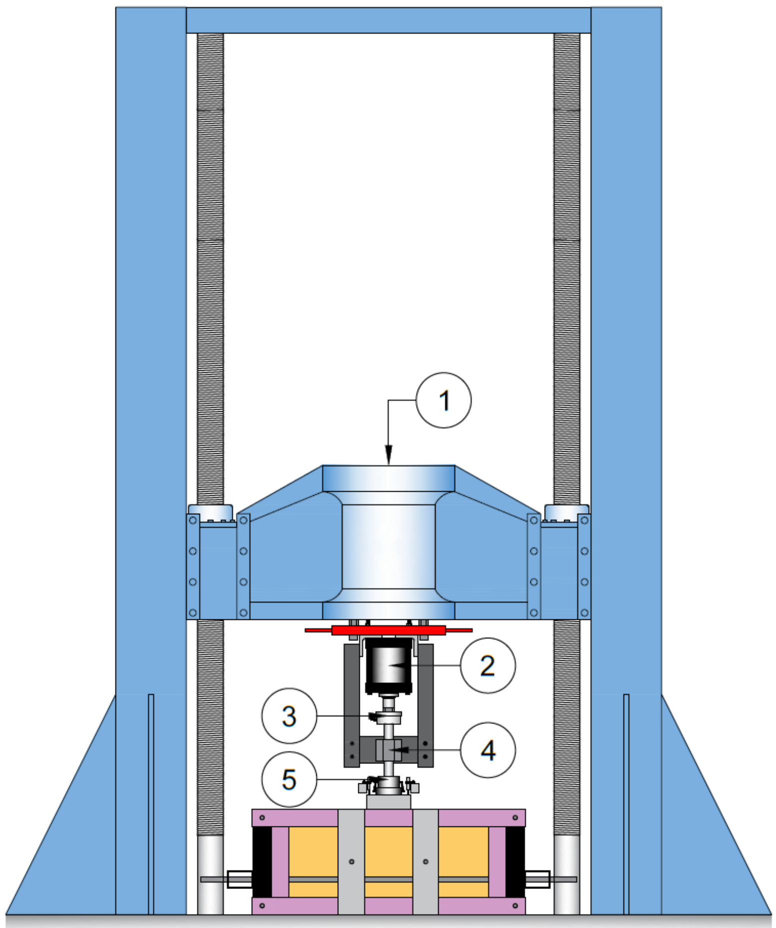

Figure A.3: Pneumatic Cyclic Loading Setup with the Soil Container (1: 400,000lb-Capacity Load Frame, 2: Pneumatic Actuator, 3: Load Cell, 4: Linear Bearing, 5: Ball Joint).

The 50kN load cell is connected to a signal conditioner that supplies it with a 0-10Vdc excitation voltage, receives the output signal in millivolts from its strain gauges arranged in a Wheatstone bridge configuration, filters out electrical noise from its output signal and amplifies it to a 0-10Vdc signal that can then be used for data acquisition purposes and as a feedback signal to control the delivery of the cyclic loading by the pneumatic system.

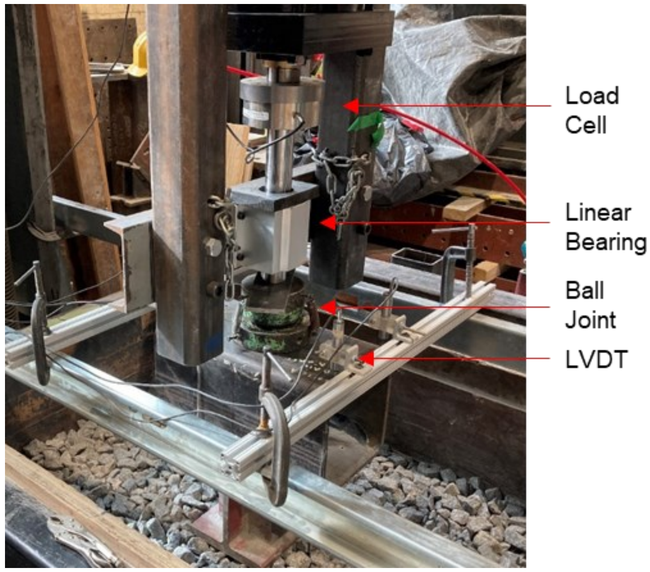

Figure A.4: Load Cell, Linear Bearing, and Ball Joint.

A.3.2. Pneumatic Circuit and Process Control

The actuator is connected to a pneumatic circuit composed of two on/off valves, an air preparation unit, an electronic pressure regulator, a Proportional-Integral-Derivative (PID) controller, and a personal computer that acts as a function generator. Figure A.5 provides a simplified overview of the pneumatic circuit. Once the pneumatic circuit is connected to the laboratory's compressed air line, air is allowed to flow into the circuit by turning on the on/off valves. The compressed air first goes through the air preparation unit which consists of one 5-micron particulate filter placed next to the air tap and one 5-micron particulate filter and one 0.3-micron coalescing filter located immediately upstream of the electronic pressure regulator to remove solid particles, water droplets, and compressor oil from the air stream. Such a filtration arrangement is required to provide clean compressed air that meets the operating requirements of the electronic pressure regulator which is designed to function with compressed air filtered in accordance with ISO 8573-1:2010.

Once the air is filtered to the required standard, it travels down the circuit's tubing to reach the electronic pressure regulator. The electronic pressure regulator is a three-port two-way valve that converts an input electrical signal, either a 0-10Vdc voltage or a 4-20mA current, into a proportional air pressure output. The regulator used in the pneumatic circuit presented herein has a 2.5ms response time and uses direct-acting voice-coil technology to operate at pressures ranging from 0psi (0MPa) to 145psi (1MPa) while delivering a smooth and accurate control of the air pressure output. The pressure regulator is manufactured such that it comes readily connected to a PID controller located in its casing.

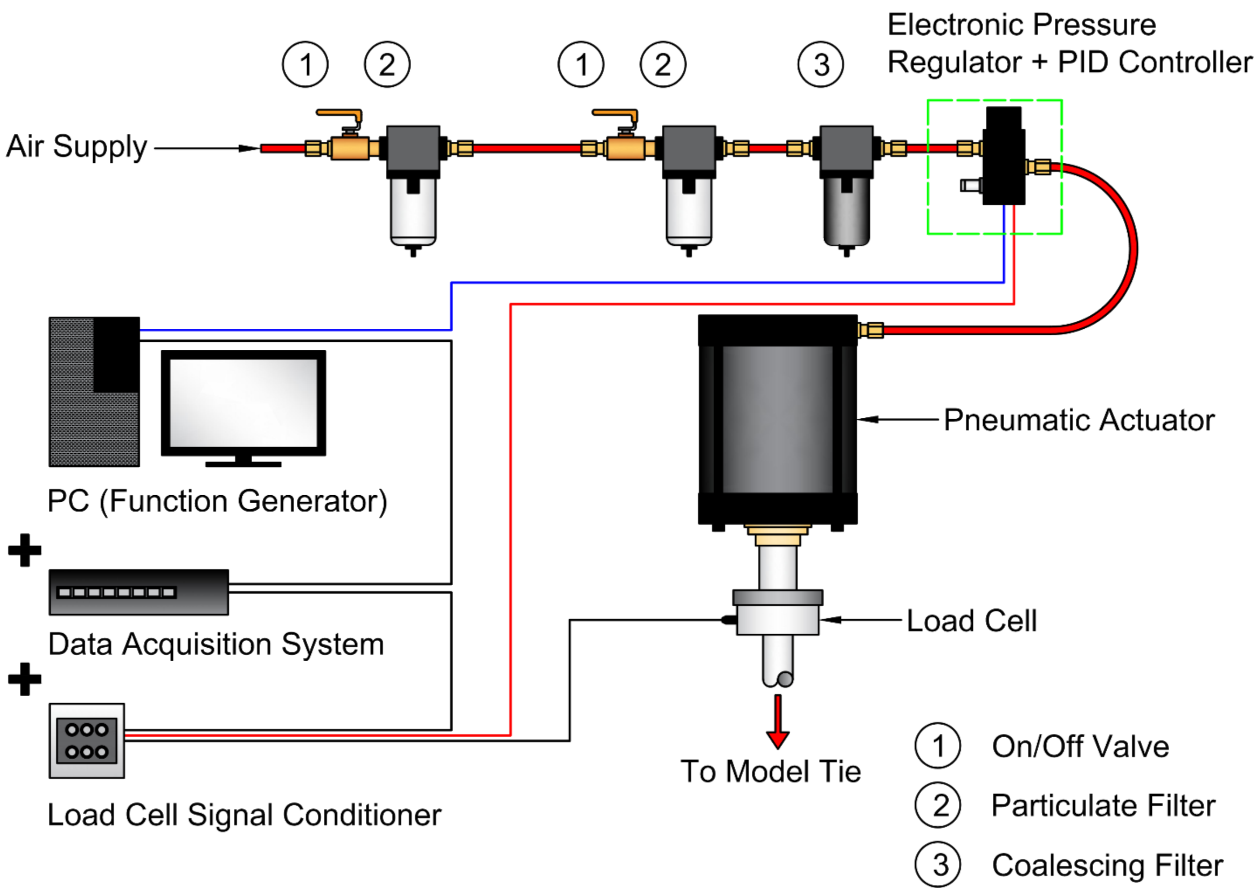

Figure A.5: Simplified Schematic of the Pneumatic Circuit.

The pressure regulator combined with the PID controller works as a closed-loop system and plays a pivotal role in the delivery of cyclic loading. The regulator possesses three ports as shown in Figure A.5: one air inlet port connected to the upstream tubing that comes out of the air filtration unit, one working port linking the regulator to the actuator, and one exhaust port. The regulator can allow air to flow in one of two directions at any given time, i.e., either from the air supply line into the actuator or from the actuator to the exhaust port. When air is allowed to flow into the actuator, the air pressure in the bore volume located above the piston increases which in turn increases the compressive force delivered by the actuator's piston rod. On the other hand, when the regulator allows air to flow out of the actuator toward the exhaust port, air is discharged into the atmosphere thereby decreasing the compressive force applied by the cylinder's piston rod.

The electronic pressure regulator is connected to a personal computer that generates a 0-10Vdc command signal matching the desired loading waveform through software provided by the regulator's manufacturer. The command signal is relayed to the pressure regulator's PID controller which in turn converts it into a fast and accurate pressure output that determines the magnitude of the compressive force delivered by the pneumatic cylinder. The PID controller also receives a 0-10Vdc feedback signal from the load cell. If a difference exists between the desired force output as defined by the command signal fed to the pressure regulator and the force measured by the load cell, the PID controller applies a correction to the opening and closing of the regulator's valve such that the measured force matches the desired force output more closely. The correction applied by the controller is a function of its proportional, integral, and derivative gains. As such, preliminary tests should be conducted prior to the start of a given experimental campaign to tune the PID controller and sure a smooth response of the pressure regulator to the desired command signal.

A.3.3. Displacement Measurement and Data Acquisition

An aluminum frame spanning across the soil container is built using lightweight aluminum beams to support linear variable displacement transducers (LVDTs) such that the displacement of the model tie or footing placed on the soil sample may be monitored as it is subjected to loading. The LVDTs as well as the load cell mounted on the actuator's piston rod are connected to a data acquisition system that logs their output signals at a frequency of 100Hz.